Additive Manufacturing-Induced Roughness in Hydrogen-Fuelled Jet Burners: Experimental Characterisation and Numerical Modelling

Robin Christopher Vivoli

A thesis submitted for the degree of:
Doctor of Philosophy in Mechanical Engineering

Cardiff University

September 2025

Table of Contents

Figure Index

Table Index

Nomenclature

Δ	Approximate Mesh Size for High Physical Resolution Simulations
$\Delta_{\vert\vert}$	Grid Spacing Parallel to The Wall
Δh_c	heat of combustion
Δt	Time Step
Δx	Distance Across a Cell
μ_t	Turbulent Eddy Viscosity
μ	Dynamic Viscosity
8G	Grit-Blasted ALM Swirler, $S_g = 0.8$
8M	Machined Swirler, $S_g = 0.8$
8R	“Raw” ALM Swirler, $S_g = 0.8$
ACE	Advanced Combustion System for High Efficiency
AM	Additive Manufacturing
ASME	American Society of Mechanical Engineers
AU	Arbitrary Units
BECCS	Bioenergy with Carbon Capture and Storage
BLF	Boundary Layer Flashback
C1	Rough simulations with literature-based k_s correlation
C2	Rough simulations with user-defined k_s correlation
C2-8M	Novel Correlation Applied to 8M Swirler
CCGT	Combined Cycle Gas Turbine
CCUS	Carbon Capture, Utilisation, and Storage
CFD	Computational Fluid Dynamics
CL	Chemiluminescence
CMF	Coriolis Mass Flowmeter
Co	Courant Number
CRZ	Central Recirculation Zone
C_μ	K-Omega model constant
Da	Damköhler Number
DDES	Delayed Detached Eddy Simulation
DEM	Discrete-Element Method
DES	Detached Eddy Simulation
DESNZ	Department for Energy Security and Net Zero
DLE	Dry Low Emissions

DNS	Direct Numerical Simulation
e	Energy Dissipation Rate
E	Log Law Offset
EB	Elliptic Blending
EDC	Eddy Dissipation Concept
EDM	Electron Discharge Machining
ER	Equivalence Ratio
f	Roughness function
FCV	Flow Control Valve
FR-C	Fixed Roughness Correlation
FTT	Flow Through Time
FWHM	Full Width at Half Maximum
GHG	Greenhouse Gas
GR-C	Guaranteed Roughness Correlation
G_t	Angular Momentum
GT	Gas Turbine
GTRC	Gas Turbine Research Centre
G_x	Axial Momentum
h	Mesh Grid Height
HHC	High Hydrogen Content
HPGSB-2	High Pressure Generic Swirl Burner (Mk. II)
HPOC	High-Pressure Optical Chamber
ID	Inner Diameter
IDDES	Improved Delayed Detached Eddy Simulation
IEA	International Energy Agency
J	Momentum Ratio
JICF	Jet-in-Crossflow Burner
k	Turbulent Kinetic Energy
Ka	Karlovitz Number
KHI	Kawasaki Heavy Industries
k_{res}	Resolved Turbulent Kinetic Energy
k_s	Equivalent Sand-grain Roughness
k_s^+	Roughness Parameter
k_{SGS}	Turbulent Kinetic Energy modelled by the Subgrid-scale model

k_{tot}	Total Turbulent Kinetic Energy
L_0	Integral Length Scale
LBO	Lean Flame Blowoff
LDA	Laser Doppler Anemometry
Le	Lewis Number
LES	Large Eddy Simulation
LHV	Lower Heating Value
L_t	Integral Length Scale
$\dot{m}$	Mass Flowrate
M1	Machined insert
MHPS	Mitsubishi Hitachi Power Systems
NG	Natural Gas
NO_x	Nitrous Oxides
OEM	Original Equipment Manufacturer
ORZ	Outer Recirculation Zone
P	Burner Ambient Pressure
P_{BB}	Bluff Body instrumentation port
P_{CC}	Burner Face instrumentation port
PJB	Premixed Jet Burner
Q	Mesh Quality Indicator for DES
r	Radial Coordinate
R	Rough Model
R2	Rough insert
Ra	Arithmetic Average Surface Roughness
RANS	Reynolds-averaged Navier–Stokes Equations
RDO	Rough Displaced Origin
Re	Reynolds Number
R_{nozzle}	Swirler Nozzle Radius (20 mm)
Rp	Maximum peak height above the mean line, within a single sampling length
Rq	RMS Surface Roughness
RQL	Rich burn, Quench, Lean burn
Rv	Maximum valley depth below the mean line, within a single sampling length
Rz	Ten-Point Mean Surface Roughness
S	Fuel Factor

S_{conv}	Conventional Swirl Number
S_g	Geometric Swirl Number
SGS	Subgrid-Scale
S_l	Laminar Flame Speed
SLM	Selective Laser Melting
SN	Swirl Number
SRS	Scale Resolving Simulation
S_T	Turbulent Flame Speed
T_{CC}	Combustion Chamber Temperature
T_{EG}	Exhaust Temperature
TI	Turbulence Intensity
T_{inlet}	Inlet Temperature
TP	Thermal Power
TP	Thermal Power
U	Bulk Flow Velocity
$\bar{u}$	Mean Nozzle Exit Axial Velocity
$\bar{u}'$	Velocity Fluctuation Magnitude
U	Velocity Magnitude
u^*	Friction velocity Scale
u'_{RMS}	Fluctuating Axial Velocity
u^+	Dimensionless velocity
u_{max}	Maximum Axial Velocity at Nozzle Exit
U-RANS	Unsteady RANS
U_x	Axial Velocity
U_θ	Tangential Velocity
v	Kinematic Viscosity
V	Volume Flowrate
VDI	Verein Deutscher Ingenieure
WLE	Wet Low Emissions
WMLES	Wall-modelled LES
X_x	Mole Fraction of x
y	Distance to the wall
y^+	Dimensionless wall distance
y_0^+	Displaced Origin

y_m^+	Point at which the viscous sublayer meets the log-layer
Z	Mixture Fraction
δ	Boundary-layer Thickness
δ_l	Flame Thickness
η	Kolmogorov Length Scale
κ	von Karman constant
λ	Taylor Length Scale
ρ	Density
τ	Wall Shear Stress
ϕ	Equivalence Ratio
X	Mole (volume) fraction
γ	K-Omega Blending Function
ω	Specific Dissipation Rate

Acknowledgements

I would like to take this opportunity to sincerely thank my supervisory team at Cardiff University for their invaluable support, guidance, and mentorship throughout the course of this PhD. My gratitude also extends to the wider CDT team for leading the programme, and to the staff at GTRC for their assistance in the design and execution of the experimental campaigns that form a core part of this work.

I am grateful for the financial support and technical insight provided by Jadeed Beita from Siemens Energy, whose industrial perspective has helped shape the practical relevance of this research.

A heartfelt thank you goes to my colleagues in W1.28 and beyond, whose friendship and support have been instrumental in making this journey not only possible, but truly memorable.

To my Welsh colleague, thank you for your perspective, borrowed meeting time, and your always insightful input that helped deepen the quality of this research.

To my ever-persistent Irish colleague, your tireless push for work-life balance, unwavering encouragement, and insistence on regular pub outings provided much-needed levity. You were also a driving force behind my impulsive (but ultimately very worthwhile) investment in new camera gear, and you rekindled my love for trainspotting. Our shared outings and photo missions became an unexpected but vital antidote to PhD fatigue. I genuinely couldn’t have made it through without those moments.

And finally, a massive thank you to my fellow ping pong enthusiast from Pembroke Dock, your quick reflexes and even quicker wit made for countless hours of laughter and much-needed distraction. Your camaraderie brought joy to even the longest of days.

Diolch yn fawr to all who made this journey what it was.

Journal publications and conference proceedings list

Journal Publications:

- **Vivoli, R.**, Goktepe, B., Pugh, D., Morris, S., Bowen, P., & Valera-Medina, A. (2025). Insights from swirl number and ambient pressure variations with a hydrogen/ammonia swirl stabilized diffusion flame. *International Journal of Hydrogen Energy*, *190*, 151941. https://doi.org/10.1016/j.ijhydene.2025.151941
- **Vivoli, R.**, Pugh, D., Goktepe, B., & Bowen, P. J. (2025). Modeling of Roughness Effects on Generic Gas Turbine Swirler via a Detached Eddy Simulation Low-y+ Approach. *Energies*, *18*(19), 5240. https://doi.org/10.3390/en18195240
- **Vivoli, R**., Pugh, D., Goktepe, B., Hewlett, S., Giles, A., Marsh, R., Morris, S., & Bowen, P. (2025). Surface Roughness Effects on the Operability and Performance of a Hydrogen Jet Burner. *Journal of Engineering for Gas Turbines and Power*, 1–33. https://doi.org/10.1115/1.4069474
- Pugh, D., Bowen, P., Navaratne, R., Goktepe, B., Giles, A., Valera Medina, A., Morris, S., & **Vivoli, R.** (2024). Influence of Variable Swirl on Emissions in a Non-Premixed Fuel-Flexible Burner at Elevated Ambient Conditions. Journal of Engineering for Gas Turbines and Power, 146(6). https://doi.org/10.1115/1.4063786

Conference Proceedings:

- **Vivoli, R.**, Pugh, D., Goktepe, B., Hewlett, S., Giles, A., Marsh, R., Morris, S., & Bowen, P. (2025, June 16). Surface Roughness Effects on the Operability and Performance of a Hydrogen Jet Burner. *Volume 3A: Combustion, Fuels & Emissions*. ASME Turbo Expo 2025: Turbomachinery Technical Conference and Exposition. Memphis, Tennessee, USA. https://doi.org/10.1115/GT2025-151389
- Pugh, D., Bowen, P., Navaratne, R., Goktepe, B., Giles, A., Valera Medina, A., Morris, S., & **Vivoli, R.** (2023, June 26). Influence of Variable Swirl on Emissions in a Non-Premixed Fuel-Flexible Burner at Elevated Ambient Conditions. *Volume 3A: Combustion, Fuels, and Emissions*. ASME Turbo Expo 2023: Turbomachinery Technical Conference and Exposition. Boston, Massachusetts, USA. https://doi.org/10.1115/GT2023-102457

Summary

Achieving the UK government's net-zero targets requires key transitions, notably the electrification of domestic heating and transport. While this shift reduces overall energy demand, it necessitates a significant expansion of electricity generation capacity. Although renewable energy sources are expected to dominate the UK's electricity mix, their intermittent nature means Combined Cycle Gas Turbines (CCGTs) will remain essential for system balancing. CCGTs could play a pivotal role during the energy transition if adapted to operate with low- or zero-carbon fuels. Among these, hydrogen has emerged as a promising zero-carbon energy carrier; however, its distinct combustion characteristics demand substantial modifications to current GT combustors and fuel delivery systems to enable 100% hydrogen combustion and meaningful emission reductions. Additive Manufacturing (AM) is increasingly employed to produce critical gas turbine components such as burners, offering advantages that support designing for greater hydrogen capability. However, the relatively poor surface finish associated with AM has been shown to influence combustor performance and flow characteristics. This study investigates the impact of AM-induced surface roughness on state-of-the-art burner configurations operating with hydrogen, focusing on its effects on stability limits and flow-field behaviour.

A series of parametric experimental combustion tests at atmospheric pressure under hydrogen-firing conditions were conducted using two simplified jet burners: a perfectly premixed jet burner (PJB) and jet-in-crossflow (JICF) burner. Both designs allow for inserts representative of conventional machining and AM surface finishes. The objective was to evaluate how surface roughness affects operability and performance across different fuel injection strategies. Experimental findings, combined with insights from numerical simulations of legacy swirl burners with known roughness sensitivity, were used to develop a validated roughness correlation for the PJB under both reacting and isothermal conditions. This correlation was subsequently applied to the JICF configuration to infer additional roughness effects.

The integration of experimental data with the developed numerical framework provides a basis for incorporating surface roughness effects into CFD models, informing gas turbine manufacturers on design adjustments and post-processing considerations for AM-produced burners. This work also lays the foundation for more detailed experimental and computational investigations into roughness-induced phenomena in hydrogen-fuelled combustion systems.

Chapter 1. Introduction

1.1. Background – Gas Turbines and Pathways to Net Zero

Following the goals set by the European Green Deal and the UK's commitment to be powered entirely by clean energy by 2035, the topic of carbon neutrality and how to reach it has found centre stage in many political agendas [1,2]. In 2021, electricity generation accounted for ~20% of total UK greenhouse gas (GHG) emissions making it the second largest single source [3]. Given the close link between electricity generation and heat, such as in combined heat and power systems [4], and the widespread use of hydrocarbons for industrial heat through burners [5], technological advances that improve efficiency and reduce emissions could have far-reaching impacts [3,4]. Decarbonising this sector is therefore critical to achieving ambitious net-zero targets.

Energy research has seen a shift in the past decades, moving from predictive or forecasting approaches to methodologies that offer more tentative claims and explore various plausible scenarios [6]. Out of the many independently developed pathways proposed to achieve the UK's net-zero goals [7,8], most generally agree on the following. Firstly, electrification of domestic heating and transport [9] is the most cost-effective means of curbing fossil fuel use. Secondly, electrification and associated efficiency gains are expected to lower total final energy demand [6]. However, as fossil fuels are phased out and major end-use sectors such as heating and transport are electrified, demand for electricity will increase, necessitating an expansion of electricity generation capacity [2,7]. According to the most ambitious National Grid future energy scenario, shown in Figure 1.1, renewables and particularly wind and solar are going to be responsible for most electricity generation with the use of fossil fuel being phased out by 2035 [7].

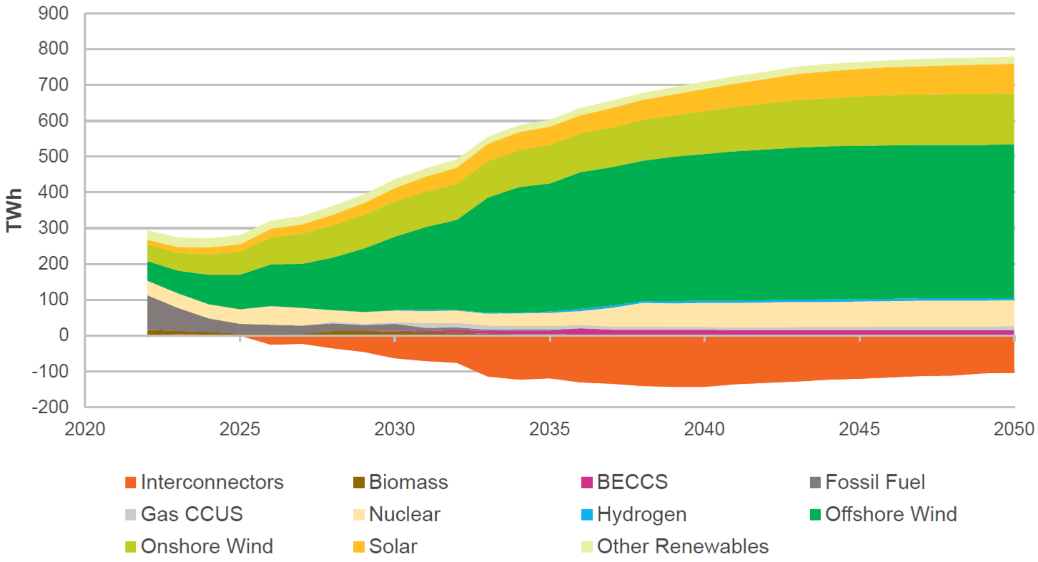

Figure 1.1 *- Electricity generation output according to the "Leading the way" scenario (from National Grid ESO* [7] *p. 126).*

Uptake of renewables has already increased substantially since 2012 [3] with it now making up approximately 50% of the UK capacity (Figure 1.2). This increasing reliance on non-dispatchable energy mean extreme weather conditions such as ‘Dunkelflaute’ (extended periods of simultaneous wind and solar shortfall) can cause significant challenges when it comes to balancing of both current and future grids [10]. Combined cycle gas turbines (CCGTs) currently play a critical role in providing dispatchable capacity and system flexibility and, as shown in Figure 1.2, have accounted for over a quarter of UK electricity capacity since the early 2000s [3]. While CCGTs alone would not fully replace renewable generation during such ‘Dunkelflaute’ events, given their current share of total capacity, the ability to operate these assets on low- or zero-carbon fuels, such as hydrogen, would be vitally important in maintaining security of supply. As such, fuel-flexible CCGTs are likely to remain central to grid balancing during the transition to net zero and as part of long-term low-carbon energy strategies [11].

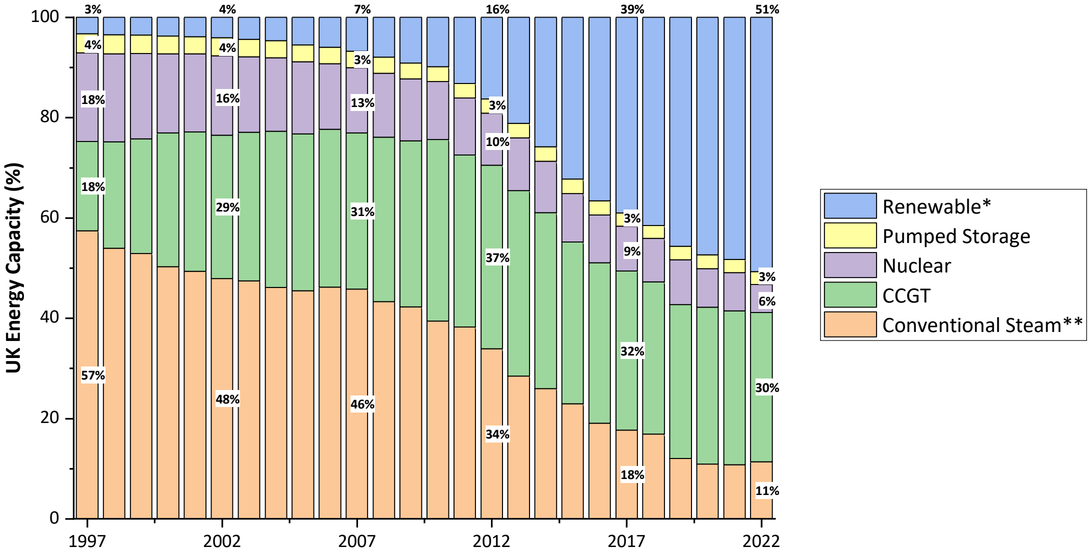

* Capacity on an installed capacity basis

** Includes coal, non CCGT gas, oil and mixed/dual fire. Thermal renewables not included

***Figure 1.2** - Normalised UK electricity capacity from 1997 to 2022 (data from DESNZ* [3]).

1.2. Hydrogen as an Energy Vector – Gas Turbine Fuel Switching

The use of hydrogen as a zero-carbon energy vector has gained significant interest in the past decade [12]. During periods of high wind energy production and low demand for instance, having the possibility to store this excess electricity as hydrogen via electrolysis would help mitigate the intermittent nature of renewable energy [13]. Global hydrogen production reached 95 Mt in 2022 with most of it being used as a feedstock to produce methanol, ammonia and other chemical process feedstock [14]. If new use cases for hydrogen are therefore expected to gain widespread adoption in future energy scenarios, global production must both increase and decarbonise.

Currently, as shown in Figure 1.3(A), hydrogen production is very much reliant on fossil fuels, though numerous low-emission hydrogen production projects have been announced [15]. If the latter all reach completion, an annual global low-carbon hydrogen production capacity of between 20 Mt and 38 Mt, mostly via electrolysers, could be reached by 2030 [14].

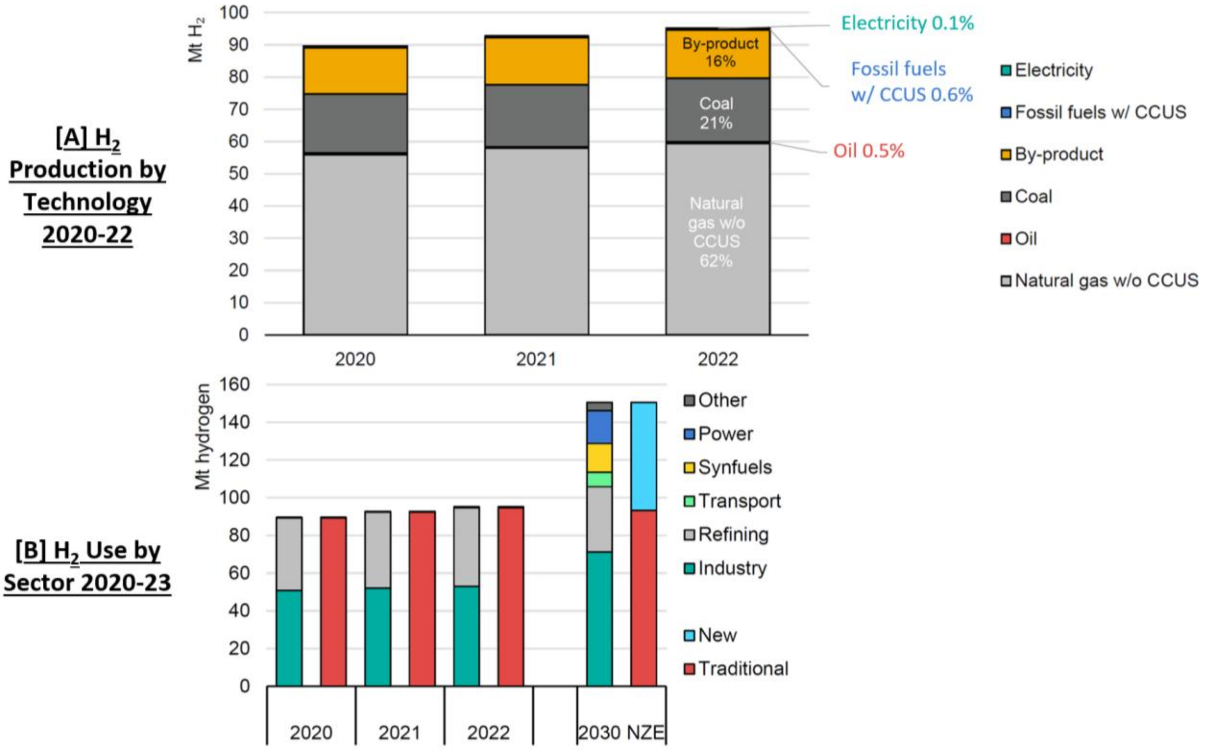

NZE = Net Zero Emissions by 2050 Scenario. "Other" includes building and biofuels upgrading

Figure 1.3 *- Hydrogen production by technology [A]. Hydrogen use by sector [B] (from IEA* [14] *p. 20, 64).*

As can be seen from Figure 1.3(B), according to the International Energy Agency (IEA) net zero by 2050 scenario, nearly 40% of hydrogen usage in 2030 will be coming from new applications [16]. Power generation and synthetic fuel production are expected to make up most of this new demand. When it comes to power generation, hydrogen would most likely primarily be used in gas turbines either as a gas blended with conventional fuels such as methane [17], or as a converted chemical sub-species such as ammonia [18].

The combustion behaviour of hydrogen is markedly different to that of conventional fossil fuels: when compared with methane and natural gas, it is far more reactive, its adiabatic flame temperature is higher, and its flame speed is close to an order of magnitude faster under equivalent conditions [19]. As will be covered in Section 2.2, these characteristics therefore potentially provide lower flame stability, higher NO_x emissions, greatly modified thermoacoustic behaviours and enhanced risks of flashback and auto-ignition [11]. Utilising high percentages of hydrogen in current lean premixed systems is therefore very challenging [20]. According to both Siemens Energy and Mitsubishi Hitachi Power Systems (MHPS) for instance, such combustors and fuel delivery systems designed to operate with conventional fuels can accept hydrogen volume fractions below 20% without needing to be modified [20,21]. Higher hydrogen volume fractions can be achieved via Wet low Emission (WLE) systems but at the cost of increased NO_x emissions, reduced efficiency and higher operating costs [22].

The maximum hydrogen content allowed in current lean premixed Dry low Emission (DLE) systems varies substantially both depending on the manufacturer and turbine type though no DLE system on the market today is able to operate with the full 0 – 100 vol.-% hydrogen content range. Currently, state-of-the-art DLE gas turbine combustors intended for use with high hydrogen content (HHC) fuels can operate reliably when burning fuels containing up to 60 vol.-% hydrogen [23]. Unfortunately, as shown in Figure 1.4, because of the low volumetric energy density of hydrogen, CO_2 reductions only start to become significant when utilising fuel blends containing over 75 vol.-% hydrogen [22].

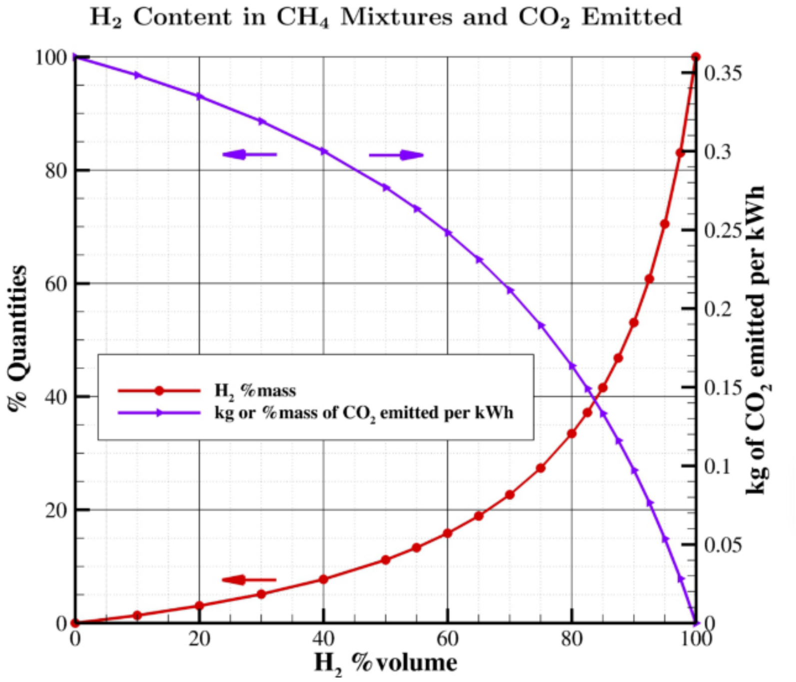

Figure 1.4 *- CO_2 emissions (assuming an electrical efficiency of 55%) vs hydrogen content within methane blends (from Giacomazzi et al [22] p. 126).*

Given gas turbines must be able to reliably operate with hydrogen blends > 75 vol.-% in order for significant reductions in CO_2 emissions to be achieved and the drawbacks associated with WLE systems, most if not all major gas turbine Original Equipment Manufacturers (OEMs) are investing significant R&D resources into the development of DLE systems capable of hydrogen-firing up to 100 vol.-% [20,24,25].

1.3. Combustor Design for HHC Fuels – Additive Manufacturing

The use of Additive Manufacturing (AM) is gaining more widespread adoption thanks to its well documented advantages including weight and part count reduction, increased design freedom and accelerated development cycles [26–28]. These characteristics make AM very appealing to gas turbine OEMs as can be seen from the rapid increase in ASME Turbo Expo papers on the topic since 2015 shown in Figure 1.5 [29].

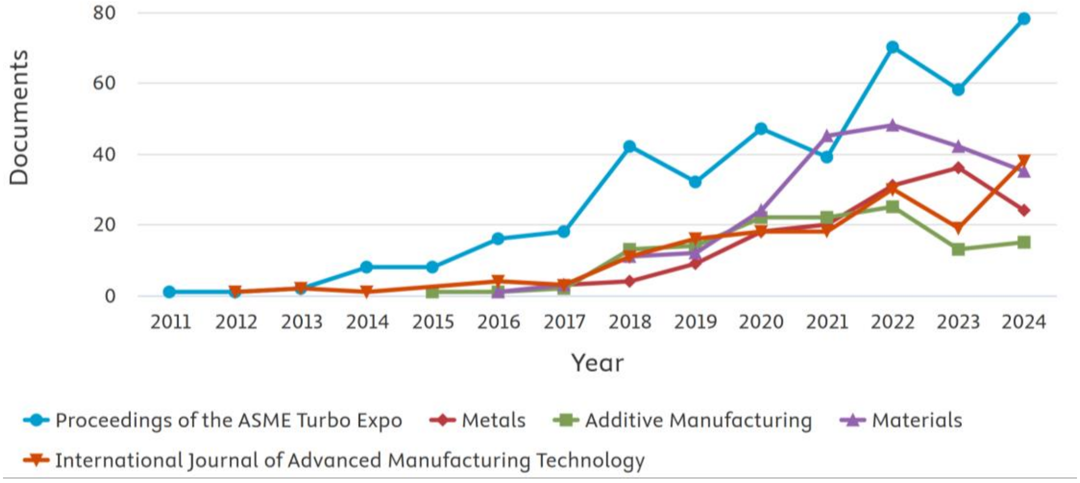

Figure 1.5 *- Papers published on the topic of Additive Manufacturing and Gas Turbines since 2010 (from Scopus* [29]*).*

The total number of journal papers published in the Turbo Expo proceedings remained broadly consistent over the 2011–2024 period [30], indicating that the observed growth in AM publications shown in Figure 1.5 reflect a genuine increase in research interest. In contrast, other research areas appear to have reached peak interest around 2021, with publication numbers plateauing or declining thereafter.

Given the rapid improvements AM has made in the last decade, it is no longer only utilised for rapid prototyping but rather many gas turbine manufacturers utilise it to produce critical components such as entire combustor assemblies (Figure 1.6) [31,32], swirlers and turbine blades [33]. Furthermore, AM has been utilised to perform precision repairs on in-service components extending their operational life [34].

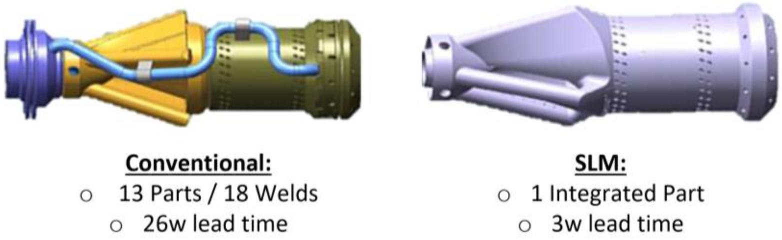

Figure 1.6 *- Conventionally manufactured vs SLM printed SGT-700/800 burners (from Magnusson and Andersson* [32] *p.4).*

1.3.1. Roughness Effects

The poor surface quality of AM components is one of the primary drawbacks of this technology [35,36]. Careful consideration must be given to parameters such as machine settings [36], powder size [37] and build orientation [38] to minimise surface roughness. Even with appropriate parameter selection, additional post processing steps such as grit blasting, large-area electron beam irradiation [39] or chemical polishing [40] may still be required adding time and expense.

Gas turbine burner swirlers are prime candidates for production via AM. Giuliani et al. [41] showed how the increased design freedom enabled the creation of swirler geometries with enhanced lean blow off limit and reduced pressure drop. However, the unprocessed “raw” surface finish of these AM swirlers was found to have a measured effect on pressure drop [41]. Previous experimental work performed at Cardiff University’s Gas Turbine Research Centre (GTRC) has shown how the roughness of swirler wetted surfaces can affect axial velocities, heat release, NO_x emissions and operability limits [42]. Surface roughness should therefore be considered carefully starting from the design stage all the way through to manufacturing and post processing.

Understanding the effects of roughness on boundary layer flashback (BLF) is of prime interest. The need for lean-premixed burners able to accommodate a wide range of vol.-% H_2, has meant operating conditions with a significantly increased flashback risk are reached [43]. Both two-dimensional numerical simulations [44] and experimental work [45] have shown surface roughness and micro-surfaces respectively have the potential to enhance BLF resistance. The increased roughness having been found to increase heat loss near the wall and enhancing boundary layer development. Computational fluid dynamics (CFD) can help shed further light on these roughness effects, by enabling detailed data interrogation in locations that cannot easily be reached experimentally.

When it comes to adding roughness effects to a CFD model three main approaches exist, listed below in order of increasing computational demand [46]:

a) Model roughness via empirical correlations converting measured roughness (e.g. Ra, Rq, Rz) to an “equivalent sand-grain” roughness (k_s) [47,48];

b) Utilise a “discrete-element model” (DEM) to account for roughness blockage, heat transfer, and obstruction drag [49,50];

c) Fully resolve the roughness features [51,52].

Method a) is available in the majority of CFD solvers and is straightforward to implement though the reliance on k_s is a major limiting factor [46,53]. Approaches b) and c) have the advantage of not relying on a k_s correlation though the much higher computational costs make implementation in intricate turbomachinery geometries impractical.

1.4. Summary and Research Question

Key pathways to achieve the net-zero goals set by the UK government include the electrification of domestic heating and transport which mean electricity capacity will need to expand. Though renewables are soon expected to make up most of the UK electricity capacity, their non-dispatchable nature mean CCGTs will still play a crucial balancing role and could be pivotal during the energy transition if adapted to low or zero-carbon fuels. The use of hydrogen as a zero-carbon energy vector has gained significant interest though, due to it having markedly distinct combustion characteristics, current CCGT combustors and fuel delivery systems need substantial modifications to handle hydrogen volumes greater than 20%. Gas turbine OEMs are investing significant resources into increasing the hydrogen firing capabilities of DLE systems towards 100%. Current state-of-the-art combustors are capable of handling up to 60 vol.-% hydrogen, one of the major limiting factors being the propensity of HHC fuels to flashback. Considering significant CO_2 reductions require blends with over 75 vol.-% hydrogen, further development work is still required. AM is being increasingly utilised to produce critical gas turbine components, its well documented advantages aiding the push towards higher hydrogen capabilities. The poor surface finish associated with this technology has been shown to have measured effects on swirl-stabilised combustor performance and flow-fields. Understanding how this surface roughness affects novel burner architectures with particular focus on BLF, is of interest for developing lean-premixed burners capable of operating safely with high hydrogen volumes. Numerical simulation work can provide insights into these effects, though accurately accounting for roughness is far from straightforward.

Building upon these findings the following broad research question can be highlighted:

How does surface roughness associated with AM influence flame stability, operability, and fuel distribution in newly developed hydrogen-fuelled gas turbine burner architectures, and how can these effects be quantified to support roughness-aware CFD modelling?

1.5. Thesis structure

This thesis is organised into eight Chapters, each contributing to a comprehensive investigation of surface roughness effects on the performance and operability of hydrogen-fired jet burners. Both experimental and numerical approaches are employed, including the development of new test facilities and a novel modelling correlation.

A summary of the contents in each Chapter is provided below:

Chapter 1:

Introduces the motivation, research question, and overall structure of the work.

Chapter 2:

Provides a detailed literature review. It begins with an overview of the unique properties of hydrogen that make its combustion challenging, followed by a review of current gas turbine (GT) combustor technologies and their readiness for hydrogen operation. The importance of swirl in legacy burner designs is discussed, alongside the growing use of Additive Manufacturing (AM) in combustion systems. Special attention is given to the role of AM-induced surface roughness on burner performance and the complexities it introduces in numerical modelling. Key challenges in simulating roughness effects accurately are then presented followed by outlining the thesis aims and objectives.

Chapter 3:

Outlines the theoretical framework used throughout the thesis. This includes a review of turbulence modelling strategies, wall treatment methods for rough surfaces, and mesh resolution requirements for high-fidelity simulations. The Chapter also introduces the design and commissioning of the Premixed Jet Burner (PJB) and jet-in-crossflow (JICF) rigs, purpose-built for testing different surface finishes under both isothermal and reacting conditions.

Chapter 4:

Introduces the first results Chapter, presenting numerical studies on a generic swirl burner geometry. Validation against isothermal and methane-reacting experimental data is performed, with several DES approaches evaluated for their ability to capture roughness effects in resolved boundary layers (low-y^+). Initial application of literature-based k_s correlations proves inadequate, prompting development of a new correlation to maintain fully rough regime behaviour. The proposed correlation demonstrates strong performance particularly under reacting conditions.

Chapter 5:

Reports experimental results from the PJB rig. Tests were performed with both smooth and rough-walled inserts, the latter replicating typical Selective Laser Melting (SLM) surface textures. Data collected under isothermal and hydrogen-fired conditions provide insight into the influence of surface roughness on flame behaviour, operability limits and flow structure.

Chapter 6:

Presents the numerical investigation of roughness effects on the PJB under both isothermal and reacting conditions. The isothermal dataset introduced in Chapter 5 was first used to evaluate existing correlations, with the Chapter 4 formulation found to consistently overpredict roughness effects. This motivated the development of a new k_s correlation that incorporates both measured surface roughness and burner bulk flow parameters. Calibrated against the isothermal dataset, the correlation demonstrated strong predictive accuracy and was subsequently applied to hydrogen-fired reacting flow simulations. Comparison with experimental data confirmed its ability to capture roughness-induced changes across a range of thermal loads and equivalence ratios, thereby establishing its suitability for both isothermal and reacting flow modelling.

Chapter 7:

Provides experimental results for PJB and JICF configurations, comparing roughness effects on flame composition and stability when shifting from fully premixed to jet-in-crossflow, industrially relevant setups. Methods align with Chapter 5, enabling assessment of how fuel delivery changes influence roughness-driven operability variations.

Chapter 8:

Concludes the thesis by summarising the key findings and contributions. It also outlines limitations of the current work and suggests future research directions.

Chapter 2. Literature Review

Chapter 2 presents a comprehensive review of the literature on hydrogen combustion in gas turbines, aimed at providing rationale for the objectives outlined in this thesis. It begins by examining the combustion characteristics of H_2 and comparing them to those of hydrocarbons. Following this, the challenges associated with burning hydrogen in gas turbines are discussed. The Chapter then reviews state-of-the-art gas turbine combustion systems focusing particularly on those designed for high hydrogen content applications. The role of swirlers in these systems is analysed, emphasising how surface roughness from additive manufacturing can affect their performance. Finally, various methods for incorporating roughness effects in numerical simulations are reviewed.

2.1. Combustion Characteristics of H_2

Hydrogen gas is the smallest of all elements, being roughly eight times lighter than methane [54]. It is also the most abundant element in the universe though its extreme reactivity means that, on Earth, it cannot be found as a standalone molecule [25]. The combination of high reactivity and low density makes its combustion characteristics very different to those of fossil fuels as shown in Table 2.1.

Table 2.1 *- Comparison of H_2 and CH_4 properties.*

	H_2	**CH_4**
Molecular Weight (kg / kmol) [54]	2.016	16.04
Density* (kg / m^3) [54]	0.08	0.65
Self-Ignition Temperature (K) [24]	845 - 858	813 - 905
Minimum Ignition Energy (mJ) [24]	0.02	0.29 - 0.33
Flammability range (ϕ) [55]	0.1 - 7.14	0.5 - 1.67
Adiabatic Flame Temperature (K) [24]	2318 - 2400	2158 - 2226
LHV (MJ/Kg) [24]	118.8 - 120.3	50
LHV* (m^3/Kg) [24]	10.78	35.8
HHV (MJ/Kg) [54]	141.75	55.5
HHV* (m^3/Kg) [54]	11.6	36.17
Lower Wobbe Index* (MJ/m^3) [54]	40 - 48	47 - 53

* Values at normal temperature and pressure

On a gravimetric scale, the lower heating value (LHV) of hydrogen is roughly 2.4 times larger than that of methane whilst, on a volumetric basis, it is roughly 3 times smaller. To achieve similar energy outputs, higher volumetric flowrates are therefore necessary meaning fuel supply systems with higher capacities are needed [25]. Furthermore, it is important to note that, when hydrogen is mixed with fossil fuels, the overall volumetric LHV will be reduced [56].

The flammability range of hydrogen is extremely wide as shown in Figure 2.1. When added to slower burning fuels, it expands the flammability limits of the mixture thus enabling leaner combustion, improving both emissions and system efficiency [24,56].

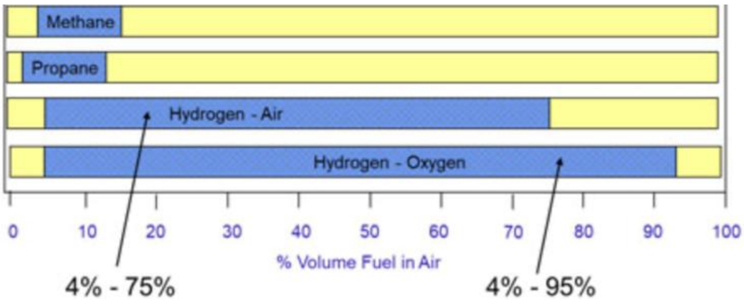

Figure 2.1 *- Hydrogen flammability range comparison with other fuels. (from WHA* [57]*).*

Given this broad flammability range and low minimum ignition energy (Table 2.1), any leak presents a substantially increased risk of ignition. This is particularly significant considering hydrogen has an extremely small molecular size meaning the probability of leaks is higher. Far more attention must therefore be given to ensure the risk of leaks is minimised and that appropriate detectors and ventilation measures are implemented [57].

The adiabatic flame temperature of hydrogen is higher than that of natural gas and methane at the same stoichiometry therefore leading to potential increases in NO_x emissions [24]. From a design standpoint, changes in adiabatic flame temperature can have a significant effect given they influence both cooling requirements and combustion efficiency [25].

The peak laminar flame speed of pure hydrogen is approximately an order of magnitude faster than that of natural gas (NG) and methane [11,58]. Increases in laminar flame speed can also be substantial for hydrogen fuel blends as shown in Figure 2.2.

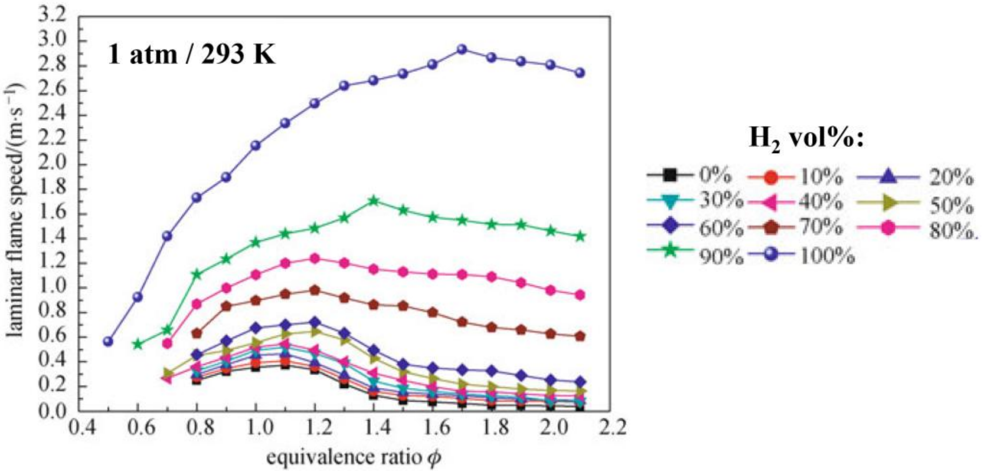

Figure 2.2 *- Laminar flame speeds of H_2/NG/air mixtures versus equivalence ratio (from Dong et al.* [59] *p. 420).*

The turbulent flame speed (S_T) of a fuel blend also increases with increasing hydrogen content, though, as shown in Figure 2.3, when the hydrogen content is over 50 vol.-%, this occurs drastically and nonlinearly when compared with the laminar flame speed increase [60,61].

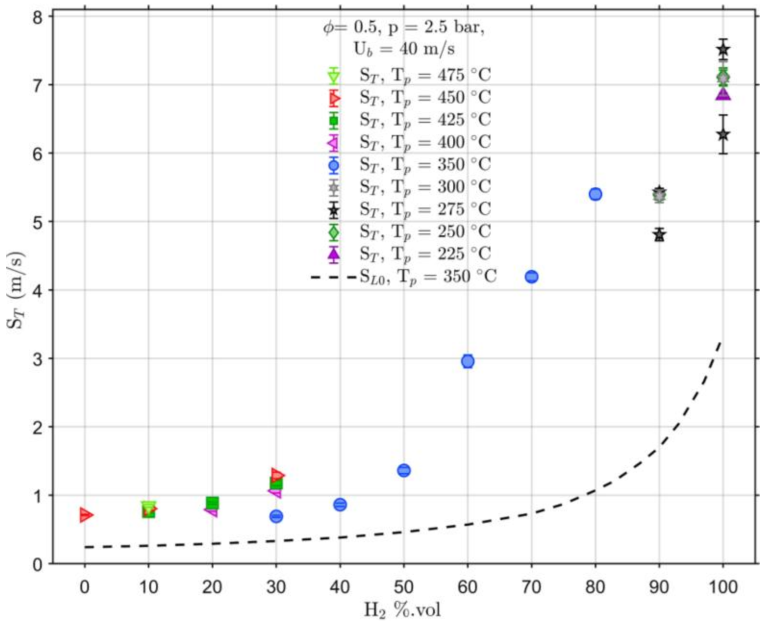

Figure 2.3 *- S_T as function of H_2 vol.-% (CH_4 blend) for different preheating temperatures (T_p). (from Faldella et al. [61] p. 5)*

Overall, higher flame speeds imply greater risks of flashback and, consequently, the resulting flame will have a far smaller operating range as defined in Section 2.2.3. In addition, higher flame speeds lead to a reduced combustion duration and shorter flames the position and centre of heat release of which will be shifted upstream closer to the burner outlet as is shown in Figure 2.4 [56], [60,62].

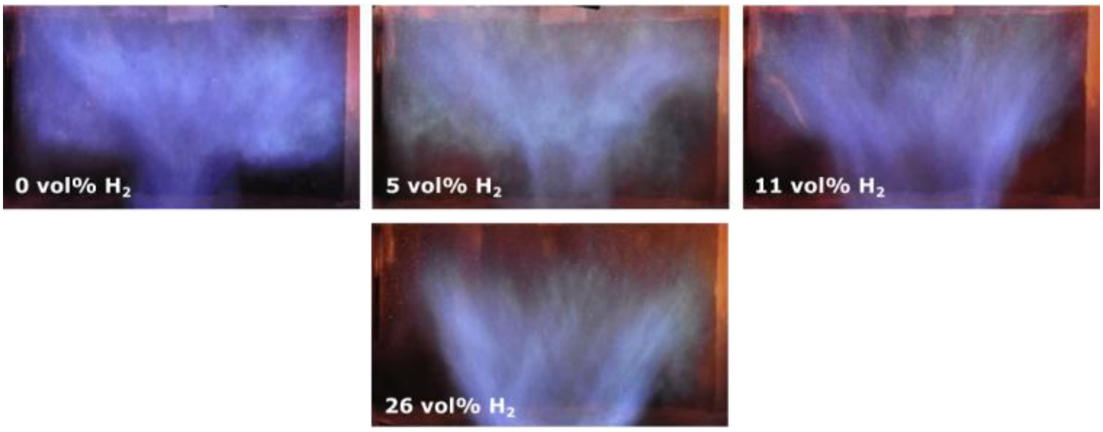

Figure 2.4 *- Typical hydrogen enriched natural gas flames. (From Ge. et al* [63] *p. 14027).*

The higher flame speed of hydrogen would theoretically allow for shorter combustion chambers which carries the advantage of reducing combustion residence times, NO_x formation and cooling requirements. At the same time, shorter combustion chambers would have the major drawback of drastically limiting the fuel flexibility of the system [24].

Regardless of fuel type, the range of equivalence ratios in which stable operating conditions are reached is delimited by blowoff and flashback. HHC fuels present a distinct behaviour when approaching blowoff conditions. As a general definition, blowoff occurs when the flow velocity of the mixture is faster than the burning velocity. This causes the flame to detach from the burner and propagate at a distance from it [24]. Once blowoff conditions are reached, lean flame blowoff (LBO), characterised as flame extinction caused by a reduction in the fuel-air ratio beyond a minimum limit at which a given geometry can sustain a flame [64], may occur. Whilst natural gas and methane flames enter an evident extinction/reignition phase when nearing blowoff, hydrogen can exhibit different behaviour such as taking a nearly steady columnar appearance whilst slowly extinguishing as shown in Figure 2.5 [65]. The distinction between blowoff and LBO can therefore become mostly semantic when dealing with HHC fuels.

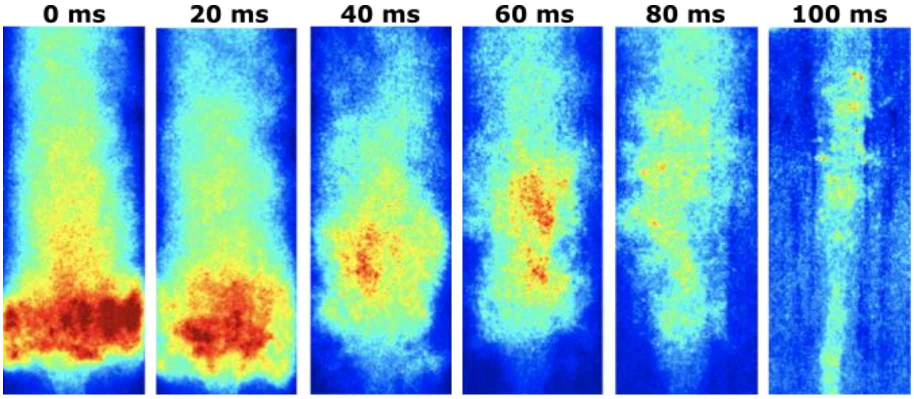

Figure 2.5 *- 50/50 CH_4-H_2 blend at near blow-off conditions $\varphi = 0.35$ (from Lieuwen and Zinn [65] p. 60).*

Flashback occurs when the local flame speed is faster than the velocity of the fuel/air mixture leaving the duct [66]. The flame will therefore propagate upstream causing damage to the fuel injectors [24] as is shown in Figure 2.6. Due to the high reactivity of hydrogen, the risk of flashback is inherently increased. This is one of the main challenges being faced by gas turbine manufacturers and will be covered more thoroughly in Section 2.2.3.

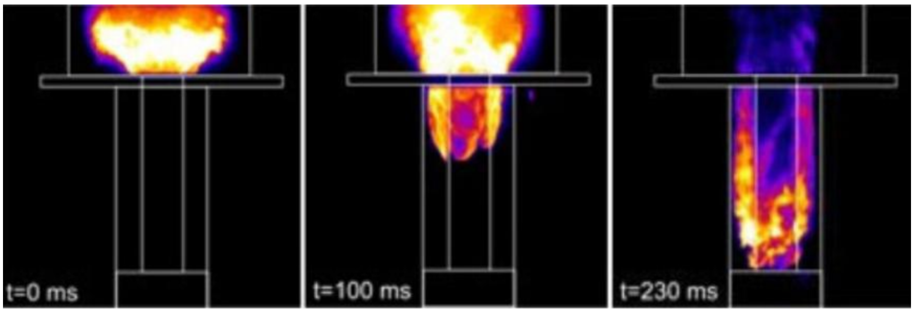

Figure 2.6 *- Flashback visualisation (from Mitsubishi Power* [67]*).*

2.1.1. Thermodiffusive Effects

A key distinction between hydrogen and fossil combustion lies in their Lewis numbers (Le), the ratio of thermal diffusivity to mass diffusivity [68]. Hydrogen exhibits a remarkably low Lewis number (Le $\ll 1$) because its mass diffusivity is substantially higher relative to its thermal diffusivity [69,70]. In contrast, fossil fuels have Lewis numbers closer to unity (Le ≈ 1), indicating more balanced heat and mass transport [69]. This disparity leads to pronounced thermodiffusive instabilities in lean hydrogen flames. In low-Le conditions, differential diffusion amplifies small perturbations in the flame front, causing cellular structures, enhanced flame wrinkling, and significantly elevated local flame speeds [71,72]. Numerical studies have shown such instabilities can result in flame speeds up to four times higher than the laminar burning velocity in lean H_2/air flames [72] as well as anomalous behaviour when nearing flashback limits [73,74].

2.2. Challenges Associated with HHC Fuels

In the pursuit of attaining safe and reliable gas turbine operation with hydrogen contents reaching 100%, several difficulties arise due to the fuel properties differing significantly from those of conventional fossil fuels as covered in Section 2.1. Major challenges, which will be investigated below, include higher NO_x emissions, risks of autoignition, reduced operability limits and greatly modified thermoacoustic behaviours

2.2.1. NO_x Emissions

NO_x emissions (incorporating NO and NO_2) form when fuel is burnt at high temperatures and are one of the main gases responsible of the production of acid rain and smog. They also play a role in exacerbating global warming [75]. Powerplants and subsequently gas turbines therefore have to follow ever more stringent regulations limiting the amount of NO_x emissions that can be emitted [76].

In addition to thermal NO_x, which arises from high-temperature reactions between nitrogen and oxygen, other mechanisms can contribute to NO_x formation during combustion [77,78]. Prompt NO_x forms very rapidly in fuel-rich regions through reactions involving hydrocarbon radicals and atmospheric nitrogen. Fuel NO_x originates from nitrogen bound in the fuel itself, particularly in liquid (such as ammonia) or solid fuels, and is released as nitrogen oxides during oxidation. Although these mechanisms can be significant depending on fuel type, flame structure, and operating conditions, thermal NO_x typically dominates in high-temperature gas turbines [79]. In hydrogen combustion, the lack of both fuel-bound nitrogen and hydrocarbon radicals ensures that thermal NO_x is the dominant and practically exclusive source of nitrogen oxides [19].

Due to the high temperatures at which hydrogen burns, it has been widely reported in the literature that NO_x emissions can increase exponentially with the addition of higher hydrogen concentrations [25,80,81]. Whilst this can be the case, depending on the normalisation methods used to compare emissions from different fuel blends, it has been shown that NO_x values of HHC fuels can be overpredicted by up to 37% [82]. According to the widely utilised BS ISO 11042-1:1996 standard for instance, raw volumetric stack concentration of pollutants are first to be dried utilising equation [2.1] and then diluted to 15% O_2 via equation [2.2] [83].

$$NO_{x\ dry} = \frac{NO_{x\ measured}}{1-\chi_{H_2O}} \qquad [2.1]$$

$$NO_{x\ dry\,15\%\,O_2} = NO_{x\ dry} \cdot \left(\frac{0.209-0.15}{0.209-\chi_{O_{2Dry}}}\right) \qquad [2.2]$$

When compared to hydrocarbons however, for a given thermal power, hydrogen combustion requires less oxygen and generates products with a higher proportion of H_2O as can be seen below:

$$3.3H_2 + 1.65Air \Rightarrow 3.3H_2O + 6.2N_2 \qquad [2.3]$$

$$CH_4 + 2Air \Rightarrow CO_2 + 2H_2O + 7.52N_2 \qquad [2.4]$$

Consequently, exhaust samples from HHC fuels will be more concentrated once dried and will require less dilution to reach a target O_2 concentration. Even when the mass of NO_x emissions is identical, fuels containing higher fractions of hydrogen will therefore have higher reported values when using the ppmv at 15% O_2 method with no correction factor [84].

This fuel dependent relationship between pollutant mass production and measured ppmv is well known in the environmental community but, until recently, less so in the combustion community [84]. It is accounted for via so called Fuel Factors (*S)* defined as the flue gas volume per unit of useful thermal energy supplied by the fuel [82]. Values of *S* for different fuels can either be calculated from first principals [82] or found in emissions standards such as EN ISO 16911-1 [85]. A collection of *S* values for different fuels is shown in Table 2.2.

***Table 2.2** - Fuel Factor values and relative change compared to natural gas (from ETN* [82] *and EN ISO 16911-1* [85]*).*

	Natural Gas	Gas Oil	Fuel Oil	Hard Coal	Hydrogen
S **(m^3/MJ) at 15% O_2 dry**	0.845	0.859	0.873	0.901	0.616
% change – Natural Gas as reference	1.000	0.984	0.968	0.938	1.372

As can be seen from Table 2.2, the fuel factors of the hydrocarbons shown present little deviation between each other. If the reported NO_x values were therefore not corrected, a nearly negligible difference would be seen. For hydrogen however, S is ~30% smaller than that of natural gas thus a significant overestimation of its NO_x emissions would be made if the correction was not applied.

Rather than having to look up or calculate fuel factors, a different normalisation approach to ppmv at 15% O_2 could be utilised. Douglas et al. [86] for instance suggested three alternative methods for comparing emissions more consistently across different fuels. Out of the three, reporting emissions as a ratio of pollutant mass over heat input (equation [2.5]) seems to have the most promise.

$$NO \frac{\dot{m}_{NO}}{Q_{in}} = \frac{\chi_{NO} \cdot \rho_{NO} \cdot \dot{V}_{EG}}{\Delta h_c \cdot \rho_{NO} \cdot \dot{m}_{fuel}} \qquad [2.5]$$

Regardless of how NO_x emissions are normalised, political and environmental pressures mean continuous efforts will be needed to reduce them further. One of the simplest ways of reducing thermal NO_x formation is by lowering the combustion temperatures via the injection of steam or nitrogen though this decreases overall efficiency [11]. Alternatively, post-combustion De-NO_x technologies such as Selective Catalytic Reduction could be used, though retrofitting is very difficult and costly [11]. Given the drawbacks associated with the latter methods, reducing combustor NO_x emissions via lean premixed combustion (Dry Low Emission – DLE) is the preferred option and is where most research is being undertaken [87].

2.2.2. Autoignition

Autoignition can be defined as the spontaneous self-ignition of a combustible mixture. Regardless of the fuel type, once it is sufficiently mixed with an oxidiser and reaches specific temperatures and pressures, there is a finite amount of time, identified as ignition delay time, before it will spontaneously combust [79]. Considering modern gas turbine inlet pressures and temperatures are typically high enough for autoignition to occur, knowing the ignition delay time of the fuels intended to be used is crucially important when designing combustion systems [88]. This is particularly the case for DLE systems given they operate with high levels of pre-mixing. As can be seen in Figure 2.7, ignition delay times decrease with hydrogen addition due to its high reactivity and low minimum ignition energy [66,89]. Lowering of the ignition delay time means designing flexible DLE combustion systems capable of operating with fuels containing a wide range of hydrogen is extremely challenging [24].

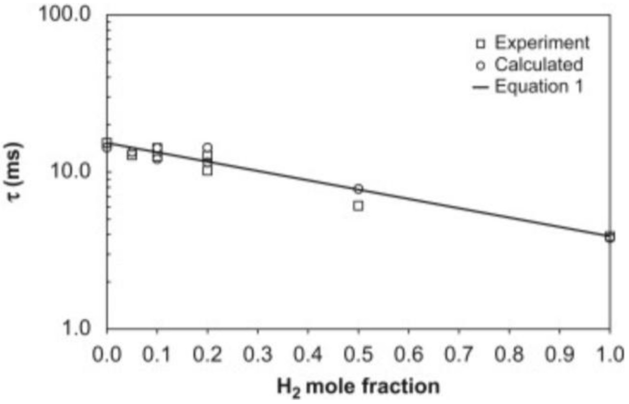

Figure 2.7 *- Ignition delay times vs hydrogen mole fraction (from Gersen et al. [89] p. 1961).*

2.2.3. Operability Limits

Operability limits can be said to have a fluctuating dependency on hydrogen addition. For fuels containing low hydrogen vol.-%, operability limits are increased and the blowoff flame temperature reduced, particularly at low combustor pressures and inlet temperatures [56]. In parallel, particularly at higher combustor pressures, fuels containing higher vol.-% H_2 will experience flashback at significantly lower equivalence ratios than conventional fuels [90]. Hydrogen induced changes in the stability limits of a swirling premixed combustor are shown in Figure 2.8.

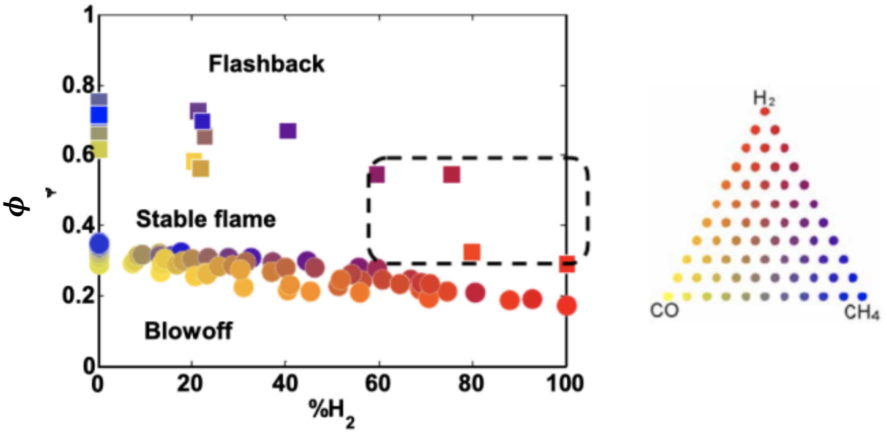

Figure 2.8 *- Lean Blowoff and Flashback limits of Syngas [left], colour coding for different fuel compositions [right]. (From Noble et al.* [90] *p. 4-5).*

From Figure 2.8, it is evident that one of the major factors limiting current state-of-the-art lean premixed systems to a ~60 vol.% hydrogen fraction or lower is the greatly reduced operability limits of HHC fuels [91]. This operability window is further worsened by the high inlet temperatures and pressures at which gas turbines operate. In addition, the risk of flashback is inherently increased in systems that utilise premixing of fuel and air before combustion. It can be prevented by increasing the bulk flows within the burner however this has the undesired effect of increasing pressure drop [92].

2.2.3.1. Boundary Layer Flashback

As already introduced in Section 2.1, flashback is of major operational concern when it comes to premixed combustion. Even more so when dealing with fast hydrogen flames. Independent of fuel type, flashback may arise from autoignition, combustion instabilities, or flow-field conditions that promote *bulk* and *boundary-layer* flashback (BLF) [93]. Of these, bulk and boundary-layer mechanisms are the most significant: bulk flashback occurring when the flame propagates upstream through the core flow, while BLF is initiated in the near-wall region. Both are visualised in Figure 2.9. Whilst *bulk* flashback can be said to be triggered when the ratio between bulk flow (*U*) and laminar flame speed (S_l) becomes < 1, a more complex relation exists for BLF. At the wall in fact, *U* goes to zero thus, according to the bulk flashback criterion, flashback should always occur. This however is not the case as flame quenching occurs near the wall due to a reduction in temperatures [94].

Another criterion is usually applied near walls. In particular, in the zone (*d*) where local flow speed is less than the flame speed, flashback can occur if *d*:

- is large enough for the flame to propagate in.
- is larger than the quenching distance which is of the order of the flame thickness δ_l.

Assuming that the velocity profile is linear near the wall, the size *d* is controlled by the velocity gradient at the wall $g = dU/dy$. Based on this, Von Elbe et al. [95] first introduced the critical velocity gradient concept where the flame can be said to move upstream along the wall if the flow speed *U* at a distance δ_l is less than the flame speed S_l ($S_l / \delta_l = 1$).

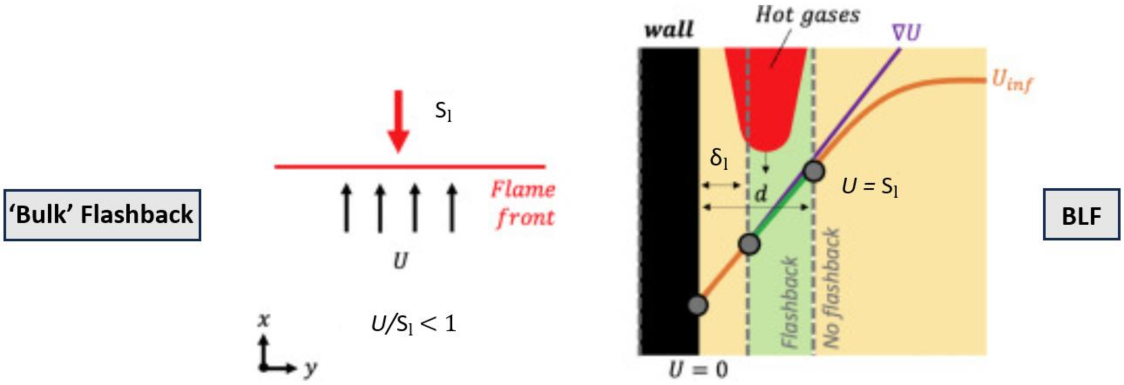

Figure 2.9 - Comparison of 'Bulk' Flashback [left] and BLF [right] (From Bertsch et al. [94]).

Hydrogen addition demonstrably influences the conditions under which flashback occurs as already discussed at the onset of Section 2.2.3. The increased reactivity of hydrogen resulting in a heightened propensity for flashback that scales with its concentration [90]. This trend is observed in both bulk flashback and BLF. However, findings by Bertsch et al. [94] indicate that, in the case of BLF, hydrogen may exhibit non-intuitive behaviour. Their direct numerical simulations (DNS) of BLF in lean hydrogen–air flames revealed that, although a decreasing ratio of laminar flame speed to flame thickness (S_l/ δ_l) generally correlates with an increasing critical velocity gradient required to suppress flashback, consistent with previous literature [96,97], very lean hydrogen flames ($\phi \leq 0.4$) exhibit an absolute flashback speed that is higher than anticipated. This anomalous behaviour has been attributed to pronounced thermodiffusive effects, wherein, as introduced in Section 2.1.1, the high diffusivity of hydrogen relative to other species intensifies preferential diffusion phenomena, potentially destabilising the flame front and facilitating upstream propagation despite adverse velocity gradients [73,74].

Given the aforementioned modifications to flashback characteristics induced by hydrogen enrichment, it follows that previously documented effects of surface roughness on flashback and stability limits may not directly translate when the fuel is substituted with hydrogen. Consequently, caution is warranted when extrapolating conclusions drawn from hydrocarbon-fuelled systems [44,45] to hydrogen-based configurations. In light of these complexities, dedicated investigations into the role of surface roughness on flashback phenomena in hydrogen-fuelled systems are warranted to establish an accurate understanding and to inform safe combustion system design.

2.2.4. Thermoacoustic Instabilities

Thermoacoustic instabilities are considered one of the most challenging fields of combustion research and can be defined as unwanted, large amplitude oscillations of one or more natural acoustic modes of a combustor caused by the resonant interaction between fluctuating flow and unsteady heat release [98,99]. If left uncontrolled, these instabilities can cause many unwanted effects including increased heat transfer rates, component vibrations, flame blow-off and flashback [100]. Over time, these oscillations can result in substantial system deterioration and, in worst-case scenarios, lead to structural damage or failure as shown in Figure 2.10.

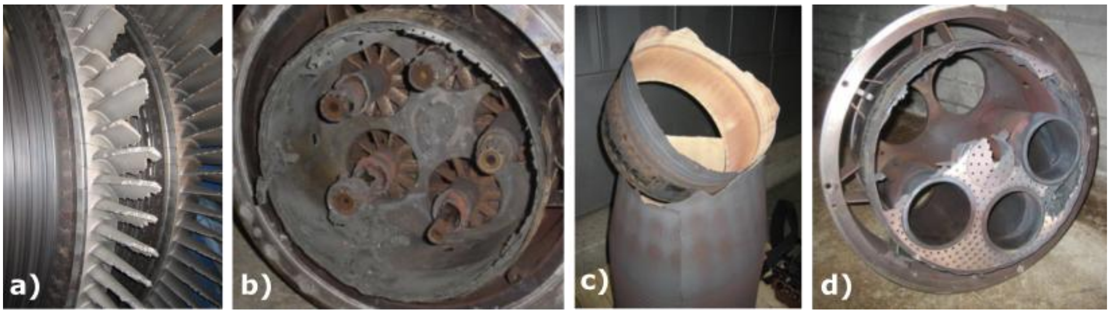

Figure 2.10 *- Thermoacoustic instability induced damage in a turbine blade [a], burner assembly [b], gas turbine liner [c], combustor face plate [d]. (From Emmert* [101] *p.1 and Morgans* [102] *p. 8).*

When developing gas turbine combustors capable of operating with HHC fuels, important consideration must be given to the substantial changes in thermoacoustic instability characteristics associated with burning these fuels [62]. Combustors that remain stable with hydrocarbons may become unstable when hydrogen is introduced, as illustrated in Figure 2.11.

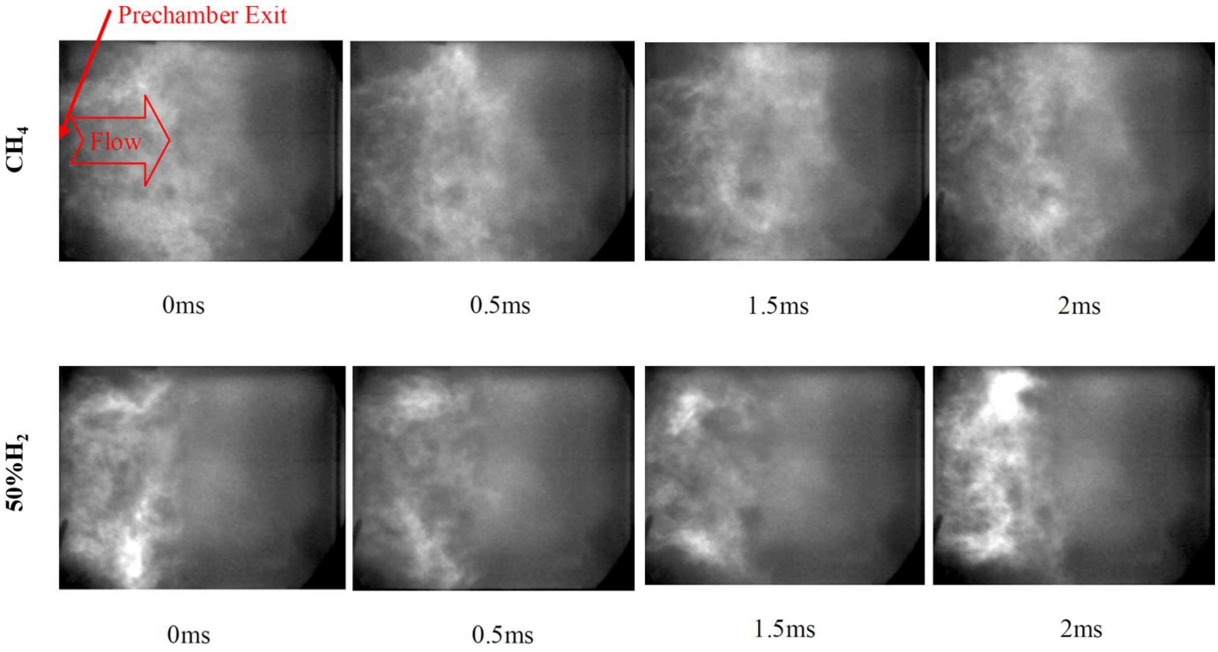

Figure 2.11 *- High speed images of atmospheric natural gas [top] and 50% H2 [bottom] flame (from Lam et al. [103] p. 7-8).*

From Figure 2.11 it can be seen that, whilst the natural gas flame presents little changes across the different frames and has evenly distributed luminosity suggesting heat release is uniform, the opposite is true for the hydrogen flame [103]. Both a greater understanding of the physical mechanisms contributing to combustion dynamics of HHC fuels and reliable, real-time monitoring and control systems are therefore needed [11].

Research suggests that the amount of hydrogen needed to trigger dynamic instabilities is lowered as pressure is elevated. During a series of studies performed at atmospheric pressure, 2 bar and 3 bar, Zhang and Ratner [104] found that, for the same hydrogen concentration, increasing the operating pressure enhanced flame front wrinkling. It was also found that increasing the combustion pressure lowered the amount of hydrogen needed to trigger combustion instabilities. Similar findings were observed by Emadi et al. [105].

Lam and Parsania [103] evaluated the performance of the Siemens Energy SGT-400 combustor when fuelled with blends of natural gas and up to 20 vol.-% hydrogen at full engine pressure and temperature. For the hydrogen enriched fuels, it was found that combustion dynamics shifted to a higher frequency and that the amplitude of combustion oscillations rose sharply with increasing inlet pressure and combustor exit temperature. At the same full load firing temperature, these fluctuations were in fact reported to be three times higher than those for pure natural gas. Similar conclusions were drawn when investigating the performance of the third generation DLE burner used by Siemens Energy in the SGT-800 [106]. In this case, the use of hydrogen-enriched fuel resulted in a one-third decrease in the amplitude of the lower frequency mode whilst the amplitude of the higher frequency mode doubled.

From a surface roughness perspective, its primary influence on thermoacoustic instability arises from its effect on flow dynamics within the combustion chamber, particularly in the near-wall boundary layer [107,108]. Han et al. [109] reported that increasing roughness on the outer wall of a swirling combustor can suppress flame shape transitions and delay the onset of thermoacoustic instability, likely due to weakened vortex structures and reduced strain rates in the outer shear layer. In contrast, roughness on inner walls was found to exacerbate thermoacoustic instability. Other works [42] have also highlighted changes in surface roughness can exacerbate thermoacoustic instabilities. Although studies on the effects of surface roughness remain limited, these findings indicate that further research is warranted to better understand roughness effects on both instability mitigation and exacerbation.

From the studies reported in this Section it can therefore be seen that combustion instabilities in hydrogen-enriched flames can be further exacerbated by increasing the combustor operating pressure. This therefore indicates that atmospheric test results cannot be directly applied or extrapolated to pressurised conditions. At the same time, it has also been shown that combustor destabilisation due to hydrogen addition at elevated pressure is highly dependent on the specific combustor design and operational parameters [62].

2.3. Combustion Systems

The drive to reach higher efficiencies together with wanting to increase the firing capabilities of HHC fuels has meant that keeping NO_x emissions within the ever more stringent legal limits has and will be a major challenge. As was mentioned in Section 2.2.1, reducing combustor temperatures through lean combustion or exhaust gas recirculation is the preferred strategy for limiting NO_x formation, avoiding reliance on costly flue-gas treatment systems [11]. The two main direct NO_x reduction strategies are water or steam injection known as Wet Low Emission (WLE) and high levels of fuel-air premixing at a low equivalence ratio known as Dry Low Emission (DLE). The current hydrogen capabilities of both systems are shown in Figure 2.12.

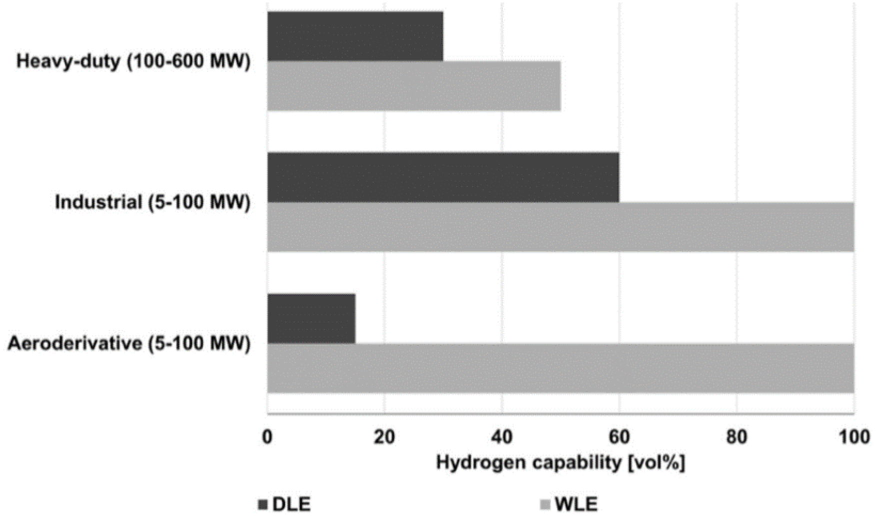

Figure 2.12 *- Current hydrogen capabilities of DLE and WLE gas turbines. (From Stefan et al.* [110] p. 2*).*

The basic mode of operation, advantages and disadvantages of both systems will be presented below with more attention being given to state-of-the-art DLE technologies as these are the systems on which OEMs are investing significant R&D efforts.

2.3.1. Wet Low Emission systems

WLE systems are based around diffusion combustors. This type of combustor operates by injecting fuel and air independently and then mixing them via turbulent diffusion in the combustion chamber. This lack of premixing means diffusion combustors are generally very stable and are therefore capable of handling fuels containing up to 100 vol.-% hydrogen. In parallel, poor mixing prior to combustion leads to richer flames, higher temperatures and subsequently higher NO_x emissions. A state-of-the-art diffusion system burning 100 vol.-% hydrogen for instance will produce three times greater NO_x emissions than an equivalent natural gas system [24]. WLE systems try to mitigate this via the injection of steam into the combustion chamber as shown in Figure 2.13 [111].

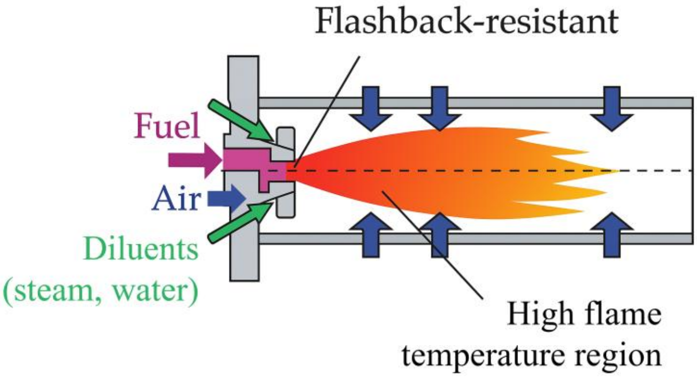

Figure 2.13 *- WLE schematic (from Asai et al.* [112]).

The large amount of dilutants needed when operating a WLE system add complexity to the system, increase costs and reduce the overall cycle efficiency. If retrofitting, significant hardware modifications are required to enable the system to cope with the increased fuel flow rate. Finally, though dilution helps reduce NO_x levels, WLE NO_x emissions are still higher than those of equivalent DLE systems [113].

2.3.2. Dry Low Emission systems

Premixed lean combustion is currently state-of-the-art in heavy-duty stationary gas turbines. These systems are based around lean-premixed combustors that, as the name suggests, premix the fuel with a large amount of excess air before it enters the combustion chamber [79]. Extensive premixing and low equivalence ratios mean combustion temperatures are reduced and hotspots avoided thus reducing thermal NO_x formation. A typical lean-premixed combustor is shown in Figure 2.14.

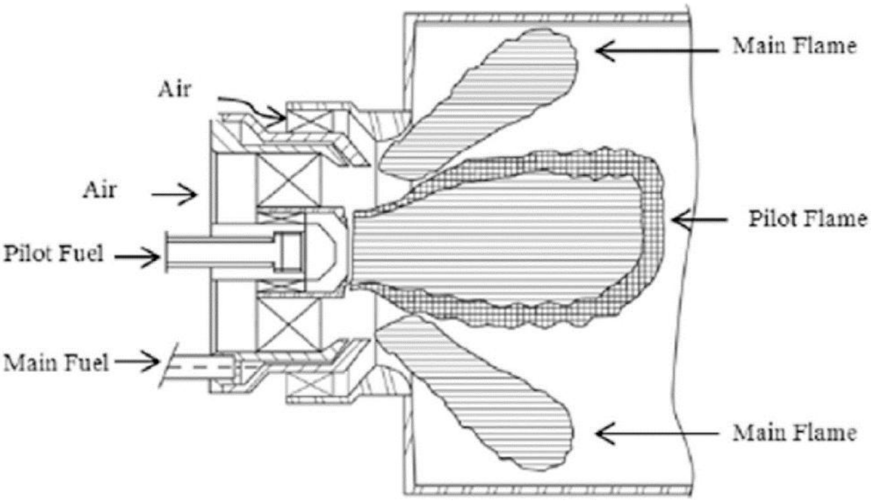

Figure 2.14 *- Lean-premixed DLE combustor. (From Liu et al.* [114] *p. 31).*

As can be seen from Figure 2.14, DLE systems have two fuel circuits: main fuel and pilot fuel. The main fuel, comprising ~97% of the total volume, is injected into the air stream immediately downstream of the swirler at the inlet to the premixing chamber. The pilot fuel is injected directly into the combustion chamber with little to no premixing. The latter is utilised to create a locally richer and more stable flame which acts as an anchor providing greater LBO resistance. Swirlers are also often utilised to create the flow conditions necessary to stabilise the flame.

Whilst the hydrogen capabilities of gas turbines vary significantly across the fleet of different OEMs, as was shown in Figure 2.12, DLE systems currently offer less flexibility than their WLE counterparts [110]. Given DLE combustors operate close to LBO with a large amount of fuel-air premixing, hydrogen concentrations higher than 30 vol.-% are proving difficult to achieve. Current state-of-the-art DLE combustors intended for use with HHC fuels such as the DLN 2.6 designed by GE [25] and those present in the SGT-600-700-800 [21,115] are capable of operating reliably with up to 50 vol.-% and 60 vol.-% hydrogen respectively [23]. This is because, considering the combustion characteristics of hydrogen described in Section 2.1, DLE burners become far more susceptible to flashback, autoignition and thermoacoustic instabilities once hydrogen fuel content is increased above 60 vol.-% [90].

Considering DLE systems offer significant advantages when it comes to efficient and low emission combustion, most major gas turbine manufacturers are investing significant R&D efforts into expanding their hydrogen-firing capabilities up to 100 vol.-%. Below some of the main emerging DLE technologies will be presented.

2.3.2.1. Staged Combustors

Staged combustion, the main example of which is often also referred to as RQL (Rich burn, Quench, Lean burn), was introduced in 1980 by Mosier et al. [116] as a method to reduce NO_x emissions in stationary gas turbines. It is still being utilised and developed today receiving particular attention for ammonia combustion [117]. As shown in Figure 2.15 RQL combustion can be divided into two stages: an initial fuel rich stage ($\phi > 1$) and a secondary fuel lean stage.

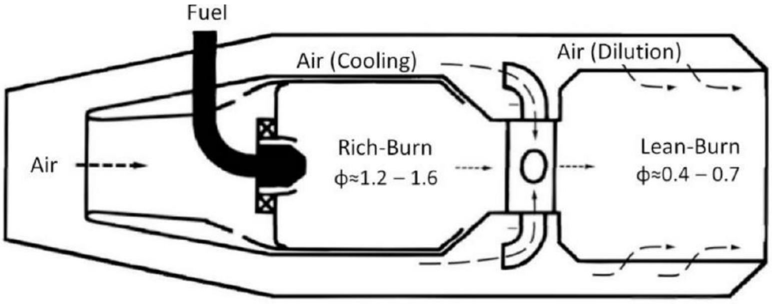

Figure 2.15 - RQL schematic (from Cecere et al. [25] *p.14).*

The primary rich stage implies stable combustion whilst limiting NO_x formation thanks to low combustion temperatures and limited oxygen availability. The addition of dilution air in the second stage combusts all unburnt products from the first stage. Whilst this dilution drops the overall combustion temperatures, thermal NO_x can still form when the mixture inevitably passes through stoichiometry. To ensure thermal NO_x emissions are kept to a minimum, mixing of the dilution air must occur rapidly and uniformly [118].

Fuel delivery can also be staged. The independent control of different fuel pathways allowing for an extension of the stable operation range and an increase in efficiency during partial loads [119]. Axial fuel staging has been implemented in a number of state-of-the-art systems such as the 7HA.02 burner found in the HA class GE turbines [120] and the DCS from Siemens Energy [121]. In axially staged combustors, fuel is injected axially downstream of the main burner as shown in Figure 2.16.

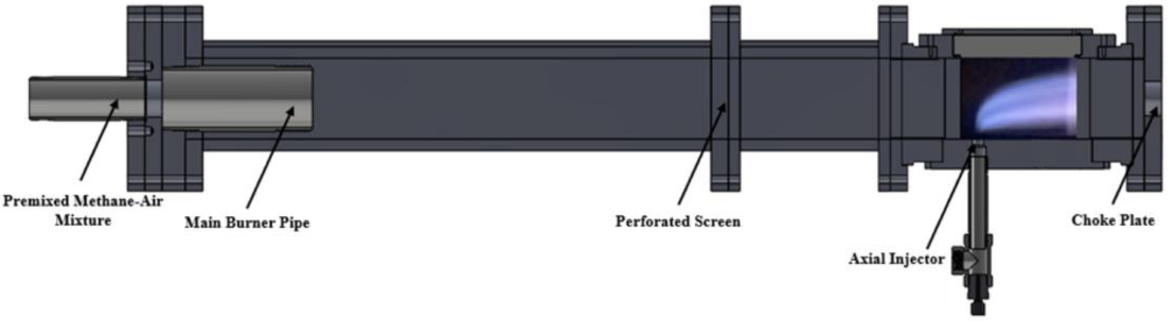

Figure 2.16 *- Experimental axially staged combustor. (From Stiehl et al.* [122] *p. 6).*

2.3.2.2. Micro-mix Combustors

Many gas turbine manufacturers are focusing their development efforts on micro-mix combustion, in order to increase flashback resistance and reduce NO_x emissions when burning HHC fuels. When compared with conventional swirl stabilised DLE combustors, micro-mix combustors are made up of numerous small-scale, closely packed injectors [62,123]. The main idea being to redistribute the heat release over a large number of small, compact flames with small recirculation zones which reduce the residence time of the reactants and subsequently the formation of NO_x [124]. To avoid flashback, the injectors are sized so that the reactant entry speed into the combustion chamber is greater than the flame speed [125]. While some micro-mix concepts feature short premixing sections, other designs feature small-scale jet-in-crossflow arrangements [126,127]. Short premixing sections help promote rapid premixing time scales whilst small-scale jet-in-crossflow arrangements ensure quick and intense mixing of non-premixed fuel and air while still accomplishing good aerodynamic flame stabilisation. Examples of both concepts are shown in Figure 2.17.

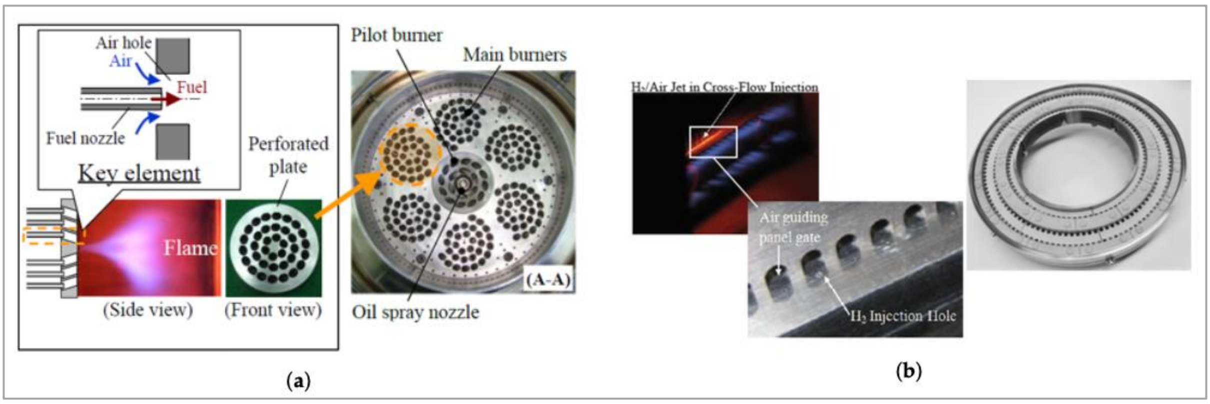

Figure 2.17 *- [A] Premixed concept developed by Mitsubishi Hitachi Power Systems. [B] Jet-in-crossflow concept developed by Aachen University and Kawasaki Heavy Industries. (From Beita et al.* [62] *p. 49).*

Micro-mix combustors designed by GE and Kawasaki Heavy Industries (KHI) operate via the jet-in-crossflow configuration. The GE DLN 2.6e multi-pipe mixer system was tested under class H conditions with fuels containing up to 50 vol.-% hydrogen and was found to perform very well in terms of pollutant emissions [128]. The KHI burner, based on the Aachen University prototype, has been run under commercial operating conditions with up to 100% hydrogen in the M1A-17 gas turbine [25]. As illustrated in Figure 2.18, the jet configuration promotes the formation of inner and outer vortices, which act to stabilise the flame.

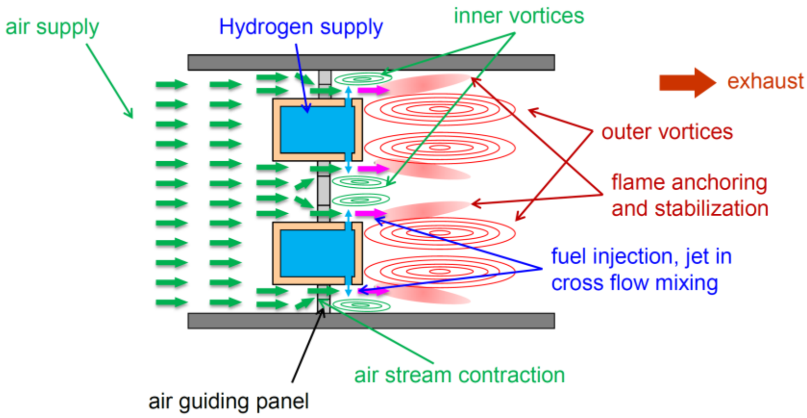

Figure 2.18 *- Schematic of KHI micro-mix combustor design (from Ayed* [129]*).*

Mitsubishi Hitachi Power Systems (MHPS) is developing a multi-cluster combustor system. In this micro-mix combustor, jets are arranged in clusters with each cluster forming one flame (Figure 2.17a). Fuel is either injected in crossflow or coaxially and the jets are orientated to create either a converging or diverging swirling flow [25]. The six clusters are arranged around a central pilot and are split across two different fuel supply systems. This allows for fuel staging to be performed by switching combustion modes depending on the conditions. Low emissions and high operability are therefore reached over the entire operating range [112].

2.3.2.3. Jet-Based Combustors

To address the aforementioned issues with high hydrogen content fuels, Siemens Energy has directed development efforts towards a diffusion based piloted, jet-based concept similar to the Advanced Combustion System for High Efficiency (ACE) technology utilised in the SGT-5/6 9000HL gas turbines [119]. Such a burner concept, a schematic of which is shown in Figure 2.19, presents a main burner comprising of multiple jet-based injector/premix passages per burner. Additionally, the configuration incorporates a central swirl-stabilised pilot burner and axial staging [119,130].

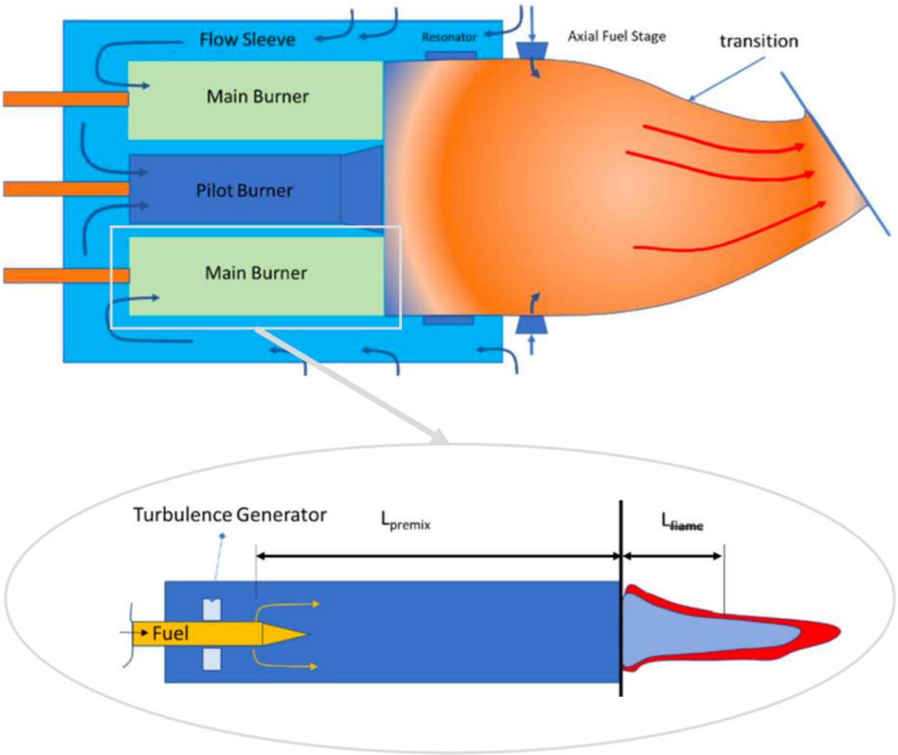

Figure 2.19 *- ACE combustor schematic depiction with detailed main burner view (from Krebs et al. [119] p. 3).*

The lack of swirling flow in the main burners, achieved through jet-in-crossflow fuel injection, promotes enhanced boundary layer development, elevated axial velocities, and intense turbulent mixing, key factors in the reduction of NO_x emissions. Moreover, the lack of swirl diminishes the likelihood of flow separation, and when combined with high axial momentum, contributes to improved flashback resistance. These characteristics render the premixed jet configuration particularly promising for high-hydrogen applications [119,130].

Results from full-scale engine testing under industrial operating conditions have demonstrated that this burner architecture is capable of achieving low NO_x emissions during hydrogen combustion across a broad load range [119]. Furthermore, strong flashback resistance was observed, enabling operation near full load with only a minor derating when utilising 100% H_2 [130,131].

2.4. Swirlers

Swirlers are some of the most effective devices used to impart flame stability [132]. In modern burners they have the function of creating flow conditions that favour the settling of a vortex-stabilised flame, combined with the proper fuel placement [41]. Furthermore, they can help control flame intensity and prevent the formation of NO_x [133]. The two main types of swirler geometries that are currently utilised are axial and radial. Both are shown in Figure 2.20.

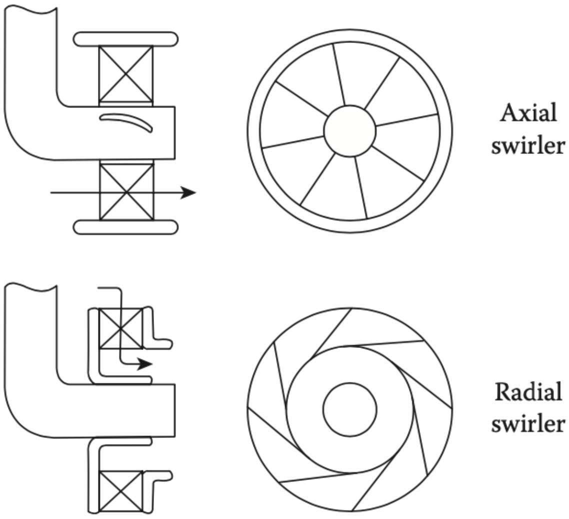

Figure 2.20 *- Two main swirler geometries (from Lefebvre et al. [134] p. 142).*

In an axial swirler the air flows through helical vanes having an axis parallel with the flow. These vanes can either be flat or curved though the latter have been shown to achieve higher efficiencies and lower pressure drops. Radial swirlers have a simpler geometry consisting of milled grooves set tangentially to the axial flow path. Higher pressure losses are usually measured as the air is forced to follow a minimum of two bends [41].

Radial swirlers are widely used in DLE combustors [25] and, though their flow characteristics have not been as widely studied as for axial swirlers, it has been shown that the flow fields generated by both swirler types have qualitatively similar characteristics [134].

The flow field generated by a swirler is widely reported to be axisymmetric [135–137] presenting both central and outer recirculation zones. Central recirculation zones (CRZ) are characterised by strong reversed flows and internal stagnation points which provide the main stabilisation mechanism. Flame stabilisation is also provided by the low-pressure outer recirculation zones (ORZ) formed by the rapid expansion of the flow entering the combustion chamber [98]. Both these flow characteristics are shown in Figure 2.21.

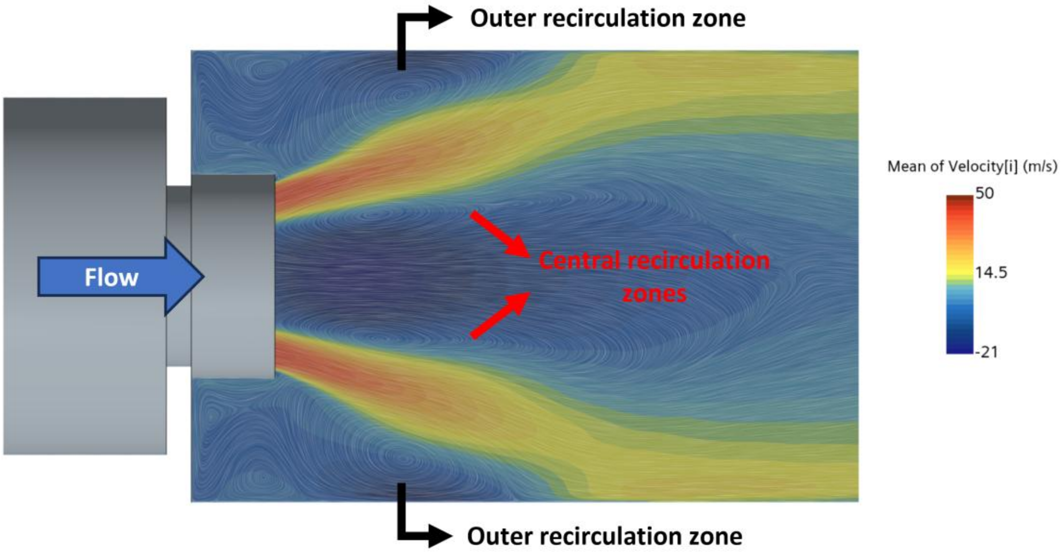

Figure 2.21 - *Flow characteristics of a generic radial tangential gas turbine swirler.*

The steep velocity gradients caused by the presence of the CRZ and ORZ mean strong inner and outer shear layers are formed between the main exiting flow and the central and outer recirculation zones respectively [98]. These shear layers provide enhanced mixing of fuel and oxidiser particularly for diffusion flames and can also influence the flame shape. With conventional fuels such as methane, the main flame front tends to be located along the inner shear layer leading to a "V" shaped flame. With the addition of hydrogen however, flame fronts have been shown to develop along the other shear layer too leading to an "M" shaped flame [138]. The effect of hydrogen enrichment of the outer shear layer flame development is shown in Figure 2.22.

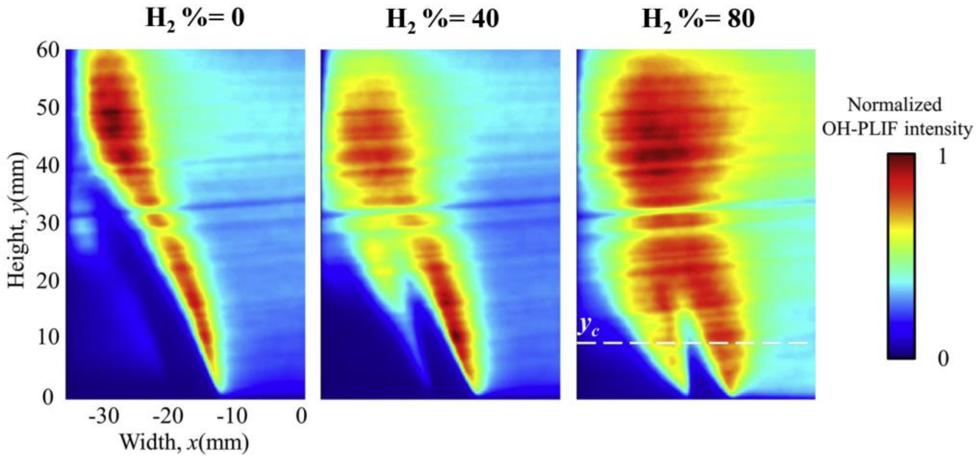

Figure 2.22 - *Normalised OH-PLIF images of swirling (SN = 0.7) lean premixed CH_4/H_2 flames (from Mao et al.* [138]*).*

2.4.1. Swirler Design – Swirl Number

Three of the main parameters considered when designing swirlers are: swirl number (SN), mass flow, and swirler area [133]. Out of these three, SN is by far the most important [139,140]. Depending on the degree of swirl, the flow field can be seen to change significantly as shown in Figure 2.23.

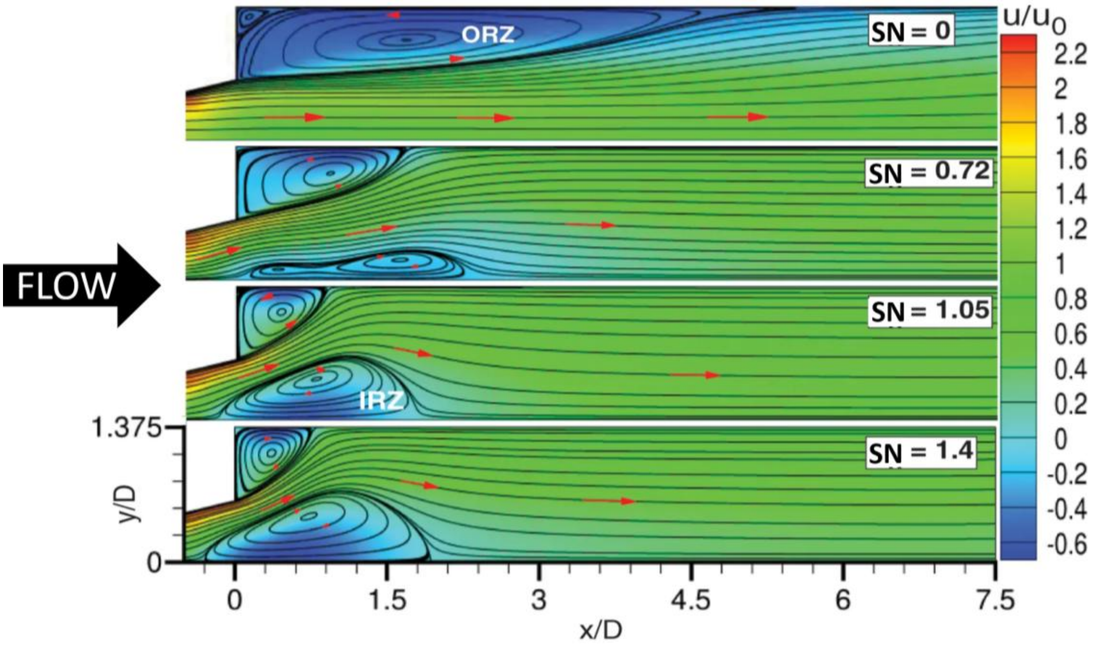

Figure 2.23 *- Streamline contours of swirling flows with increasing SN (from Abdelkader et al. [141]).*

From Figure 2.23, it's evident that, as SN increases, the primary flow exiting the nozzle is pushed radially outwards therefore implying a change in the axial velocity distribution. It can also be seen that, for $SN < 0.4$, no CRZ is achieved hence the swirl is described as weak. Most swirlers utilise $SN > 0.6$ to ensure they operate under strong swirl conditions [134]. As SN increases above 0.4, both the CRZ and ORZ experience significant shifts in their strength and location. An enhanced central recirculation zone indicates improved mixing, resulting in better blending of reactants. This, in turn, has been shown to reduce overall temperatures and improve emissions particularly when dealing with HHC fuels [140,142].

Specific expressions exist for calculating the SN for several different types of swirl generators though, generally, it can be defined as the ratio of the axial flux of angular momentum (G_t) to the axial flux of the axial momentum (G_x) as shown in equation [2.6] [143].

$$SN = \frac{G_t}{G_x R_{nozzle}} \qquad [2.6]$$

Where:

R_{nozzle} = Burner nozzle inner diameter

2.4.2. AM Potential

AM has the potential of offering substantial improvements to the performance of current gas turbine swirlers. The enhanced design freedom creating the opportunity for fundamentally new design concepts to be realised. Whilst many works focusing on recreating existing turbomachinery components can be found in the literature [144,145], those investigating the creation of novel designs not previously manufacturable are scarce. Giuliani et al. [41] produced one of the few papers found on this latter topic. During their research they designed and manufactured a series of prototype swirlers, shown in Figure 2.24, using advanced mathematical shapes such as helicoids and single vane S-shape designs.

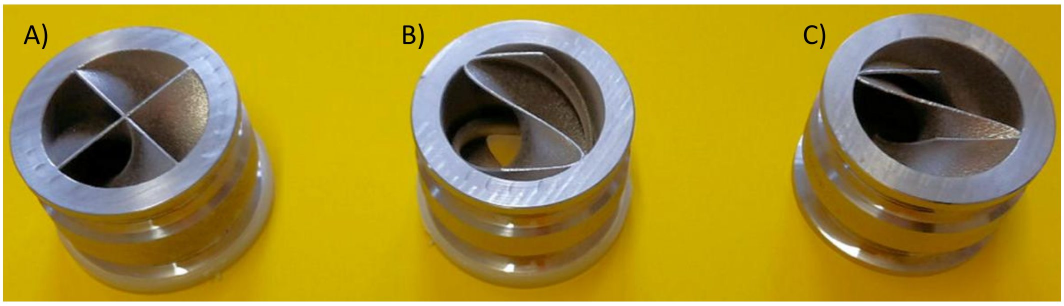

***Figure 2.24** – Prototype AM Swirlers (from* Giuliani et al. 2018 *p. 7).*

During testing with propane at ambient pressure and temperatures it was found that, out of the three geometries, C was found to have the widest stable operating range before reaching LBO. It was hypothesised this was due to the strong swirl generated even at low speed. In addition, though the increased design freedom enabled the creation of swirler geometries with enhanced lean blow off limit and reduced pressure drop, the unprocessed "raw" surface finish of these AM swirlers was found to have a measured effect on pressure drop [41].

The poor surface quality of AM components is one of the primary limitations of this technology with expensive and time-consuming post processing methods often utilised to achieve acceptable surface finishes, as mentioned in Section 1.3.1 [35,36]. This increased surface roughness should not be viewed solely as a drawback; instead, in combustion applications, it has been demonstrated to have the potential to yield beneficial effects. Previous experimental work performed at Cardiff University's Gas Turbine Research Centre (GTRC) for instance showing how increasing the roughness of swirler wetted surfaces can affect axial velocities, heat release, NO_x emissions and operability limits [42].

2.5. Surface Roughness

The surface finish of a component must be carefully considered to ensure acceptable performance, service life and quality for the given application. International standards, such as BS 1134:2010, exist to quantify it consistently and provide the expected surface roughness ranges associated with different manufacturing techniques [146]. Below an overview of different roughness measurement techniques and parameters will be presented followed by sections on factors affecting AM surface finish and roughness effects on gas turbines.

2.5.1. Surface Roughness Measurement

2.5.1.1. Measurement Techniques

Surface roughness is a key parameter in many engineering applications, and several methods have been developed to quantify it. Contact profilometry is one of the most widely used techniques [42,147,148], where a stylus is drawn across the surface and its vertical displacement is recorded to produce a surface profile, as shown in Figure 2.25 [149]. This method provides high-resolution measurements and is particularly effective for capturing microscale roughness features, although it can potentially damage delicate surfaces.

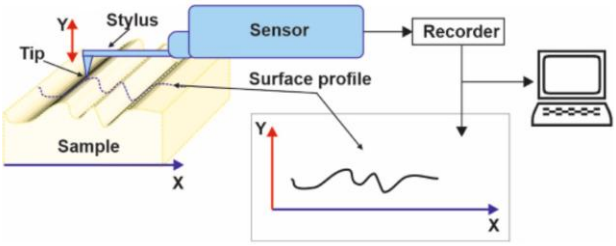

Figure 2.25 - Working principle of the stylus profilometer (from Ruzova et al. [149]).

Optical techniques offer a non-contact alternative. White-light interferometry and confocal microscopy use light interference or focused laser scanning to precisely map the surface topography [150]. These methods are especially useful for fragile, soft, or highly reflective surfaces and can generate three-dimensional surface maps, allowing the calculation of various roughness parameters.

Atomic force microscopy represents a high-resolution technique capable of measuring roughness at the nanometre scale. It scans a sharp tip over the surface, producing extremely detailed surface profiles suitable for research applications where nanoscale roughness is relevant [151].

Each method has trade-offs in terms of resolution, area coverage, speed, and potential for surface damage, and the choice depends on the scale of roughness of interest and the properties of the surface being measured [149].

2.5.1.2. Roughness Parameters

Roughness parameters are utilised to statistically characterise surface properties. They can be calculated either over a sampling line (*R* parameters) or on a sampling area (*S* parameters) [152]. *R* values have seen more widespread adoption though, because measurements are only performed over a line, the error associated with such technique depends greatly on both the surface topography and size, orientation and number of samples taken [153]. *S* values are considered more meaningful as both vertical and horizontal height deviations are taken into account. This being said, the 3D profilometers needed to capture *S* values are far more expensive and less widely available than the legacy contact-type measuring instruments.

Commonly used *R* parameters and their relative differences when applied to the same arbitrary roughness profile are shown in Figure 2.26. Their formulation can be found in the appropriate ISO standards as well as in other technical guides [146,154].

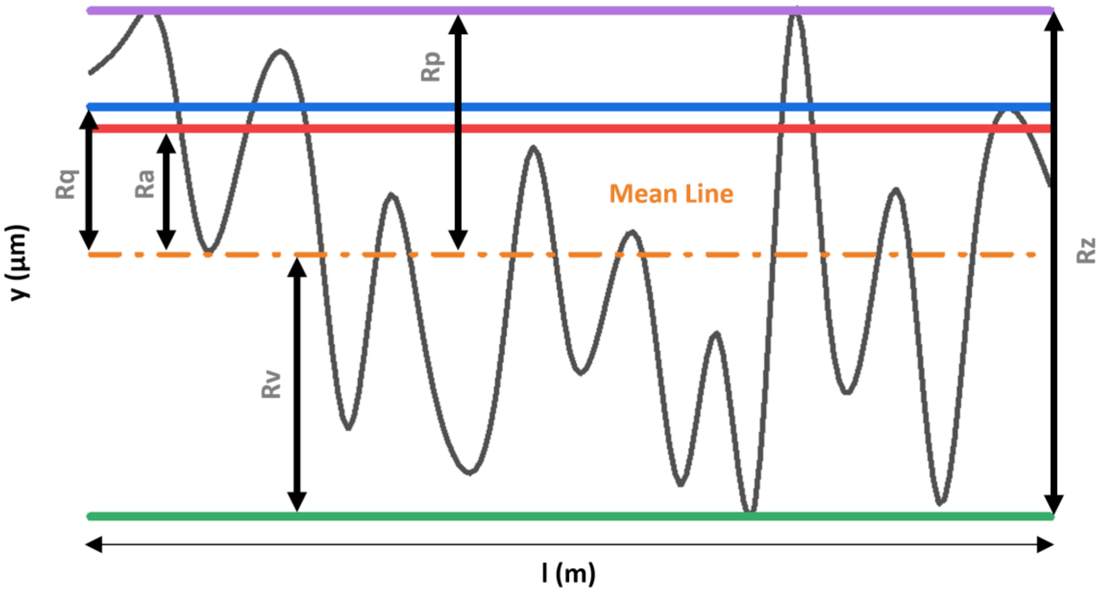

Figure 2.26 - Representation of common R parameters calculated for arbitrary roughness profile.

The Rp, Rv and Rz parameters all represent peak measurements taken along the sampling line therefore, even when ten-point averaging is applied [146], a greater sensitivity to occasional high points or deep valleys is present when compared with Rq and Ra parameters. Of the latter two, the Rq statistically defines the standard deviation of the surface height distribution and is thus more physically significant than Ra which corresponds to the average of the absolute deviations from the mean surface profile [152]. Relying solely on the Ra parameter can in fact lead to misinterpretation of the surface topology since, as can be seen from Figure 2.27, different surface structures can possess the same Ra value.

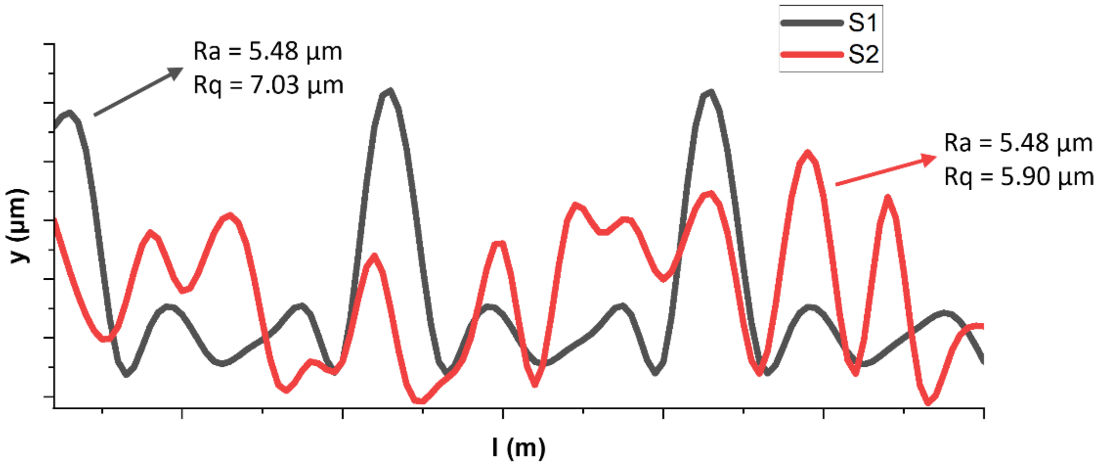

Figure 2.27 *- Ra and Rq values calculated for arbitrary discontinuous (S1) and evenly textured (S2) rough surfaces.*

Whilst the two profiles shown in Figure 2.27 are clearly very different, the jagged nature of the S1 profile is not captured by the Ra values. Both Ra values are in fact identical with significant differences only present for the Rq values. It can also be noted that, for the S2 case, minimal variation exists between the Ra and Rq values indicating the profile presents a homogeneous roughness. Comparing Ra and Rq for the same profile can therefore help understand the topology of the surface.

2.5.2. Considerations for AM

The inherent surface roughness associated with AM has the potential to negatively affect part performance as has already been mentioned in Sections 1.3.1 and 2.4.2. Selective Laser Melting (SLM) is one of the main technologies utilised for the production of metallic components thanks to the broad range of alloys available [155,156]. When compared to other conventional subtractive manufacturing techniques (Figure 2.28), the range of "raw" unprocessed surface finishes achievable via SLM is far wider due to the numerous build and material parameters at play [35].

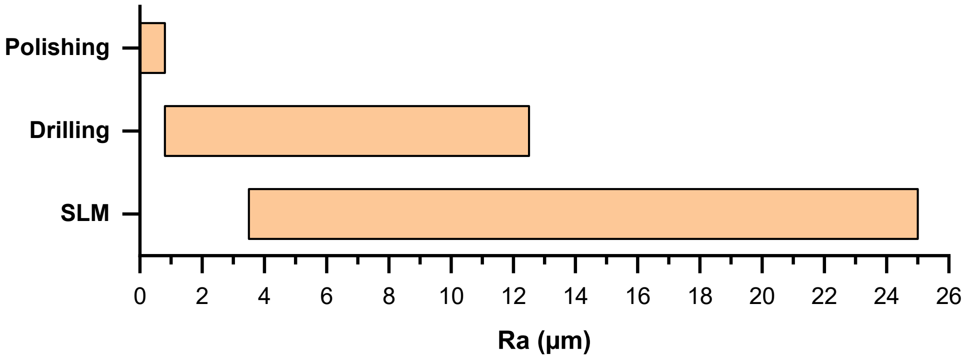

Figure 2.28 *- Typical surface roughness of metal AM and conventional processes (values from* [35,146]).

Understanding how each of these parameters affect the final surface finish of a printed part is an active area of research with 21% of the papers categorised by Obilanade et al. [157] found to be focusing on this topic. General consensus can be found in the literature suggesting surface roughness increases with increasing laser power [158,159]. Contradictory results are found for other important parameters such as the laser scan velocity [159,160], powder size [157,161] and hatch spacing [162,163]. It can therefore be seen that, whilst parameter optimisation has been studied fairly extensively, it is still to reach maturity [157]. An emerging research area is the use of machine learning to predict and provide real time monitoring of surface roughness based on parameter settings and printing conditions [164,165]. Whilst initial results are promising, such approaches are still in their infancy and therefore need further development.

Given the high roughness of as printed AM components, a number of post processing methods are utilised to generate a smoother surface. These include grit blasting [42], laser polishing [166] and chemical polishing [40]. Depending on the post-processing method chosen, both the geometric and material properties of the outer surface can be affected therefore careful consideration must be taken [167,168]. Furthermore, for very intricate components or parts that include closed channels, additional deliberation is needed to avoid selecting an approach which is either costly or unfeasible [157]. Overall, limited standardisation currently exists for post-processing with less than 1% of ISO/ASTM standards focusing on surface finishing [169].

2.5.3. Effects on Gas Turbine Performance

Over the last fifty years, extensive research has delved into investigating the impact of both engineered and natural degradation-induced roughness on gas turbine performance. Surface roughness has been found to influence vortex shedding [170] and wall shear stress [171]. Furthermore, it has also been shown to cause earlier boundary layer transition, increased boundary layer momentum loss and/or flow separation [46] and enhanced BLF resistance [44,45]. The effects of surface roughness within the compressor and turbine have been found to be primarily dependent on Reynolds number and roughness size [172,173]. At low Reynolds numbers for instance, roughness reduces losses by eliminating laminar separation bubbles while, at high Reynolds numbers, roughness increases losses as it can cause the boundary layer to thicken to the point of separation. In the turbine, roughness has the additional undesired effect of increasing convective heat transfer [174,175].

Though this extensive research on the impact of surface roughness on gas turbines means some consensus as to the general trends exists, considerable research is still required to fully understand the role of roughness in gas turbines [46]. This is particularly the case considering the more widespread adoption of AM components has meant that surface roughness effects will be experienced from the first day of operation rather than as a consequence of wear. In addition, the increased design freedom enabled by AM means that surface roughness can be artificially increased in specific regions. Given the industry wide shift towards HHC fuels, the prospect of utilising surface roughness to enhance BLF resistance is of prime industrial relevance.

Cardiff University is one of the main institutions that, over the years, has investigated the effects of both engineered and organic surface roughness on emissions and combustion stability. Al-Fahham et al. [45] explored the utilisation of micro-surfaces to enhance resistance of swirl burners to BLF. Though this primarily numerical study revealed various structures with high potential for drag reduction, the chosen micro-surface for experimental validation was determined based on manufacturing capabilities. Scope for further research therefore exists. The study found that, with the addition of micro-surfaces, the thickness of the near-wall velocity gradient was reduced together with the boundary layer turbulence intensity. As is shown in Figure 2.29, this resulted in a higher BLF resistance.

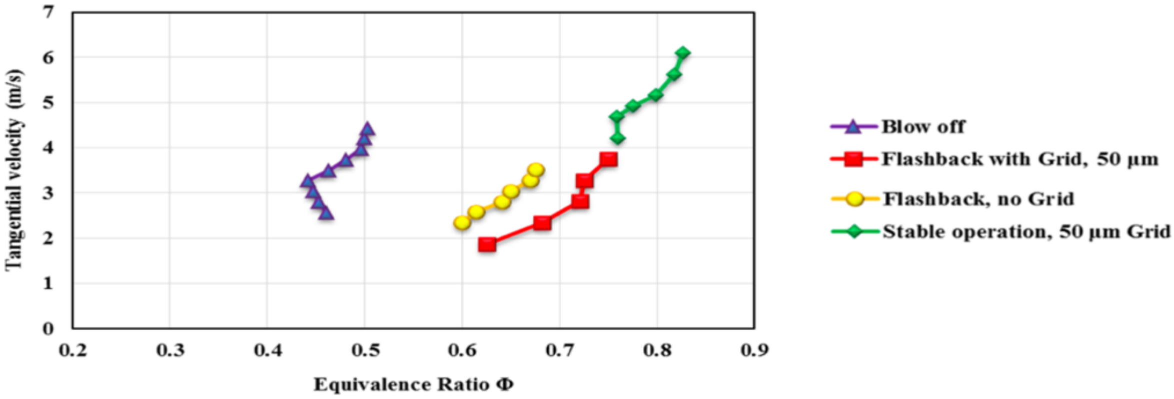

Figure 2.29 *- Comparison between cases with and without grid micro-surface (from* Al-Fahham et al. 2017 [40] *p. 7).*

Runyon et al. [42] investigated the effects surface roughness had on the flame stability of a generic gas turbine swirl burner. In this study, two identical Inconel 625 swirl nozzle inserts were constructed via AM together with a third nozzle insert manufactured via traditional machining methods. One of the swirler nozzles produced via AM underwent further post-processing by grit blasting whilst the other was left unprocessed. It was found that surface roughness influenced the flow field, turbulence intensity, and flame stabilisation location. NO_x formation was found to decrease with increasing surface roughness whilst pressure drop was found to increase. Of the three swirlers, the grit-blasted one showed the widest stable operating range. This therefore suggests that the surface roughness of wetted surfaces can improve burner stability limits and must therefore be considered carefully in the design process of AM burners.

2.6. Modelling Roughness Effects in CFD

Computational Fluid Dynamics (CFD) is an indispensable tool in iterative engineering design, enabling rapid and cost-effective optimisation without recourse to physical prototyping. It facilitates detailed investigation of flow regions that are otherwise challenging to probe experimentally. However, accurate representation of surface roughness within CFD simulations is essential, as it significantly affects flow behaviour, pressure losses, and overall system performance. In the context of gas turbines, CFD models that incorporate the influence of surface roughness on boundary layer development and transition are required to reliably predict heat transfer and aerodynamic performance [46]. As was mentioned in Section 1.3.1, roughness effects can be simulated via three main approaches shown in Figure 2.30 and briefly presented in order of increasing computational demand [46]:

a) Most turbulence models utilised today incorporate the turbulent eddy viscosity (μ_t) within their formulation with roughness effects modelled by making μ_t a function of roughness height [176,177]. Whilst this approach means adding roughness to a simulation is straightforward, measured roughness values cannot be directly input into the CFD model. Rather, the measured values must be first converted to an "equivalent sand grain roughness" (k_s) via an appropriate correlation. This parameter, coined by Schlichting [178], denotes a roughness feature and spacing that has the same effect on skin friction losses as a uniform layer of actual sand grains of diameter k_s. Considering k_s was initially derived to model skin friction effects, challenges arise when wanting to also capture other roughness induced effects such as changes in heat transfer [53,179].

b) The "Discrete Element Method" (DEM) also models roughness effects though, unlike approach a), it is not reliant on an equivalent sand-grain correlation to account for roughness blockage, heat transfer, and obstruction drag [49,50]. Because roughness is accounted for via extra terms in the governing equations this approach is a popular yet more computationally demanding alternative to k_s-based roughness models [46]. Though this method was originally developed for use with engineered roughness elements such as cones and spheres, it has been found to also work well when applied to real randomly rough surfaces [180,181].

c) Reliance on roughness models could theoretically be avoided by fully resolving the roughness via a computational grid [51,52]. Such an approach however is extremely time consuming both in terms of setup and runtime. The organic roughness patterns must in fact be replicated within CAD and applied to the surfaces of interest. Furthermore, because a very fine mesh is needed to capture these micron-scale roughness elements, computing times two to three orders of magnitude greater are needed when compared with an equivalent DEM case [182,183].

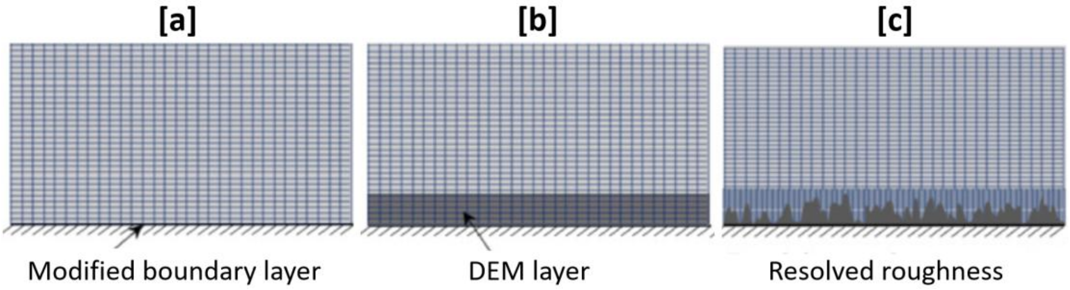

Figure 2.30 *– Comparison of the three main approaches for capturing roughness effects in CFD (from Kadivar et al.* [184]*).*

Whilst both methods b) and c) are more accurate in numerically replicating roughness effects, due to the significantly increased computational demands, they are mostly applied to very simple small three- or two-dimensional regions. For turbomachinery applications, where flow domains are extensive and highly complex and often involve reacting chemistry, method a) is therefore better suited [108].

2.6.1. Modified Boundary Layer Approach

Utilising a k_s approach may be straightforward to implement from a simulation setup standpoint though, if accurate and meaningful roughness effects want to be captured, a series of challenges are present. Firstly, as was mentioned in Section 2.6, different k_s correlations and therefore simulations are often needed to capture both flow field and heat transfer effects. Secondly, the selection of an appropriate k_s correlation is frequently a matter of trial and error. Many correlations for calculating k_s can be found in the literature often being defined for specific surface types and conditions. Furthermore, these correlations can be found to vary by over an order of magnitude for the same measured roughness values [46] as demonstrated in Figure 2.31.

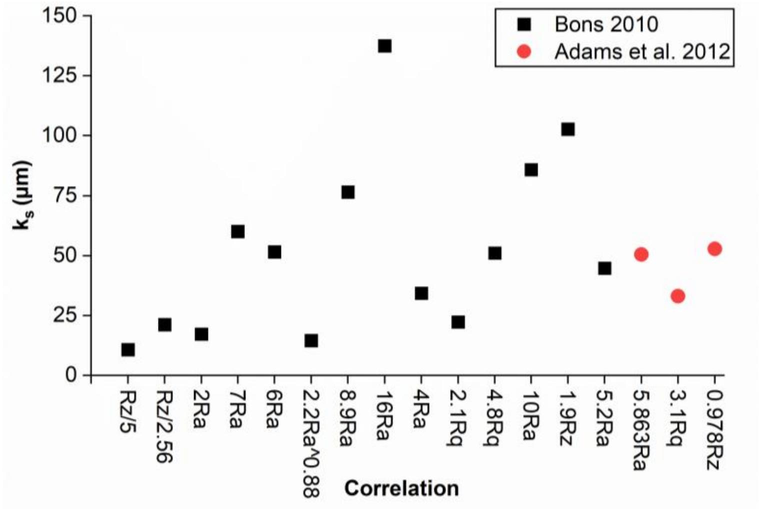

Figure 2.31 *- Comparison of k_s correlations from Bons* [46] *and Adams et al.* [185] *for same measured roughness value.*

It is important to note that the wide spread observed in Figure 2.31 is expected, as each correlation is derived for specific applications [46]. Additionally, changes in the modelling approaches utilised such as mesh resolution and physical phenomena being resolved, can significantly influence the roughness effects captured for the same $k_s$value and the sensitivity of the model itself to k_s variation [108].

Conventionally, high y^+ meshes are needed to attain physically meaningful roughness effects as the roughness height must be smaller than the height of the wall-adjacent cell [48,186]. This requirement for a mesh with $y^+ > 30$ implies resolution near the wall is lost. In addition, when dealing with intricate flow paths, such a mesh may not be physically possible. Finally, this roughness modelling approach cannot be readily applied in Large Eddy Simulations (LES), the implementation of which has only recently become available - for example, in the latest 2506 versions of STAR-CCM+. Given that LES is increasingly employed in turbomachinery studies, this represents a notable limitation.

Whilst a universal k_s correlation is unlikely to be formulated, attempts to streamline the selection process can be found in the literature. Bons [46] for instance collected a series of k_s correlations formulated over the span of half a century for determining roughness effects in gas turbines highlighting what surface types they were originally developed for. Utilising this database, an informed initial guess on the correlation needed for specific applications can be made though, as was stated by Bons [46], trial and error will still play a part. Aghaei Jouybari et al. [187] utilised machine learning to develop a high-fidelity approach for predicting k_s values. The machine learning models were trained using 45 surfaces having differing roughness profiles, with results providing an average error in the k_s value of less than 10%. Although such an approach is a significant step closer to universality, limitations still remain. Firstly, most of the roughness geometries used to train the machine learning models were not directly representative of “raw” unprocessed AM surfaces. Secondly, a high-resolution scan of the surface topography is needed for the algorithm to predict a k_s value. Depending both on the geometry shape and tools available, attaining such a scan will not always be possible and/or feasible. Finally, it is unknown if changes in the fluid type flowing over the rough surface can lead to inaccuracies in the models proposed.

With regards to needing a wall-adjacent cell height that is greater than the roughness height, exceptions can be made for both the Elliptic blending (EB) and K-Omega (ω) turbulence models. These latter two turbulence models in fact utilise specific modifications to their formulation, covered in Section 3.1.1.2.2, that theoretically enable roughness effects to still be captured even when $k_s^+ > y^+$ [186]. This being said, little to no evidence can be found in the literature suggesting roughness effects have been successfully modelled on a resolved boundary layer.

Detached Eddy Simulations (DES) can provide an alternative to LES for cases where high physical resolution is desired while capturing roughness effects, without the need to fully resolve all physical surface features within the CFD domain. In the DES approach, unsteady RANS (U-RANS) models are utilised in the near-wall regions, whilst scale resolving models (LES) and their associated sub-grid scale models are used in the regions away from the wall where large turbulence scales are predominant [188]. Given most RANS models account for roughness effects in their formulation, roughness can therefore be modelled in these near-wall regions. Krasilnikov et al. [48] successfully utilised a roughness sensitive DES approach in conjunction with a high y^+ mesh to perform full scale simulations assessing ship performance. Finding it provided a good compromise between accuracy, computational demand and physical resolution. Overall, examples of DES studies with roughness sensitivity are limited with most of the literature on the topic being associated with marine engineering. Due to the fundamentally different physics associated with liquid versus gaseous flows, such as density contrasts and differences in roughness scales (micrometres versus centimetres), there remains significant scope for further research in the context of combustion.

2.7. Summary - Thesis Aims and Objectives

It is clear from this review that, whilst transitioning gas turbines towards HHC fuels is vitally important if they are to remain relevant in future net-zero energy scenarios, significant challenges still need to be overcome. Though the effect of hydrogen addition is highly dependent on the design of individual combustors, the following general insights can be drawn. Flames become more compact and, as a result, the centre of heat release is shifted upstream closer to the burner outlet. The high reactivity of hydrogen means the risk of autoignition, and flashback is greatly increased. Hydrogen addition shifts thermoacoustic instabilities to lower equivalence ratios and flame temperatures, with elevated pressures further exacerbating these instabilities and reducing the hydrogen fraction needed to trigger them, making atmospheric test results unreliable for high-pressure conditions. DLE combustors were shown to be the current state-of-the-art for low NO_x operations though their hydrogen capabilities are generally limited due to elevated flashback risk and increased susceptibility to thermoacoustic instabilities. New burner designs, often enabled by the more widespread adoption of AM, were found to incorporate micro-mix, staged and jet-in-crossflow combustion to help mitigate some of these challenges with promising results. The vital role swirlers play in imparting flame stability was presented together with the potential design improvements the adoption of AM could bring. However, AM-induced surface roughness was shown to affect the performance of swirl-stabilised burners, yet its impact on hydrogen-fuelled novel combustor designs remains largely unexplored.

A key area of interest is the influence of surface roughness on stability limits, particularly flashback, where CFD has demonstrated considerable potential for exploring the underlying mechanisms. However, modelling the effects of roughness has proven highly case-dependent, and there is very limited data in the literature, especially for reacting flows.

Despite considerable progress in understanding hydrogen-enriched combustion in gas turbines, several critical gaps remain in the literature that limit the development of reliable, low-emission hydrogen-capable systems. AM has enabled novel burner geometries, such as micro-mix, staged, and jet-in-crossflow designs, but the effects of AM-induced surface roughness on hydrogen flames, boundary layer flashback, and overall flame stability remain insufficiently understood particularly in these novel burner architectures. Computational studies using CFD have shown potential for investigating these phenomena, yet validated models for reacting flows are limited, and experimental data for roughness-flame interactions are largely absent. Addressing these gaps is essential to inform the design of robust, high-performance hydrogen-capable gas turbines capable of operating reliably under realistic industrial conditions.

The subsequent work therefore aims to advance the understanding of surface roughness effects on the performance and flow-field characteristics of both legacy and state-of-the-art burner geometries, with a particular emphasis on hydrogen-fired operation. This is achieved through detailed experimental investigations on jet burner architectures, providing a critical dataset under both smooth and rough-wall conditions. These data serve as a foundation for the development and validation of improved roughness correlations capable of accurately capturing roughness-induced effects within a resolved boundary layer framework.

In light of these observations, the objectives of the present study are defined as follows:

1. **Perform high-fidelity Detached Eddy Simulations (DES)** on a legacy generic swirl burner using existing isothermal and methane-reacting datasets to benchmark turbulence models for their capability to capture roughness effects on resolved boundary layers in both isothermal and reacting conditions.
2. **Design and commission novel experimental test facilities** (Premixed and Jet-in-Crossflow Jet Burners) tailored for industrial relevance, featuring interchangeable inserts with varying surface roughness profiles to represent both conventional and additive manufacturing geometries.

3. **Conduct systematic experimental investigations** via the PJB and JICF configurations under atmospheric pressure in both isothermal and hydrogen-fired conditions to evaluate the influence of surface roughness and its interaction with fuel injection strategies on flame behaviour, flow field evolution, and burner operability.
4. Utilise the findings from swirl burner simulations, to **numerically capture the experimentally observed roughness effects on a jet burner architecture** under both isothermal and reacting conditions.
5. Apply the validated PJB roughness correlation to **numerically interpret mechanisms behind underlying differences in roughness-induced trends between PJB and JICF datasets**.

Chapter 3. Theoretical Background and Methodologies

Initially, Chapter 3 provides a theoretical foundation for capturing wall effects within CFD. It begins with a discussion of wall treatment strategies for smooth surfaces, providing a foundation for understanding the adjustments required for rough surfaces. The composition of turbulent flow is then examined, detailing its computation both in LES and DES. Emphasis being given to the different DES models available. Having outlined the principles of LES and DES, the Chapter addresses the meshing requirements for high physical resolution CFD models. The latter part of the Chapter focuses on outlining the design and commissioning process for a simplified, scaled-down jet burner combustion system relevant to industry. The integration of interchangeable sections allowing for investigations into roughness effects on BLF and other flow characteristics.

3.1. Numerical Theory

Numerical simulations in this work were conducted using STAR-CCM+, the CFD software employed by the industrial partner, Siemens Energy Industrial Turbomachinery Ltd. As a result, though STAR-CCM+ and its associated terminology are referenced throughout this Chapter, the theory and methodologies presented are general in scope and applicable to other CFD solvers.

3.1.1. Wall Treatment

Walls are a significant source of vorticity in most practical flow problems, making accurate prediction of flow in the wall boundary layer crucial. In fluid mechanics, the wall boundary layer can be defined as the thin near-wall region where flow velocity changes from zero (due to the no-slip condition at the wall) to the free stream value away from the wall. At low Reynolds numbers, the boundary layer is considered laminar with smooth and orderly changes in velocity. At high Reynolds numbers, the boundary layer becomes turbulent, characterised by chaotic and swirling motions within the layer. The thickness of this boundary layer (δ) is typically defined as the distance from the wall to where the flow velocity reaches 99% of the free stream velocity. Beyond this point, the effects of viscous stresses are negligible. [189,190].

The turbulent boundary layer, a visual representation of which is shown in Figure 3.1, can be split into two sub-layers: the outer layer, dominated by turbulent effects, and the primarily viscous-affected inner layer. This inner layer can be further subdivided into the viscous, buffer and log sublayers. The viscous sublayer is in direct contact with the wall. It is primarily influenced by viscous forces and exhibits nearly laminar flow. The buffer layer acts as a transitional zone between the viscous sublayer and the log layer where viscosity effects gradually give way to turbulence. The log layer is the outermost inner sublayer and experiences a balance between viscous and turbulent forces [191].

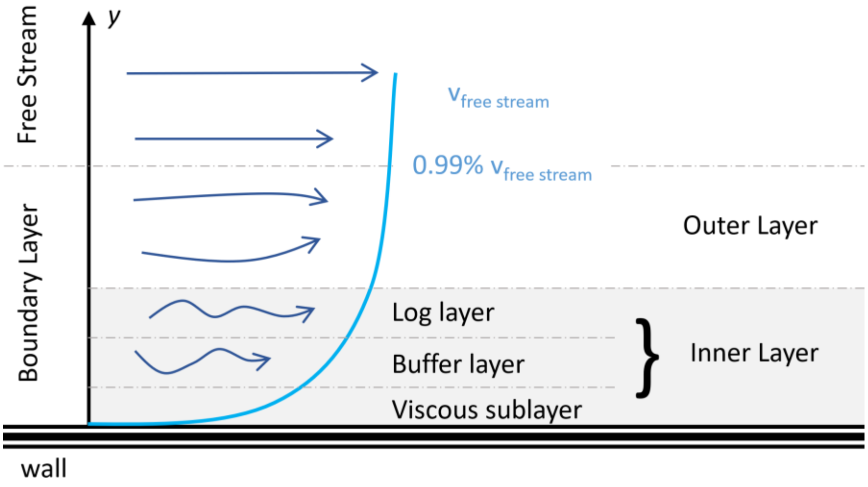

Figure 3.1 *- Annotated Diagram showing turbulent boundary layer (modified from STAR CCM+ User Manual [186]).*

When employing a turbulence model, it is essential to explicitly model the physics of turbulent boundary layers. This approach typically involves two key aspects: the near-wall modelling, responsible for dealing with local and non-local wall effects in the viscous-affected region (buffer and viscous sublayers), and wall treatment which, for RANS and DES applications, provides boundary conditions for the turbulence solvers. These boundary conditions are imposed on the centroids of near-wall cells and derived from universal field functions discussed in Section 3.1.1.1 [186].

3.1.1.1. Wall Functions

Wall functions offer algebraic approximations of key quantities such as velocity, temperature, and turbulence characteristics in the inner turbulent boundary layer. Given they are defined in terms of non-dimensional quantities, wall functions are independent of Reynolds number, turbulence model formulation and wall treatment utilised. They can therefore be considered universal. Non-dimensional definitions for both wall distance (*y*) and the wall-tangential velocity component (*u*) are shown in equations [3.1] and [3.2] respectively.

$$y^{+} = \frac{y u^{*} \rho}{\mu} \qquad [3.1]$$

$$u^{+} = \frac{u}{u^{*}} \qquad [3.2]$$

Where the friction velocity (u^*) can be defined as:

$$u^{*} = \sqrt{\frac{\tau_w}{\rho}} \qquad [3.3]$$

Wall functions can be distinguished into two categories: standard and blended. Standard wall functions are based on empirical or semi-empirical formulas that approximate the behaviour of turbulent flows in the log and viscous sublayers [192]. No standard wall functions are available for the buffer layer. Blended wall functions are continuous functions that span all three sublayers of a turbulent boundary layer. They effectively represent the buffer layer by smoothly integrating the viscous sublayer with the log layer [193]. A comparison of how both types of wall functions fit Direct Numerical Simulation (DNS) data for u^+ is shown in **Figure 3.2**.

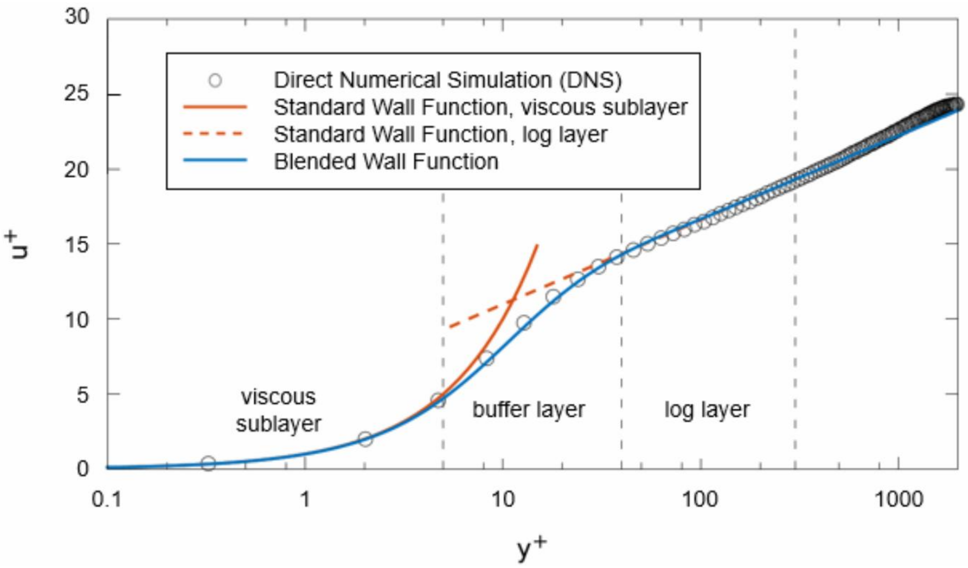

Figure 3.2 *- Standard and Blended wall functions for u^+ (from STAR CCM+ User Manual* [186]*).*

As can be seen from Figure 3.2, if standard wall functions are to be utilised, y^+ values in the buffer layer ($5 < y^+ < 30$) are to be avoided. For the blended wall function on the other hand, good fitting is achieved over the entire inner boundary layer. Although knowing the specific equations for these different velocity wall functions is not crucial since they are calculated by the solver, they will be outlined below to provide context for the subsequent discussion of roughness effects. The standard wall functions for the viscous and log layers are shown in equations [3.4] and [3.5] respectively [186].

$$u^+ = y^+ \qquad [3.4]$$

$$u^+ = \frac{1}{\kappa} \ln(E' y^+) \qquad [3.5]$$

The blended wall function, also known as Reichardt's law is [194]:

$$u^+ = \frac{1}{\kappa} \ln(1 + \kappa y^+) + C \left(1 - e^{-\frac{y^+}{y_m^+}} - \frac{y^+}{y_m^+} e^{-b y^+} \right) \qquad [3.6]$$

Where y_m^+ corresponds to the theoretical intersection of the viscous sub-layer and the log-layer solution and:

$$C = \frac{1}{\kappa}\ln\left(\frac{E'}{\kappa}\right) \qquad [3.7]$$

$$b = \frac{1}{2}\left(\frac{y_m^+\kappa}{C} + \frac{1}{y_m^+}\right) \qquad [3.8]$$

The turbulent energy coefficient E' can be defined as the ratio of the log law offset (E) and the roughness function *f.* The role of this roughness function and how roughness walls are modelled will be covered in more detail in Section 3.1.1.2.

3.1.1.2. Wall Treatment for Rough Walls

In general, the effect of wall roughness is modelled by modifying how the wall functions, described in Section 3.1.1, are applied. Two primary approaches exist often referred to as *Rough Model* (R) and *Rough Displaced Origin Model* (RDO). Both operate by shifting the log layer of the inner boundary layer closer to the wall as shown in Figure 3.3. However, the approach with which this is done varies depending on the method leading to differences in simulation requirements and results.

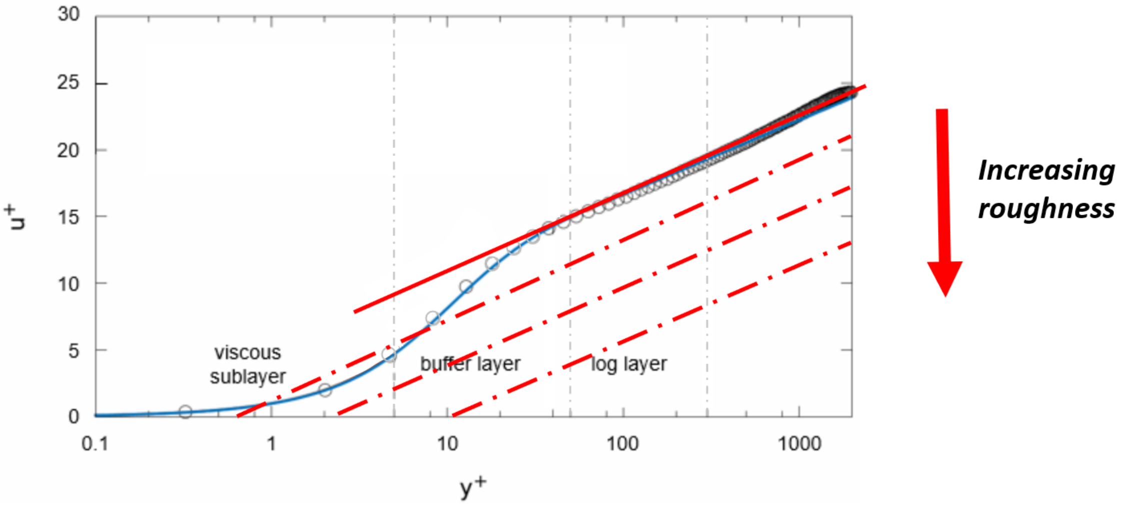

Figure 3.3 *- Modelled roughness effect on u⁺ (modified from STAR CCM+ User Manual* [186]*).*

Regardless of the method employed, a roughness parameter often referred to as *Roughness Reynolds number* (k_s^+) is utilised to describe the correlation between *equivalent sand-grain roughness* (k_s) and the wall distance (y). This non-dimensional roughness parameter k_s^+ can be defined as:

$$k_s^+ = \frac{k_s\, u^* \rho}{\mu} = \frac{k_s}{y} y^+ \qquad [3.9]$$

As can be seen from Equation [3.9], the formulation for k_s^+ is very similar to that for y^+ (equation [3.1]) though, rather than having wall distance as the required quantity, it has k_s. Equivalent sand-grain roughness represents the height of the sand grains that, in the fully rough regime, would produce the same drag effect on fluid flow as the actual irregularly rough surface as shown in Figure 3.4 [152].

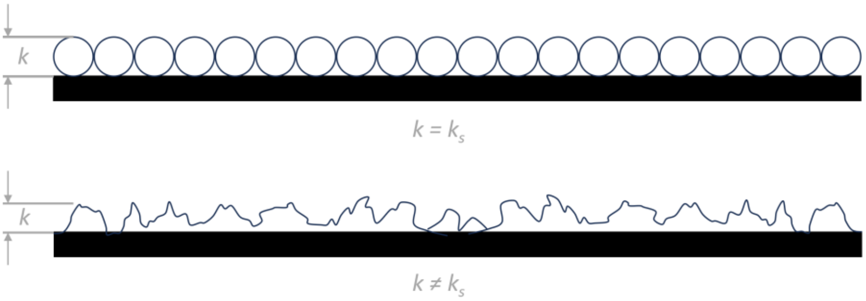

Figure 3.4 - *Equivalent sand-grain concept.*

The concept of equivalent sand-grain roughness was first introduced by Schlichting [195], who studied various surface roughness topologies and correlated the resulting skin friction losses to those achieved by Nikuradse [196] when utilising actual sand-grains. The Schlichting correlations were re-evaluated nearly half a century later by Coleman et al. [197] utilising more accurate data. Various formulas have since been proposed to relate measured surface roughness (e.g. Ra, Rz, Rq) to equivalent sand-grain roughness, as reviewed by Bons [46] and explained in Section 2.6.1.

3.1.1.2.1. Roughness Model

The roughness model is widely used across a large number of different solvers and turbulence models. It utilises a roughness function f to compute the effective log law offset, $E' = E/f$. From equation [3.5], this downward shift is achieved by increasing the magnitude of the roughness function f as shown in Figure 3.5.

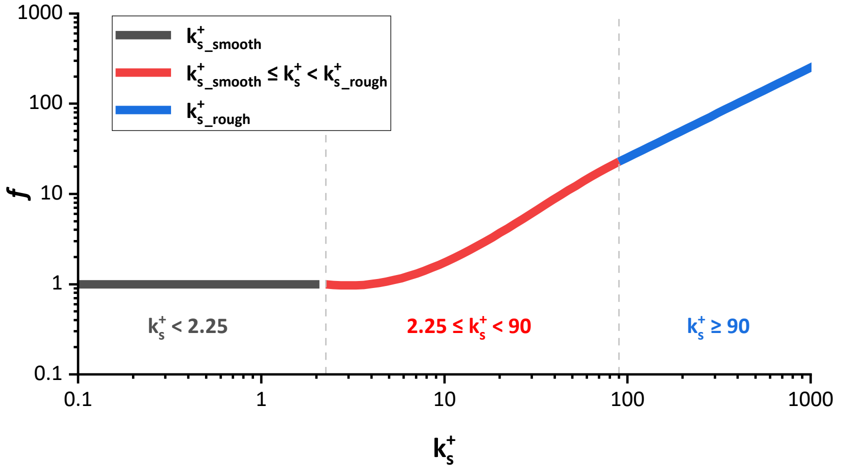

Figure 3.5 - *Change in f with changing k_s^+.*

The roughness function *f* utilised in STAR CCM+ to produce the graph shown in Figure 3.5 is based on the expression given by Jayatilleke [198] and can be defined as:

$$f = \begin{cases} 1 & , \quad k_s^+ \leq k_{s\ smooth}^+ \\ \left[B\left(\dfrac{k_s^+ - k_{s\ smooth}^+}{k_{s\ rough}^+ - k_{s\ smooth}^+} \right) + Ck_s^+ \right]^a & , \quad k_{s\ smooth}^+ < k_s^+ < k_{s\ rough}^+ \\ B + Ck_s^+ & , \quad k_s^+ > k_{s\ rough}^+ \end{cases} \qquad [3.10]$$

Where:

$$a = \sin\left[\frac{\pi}{2} \frac{\log(k_s^+ / k_{s\ smooth}^+)}{\log(k_{s\ rough}^+ / k_{s\ smooth}^+)} \right] \qquad [3.11]$$

B and C are STAR CCM+ model coefficients set to 0 and 0.253 respectively by default [186]. With similar values utilised in other commercially available software [199]. Modifications to these latter two parameters are primarily intended to define non-uniformity in the surface roughness [196,198]; however, this aspect is not investigated in the present study due to the extremely limited information available in the literature [200]. The $k_{s\ smooth}^+$ and $k_{s\ rough}^+$ parameters define what value of k_s^+ is to be considered the cutoff for the hydrodynamically smooth and fully rough regimes respectively. Conventionally, the flow is considered smooth for $k_s^+ < 2.25$, fully rough for $k_s^+ \geq 90$ and transitional for $2.25 \leq k_s^+ < 90$ thus $k_{s\ smooth}^+ = 2.25$ and $k_{s\ rough}^+ = 90$ [201]. Given density, velocity and viscosity values will not change drastically between a smooth and rough simulation, k_s is the main factor influencing the rough flow regime as shown in Figure 3.6.

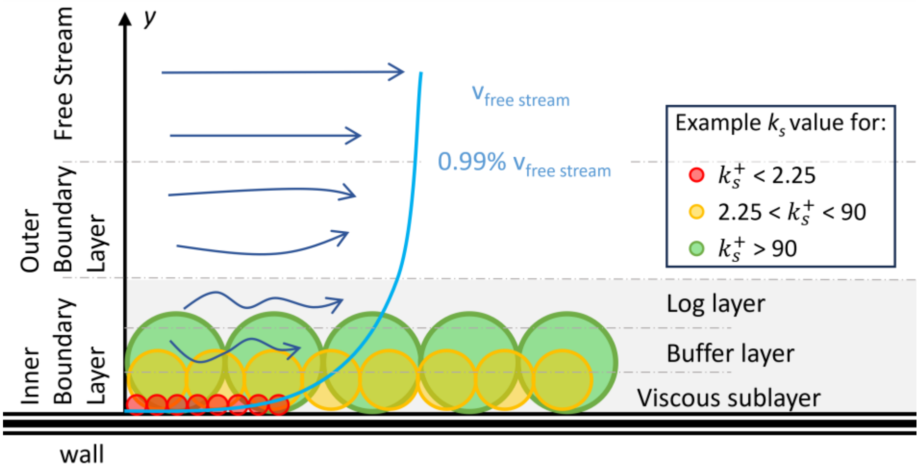

Figure 3.6 *- Annotated Diagram showing turbulent boundary layer with overlay of ks hights associated with different roughness regimes (modified from STAR CCM+ User Manual* [186]*).*

From Figure 3.6 it can be seen that, for k_s^+ < 2.25, the roughness is within the viscous sublayer making it almost invisible to the flow hence it is considered hydrodynamically smooth. For transitionally rough k_s^+ values, roughness starts to protrude into the buffer layer therefore starting to generate turbulence. Finally, for fully rough k_s^+ values, roughness protrudes well into the log layer making viscous effects near the wall negligible. This being said, it is important to consider that k_s^+ values shouldn't be seen as a representation of how much of the boundary layer is physically occupied by the modelled roughness, rather it expresses k_s in viscous units.

Ensuring that $y^+ > k_s^+$ is essential for accurately capturing the effects of surface roughness on the boundary layer when utilising the *Roughness Model* approach. If $y^+ < k_s^+$, the roughness elements will therefore be greater than the first cell height ($k_s > y$), leading to inadequate resolution of these elements and the model losing its physical meaning. In such cases, STAR CCM+ limits the local k_s values to be equal to the wall distance of the wall-adjacent cell. If a low-y^+ mesh is utilised it can therefore be seen that no meaningful roughness effects would be captured. In addition, for large k_s^+, the shifted log profile can stop intersecting the $u^+ = y^+$ curve (i.e. the viscous sublayer profile). If this occurs in the transitionally rough regime, the log profile is utilised instead. Taking these limitations into account, the u^+ velocity profiles for different k_s^+ values shown in Figure 3.7 are obtained.

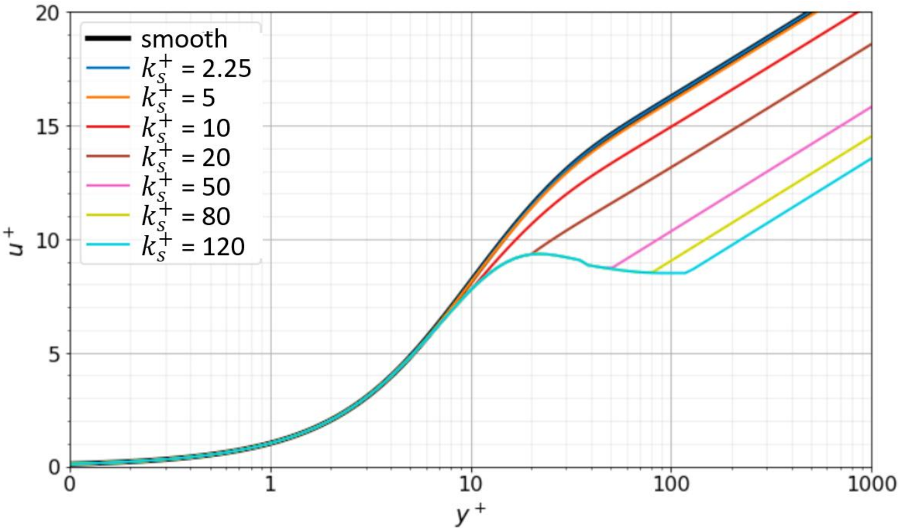

Figure 3.7 *- Changes in u^+ velocity profiles for different k_s^+ values when utilising the Roughness Model approach (modified from Simcenter STAR CCM+ [202]).*

From Figure 3.7, it can be seen that wall roughness has no impact in the viscous sublayer. For roughness heights resulting in k_s^+ > 10, physically meaningful effects will in fact only be captured if meshes having a y^+ > 20 are employed. Typically, k_s^+ values for rough surfaces range between 30 and 100, indicating that the first cell height in the mesh should be positioned within the log layer rather than the viscous or buffer sublayers to accurately capture roughness effects [48,186]. Consequently, when employing the Roughness Model, it is not possible to accurately capture roughness effects while simultaneously maintaining a high-resolution boundary layer mesh (low-y^+).

3.1.1.2.2. Rough Displaced Origin Model

The RDO technique was introduced in the past 20 years to handle complex boundaries by simplifying the computational domain and adjusting the boundary conditions to reflect the physical geometry accurately [203,204]. Consequently, it does not have as widespread use as *R*. It only being available within the Elliptic Blending (EB) and K-ω turbulence models for STAR CCM+ 23.02 for instance. Unlike the *Roughness Model* approach which relied on the computation of a roughness function *f*, RDO calculates the displaced origin y_0^+ which depends on k_s^+ but uses different limiting values as shown in Figure 3.8.

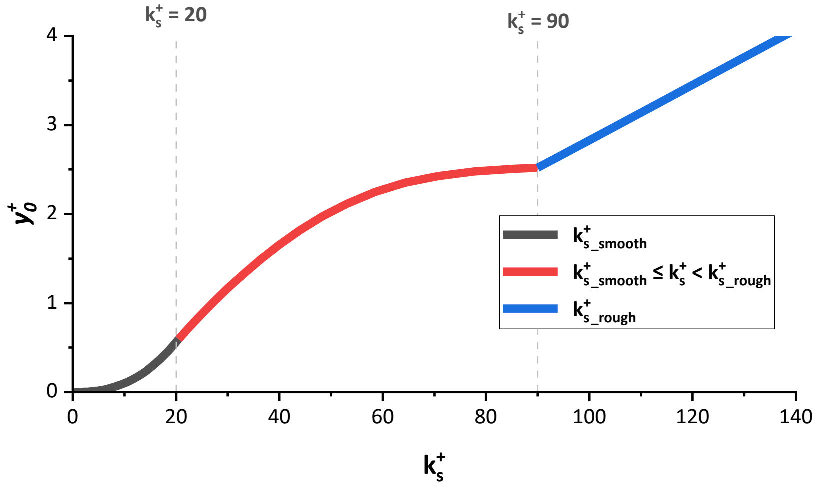

Figure 3.8 *- Displaced origin (y_0^+) values as a function of changing k_s^+*

The calculated displaced origin shown in Figure 3.8 is then combined with the blended wall function (equation [3.6]) in a modified version of Reichardt's law (modifications shown in blue in equation [3.12]) to compute the roughness induced offset in u^+.

$$u^+ = \frac{1}{\kappa}\log(1+\kappa y^+) + F_r\left[1 - e^{-\frac{y^+}{y_m^+}} - \frac{y^+}{y_m^+}e^{-by^+}\right] \tag{3.12}$$

Where:

$$F_r = \frac{1}{\kappa}\ln\left(\frac{1}{\kappa y_0^+}\right) \tag{3.13}$$

and

$$y_0^+ = \begin{cases} 0.56\left(\dfrac{k_s^+}{k_{s\;smooth}^+}\right)^{2.5} & ,\ k_s^+ < k_{s\;smooth}^+ \\ 0.63\,\zeta(k_s^+) + 0.028k_s^+ & ,\ k_{s\;smooth}^+ < k_s^+ < k_{s\;rough}^+ \\ 0.031k_s^+ - 0.27 & ,\ k_s^+ > k_{s\;rough}^+ \end{cases} \tag*{[3.14]}$$

$$\zeta(k_s^+) = \sin\left[\pi\left(\frac{k_s^+ - 20}{70}\right)^{0.9}\right] \tag*{[3.15]}$$

It is important to note that, when utilising the RDO method, whilst $k_{s\;rough}^+$ = 90 as per the *Roughness Model* method, $k_{s\;smooth}^+$ is increased to 20 meaning the flow is considered transitionally rough when 20 ≤ k_s^+ < 90. This means that, with this increased default $k_{s\;smooth}^+$ limit, the RDO model is not able to capture roughness effects for lower k_s^+ values (< 20). However, as can be seen from Figure 3.9, meaningful roughness effects should theoretically still be captured even when $y^+ < k_s^+$ [186].

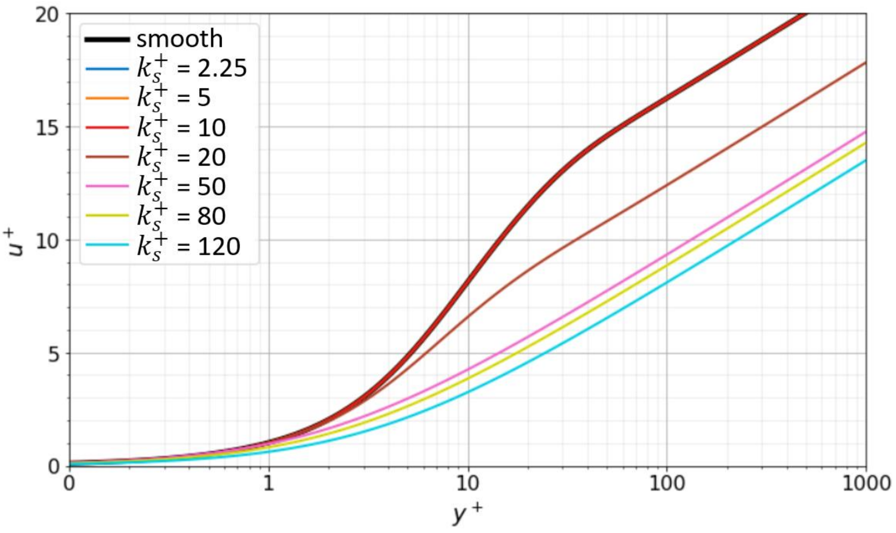

Figure 3.9 *- Changes in u⁺ velocity profiles for different k_s^+ values when utilising the RDO approach (modified from Simcenter STAR CCM+ [202]).*

3.1.2. Turbulence Modelling

Turbulent flows can be described as a complex combination of eddies of various sizes that interact dynamically within the fluid. The largest eddies, known as "integral eddies," are generated when the flow first becomes unstable and, being very vigorous, account for ~80% of the total turbulent kinetic energy (*k*). Medium-sized eddies, referred to as "Taylor eddies," play a role in the transfer of energy between scales and can therefore be considered “hybrid”. Whilst they in fact account for most of the remaining *k* (~20%), they also present dissipation which is typically associated with eddy decay. The smallest eddies, known as "Kolmogorov eddies," are where the kinetic energy is dissipated into heat through viscous forces [205]. As eddies evolve over time, kinetic energy transfers from larger eddies to progressively smaller ones. This transfer continues until the energy reaches the smallest scale eddies [205]. This process, known as the energy cascade, is shown in Figure 3.10.

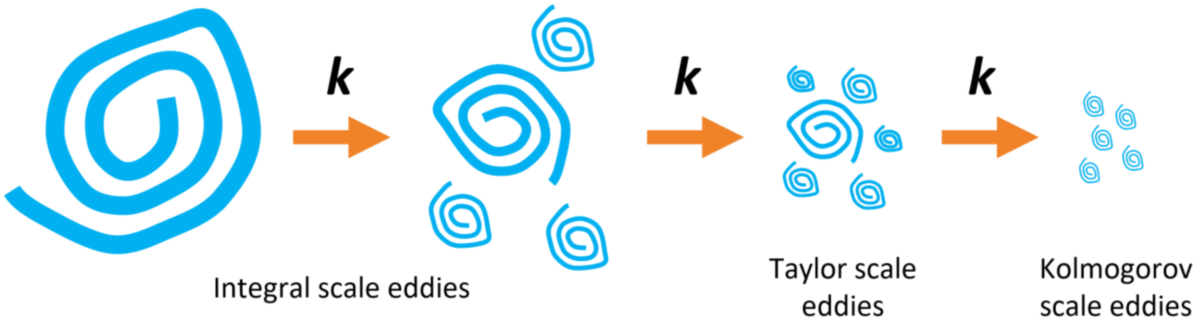

Figure 3.10 *- The turbulent energy cascade.*

3.1.2.1. Large Eddy Simulation

The primary objective of the LES technique is to minimise the errors associated with turbulence modelling assumptions by explicitly solving for a larger portion of the turbulence while only modelling a smaller portion. Such an approach is further supported by the notion that smaller eddies exhibit self-similarity, making them amenable to simpler and more universal models [206]. The simulation is therefore split into two parts. In the first of the two, large eddies are explicitly resolved. The solver capturing their behaviour directly. In the second, known as the subgrid portion, the smaller eddies are modelled via a subgrid-scale (SGS) model [207].

The computational approach is made by choosing a filtering length scale. If the eddy size is greater than this length scale, it is resolved whilst if the eddy is smaller, it is modelled [207]. This filtering length scale must be small enough to capture a sufficiently large proportion of *k.* A general and widely accepted method for evaluating the quality of LES results was introduced by Pope [208], who suggested a well-resolved simulation should capture ≥ 80% of the total turbulent kinetic energy (k_{tot}).

The mesh size plays a vital role in determining how much of *k* is resolved as, if the eddies are smaller than the grid size, they cannot be captured as shown in Figure 3.11 [207]. The process behind the generation of high physical resolution meshes will be presented in the Section 3.1.2.3.

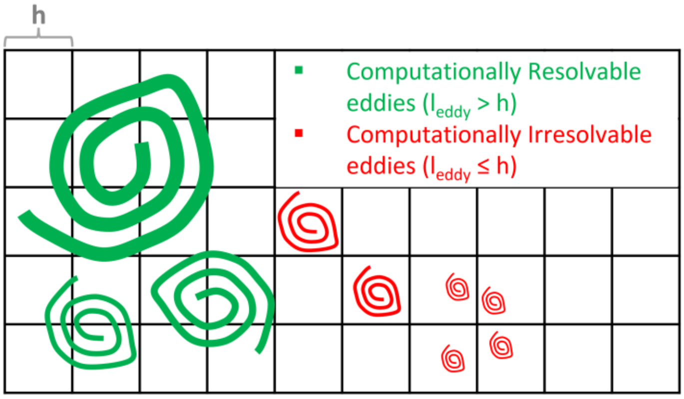

Figure 3.11 *- Resolvable and modelled eddies on a fictitious mesh.*

3.1.2.2. Detached Eddy Simulation

The detached-eddy simulation (DES) method is an unsteady simulation technique that combines the strengths of both RANS and LES [209]. U-RANS is utilised for resolving flows in boundary layers whilst LES is employed to capture the core flow regions where large turbulence scales are predominant [188]. The DES approach therefore provides superior results to RANS and U-RANS when it comes to resolving the multi-scale turbulent structures whilst providing a reduction in the computational cost when compared with LES [210]. Because RANS is in fact utilised in the boundary layer, where mostly small-scale eddies are present, a coarser grid is needed in this region when compared to LES.

Since its inception, two improved variants have been introduced named Delayed Detached-Eddy Simulation (DDES) and Improved Delayed Detached Eddy Simulation (IDDES) respectively. The DDES approach was developed by Spalart et al. [211] to overcome the incorrect behaviour exhibited by the initial formulation when dealing with thick boundary layers and areas with high spatial refinement. If the grid spacing parallel to the wall ($\Delta_{||}$) became less than the boundary-layer thickness (δ) as shown in Figure 3.12, the original DES formulation would in fact apply LES in the near wall region and, because a fine enough mesh was not present, large errors would occur leading to a reduced skin friction and premature separation. The introduction of a delay factor enhanced the ability of the model to distinguish between LES and RANS in these ambiguous regions [186]. Whilst the DDES formulation therefore better aligns with the objectives of DES, Spalart et al. [211] expressed the desire to implement some wall-modelled LES (WMLES) capabilities within DES both for thick and thin boundary-layer regions.

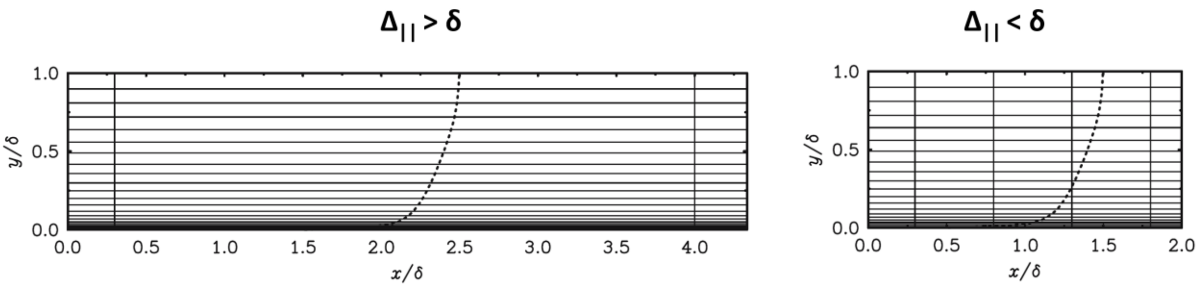

Figure 3.12 *- Grids in a boundary layer. Non-ambiguous spacing for original DES [left]. Ambiguous spacing [right]. Dotted line representing mean velocity. (from Spalart et al.* [211] *p. 182).*

To address the long-term objectives outlined by Spalart et al. [211], Shur et al. [212] introduced the IDDES formulation. As the name suggests, this model improves on DDES by combining it with an improved RANS-LES hybrid model aimed at WMLES. For IDDES, the subgrid length-scale includes a dependence on the wall distance. This approach allows RANS to be used in a much thinner near-wall region, in which the wall distance is much smaller than the boundary-layer thickness [186]. Consequently, WMLES is applied in the near-wall regions giving better resolution of the fine turbulent structures as shown in Figure 3.13.

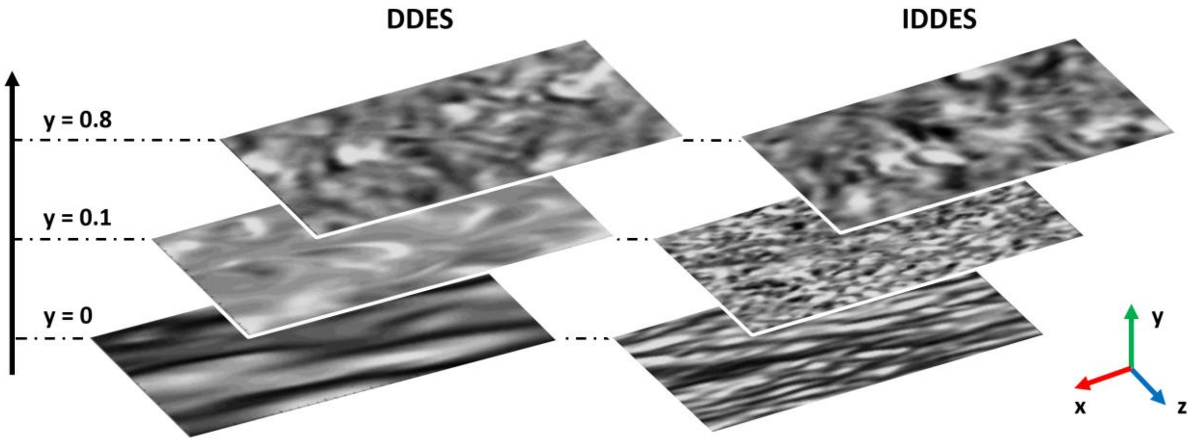

Figure 3.13 *- Comparison of XZ cross-sections on instantaneous vorticity magnitude at different distances from the wall (from Shur et al.* [212] *p. 1644).*

From Figure 3.13, enhanced resolution is apparent with IDDES, translating to a better representation of the flow features. DDES fails to do so particularly in near wall regions where these instantaneous results take one a more time-averaged and two-dimensional look. Both models behave very similarly closer to the flow centre [212].

3.1.2.3. Mesh Requirements for High Physical Resolution CFD

Regardless of the simulation approach utilised, one of the main aspects considered when generating a mesh is ensuring mesh independent solutions are achieved whilst avoiding excessive computational costs. Overlooking this mesh dependency can in fact lead to inaccuracies in numerical calculations [213]. In the case of RANS simulations, the implementation of mesh dependency assessments is comparatively direct [214–216]. The same physical problem is simulated using increasingly finer meshes with values for scalar fields of interest taken at pre-specified monitoring points. Data from these monitoring points is then plotted against the number of mesh elements in order to highlight at which point the results become independent of mesh size.

When utilising high physical resolution solvers such as LES and DES, mesh dependency tests cannot be directly performed as errors in numerical discretisation and subgrid-scale (SGS) models are both mesh dependent [217,218]. Rather, as was mentioned in Section 3.1.2.1, the amount of k resolved is used as a metric for assessing the quality of a LES/DES mesh [207,219]. As the integral eddies are known to make up ~4/5 of k_{tot}, assessing their size via a homonymous length-scale can help inform the mesh resolution needed to ensure ≥ 80% of k_{tot} is captured. The integral length scale (L_0) can be deduced as a relationship between dimensional arguments. The formulation proposed by both Rodriguez and Basu et al. [205,220] is shown in equation [3.16].

$$L_0 = \frac{k^{\frac{3}{2}}}{\varepsilon} \tag{3.16}$$

Both the k and the energy dissipation rate (ε) can be obtained from preliminary RANS simulations. Thus, equation [3.16] can be turned into a field function within the CFD solver providing a visual aid for identifying areas requiring volume refinements. Additionally, given the mesh size needs to be smaller than the eddies that are required to be resolved, equation [3.17] can be utilised to facilitate the determination of appropriate cell sizes (Δ) within the fluid domain. Areas needing further refinement can be highlighted by implementing equation [3.18].

$$\Delta = \frac{L_0}{5} \tag{3.17}$$

$$Q = \frac{L_0}{cell\ volume^{\frac{1}{3}}} \tag{3.18}$$

With it noted, that if $Q < 5$ the mesh should be refined further.

In addition to these user-defined equations, STAR CCM+ also provides built-in field functions for the Taylor (λ) and Kolmogorov (η) length scales. A reasonable local cell size can therefore also be determined by ensuring $\eta < \Delta < \lambda$ keeping in mind that, for LES, as Δ tends towards η, the results will increasingly resemble those obtained from DNS [186].

3.2. Hydrogen Jet Burner

Numerous innovative burner configurations are being developed to address the challenges posed by HHC fuels, with efforts focused on achieving safe and reliable hydrogen firing capabilities of up to 100 vol.-% [119,120,127]. One such burner architecture, discussed in Section 2.3.2.3, involves utilising burners with a jet-in-crossflow configuration [119,127]. Such burners ensure rapid mixing and high bulk flow velocities which help reduce NO_x formation by minimising residence time. The absence of flammable fuel/air mixtures prior to fuel injection prevents flashback from propagating further upstream thereby reducing the risk of significant damage. As AM becomes increasingly integral to the production of novel burners, as highlighted in Section 1.3, and considering Runyon et al. [42] and Psomoglou et al. [221] have shown surface roughness has a measurable effect on the performance of traditional burners, it is crucial to quantify the impact of roughness on this new generation of advanced combustion systems. The primary objective of this study is to investigate the sensitivity of an industry-relevant jet burner configuration to surface roughness, utilising specially designed experimental rigs and diagnostic methodologies outlined in Sections 3.2.1 – 3.2.2.

3.2.1. Rig Design

Novel jet burners inspired by industrial combustor architectures, as described by Krebs et al. [119] and overviewed in Section 2.3.2.3, were designed and constructed at Cardiff University's Gas Turbine Research Centre (GTRC) to allow for the testing of various surface finishes. The final aim of this work was to investigate roughness effects on a jet-in-crossflow (JICF) burner. However, in order to isolate variables, simplify initial numerical work and determine the influence of differing fuel delivery methods, data also wanted to be collected in a fully premixed version of the burner (PJB). Critical dimensions, including the premixing length and nozzle diameter, were selected for their industrial relevance and kept consistent across both the JICF and PJB variants. Instrumentation probe locations were also unchanged. The design of both burner variants together with that of the different roughness inserts and diagnostic techniques utilised is presented in Sections 3.2.1.1 – 3.2.1.5.

3.2.1.1. PJB Configuration

The PJB variant eliminates the potential for fuel/air unmixedness by using a premixed charge, simplifying the rig both physically and numerically and ensuring that any changes observed when altering the surface finish can be attributed solely to the surface modification. Though fuel would no longer be injected radially into the air stream via a central fuel lance, a bluff body with the same outer dimensions is used to generate comparable velocity flow-fields downstream.

The experimental rig was mounted in a vertical orientation, with the flame propagating vertically upward. The resulting assembly for this PJB is shown in Figure 3.14.

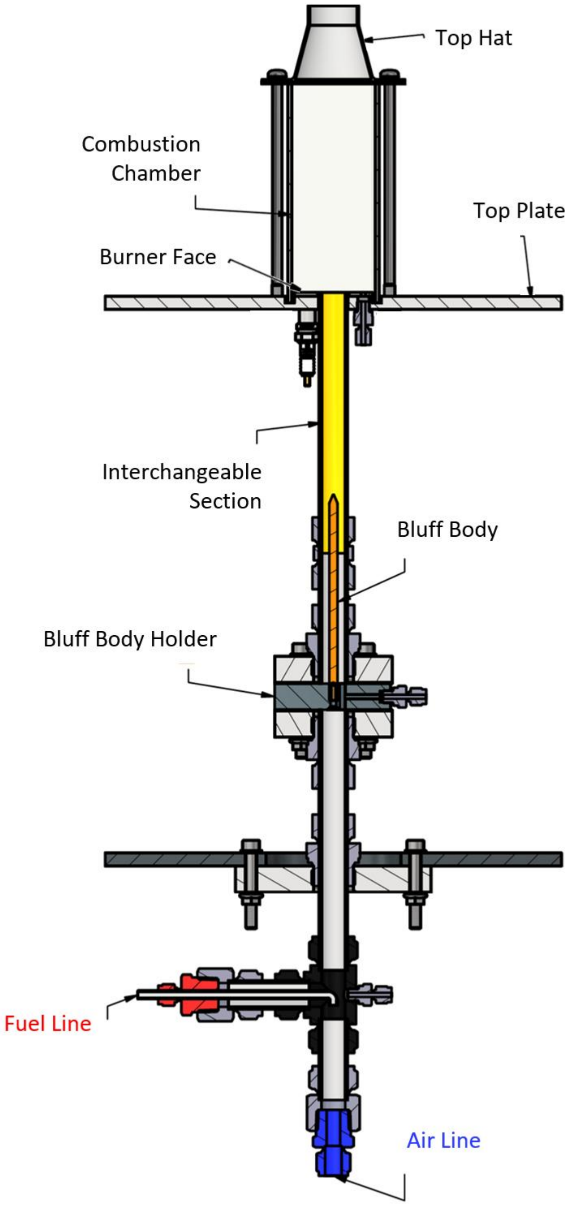

Figure 3.14 *– Scaled cross-section view of the PJB assembly.*

Fuel is injected upstream of the bluff body assembly in a counterflow configuration to ensure a high level of premixing as covered in Section 3.2.3. The last 200 mm long section of the premixing channel, shown in yellow in Figure 3.14, was designed to be easily interchangeable and will serve as the area to analyse the effects of inserts with different finishes. The process behind the selection and application of different surface finishes to these interchangeable sections is detailed in Section 3.2.1.4. Engineering drawings and the bill of materials list for the rig are collected in Appendix D.1.

Combustion chamber confinement was provided by quartz walls to enable optical access. The PJB was originally designed to accommodate a 64 × 64 mm square quartz enclosure with flat plates, offering improved flow-field characterisation under reacting conditions. Following the initial test campaign, results of which are presented in Chapter 5, this confinement failed. Due to long replacement lead times and the removal of PIV from the study scope, the enhanced optical access afforded by the square flat-panel configuration was no longer required. Consequently, it was replaced with a quartz cylinder (100 mm internal diameter, 200 mm length). This cylindrical confinement was also used for the JICF configuration, as shown in Figure 3.15, ensuring that the same confinement was employed across both burners for the analysis of fuel-delivery strategy and roughness effects in Chapter 7. Consequently, despite a twofold increase in expansion ratio, comparisons were limited to datasets with matching expansion ratios.

3.2.1.2. Jet-In-Crossflow Configuration

Fuel and air delivery systems were modified for the JICF configuration to accommodate radial fuel injection via a fuel lance, designed to match the external dimensions of the PJB bluff body, which it replaced. All other components and hence critical dimensions were carried over from the PJB. This modification enabled a closer approximation to the industrial combustor architecture described in Section 2.3.2.3 and by Krebs et al. [119] due to the fuel lance presenting eight evenly spaced 0.9 mm diameter holes injecting fuel radially into the airstream. The resulting JICF burner assembly, mounted in a vertical orientation as the PJB, is shown in Figure 3.15.

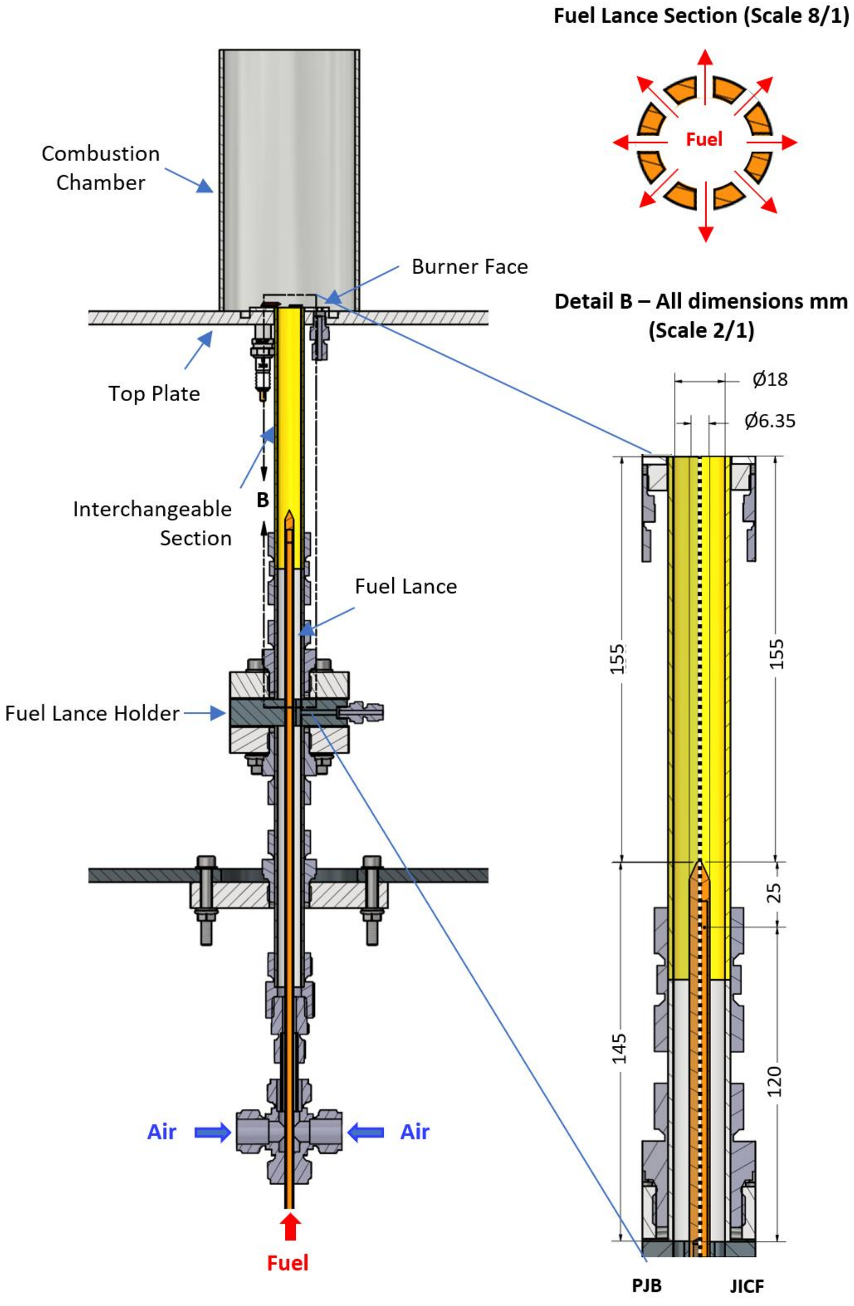

Figure 3.15 – *Scaled cross-section view of the JICF [left]. Detail B half-insets highlighting key dimension comparison between PJB and JICF configurations [right]. Section view of JICF central fuel lance for fuel flow visualization [top-right]*

As illustrated in Figure 3.15, the air delivery system was modified relative to the PJB configuration to accommodate the repositioned fuel line, which now exits at the base of the burner, previously the location of air injection in the PJB setup. Although air is still introduced at the base in the JICF configuration, it is now delivered radially via a cross-manifold. Co-axial fuel and air delivery not being possible due to size constraints. From preliminary isothermal CFD simulations, this design enables uniform distribution of air through opposing inlets, thereby promoting a homogeneous flow field downstream.

3.2.1.3. Instrumentation Probes and Ignitor

The same instrumentation and probe locations were used for both the PJB and JICF configurations. Holes were drilled into the top plate to allow for the insertion of the ignitor and instrumentation probes at the base of the combustion chamber as shown in Figure 3.16 [A]. The ignitor was bent at a 90° angle from its insertion point to ensure it sparked against the tip of the burner outlet nozzle, minimising its impact on the flow field. Its location remained unchanged in both PJB and JICF configurations. Holes were also drilled radially into the bluff body / fuel lance holder in order for instrumentation probes to be inserted into the premixing chamber as illustrated in Figure 3.16 [B].

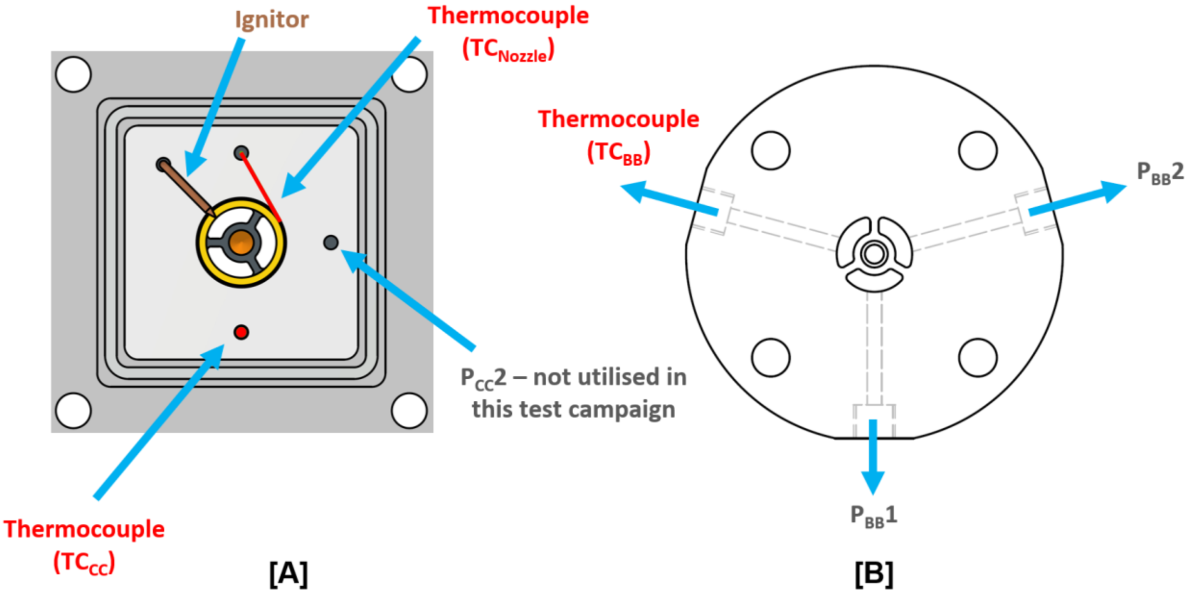

Figure 3.16 *– Radial views of burner face [A] and bluff body holder [B] with ignitor and instrumentation probe location.*

From Figure 3.16, temperatures at both the burner face (TC_{CC}) and nozzle tip (TC_{Nozzle}) were measured within the combustion chamber. The burner-face temperature was obtained using a K-type thermocouple protruding approximately 1 mm from the ceramic surface into the chamber. The nozzle-tip temperature was measured using an N-type thermocouple in contact with the external surface of the burner nozzle.

Additionally, a K-type thermocouple was installed in the airstream of the bluff-body/fuel-lance holder (TC_{BB}) to provide air-inlet temperature measurements and, under fully premixed operation, to indicate excessive flame flashback. Spare ports in both the burner face (P_{CC}) and bluff body holder (P_{BB}) were not designed for a specific instrumentation probe. Instead, they were included to ensure long-term adaptability of the rig, enabling flexibility for a range of diagnostics such as pressure drop, dynamic pressure, or static pressure/temperature measurements. Additionally, if not required, they could easily be sealed off.

3.2.1.4. Rough Insert Design and Manufacture

For this work, a comparison between surface textures produced by conventional manufacturing techniques and AM was undertaken. Two interchangeable inserts were created: one was conventionally manufactured (“M1”) with AM initially considered to produce the rough insert. However, due to the well-documented issues with warping [222,223], high costs, and difficulty in precisely controlling the surface finish [35], a more reliable method was chosen to replicate surface textures comparable to those achievable via AM. Methods such as grit blasting and coating application were considered impractical for adding roughness to the inner walls of a long hollow cylinder. Drawing from findings in the literature [224,225], Electron Discharge Machining (EDM) was selected for texturing the rough insert (“R2”).

Ablyaz et al. [224] proposed using EDM as an alternative method for creating surface textures, especially for thin-walled parts. From the investigations performed by Karmiris-Obratański et al. [225] on the effects of EDM machine settings on the surface finish of grade 2 Titanium, the following general conclusions can be drawn. Firstly, by increasing the pulse-on current, and thus the machining power, the depth of the formed craters is increased. Secondly, by increasing the pulse-on time, the crater diameter is increased. By varying these two machine settings, a variety of surface textures can be achieved as shown in Figure 3.17.

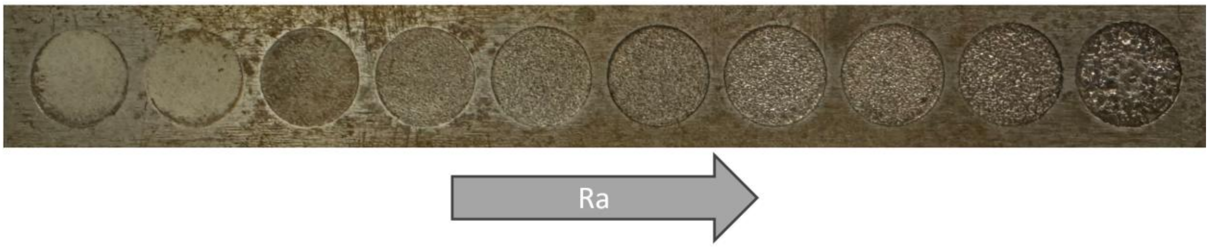

Figure 3.17 *- Test piece from Cardiff University showing surface finishes achievable with EDM.*

Achieving uniform surface roughness using EDM on internal cylindrical surfaces is challenging due to variations in discharge conditions and debris flushing [224,225]. Previous studies [226] have shown that electrode geometry influences roughness uniformity, with hollow electrodes in particular producing more irregular surface textures. Consequently, a solid electrode was used in this work to promote more stable machining conditions and improved roughness uniformity.

Previous studies have shown that as-printed parts can be seen to present a wide range of surface finishes [35,157]. Psomoglou et al. [221] investigated roughness effects on AM swirlers with a maximum arithmetic average roughness (Ra) value of ≈ 9 µm. Since the roughness-induced changes observed were minimal, investigations at higher surface roughness were advised. For this work, an R2 insert with a surface finish of Ra ≈ 20 µm was therefore selected to represent AM downskin surfaces with an angled build orientation. This choice reflects the well-documented observations that a worsening surface finish is primarily influenced by the laser incidence angle deviating further from horizontal and the challenges associated with downward-facing surfaces during the printing process [227,228]. By adopting such an approach, the usefulness of not only surface polishing but also the addition of artificially increased roughness would be assessed.

Both inserts were machined from round bar stock to account for material loss in the EDM process and ensure comparable final internal diameters. The R2 inner diameter was therefore initially undersized compared to the M1 one which was reamed to achieve the final specified diameter. After the EDM process was performed, measurements showed the R2 radius to be within ±0.100 mm of the reference, with deviations similar to those of other AM components found in the literature [229,230]. The two resulting inserts, along with example surface profiles that visually demonstrate changes in surface finish, are presented in Figure 3.18.

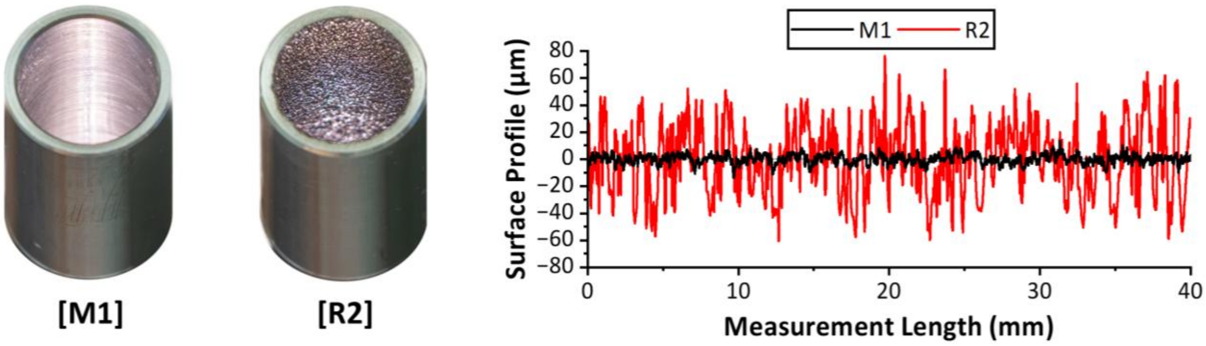

[M1] **[R2]**

Figure 3.18 *- Conventionally machined (M1) and EDM (R2) interchangeable inserts with example profiles respective of the two surfaces. Profiles measured via the Taylor Hobson Form TalySurf Series 2 profilometer as described in Section 3.2.1.4.1.*

3.2.1.4.1. Surface Finish and Form Characterisation

Prior to conducting any experimental work, the form and surface roughness of all interchangeable inserts were measured. Of the surface measurement techniques outlined in Section 2.5.1.1, contact profilometry was selected, as it was the primary technique available at Cardiff University and, unlike optical methods, did not require sectioning of the insert to access the internal roughened surface. A Taylor Hobson Form TalySurf Series 2 profilometer, used extensively for tribology and SLM surface roughness studies [42,147,148], was employed. A standard inductive pick-up stylus arm equipped with a 90° conisphere diamond stylus, featuring a 2 µm nominal radius and a vertical resolution of 16 nm, was employed. Measurements and surface roughness analyses were conducted in accordance with BS EN ISO 4287/4288 guidelines. Given that the rough insert was expected to have an average surface roughness of 20 µm, an 8 mm cut-off length was used. For the machined insert, a cut-off length of 0.8 mm was applied.

Roughness measurements were taken at both ends of each insert, with all measurement spanning a 40 mm evaluation length. After each reading, the insert was rotated by 120° to take the next measurement. As shown in Figure 3.19, this process resulted in six measurements per insert, providing a detailed profile of internal surface roughness, capturing any variations in surface finish along each cylinder. Average Ra, Rq (RMS surface roughness), and Rz (ten-point average roughness) values for each insert are presented in Table 3.1. Additional details on the surface roughness quantifications mentioned in Section 3.2.1.4.1 can be found in standards such as BS 1134:2010 [146].

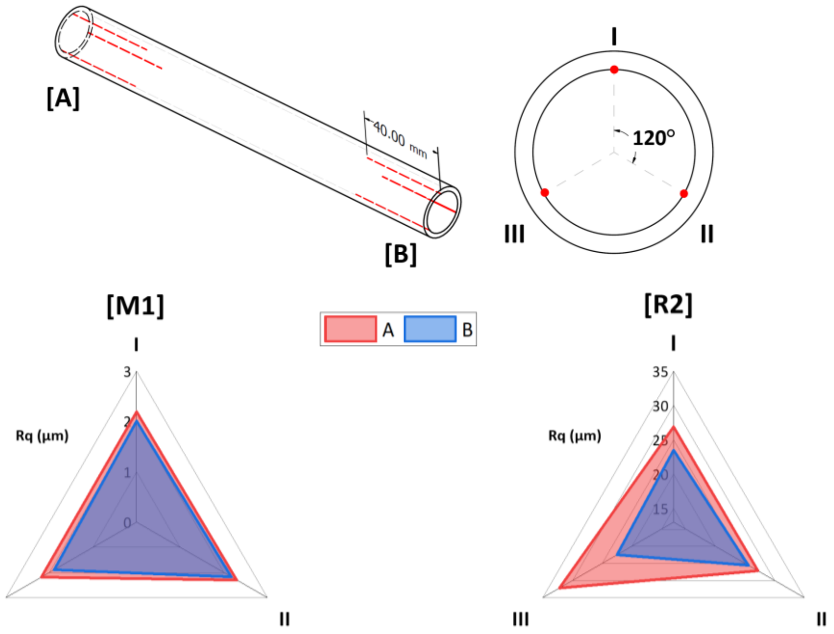

Figure 3.19 - Surface roughness measurement locations on M1 and R2 inserts [top]. M1 and R2 inserts with respective variations in internal surface finishes [bottom].

Table 3.1 *- Surface roughness measurements for each insert.*

Insert	**Measurement**	**Measurement Location**						**Average (µm)**
		A			**B**			
		I	**II**	**III**	**I**	**II**	**III**	
M1	**R_a (µm)**	1.79	1.89	1.8	1.6	1.77	1.52	1.73
	R_z (µm)	9.54	9.96	9.58	9.08	9.39	8.43	9.33
	R_q (µm)	2.19	2.3	2.19	2.01	2.17	1.89	2.13
R2	**R_a (µm)**	21.4	21.9	26.3	19.4	19.9	18.3	21.20
	R_z (µm)	139	137	146	118	138	116	132.33
	R_q (µm)	26.9	27.2	32.2	23.5	25.6	22.5	26.32

A comparison of the average surface finishes achieved for both the M1 and R2 inserts reveals an order of magnitude difference. The R2 insert closely aligns with the target roughness of ~20 µm Ra. For the M1 insert, surface roughness measurements remain consistent both radially and axially. Greater inconsistencies, particularly along the axial direction (comparing A and B measurements), are observed for the R2 insert, primarily due to electrode wear during manufacturing, which is amplified by the significant length-to-diameter ratio of the pipe. Overall, the increased surface finish variation of R2 compared to M1 would also be expected in AM processes, as it is well-documented that surface roughness along the length of AM components varies discontinuously without a clear trend [231].

Form deviation of the R2 insert relative to the smooth reference was assessed by fitting a curve to radial TalySurf measurements via the TalyMap Platinum 7.1.7288 software. The measured radii were 9.05 mm for M1 and 9.13 mm for R2, both within ~1.4% of the CAD radius (9 mm). The R2 insert exhibited deviations consistent with those reported for AM components [229,230]. Area differences between the two inserts were found to be ~1.78%. It is noted that the R2 insert has a nominally larger diameter than M1, which would typically be expected to produce lower flow velocities under identical conditions. The opposite trend, as presented in Section 5.3.1, suggests that these differences are attributable to genuine surface roughness effects rather than geometry, emphasising the influence of roughness on flow behaviour.

3.2.1.5. Air and Fuel Delivery System

For this study the same underlaying delivery system, developed for high repeatability and precise control, and previously used in other GTRC rigs, was employed [108,232,233]. Dedicated flow control valves (FCV) and Coriolis mass flowmeters (CMF) are used for precise control of both fuel and air. Air is supplied via an Atlas Copco GA 45 variable speed drive air compressor paired with a Beko Drypoint DPRA960 air dryer to lower its dew point. The dried air is supplied through two separate lines, each equipped with a Bronkhorst F203 mass flow controller capable of delivering up to 25 g/s of air, with an accuracy of ±0.5% of reading and ±0.1% of full scale. To ensure accuracy, the flow through these meters is also routed through a larger Emerson CMF025M for confirmation. The 100% H_2 fuel flow, is delivered from multi-cylinder packs (N5 CP grade 99.999%) stored in a remote onsite location through Bronkhorst M14 CMFs. These meters have a flowrate accuracy of ±0.5% of reading and are capable of providing up to ≈8 g/s of fuel. The fuel and air mass flow rates are controlled in a remote location via a PLC system which is operated by inputting the desired FCV position and monitoring the CMF output. Given that average and maximum equivalence ratio variations of ~0.96% and ~2.4%, respectively, were observed during stability limit repeatability tests in Chapter 5 and Chapter 7, there is confidence that the observed roughness trends and the overall experimental data are of satisfactory accuracy.

3.2.2. Non-Intrusive Diagnostics

A series of non-intrusive diagnostic systems were employed to provide a comprehensive characterisation of roughness effects on flame composition, flow-field and exhaust gas emissions. These systems included optical diagnostics such as Chemiluminescence (CL) and Laser Doppler Anemometry (LDA), as well as methods like exhaust gas sampling. The subsections below provide fundamental background to these diagnostics together with details of the systems used in this study.

3.2.2.1. Chemiluminescence

Chemiluminescence (CL) refers to the spontaneous emission of light from excited chemical species through an electronic exchange process, a phenomenon extensively studied since the mid-1950s [234]. Due to its ease of detection and non-intrusive nature, CL emissions from combustion are commonly used to identify flame front locations [235] and heat release dynamics [236]. In lean hydrocarbon flames, multiple excited species, including OH*, CH*, and C_2*, can be observed, with OH* receiving significant research attention [237–240]. This is particularly the case for hydrogen and high hydrogen content fuels, where, despite significantly weaker emissions compared to hydrocarbons and a much lower abundance than key ground-state intermediate species (OH, H, O) [241], its spontaneous light emission, combined with the limited or absent carbon concentration, makes OH* the predominant or sole detectable excited species. This is demonstrated in the CL spectra of hydrogen-air co-flow flames presented by Zhao et al. [237] in Figure 3.20.

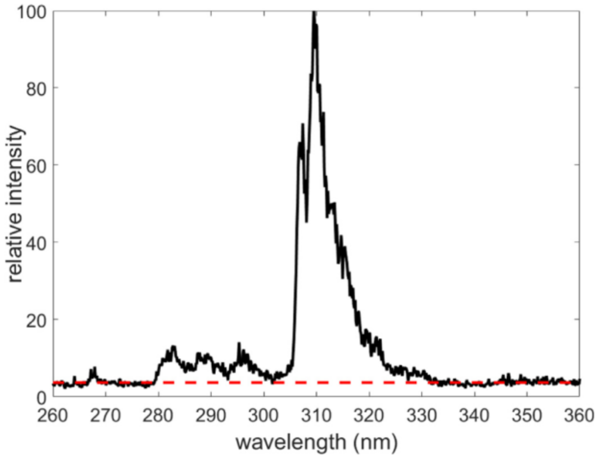

***Figure 3.20** – OH* chemiluminescence spectra acquired from a hydrogen-air co-flow flame (from Zhao et al* [237]*).*

As shown in Figure 3.20, OH* CL peaks near λ = 309 nm meaning that, for CL measurements to be made, bandpass filters corresponding to this peak wavelength must be utilised. This corresponds to the $A^2\Sigma^+ \rightarrow X^2\Pi$ electronically excited to ground state energy level transition [242]. The dominant chemical production reaction for the formation of OH* for hydrogen combustion is $H+O+M \leftrightarrow OH^*+M$ where M is a third body species [237].

A more precise reconstruction of the internal structure of a flame, including the spatial distribution of reactive species and heat release, is obtained by applying the Abel transform to the observed CL intensity data, as shown in Figure 3.21 for a swirling flame, viewed from the side with the flow from bottom up. This Abel deconvolution enables the retrieval of the true radial distribution of CL emission (such as OH*) in an axisymmetric flame by correcting for the line-of-sight integration effect, which arises when the recorded 2D image represents the cumulative emissions from multiple radial positions [142,243].

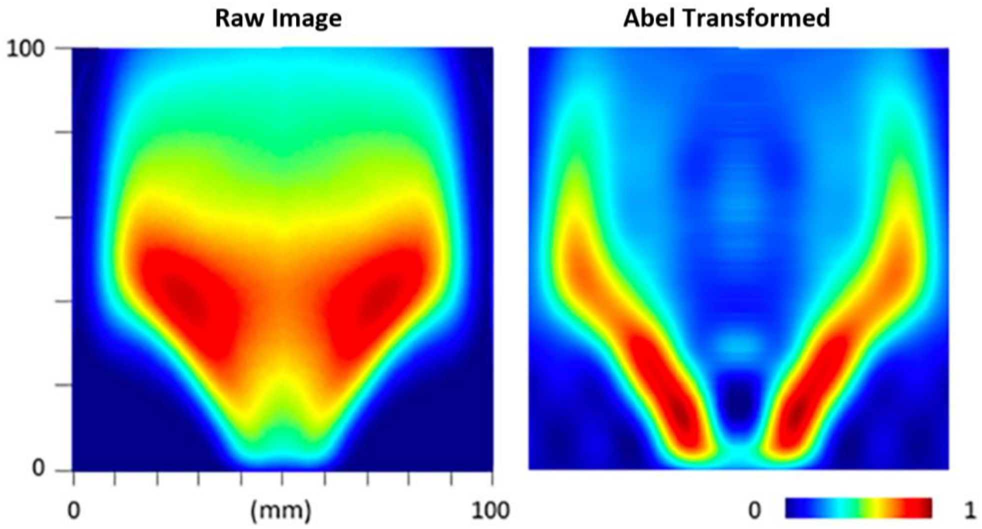

***Figure 3.21** - Raw line-of-sight OH* image [left] vs Abel Transformed OH* image [right] (from Pugh et al.* [142]*).*

Throughout this work OH* CL data were collected via a Phantom v1212 high-speed CMOS camera, a Specialised Imaging SIL40HG50 high-speed image intensifier, a UV lens (78mm F/4), and a 315 nm (±15 nm FWHM) narrow bandpass filter [42,244]. Chemiluminescence data was recorded at 4 kHz, with the image intensifier gated at 10 µs. A scaled target image was used to determine the image resolution, which, depending on the configuration, ranged between 4-4.3 pixels/mm. Each CL dataset was time-averaged over 2000 images (duration of 0.5 s). Post-processing was then performed using a modified Abel inversion algorithm as described in previous studies [244,245].

3.2.2.2. Emissions Gas Analysis

The measurement of NO_x emissions is crucial due to its significant role in environmental impact, combustion efficiency, and regulatory compliance. Unlike fossil fuels, H_2 combustion does not produce carbon-based pollutants such as CO_2; however, it can lead to high levels of thermal NO_X due to the elevated flame temperatures associated with H_2-air combustion [246].

To ensure accurate comparison of NO_X emissions across different experimental conditions, normalisation methods are commonly applied. As discussed in Section 2.2.1, the fundamental differences between hydrogen and fossil combustion mean that certain normalisation approaches may overpredict NO_X emissions for hydrogen and HHC fuels. This issue has been observed with the widely used normalisation by oxygen concentration (15% O_2) [83] where different fuel factors exist allowing for fair comparisons between HHC and fossil fuels [82]. Alternatively, normalisation based on fuel energy input has been shown to mitigate these overpredictions [86]. Therefore, careful selection of the normalisation method is essential when evaluating NO_X emissions from HHC fuels, particularly in fuel-switching scenarios.

Throughout this work exhaust gas sampling and analyses were undertaken using a standard industry system supplied by Signal Gas Analysers Ltd. A single point probe was positioned 170 mm downstream along the centreline of the burner, remaining within the quartz confinement to prevent atmospheric entrainment. The 50 m sample line was maintained at a temperature of 453 K. To minimise losses, NO_X measurements were performed hot and wet using a heated vacuum chemiluminescence analyser (Signal Instruments 4000VM). Additional flow was passed through a chiller to reduce molar water concentration below 1% before exhaust molar O_2 measurements were made using a paramagnetic analyser (Signal Instruments 9000MGA).

3.2.2.3. Laser Doppler Anemometry

Laser Doppler Anemometry (LDA), also referred to as Laser Doppler Velocimetry, is a non-intrusive optical measurement technique used to determine the velocity of fluid flow by measuring the Doppler shift of laser light scattered by small tracer particles suspended in the fluid. It provides high-resolution, pointwise velocity measurements without disturbing the flow, making it ideal for studying turbulent and complex fluid dynamics [247,248].

The working principle of LDA is based on the Doppler effect, which states that the frequency of light scattered by a moving particle changes depending on its velocity relative to the observer. LDA typically uses a dual-beam setup, where a laser beam is split into two coherent beams and then focused into the measurement volume. These beams cross at a small angle, creating an interference pattern of alternating bright and dark fringes. When seeding particles pass through these fringes, they scatter light at a frequency corresponding to their velocity. A photodetector captures the scattered light and converts it into an electrical signal while a signal processor then extracts the Doppler frequency, which is directly proportional to the velocity of the particles. An example LDA system is shown in Figure 3.22 [249]. Throughout this work a 1D Dantec Dynamics Flowlite Laser Doppler Anemometry (LDA) System was utilised [42].

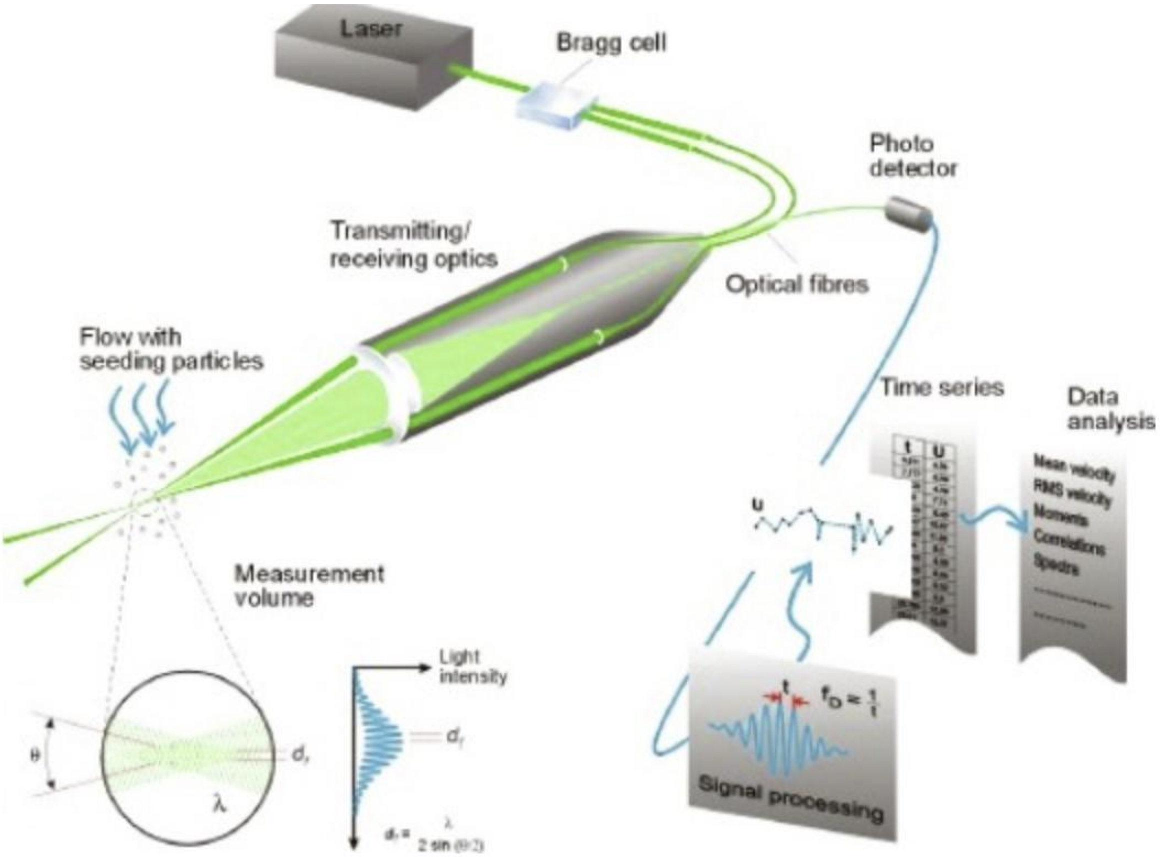

Figure 3.22 - Example LDA system (from Rohde et al. [249]).

3.2.3. Initial Numerical Simulations

Preliminary RANS simulations were conducted to compare the flow fields generated with premixed and jet-in-crossflow burner configurations and to evaluate the effectiveness of the PJB fuel delivery system in achieving high levels of premixing. Although it was predetermined that the rig would operate at atmospheric pressure with no preheating, given a wide range of thermal powers (TP) and equivalence ratios (ϕ) were going to be investigated in the actual test campaigns, an intermediate condition was selected for this initial numerical investigation. A thermal power of 21.66 kW was therefore chosen with $\phi = 0.634$ (9.6 g/s air and 0.18 g/s H_2) yielding a mean nozzle exit axial velocity of 40 m/s. STAR CCM+ 23.02 was utilised as the solver, a non-reacting regime being employed to conserve computational resources. The realisable two-layer k- ε turbulence model was used alongside a low-y^+ approach. A mesh dependency study was conducted with stable results for axial velocity, pressure and mixture fraction found for meshes having > 16 x 10^6 elements. Detailed results for this mesh dependency study can be found in Figure D.10 of APPENDIX D. A comparison of the development of axial velocity profiles within the premixing section downstream of the fuel lance/bluff body of both the PJB and jet-in-crossflow burner is shown in Figure 3.23.

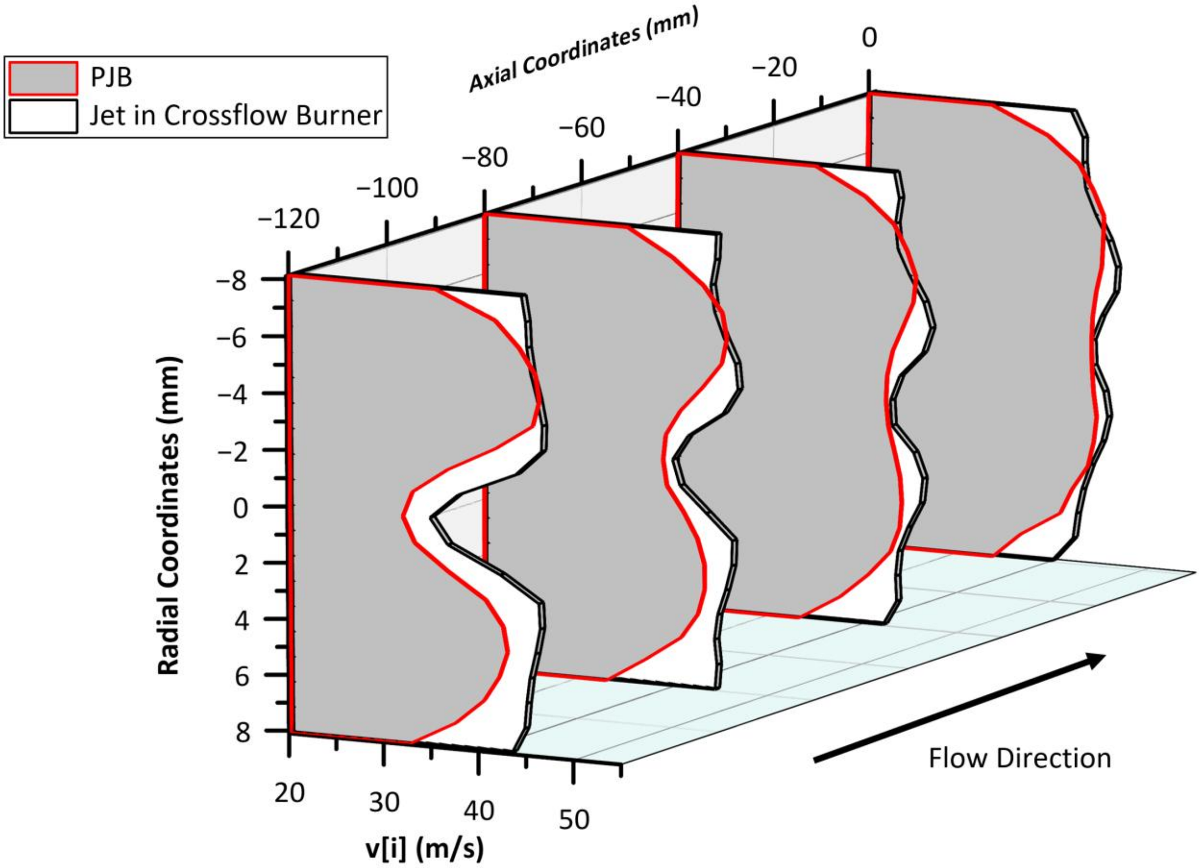

Figure 3.23 *- Comparison of axial velocity profile development within the premixing section of the jet-in-crossflow and PJB burners. The point at the 0 axial coordinate marks where the premixing tube connects to the combustion chamber.*

As can be seen from Figure 3.23, in both burners the effect of the fuel lance/bluff body weakens as the flow develops. Moreover, the velocity profiles of the jet-in-crossflow burner exhibit higher magnitudes and a more pronounced squared shape near the walls, attributed to the high-speed radial injection of fuel, which intensifies the flow in these regions. Nevertheless, the overall profiles and their evolution exhibit comparable characteristics.

The amount of premixing achieved within the PJB was assessed by looking at the mixture fraction within the premixing section. Mixture fraction (*Z*) can be calculated as follows:

$$Z = \frac{m_f}{m_f + m_{air}} \qquad [3.19]$$

A field function utilising equation [3.19] was created within STAR CCM+ and applied to the PJB domain. For the ϕ = 0.634 test case a perfectly premixed fuel and air mixture would have *Z* = 0.018466. Actual values obtained in the preliminary CFD simulation were determined by performing surface averages [186] radially along the premixing tube. Results are presented in Figure 3.24.

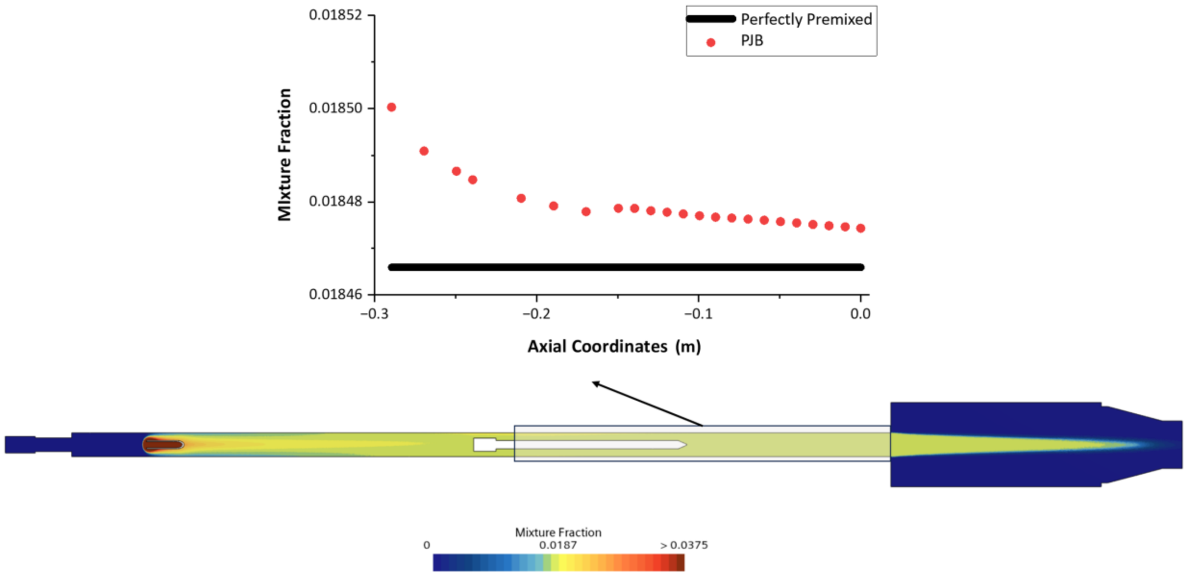

Figure 3.24 *- Mixture fraction change along the premixing section of the PJB (flow from left to right). The point at the 0 axial coordinate marks where the premixing tube connects to the combustion chamber.*

From Figure 3.24, the gap between the PJB and the perfectly premixed line can be seen to narrow as the flow progresses. It can also be seen that, once the bluff body is reached, changes in *Z* become marginal indicating a nearly uniform mixture. Whilst the ideal uniformity of a perfectly premixed scenario is not achieved, the difference at the expansion point is only ~0.045%, demonstrating that the PJB burner delivers sufficient premixing levels.

3.2.4. Experimental Facility Commissioning Work

Initial commissioning tests were conducted using the rig without the bluff body or confinement, as these components were still in the manufacturing stage. The rig was connected to both hydrogen and methane fuel lines, allowing for the use of fuel blends, particularly for initial ignition. The ignitor was positioned to the side of the burner nozzle exit, outside the flame zone, to avoid unintended flame anchoring during near-blowoff conditions. Thermocouples were placed at the nozzle outlet and 200 mm downstream to monitor potential trends as the system approached flashback conditions. The resulting setup is shown in Figure 3.25.

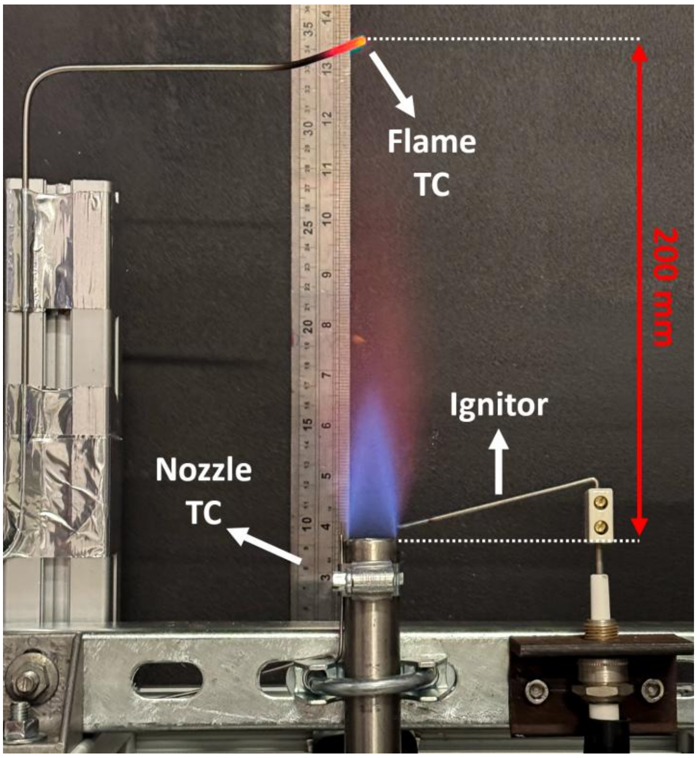

Figure 3.25 *- Setup for initial stability mapping trials.*

The initial light-up was performed with a 12.5 kW 100% CH_4 diffusion flame. Once ignition was confirmed, air was gradually introduced. However, due to flame liftoff occurring with minimal air addition (~1.5 g/s), and the inability to precisely control airflow at these lower thermal powers, the fuel was switched to a 12.5 kW blend containing 25 vol.-% H_2 and airflow set to achieve an equivalence ratio of 0.8. The hydrogen content and thermal power were then gradually increased, with the ϕ maintained at 0.8. At each stage of hydrogen increase, the methane content was first reduced, followed by an increase in hydrogen, and finally, adjustments to the air supply. The full range of fuel blends and flowrates utilised to transition to 100% H_2 can be found in Table D.2 of APPENDIX D. From this initial ignition trial, stable ignition points for the fully premixed 100% H_2 flame were found to be at 16.25 kW, 17.16 kW and 20.16 kW all at $\phi \approx 0.8$.

This setup was utilised to perform an operability sweep for thermal powers ranging from 15kW to 27kW. The 100% H_2 test matrix, comprising of 3kW thermal power increments and $0.5 \leq \phi \leq 0.9$, can be found in Table D.3 of APPENDIX D. To streamline the process, thermal power was held constant while airflow was varied to achieve all ϕ conditions. If blowoff did not occur at $\phi \geq 0.5$, airflow was further increased until blowoff was observed. Similarly, if flashback did not occur at $\phi \leq 0.9$, airflow was reduced until either flashback occurred or $\phi = 1.1$. Results are presented in Figure 3.26.

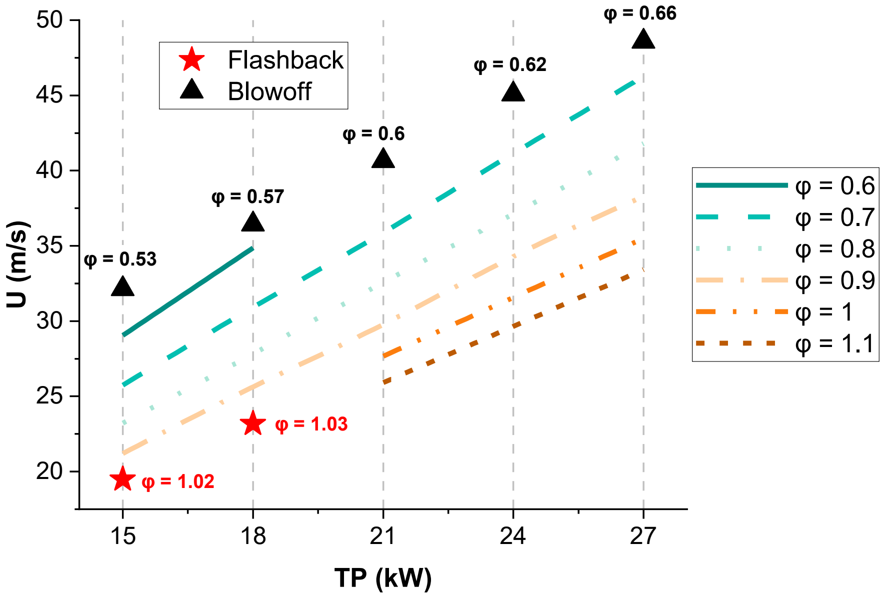

Figure 3.26 *- Initial 100% H_2 stability map for the unconfined PJB.*

Figure 3.26 demonstrates that stable combustion was achieved across the entire power range for $0.7 \leq \phi \leq 0.9$. At thermal powers ≤18 kW, flashback was observed just above stoichiometry, manifesting abruptly with an audible detonation-like sound, a characteristic typical of fully premixed configurations, leaving no uncertainty regarding its occurrence. For thermal powers > 18 kW, no flashback was detected, even at conditions above stoichiometry. Regarding blowoff, the results indicate that as thermal power increases, blowoff occurs at higher equivalence ratios due to the rise in bulk flow velocity.

Whilst the addition of the bluff body was not expected to have a significant effect on the overall stability of the finalised burner, the effects of confinement were expected to be more pronounced. Air entrainment would in fact be significantly reduced, increasing the combustion chamber temperature likely facilitating leaner combustion across the whole power range at the expense of increased flashback risk. During experimental testing of the finalised burner, the stable ignition points previously identified remained consistent, and the predicted changes in stability limits were confirmed as detailed in Chapter 5.

As observed in the initial operability sweep, flashback events during testing with the bluff body inserted occurred without ambiguity. Conversely, consistent characterisation of blowoff behaviour proved more challenging. When nearing blowoff, the flame was in fact observed to lift from the burner exit nozzle and re-anchor around the exhaust top-hat assembly. The flame stabilising on the lip/sharp edge of the exit nozzle. This re-anchoring caused by the top-hat assembly becoming visibly red-hot during operation enabling the fuel/air mixture to re-ignite in this lifted position in a pulsating manner as shown in Figure 3.27[A]. The issue was resolved by removing the exhaust top-hat assembly (Figure 3.27[B]). Without this assembly functioning as an anchor, blowoff events became clearer and allowed for consistent characterisation of the burner operability limits, which are described in detail in Chapter 5.

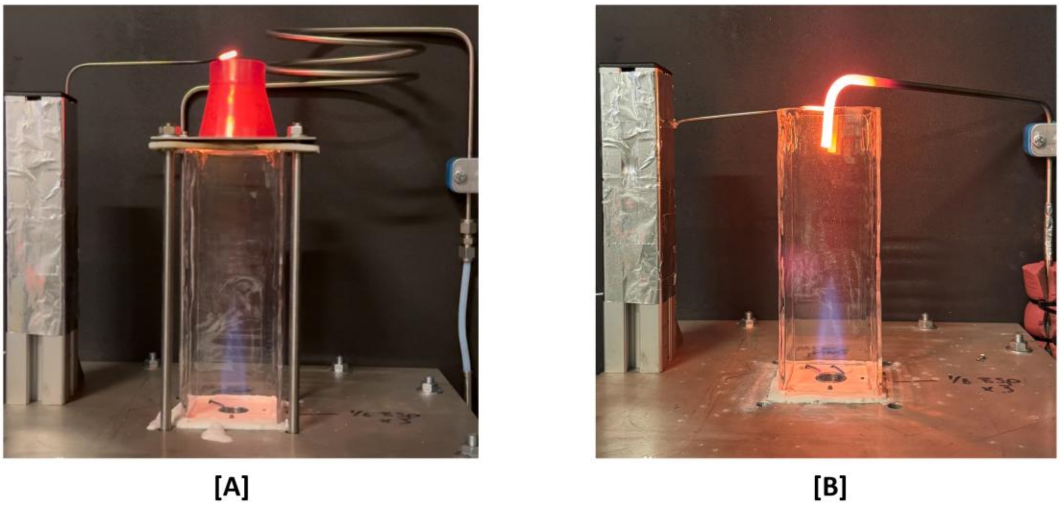

Figure 3.27 - *Comparison of PJB with [A] and without [B] the exhaust top-hat assembly.*

Chapter 4. Modelling of Roughness Effects on Generic Gas Turbine Swirler via a DES Low-y^+ Approach

Chapter 4, the primary methodology and findings of which are detailed extensively in a paper bearing the same title [250], addresses the development and application of numerical methodologies for modelling roughness effects on a Generic Swirl Burner using a low-y^+ Detached Eddy Simulation (DES) approach. This work was carried out in parallel with the design, manufacture, and commissioning of the new experimental facilities presented in Section 3.2, utilising an experimental dataset with roughness sensitivity previously collected by Runyon et al. [42]. Although swirling flames are not directly relevant to this study, this existing dataset provided a foundation for establishing and validating the numerical methods later applied in Chapter 6 to jet-based burners. The study builds on the work of Psomoglou [108], who investigated isothermal cases using a high-y^+ wall-modelled RANS method, and identified limitations in literature-based k_s correlations.

4.1. Research Scope

The aim of this investigation was to model roughness effects via a k_s correlation in conjunction with a low-y^+ DES approach. Conventionally, as already covered in Section 3.1.1.2 of Chapter 3, high y^+ meshes are needed to attain physically meaningful roughness effects as the roughness height must be smaller than the height of the wall-adjacent cell ($k_s^+ < y^+$) [48,186]. Both the Elliptic Blending (EB) and K-ω turbulence models however use specific modifications to their formulation that enable roughness effects to still be captured even when $k_s^+ > y^+$ [186].

Three DES models were examined: a smooth reference case, a rough case employing a literature-based equivalent sand-grain roughness (k_s) correlation, and a rough case using a novel correlation developed in this work. Validation was performed using existing isothermal and methane combustion data collected by Runyon et al. [42] at Cardiff University's Gas Turbine Research Centre (GTRC) on the well-documented second-generation high pressure generic swirl burner (HPGSB-2) [251,252].

The results of this study aimed to provide a guide to setting up low-y^+ simulations with roughness sensitivity including the choice of an appropriate k_s correlation for swirling flows. Analysis of the CFD simulations enabled a better understanding of the roughness induced effects on the boundary layer and other flow characteristics including changes in swirl number and recirculation zone. Allowing industry to understand roughness induced effects of AM components on gas turbine performance and operability limits as well as avoiding costly empirical test campaigns.

4.2. Materials and Methods

Previous experimental work performed by Runyon et al. [42] was used to validate the CFD simulations conducted in the current study. In particular, the fully premixed methane-air case at ϕ = 0.55 and equivalent total mass flow isothermal air case. The experiments were performed using the HPGSB-2, shown in Figure 4.1 in conjunction with the high-pressure optical chamber (HPOC) [251,252]. STAR CCM+ 23.02 was used as the CFD solver.

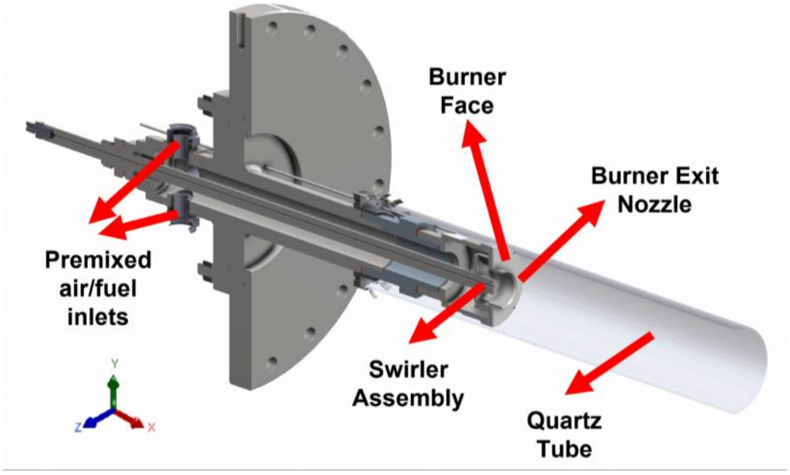

Figure 4.1 *- Section view of HPGSB-2 with Sg = 0.8 radial/tangential swirler and quartz tube installed (left to right flow).*

4.2.1. Reference Experimental Data

Experimental data were collected for three swirlers with a geometric swirl number (S_g) of 0.8. One was conventionally manufactured ("8M") whilst the other two were produced via SLM. Of the SLM-manufactured swirlers, one received no post-processing ("8R"), and the other was grit-blasted ("8G") [42]. To maximise the likelihood of capturing roughness effects in the numerical simulations, the present study focused on the data collected for the 8R and 8M swirlers, shown in Figure 4.2. Average measured surface roughness values for the 8R swirler can be found in Table E.1 of APPENDIX E.

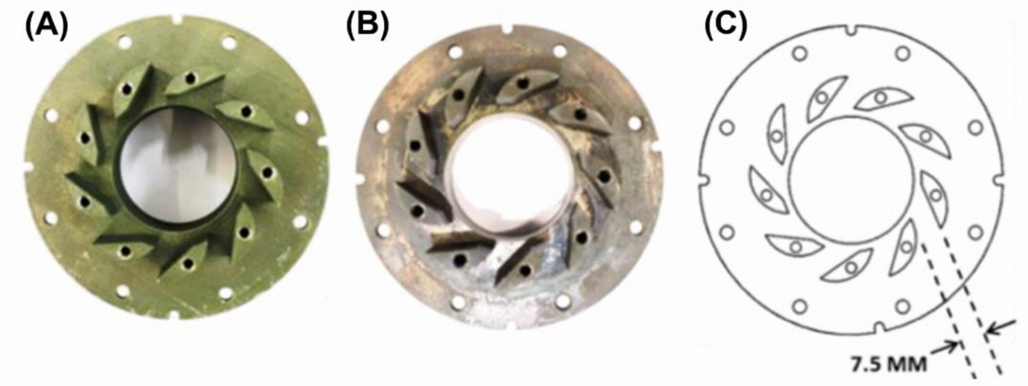

Figure 4.2 *- Swirler inserts (A) 8R, (B) 8M and (C) CAD model with critical dimensions.*

The numerically adjusted experimental axial velocities for the isothermal air flow conditions at equivalent total mass flow to ϕ = 0.55 are shown in Figure 4.3. These Laser Doppler Anemometry (LDA) measurements were taken 5 mm downstream of the burner exit nozzle starting from the centreline (r = 0) and ending just outside the burner nozzle. All the isothermal flow measurements were conducted with the quartz confinement tube removed from the HPGSB-2 [42]. The minimum axial velocities of both velocity profiles can be seen to be located at r = 0 thus suggesting the flow field is symmetric as mentioned in Section 2.4 and shown in several publications [135–137]. Insights gained from this pre-existing dataset informed subsequent LDA measurements presented in Chapter 5, which were conducted closer to the nozzle exit (2 mm rather than 5 mm) and across the full span of the PJB nozzle exit.

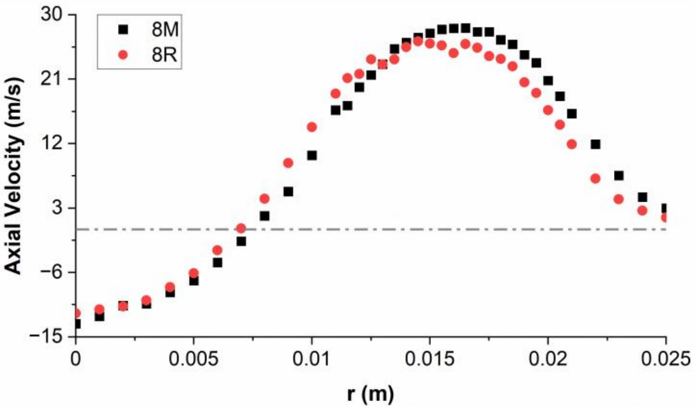

Figure 4.3 *- Axial velocity profile at equivalent air flow to φ = 0.55 (data from Runyon et al.* [42]*).*

The Abel transformed OH* chemiluminescence images for 8R and 8M are shown in Figure 4.4. More information on the capture system can be found in the paper by Runyon et al [42]. As shown, peak OH* intensity increases with increasing surface roughness, accompanied by an inward radial shift of the flame stabilisation location and a reduction in flame angle relative to the burner axial centreline.

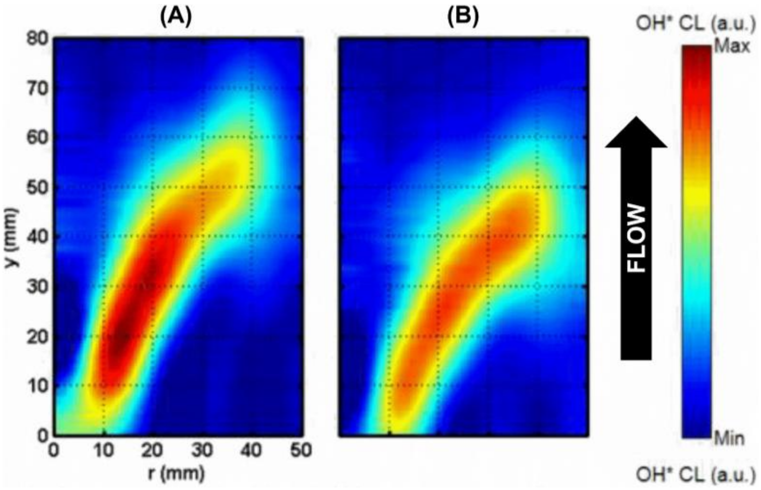

Figure 4.4 *- φ = 0.55 Abel transformed OH* chemiluminescence images for (A) 8R, (B) 8M (from Runyon et al.* [42]*).*

4.2.2. Numerical Setup

Section 4.2.2 presents the setup process for the CFD domains and meshes, followed by an overview of the DES models and settings utilised. It concludes by detailing the approach used to select the literature-based roughness correlation and to formulate the user-defined correlation.

4.2.2.1. Physics Setup

The isothermal cases were initiated as follows; the segregated flow isothermal model was utilised and the temperature set to 573 K. The reference pressure was set to atmospheric (0.101 MPa) and the default STAR CCM+ material properties for air were left unchanged. For the preliminary RANS case a mass flow inlet set to 16.1 g/s was used whilst, for the DES cases, this mass flow inlet was replaced with a velocity inlet reading data from the reference RANS simulation. The reference inlet conditions for the CH_4 cases are collected in Table 4.1.

Table 4.1 *- Summary of experimental conditions for $\varphi = 0.55$.*

P (MPa)	T1 (K)	$\dot{m}$ CH_4 (g/s)	$\dot{m}$ Air (g/s)
0.11	573	0.5	15.6

The GRI-Mech 3.0 [253] mechanism was utilised with the addition of OH^* [254,255] similar to other works in the literature [256]. The equations utilised for the addition of OH^* are compiled in Appendix A.2. Segregated flow enthalpy was selected in conjunction with the thickened flame model. The latter was chosen as a less computationally intense yet reliable alternative to complex chemistry [257,258].

4.2.2.2. Fluid Domains

Fuel and air are injected radially 426 .5 mm upstream of the swirler assembly when the HPGSB-2 is set up for premixed combustion. To reduce mesh elements and ensure flow through times were kept to a minimum, the CFD domain was given a plenum length of 245 mm with fuel and air being injected axially. This length was chosen to allow the flow to fully develop before reaching the swirler assembly. As can be seem from Figure 4.5, this shortening of the plenum did not lead to significant changes in the axial velocity profile. Downstream of the plenum and swirler assembly, separate domains were created for the reacting and isothermal cases. The quartz tube was removed for the isothermal measurements thus an expansion of approximately 8x would be experienced going from the nozzle outlet (40 mm diameter) to the HPOC walls (315 mm). The combustion chamber was therefore given a diameter of 200 mm, and all its walls were set as pressure outlets. For the reacting cases the quartz tube was not removed thus a combustion chamber with a 100 mm diameter was utilised. Downstream features were implemented to aid convergence consistent with other works [258].

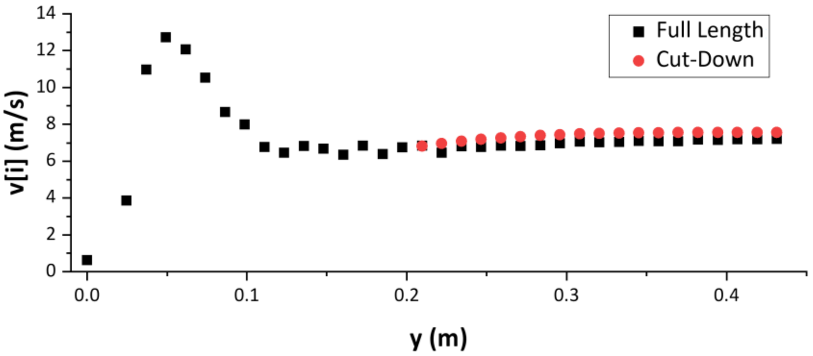

Figure 4.5 *- Comparison of axial velocity profile along full length and cut down HPGSB-2 plenum.*

Though, as explained in Section 3.1.2.3, mesh dependency tests cannot be used to assert the quality of a DES mesh, because reference RANS simulations would be utilised both to initialise the DES domains and to estimate important DES model settings such as the required time-step and mesh size, accurate RANS reference cases were needed. Guidelines and field functions presented in Section 3.1.2.3 for the creation of high physical resolution meshes were utilised to inform the positioning of refinement zones in the RANS meshes. Prism layers were applied to surfaces of interest with the first cell height being varied across different faces to achieve an average $y^+ \approx 1$. Mesh dependency tests were then performed on these RANS meshes utilising the macro described in appendix C.1. Results for monitoring points located in places of interest are shown in Figure 4.6 and Figure 4.7.

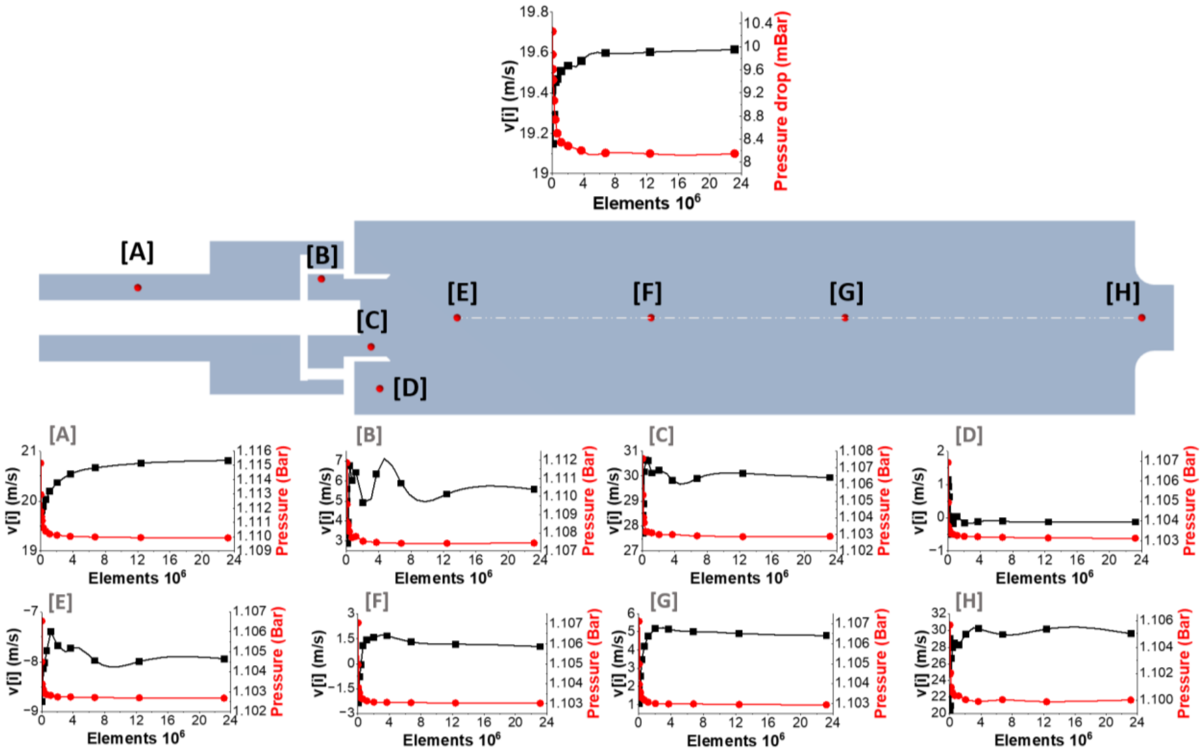

Figure 4.6 *- Nozzle exit velocity and pressure drop as a function of mesh elements [top]. Cross-section of reacting GSB fluid domain with monitoring probes and associated mesh dependency results [bottom].*

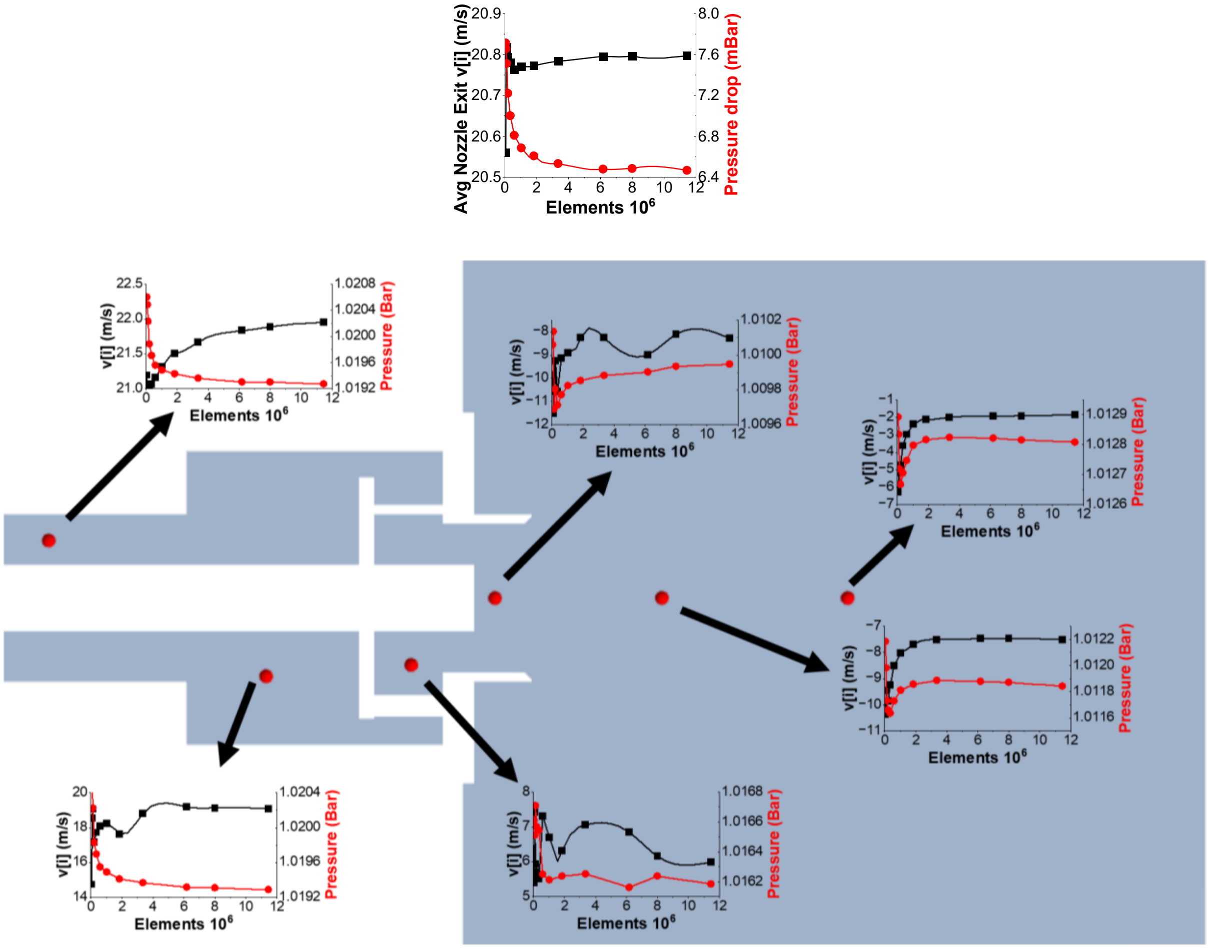

Figure 4.7 - Nozzle exit velocity and pressure drop as a function of mesh elements [top]. Cross-section of isothermal GSB fluid domain with monitoring probes and associated mesh dependency results [bottom].

From Figure 4.6, the reacting case mesh dependency results show that all monitoring points reached convergence for meshes containing ≥10 x 10^6 elements. Similarly, in the isothermal domain (Figure 4.7) most monitoring points provided stable pressure and velocity readings for meshes with more than 3 x 10^6 elements, with full convergence observed once 8 x 10^6 elements were reached.

Having established a starting mesh for both cases, further refinements were performed to ensure $Q > 5$ in the core flow regions (section 3.1.2.3) was achieved. Finally, once the core mesh size was established, a smooth transition between the latter and the prism layers was achieved by adjusting the total height and number of prism layers. The final DES meshes comprised of ~12.4 x 10^6 elements for the isothermal case and ~11 x 10^6 elements for the reacting case. The isothermal mesh comprising of more elements despite the less complex physics interactions due to the use of a physically larger domain. Both are shown in Figure 4.8.

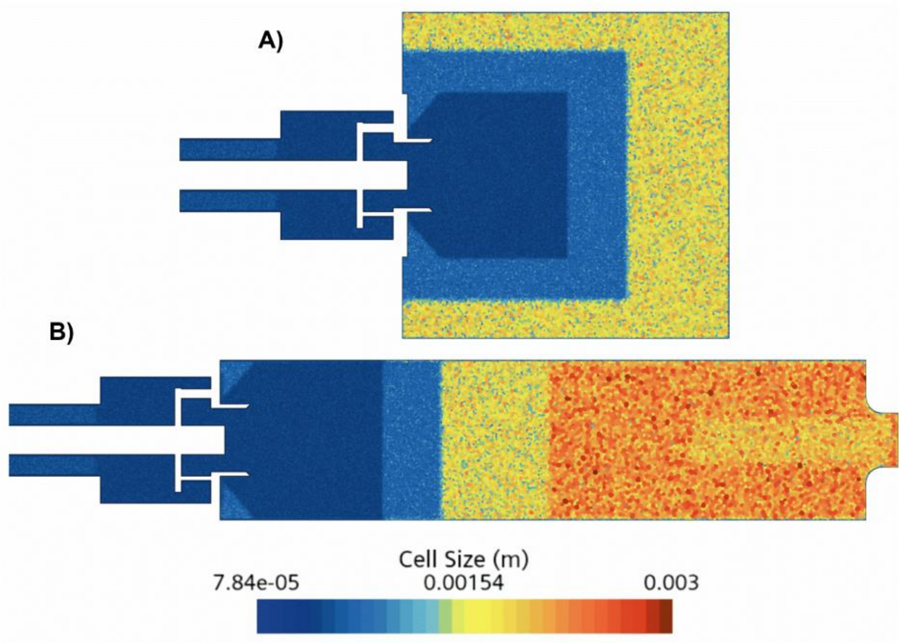

Figure 4.8 - Cross-section of the DES mesh for A) isothermal and B) reacting DES cases (flow from left to right).

Final RANS simulations were performed utilising these Figure 4.8 DES meshes to extract the relevant initialisation data for all DES cases and to verify an average $y^+ \approx 1$ was still met. Once the DES simulations had run, time and surface-averaged y^+ values were recovered and collected in Table 4.2.

Table 4.2 - Time and surface-averaged y^+ values over the swirler body and plenum faces for all DES cases.

	Isothermal y^+			Reacting y^+		
	EB	**DDES**	**IDDES**	**EB**	**DDES**	**IDDES**
Smooth	1.053	1.043	1.034	0.723	0.701	0.650
C1	1.042	1.041	1.022	0.712	0.696	0.641
C2	1.147	1.029	1.010	0.816	0.686	0.626

As can be seen from Table 4.2, values close to unity were achieved for both isothermal and reacting simulations, with the choice of turbulence model having a more measured effect on the reacting cases.

4.2.2.3. DES Setup

The DES variants available within STAR-CCM+ are Delayed Detached Eddy Simulation (DDES) and Improved Delayed Detached Eddy Simulation (IDDES). As outlined in Section 3.1.2.2, DDES utilises a delay factor to enhance the ability to distinguish between LES and RANS whilst IDDES introduces some WMLES (Wall-modelled LES) capabilities [212,259]. From Section 3.1.1.2.2, both the EB and K-ω turbulence models use specific modifications to their formulation that enable roughness effects to still theoretically be captured even when $k_s^+ > y^+$. The EB model can only be applied with DDES, while the SST k–ω model is compatible with both DDES and IDDES. Accordingly, three DES configurations were examined: EB–DDES, SST k–ω–DDES, and SST k–ω–IDDES. For each configuration, both smooth and rough simulations were conducted, resulting in nine isothermal and nine reacting cases in total.

To find a suitable estimate for the timestep (Δt), the Courant Number formula (*Co)* was rearranged as shown in equation [4.1].

$$\mathrm{Co} = \frac{U \Delta t}{\Delta x} \;\rightarrow\; \Delta t = \frac{\Delta x \, Co}{U} \tag{4.1}$$

As a *Co* close to 1 is needed in the domain of interest, equation [4.1] therefore becomes a ratio of cell size over velocity as shown in equation [4.2].

$$\Delta t = \frac{\Delta x}{U} \approx \frac{cell\ volume^{\frac{1}{3}}}{U} \tag{4.2}$$

The flow-through time (FTT) was estimated via the preliminary RANS simulations by performing a surface average of U_x in the XY plane and dividing it by the total geometry length. To reduce computing time, the plenum was shortened by 75% for all isothermal DES cases; the shortened plenum enabling a FTT reduction of ~10%. The final time-steps and FTT utilised are collected in Table 4.3.

Table 4.3 - *Time steps and FFTs for DES cases.*

	Δt (s)	**FTT (s)**
Isothermal	1E-5	0.0834
Reacting	1.25E-5	0.069

To achieve efficient convergence, 10 inner iterations were performed for each Δt. Furthermore, the SIMPLEC implicit scheme was utilised as part of the segregated flow solver [186]. All DES simulations utilised data from the preliminary RANS simulations to initialise the flow field. To eliminate the effects of initial conditions, a minimum of 3 FTT were run before time-averaging. Time-averaging was performed for a minimum of 5 FTT.

When comparing the time-averaged *Co* values of all the run DES variants, marginal deviations were found. For the sake of brevity, results were superimposed based on their reaction regime utilising the MATLAB code located in appendix B.1. Results are summarised in Figure 4.9.

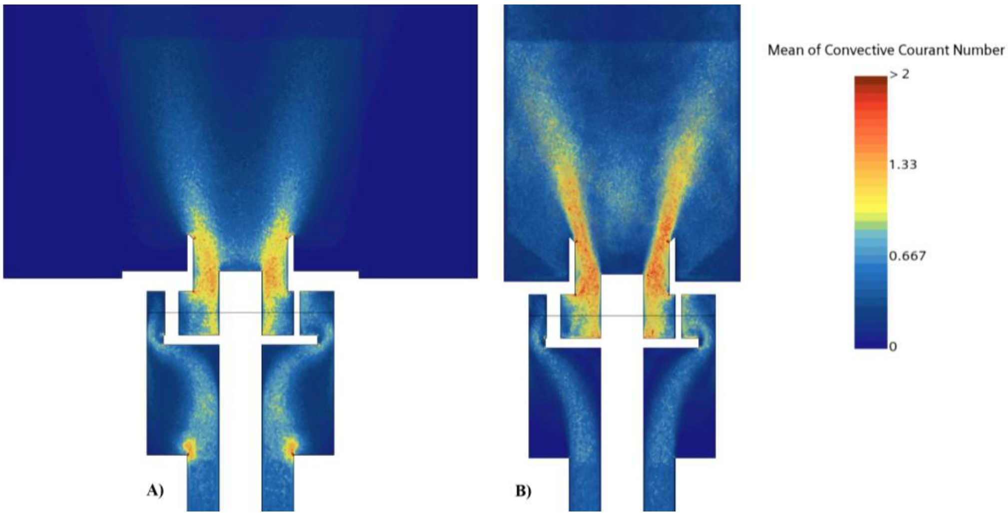

Figure 4.9 *- Superimposed isothermal (A) and reacting (B) time-averaged Co values for all DES simulations.*

From Figure 4.9, whilst both flow-fields present *Co* ≈ 1 within the swirler and nozzle exit, values for the reacting cases appear to be higher. This is likely partly due to having used a 25% larger timestep in conjunction with a finer core mesh. Furthermore, the reacting cases will have presented more vigorous convective activity, the increased fluid velocity and resulting areas of higher velocity gradients likely not being adequately captured by the reference RANS simulation utilised to approximate the timestep required. Overall, though more conservative values may be needed for reacting simulations, the approach for estimating a suitable *Co* number reported in this section was determined sufficiently robust with DES simulations having values in regions of interest close to unity.

4.2.2.4. Roughness Parameter Derivation

As outlined in Section 2.6.1, the process of selecting an appropriate k_s correlation from the literature is inherently challenging, as existing correlations are typically derived for specific flow regimes or geometrical configurations and may diverge by more than an order of magnitude when applied to identical measured roughness values. To maximise the likelihood of numerically capturing roughness effects, having performed a comprehensive review of literature-based correlations [46,185], the correlation yielding the largest k_s value was selected. This being equation [4.3], presented by Bons [46] and seemingly taken as an average of the values proposed by Barlow and Kim [260]. These k_s values, utilised in the C1 simulations, should lead to transitionally rough flow conditions.

$$k_s \approx 16Ra \qquad [4.3]$$

Simulations with a k_s value theoretically high enough to reach the fully rough regime ($k_s^+ \geq 90$) were also performed (C2). To achieve this, a novel k_s was derived following the procedure reported below. To find the appropriate roughness height for this condition, k_s^+ (equation [3.9]) was rearranged to solve for k_s, with k_s^+ subsequently set to 90, as demonstrated in equation [4.4].

$$k_s = \frac{k_s^+ \mu}{\rho\, u^*} \rightarrow k_s^{R90} = \frac{90 \cdot \mu}{\rho\, u^*} \qquad [4.4]$$

Equation [4.4] was then applied to preliminary RANS simulations, performed utilising the realisable K-ε two-layer model (R2L), and surface averages of the various swirler faces were taken. To maintain the relative differences in roughness, a multiplication factor was found by dividing the estimated k_s^{R90} by the respective measured roughness. The largest multiplication factor was applied to all measured roughness values ensuring all surfaces satisfy $k_s^+ \geq 90$. The resulting correlation is:

$$k_s \approx 156Ra \qquad [4.5]$$

It is crucial to emphasise that the correlation in Equation [4.5] was developed specifically using the geometry and flow conditions outlined in this study. As a result, it may not yield satisfactory results when applied to different domains, flow rates, or fuel types. Instead, the methodology employed to derive this novel correlation, particularly the approach in Equation [4.4], may offer greater potential for broader applicability.

It is important to note that, when equation [4.5] is applied to the measured roughness values of the 8M swirler [42], k_s values increased on average by only ~3.5% when compared with the C2 increases. If this user defined correlation therefore accurately captures roughness effects, it can be said that the C1 simulations are representative of the 8M experimental conditions. These k_s values obtained by applying equation [4.5] to the measured roughness (C2-8M) together with those utilised in the transitionally rough (C1) and fully rough (C2) simulations are collected in Table 4.4.

Table 4.4 *- C2-8M k_s values, together with k_s utilised in the C1 and C2 rough simulations with figure highlighting the swirler faces to which each roughness height was applied.*

	***C1* (mm)**	***C2* (mm)**	***C2-8M* (mm)**	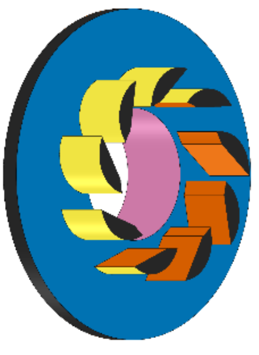
Nozzle inner	0.143	1.38	0.217	
Swirler base	0.177	1.73	0.274	
Swirler curve	0.133	1.30	0.104	
Swirler flat length	0.137	1.34	0.196	

4.3. Results and Discussion

4.3.1. Velocity Profiles

Because of the 9-blade asymmetry, velocity and OH* data was taken from the same side across all simulations. Analyses of the various simulation results was started by investigating changes in the velocity flow-fields. Axial velocity profiles for all simulations were taken 5 mm downstream of the burner nozzle exit consistent with the experimental data. Figure 4.10 presents the roughness induced velocity profile changes for each turbulence model together with a comparison of all smooth, C1 and C2 simulated velocity profiles compared with the corresponding smooth (8M) and rough (8R) experimental data.

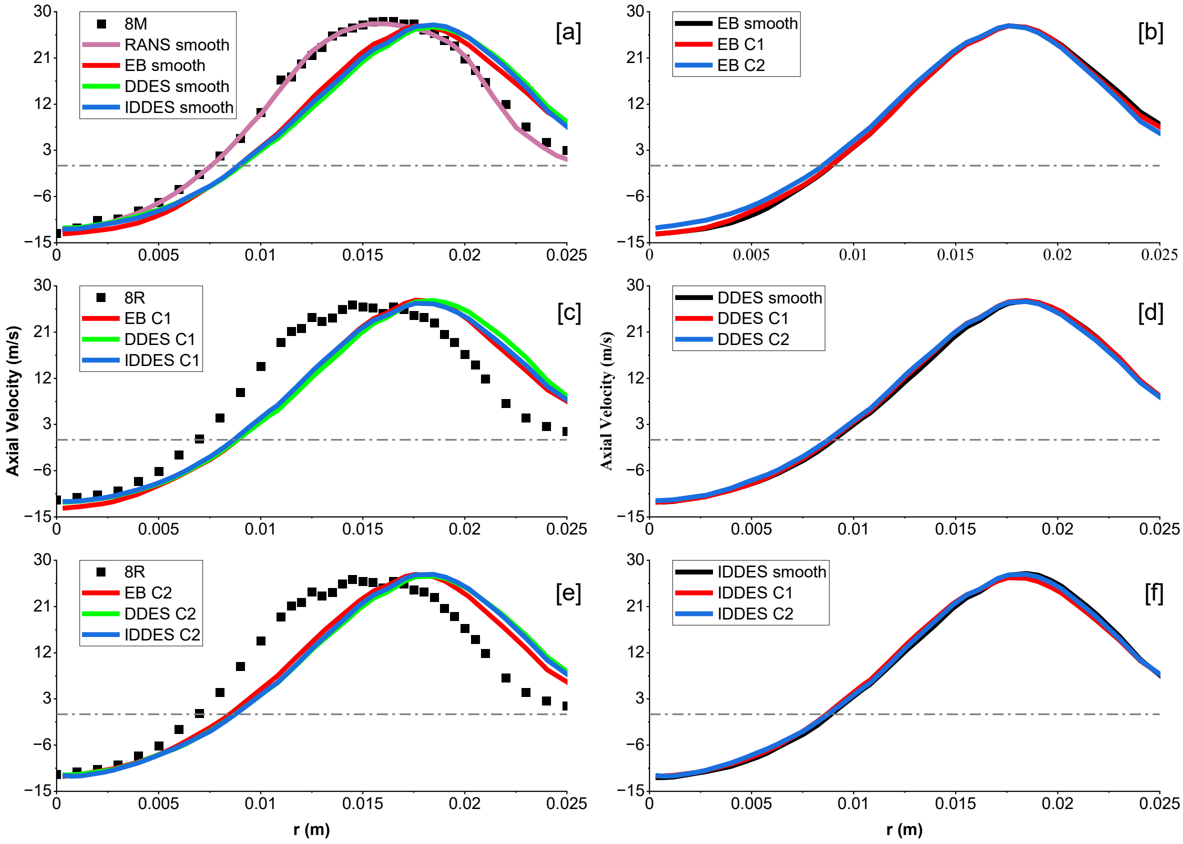

Figure 4.10 *- Comparison of simulated isothermal axial velocity profiles against experimental data (a, c, e). Roughness effects on simulated isothermal axial velocity profiles for EB (b), DDES (d) and IDDES (f) cases.*

The smooth reference RANS simulation (Figure 4.10a) performed with the R2L model presents a high degree of agreement, with the numerical data deviating by ~1% in the core flow (10 mm ≤ r ≤ 20 mm) compared with the 8M experimental data. All smooth DES cases present similar velocity profiles with their overall shape deviating by an average of ~8% compared to the reference 8M data. This indicates the choice of turbulence model has minor influence on the isothermal flow field. Experimentally, axial velocity profiles were found to shift radially inwards with peak velocities decreasing with increasing roughness [42]. For the C1 simulations (Figure 4.10c) no such trend was found. Rather, all C1 velocity profiles presented little to no deviation from their smooth counterparts. Minimal changes were also found for all but the EB C2 simulations (Figure 4.10e). The latter appearing shifted more radially inward than the other two C2 cases though no significant reduction in maximum velocity was detected. Overall, it can therefore be said that, whilst none of the isothermal rough simulations adequately captured the changes in axial velocity, the EB C2 case presented the greatest numerical shift.

Regardless of the DES model utilised, all simulations presented a radially outwards shift compared to the reference experimental data. Given the roughness induced shifts were not captured numerically, direct comparisons for the C1 and C2 cases cannot be undertaken. For the smooth cases however, this outward radial shift appears to be roughly 2 mm. Observations made by Pereira et al. [261,262] help explain this unexpected shift. Their investigation of flows around cylinders found that simulation methods with higher physical resolution such as DES produce larger and often overestimated recirculation regions [261,262]. When comparing the isothermal RANS R2L axial velocity flow-field with that generated by the DES cases as shown in Figure 4.11, similar conclusions can be drawn.

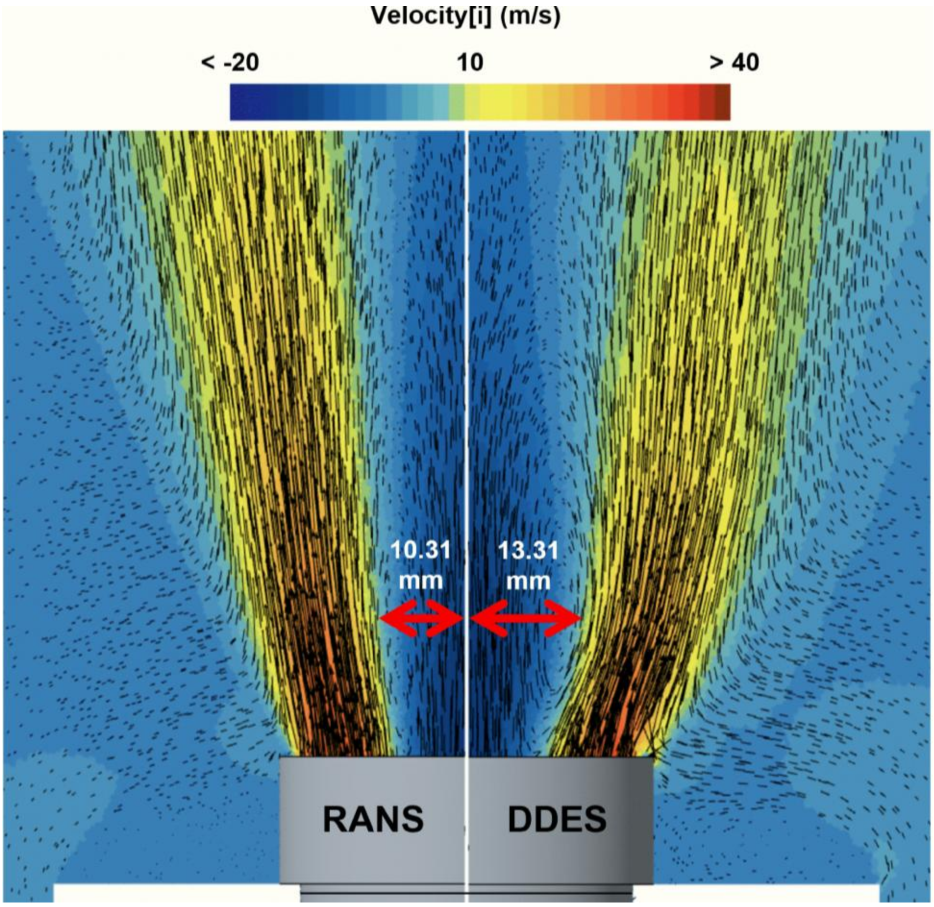

Figure 4.11 *- Isothermal velocity flow field comparison: time averaged DDES (right) RANS R2L (left).*

From Figure 4.11, the DDES flow field presents a much wider recirculation zone than the RANS counterpart. Consequently, the flow exiting the nozzle gets pushed outwards leading to a shift in the velocity profiles as observed in Figure 4.10a. Having extracted the central recirculation zones from the respective zero-velocity iso-surfaces and calculated their areas (appendix B.3), all smooth DES simulations were in fact found to have a ~29% wider and ~12% larger recirculation zone compared to the reference RANS simulation.

Whilst experimental LDA data was not available for the fully premixed reacting methane-air cases, axial velocity profiles were still collected for all simulations and plotted in Figure 4.12.

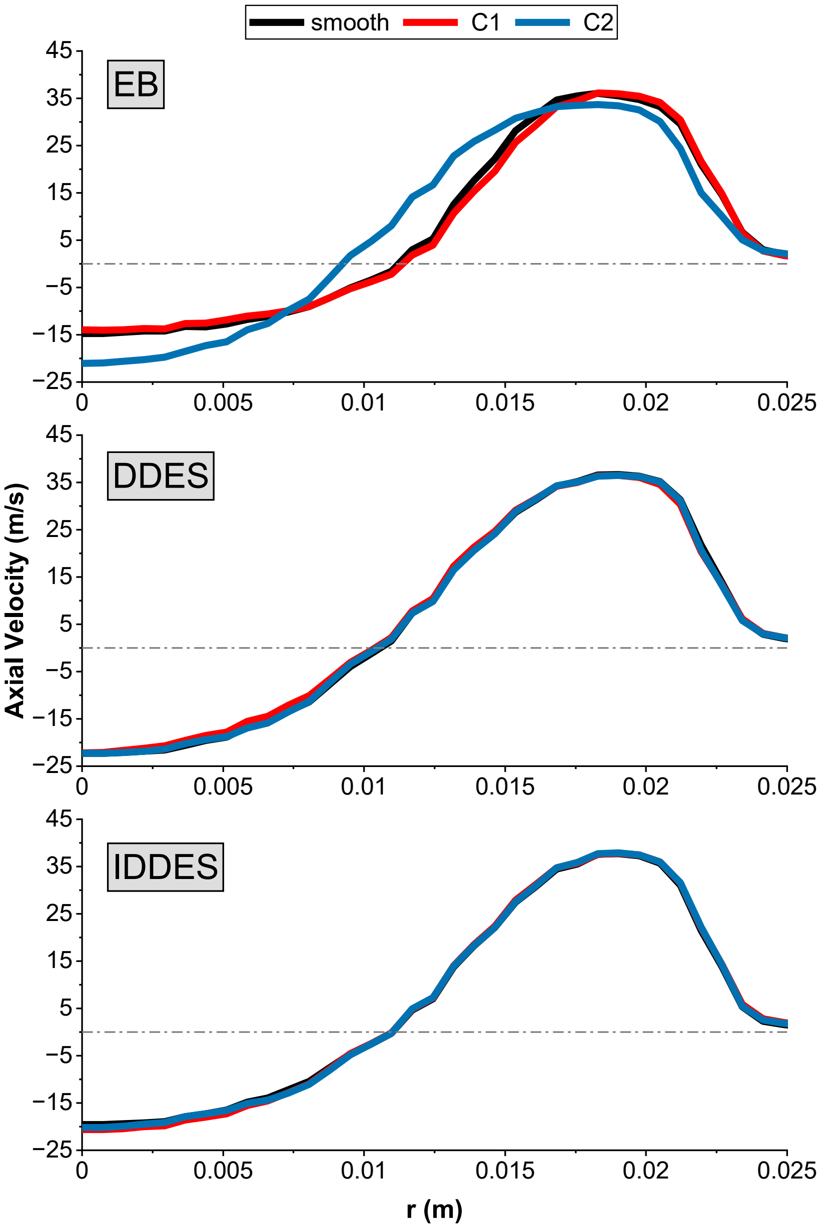

Figure 4.12 *- Reacting axial velocity profiles for all DES turbulence models and roughness heights.*

Consistent with results for the isothermal cases, minimal roughness effects were captured in all C1 cases. Furthermore, all velocity profiles captured with the IDDES and DDES models presented negligible radial shifts or reduction in maximum velocity with increasing roughness. Roughness effects were however captured in the EB C2 simulation. In this case, similarly to the experimental observations, the maximum velocity reduced by ~6.6% and shifted radially inwards by 0.73 mm. It can also be seen that, for this latter case, a shift in magnitude and location not only occurred for the maximum positive velocity, but also for the maximum negative velocity indicating significant changes in the strength of the recirculation zone and thus swirl number.

4.3.2. Swirl Numbers and Recirculation Zones

Numerical swirl numbers were calculated via equation [4.6] initially presented by Vignat et al. [263]. Because the formulation for S_{conv} differs from that used to calculate geometric swirl numbers, values obtained via equation [4.6] are expected to deviate slightly. Vignat et al. [263] for instance found S_{conv} underpredicted S_g by ~20%.

$$S_{conv} = \frac{\int_0^{R_{lim}} \rho\, \overline{U_\theta} \overline{U}_x\, r^2 dr}{R_{nozzle} \int_0^{R_{lim}} \rho\, \overline{U}_x^2\, r\, dr} \qquad [4.6]$$

Increased roughness on the nozzle walls has the potential to dampen tangential momentum, therefore, when looking at axial changes in SN within the burner nozzle, values for rough cases are expected to be lower than their smooth counterparts. To assess these changes in SN, line probes were placed across the burner nozzle and spaced 5 mm apart as shown in Figure 4.13.

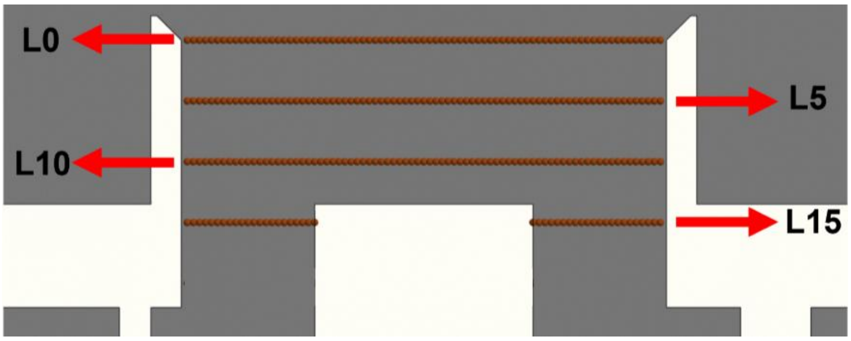

Figure 4.13 - XY plane cross-section of nozzle showing line probe location for SN analysis.

For the line probes spanning the entire width of the burner nozzle (L0 - L10), SN values were found to change substantially depending on the radial coordinates as shown in Figure 4.14.

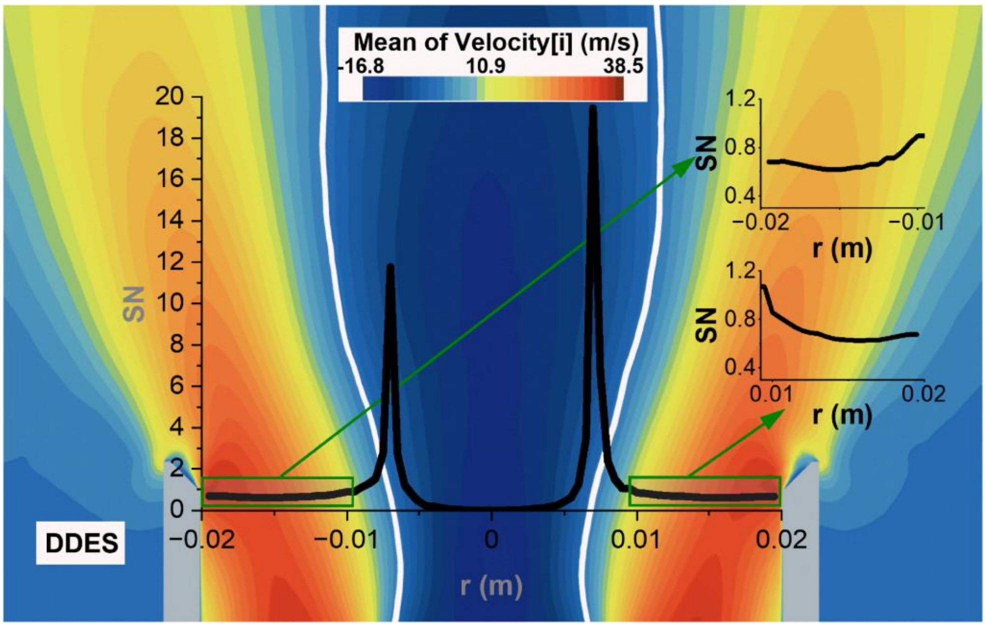

Figure 4.14 *- Isothermal DDES axial velocity with overlay of S_{conv} taken at L0. White line defines the inner recirculation zone.*

As can be seen from Figure 4.14, stable swirl numbers are achieved in the outer quarters of the burner nozzle corresponding to the flow exit. Values rapidly increase in the shear layer reaching a peak at the zero-velocity iso-surface delimiting the inner recirculation zone due to rapidly decelerated axial momentum. Within the inner recirculation zone SN values drop to near zero. Taking these factors into consideration, axial changes in SN were measured by averaging values for each line probe between ±0.009 ≤ r (m) ≤ ±0.02. Results for all isothermal and reacting simulations are collected in Figure 4.15.

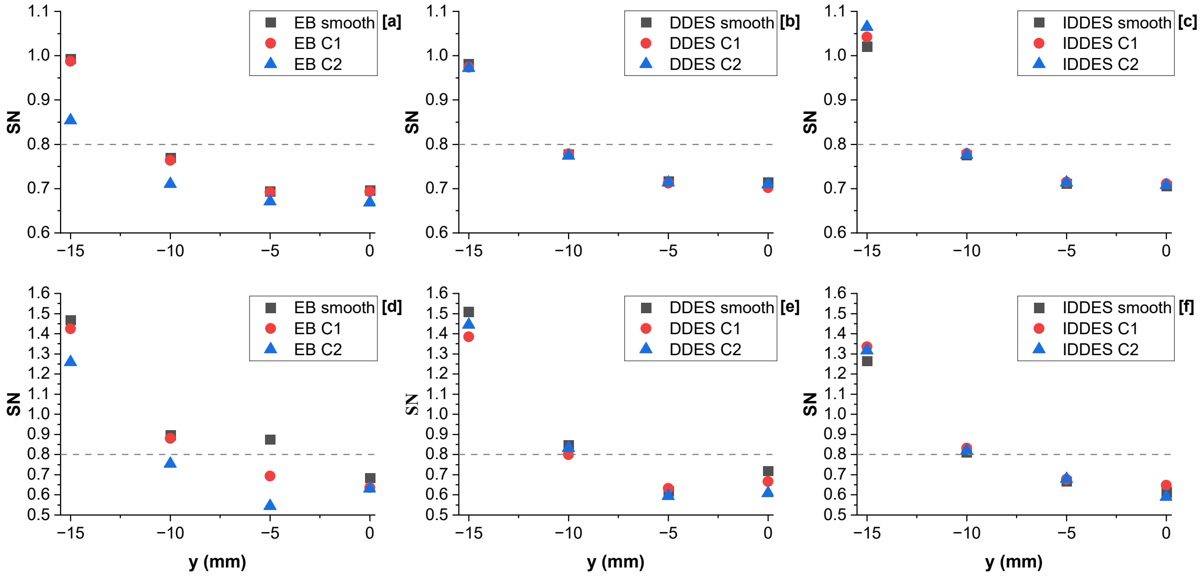

Figure 4.15 *- Changes in SN within burner nozzle. Isothermal [a, b, c] Reacting [d, e, f].*

Regardless of the turbulence model and roughness utilised, SN values can be seen to decrease as flow progresses downstream towards the nozzle exit. For the smooth cases, SN was consistent across both isothermal and reacting conditions, averaging 0.688 at the nozzle exit. Consistent with observations from the isothermal velocity profiles, significant changes in SN were only apparent for the EB–C2 case, which was approximately 4% lower than its smooth counterpart at the exit. In the reacting simulations, differences were negligible for the IDDES cases, whereas for both EB and DDES, SN decreased with increasing roughness. This roughness-induced reduction in SN at the nozzle exit aligns with trends observed in previous isothermal simulations by Al-Ajmi et al. [183].

Changes in the inner recirculation zone were assessed via zero-velocity iso-surfaces. A visual representation of roughness induced differences was achieved by overlaying recirculation zones attained with the same turbulence model as shown in Figure 4.16.

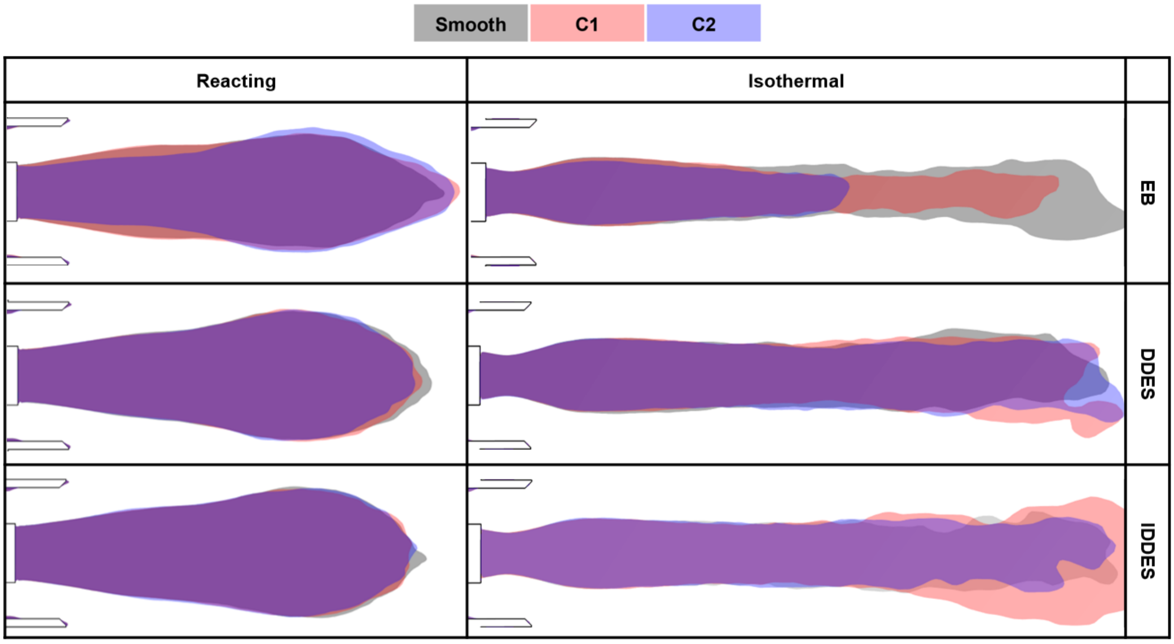

Figure 4.16 - *Overlayed isothermal [top] and reacting [bottom] inner recirculation zone boundaries for all DES cases.*

From Figure 4.16, it can be seen that, for the isothermal EB cases, the central recirculation zone decreases significantly with increasing roughness. In contrast, the isothermal DDES and IDDES cases exhibit no axial displacement, with differences only appearing further downstream from the nozzle exit. For the reacting cases (Figure 4.16 bottom), two distinct behaviours are observed: in the EB cases, the recirculation zone narrows radially with increasing roughness but retains its axial length, whereas in the DDES and IDDES cases, radial narrowing is absent, and the recirculation zone instead contracts axially with increasing roughness. The radial narrowing and axial shortening observed in the EB-reacting and isothermal cases, respectively, can be attributed to the roughness-induced reduction in swirl number discussed earlier in Section 4.3.2.

4.3.3. Effective k_s^+ and Wall Shear Stress

Effective k_s^+ and wall shear stress (τ) values were collected for the relevant swirler faces of each simulation. Faces were grouped based on the k_s value utilised and surface averages performed. Results are presented in Figure 4.17 and Figure 4.18 respectively.

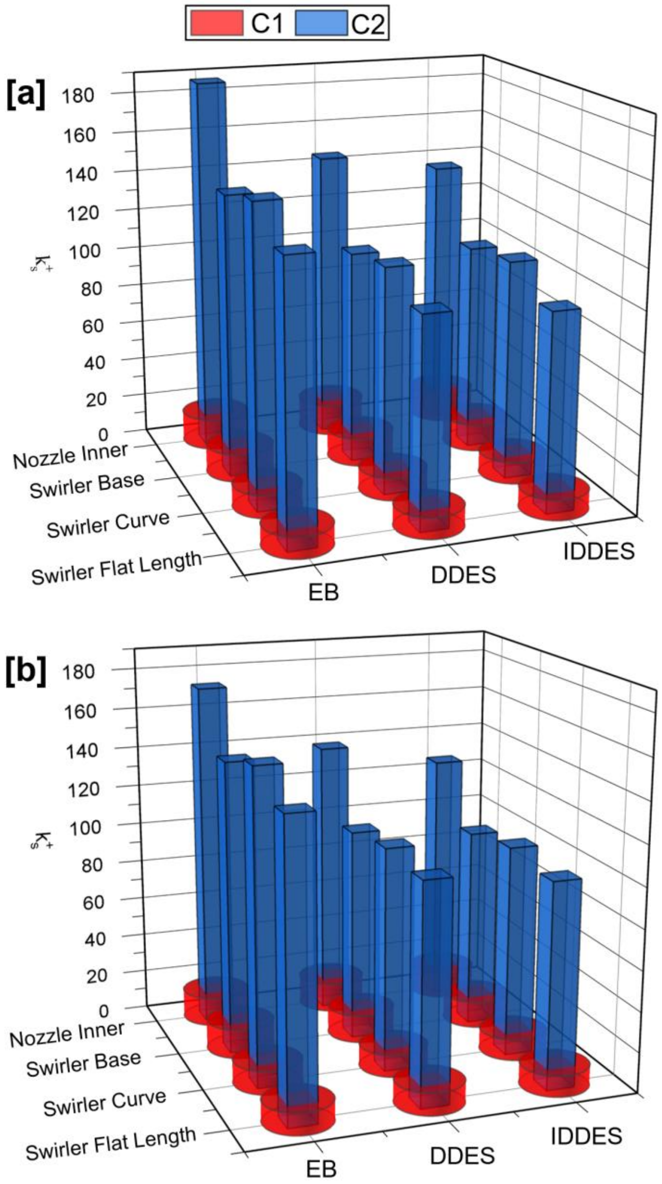

Figure 4.17 - Average k_s^+ values of swirler surfaces for isothermal [a] and reacting [b] simulations.

From Figure 4.17, k_s^+ values can be seen to increase linearly with increasing k_s. The choice of turbulence model was found to have negligible effects on the k_s^+ values of the C1 simulations with deviations being limited to a maximum of 7%. The average k_s^+ value of the C1 simulations was found to be ~12.66 indicating that all C1 cases lie at the lower end of the transitionally rough regime. Conversely, turbulence models had a measured effect on the C2 cases with both the DDES and IDDES simulations presenting average k_s^+ values respectively 24% and 28% lower than the EB ones.

Nevertheless, all C2 simulations were found to be in the fully rough regime presenting a minimum average $k_s^+ > 100$.

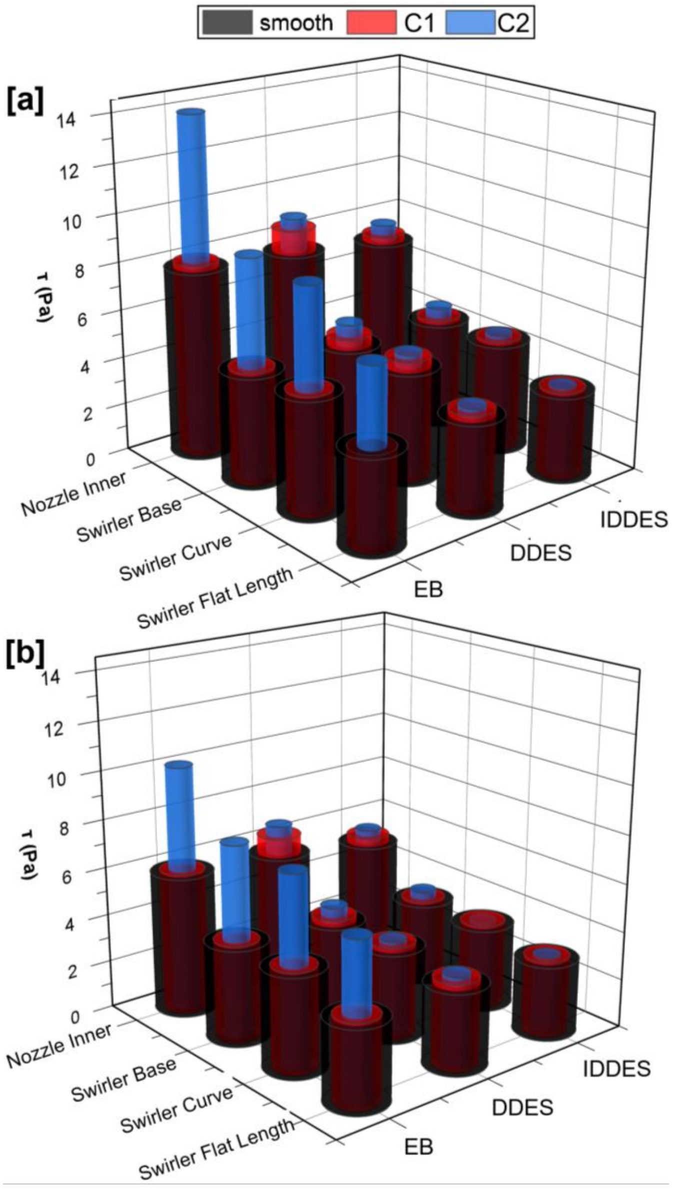

Figure 4.18 - Average τ values of swirler surfaces for isothermal [a] and reacting [b]simulations.

From Figure 4.18, values of τ can be seen to increase with increasing roughness though the rate at which this occurs is strongly dependent on the turbulence model used. For the EB cases, the C1 simulations presented very marginal increases in τ with significant increases only seen for the C2 simulations. All IDDES cases exhibited only marginal increases in τ with increasing roughness, with the C1 and C2 cases rising by approximately 4% and 8%, respectively. The DDES cases showed roughly twice the percentage increase compared to their IDDES counterparts, although these changes remain relatively minor.

4.3.4. Flame Location and Characteristics

Assessments of changes in flame shape and position were undertaken using a single iso-surface of the time averaged OH* mass fraction applied to the XZ plane of each reacting simulation. The resulting iso-surfaces were both overlayed onto the respective experimental OH* Abel transform chemiluminescence images (Figure 4.19) and superimposed based on the turbulence model utilised (Figure 4.20) and. The MATLAB code collected in appendix B.3 was utilised to calculate the areas covered by the numerical OH* iso-surfaces.

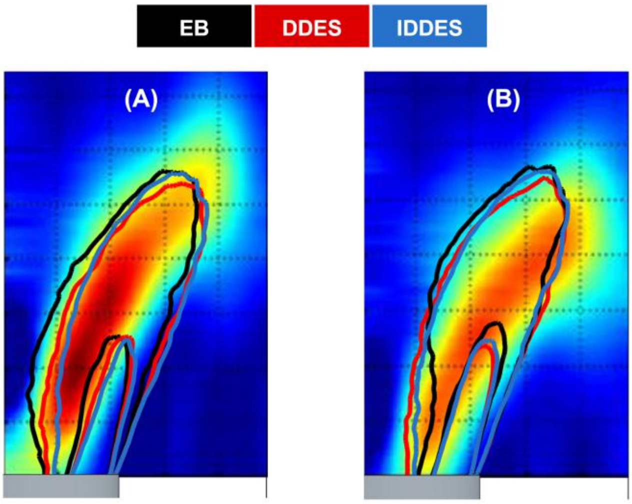

Figure 4.19 *- Comparison of simulated C2 (A) and smooth (B) OH* profiles with experimental OH* Abel transform CL data.*

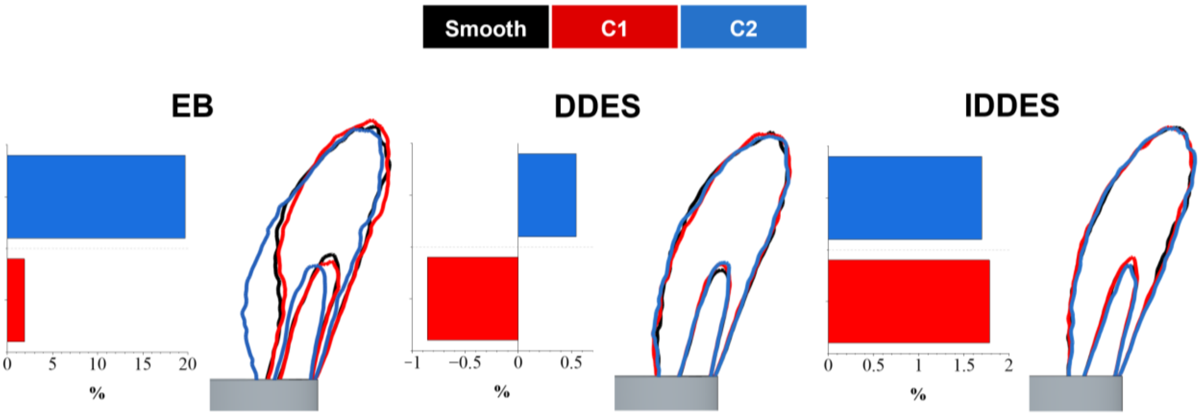

Figure 4.20 *- OH* profiles for each DES modelling approach with % area change relative to the respective smooth profiles.*

Results from Figure 4.19 show that all smooth simulations produce similar flame shapes, with overall width, length, and positioning closely matching the experimental data. For the rough cases, both DDES and IDDES simulations exhibit minimal deviations in flame position and area relative to the smooth references. By contrast, Figure 4.20 shows roughness effects are evident in the EB turbulence model, with the C2 flame displaying an approximately 20% increase in area, appearing wider, and oriented at a smaller angle relative to the burner centreline compared to the smooth counterpart.

To facilitate comparison with the reference experimental data, the centroids of each time averaged OH* iso-surface were calculated utilising the MATLAB code shown in appendix B.2. The values for the right-hand side of the flame are presented in Figure 4.21.

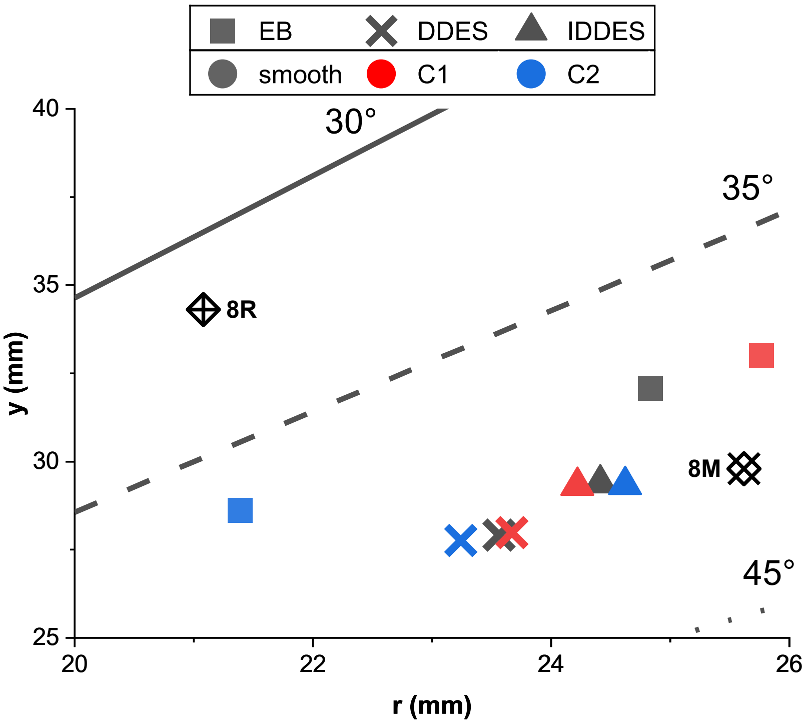

Figure 4.21 *- OH* centroids for all reacting cases with angles relative to burner centreline. 8M and 8R values for reference. Circles in legend indicating the colour code.*

From Figure 4.21, all smooth simulations can be seen to present good agreement with the 8M centroid location. The IDDES smooth case providing the best fit axially (deviation of ~1.5%) while the EB smooth case aligns best radially (deviation of ~3%). Roughness effects were found to be negligible for both the IDDES and DDES cases. The roughly ± 0.02 mm radial shifts within the IDDES cases likely arising from minor simulation variations. The rough DDES cases also show minimal shifts, though their trends are consistent with the EB results. For EB, the flame centroid shifts radially outward for C1 and inward for C2. The EB C2 centroid aligns closely with the 8R flame, deviating by ~1.5%, and, consistent with experimental observations, is ~1.5° closer to the burner centreline than the smooth counterpart. The outward shift of the C1 case was not anticipated, but its radial location deviates only ~0.6% from the 8M flame, showing better agreement than the smooth EB case. As significant shifts occur only in EB C2 and the C1 k_s values are of the same order of magnitude as the 8M–C2 values (Section 4.2.2.4), the minor roughness effects observed in EB C1 are considered representative of 8M conditions.

The wider flame generated by the EB C2 case (Figure 4.19) suggests that, as was found in the previous experimental work [42], an increase in heat release with increasing roughness may have also been captured numerically. To better verify this, time averaged OH* values of each simulation were normalised against the respective maximum OH* readings found in a constrained plane section covering the first 80 mm of the combustion chamber downstream of the burner exit nozzle. Results for all DES simulations are collected in Figure 4.22.

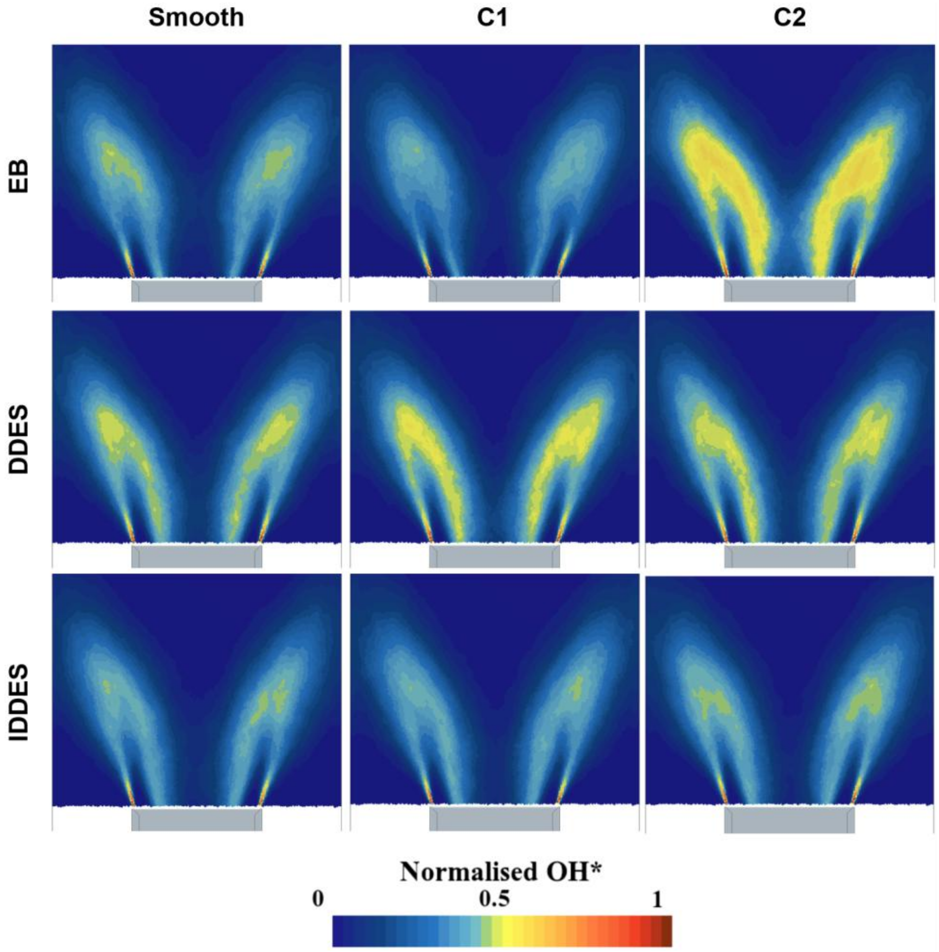

Figure 4.22 - *Normalised mass fraction of OH* for all DES simulations.*

Figure 4.22 further illustrates that both the IDDES and DDES models capture negligible roughness effects. Comparison of the two models highlights differences in the OH* distribution: IDDES cases exhibit the highest concentrations near the flame root, whereas DDES cases show a greater proportion of OH* within the flame body. Significant roughness effects are observed only for the EB C2 case. This is attributed to enhanced heat release along the shear layer induced by the increased turbulence intensity, which acts to increase localised flame consumption speed [42,264].

4.4. Summary

The feasibility of modelling surface roughness effects using a high-fidelity, low-y^+ approach on a generic swirl burner was evaluated under both isothermal and reacting conditions. Smooth reference cases were compared against rough simulations, where k_s values were obtained from both literature-based and user-defined correlations. Three different DES variants were applied, and results were validated against experimental data, with further analysis of roughness impacts on SN and central recirculation zone location performed. The choice of turbulence model and DES variant was found to influence sensitivity to roughness, with the EB–DDES combination producing the largest roughness-induced variations in k_s^+ and τ. In the isothermal cases, numerical shifts in axial velocity profiles were consistently smaller than experimental measurements, regardless of correlation. In the reacting cases, however, roughness-induced shifts in velocity profiles and flame centroid location were observed, with the novel correlation (C2) demonstrating strong agreement with experimental data. Both central recirculation zone size and SN were found to decrease with increasing roughness.

Key findings of this work are as follows:

- Of the three DES models investigated, EB exhibited the highest sensitivity to roughness in both isothermal and reacting conditions. This turbulence model should therefore be prioritised when employing a low-y^+ mesh to capture roughness effects.

- Literature based k_s correlations proved inadequate when coupled with a low-y^+ approach. All reacting and isothermal simulations failing to capture meaningful roughness effects. Significant effects were captured only when applying the novel correlation developed in this work ($k_s^+ > 90$).

- For identical k_s values, roughness effects were more pronounced under reacting conditions, likely due to differences in the underlying physics captured in reacting simulations, including density variations and altered mixing. This indicates that roughness correlations may need to be fluid- or combustion-specific.

The novel correlation has demonstrated promising predictive capability, especially under reacting conditions. Applying it to alternative geometries or flow conditions, particularly at elevated pressure, may however result in reduced accuracy. Nonetheless, the methodology used to derive this correlation offers potential for broader applicability. Its performance on a jet-based hydrogen burner configuration will be assessed in Chapter 6.

Chapter 5. Surface Roughness Effects on the Operability and Performance of a Hydrogen Jet Burner

In Chapter 5, the primary methodology and findings of which are detailed extensively in a paper bearing the same title [265], the influence of surface roughness on an industry relevant jet burner configuration is quantified under hydrogen fired conditions at atmospheric pressure.

5.1. Introduction

In gas turbine applications, experimental studies have demonstrated the influence of increased roughness of “raw” AM components on axial velocities, heat release, NO_x emissions, and operability limits in swirl-stabilised burners using both fossil and high hydrogen content (HHC) fuels [42,221]. Increased surface roughness has also been shown to enhance boundary layer flashback (BLF) resistance [44,266]. This phenomenon is especially critical for lean premixed combustion of HHC fuels, where the high diffusivity and reactivity of H_2 significantly amplify flashback propensity [43,267,268]. Demonstrating that the inherent surface roughness of “raw” unprocessed AM components can improve BLF resistance would therefore indicate significant potential for commercial benefit.

Numerous innovative burner configurations are being developed to address the challenges posed by HHC fuels as covered in Section 2.3. Among these, jet-in-crossflow configurations represent a notable approach [119,127]. As AM becomes increasingly integral to the production of novel burners, and given surface roughness has known measurable effects on the performance of traditional burners, it is crucial to quantify how roughness impacts this new generation of advanced combustion systems.

5.1.1. Research Scope

A premixed jet burner (PJB), described in detail in Section 3.2.1.1, was designed with an interchangeable section near the end of the premixing chamber allowing the study of different surface textures. Initial characterisation of the PJB with a traditionally machined insert was performed prior to analysing a rough insert. The latter mimicking a worst-case surface finish of a "raw" unprocessed AM component produced using Selective Laser Melting (SLM) [35]. These two inserts were utilised to evaluate the effect of surface roughness on flame shape, burner stability limits and emissions via high-speed, time-resolved velocimetry and OH* chemiluminescence. Emissions and flame composition investigations are undertaken for thermal powers (TP) of 15, 20 and 25 kW over a range of equivalence ratios (ϕ) (0.4 – 1.0), with a more detailed look at flashback limits performed at lower thermal powers (10, 12.5 and 15 kW) over a range of bulk exit velocities (14.2 – 18.75 m/s). Table 5.1 presents a summarised test matrix detailing all test points and the corresponding data collected.

Table 5.1 - Chapter 5 test matrix highlighting what data is collected for each test point

TP (KW)	Stable Points (ϕ) OH* CL collected	Stable point (ϕ) isothermal LDA collected	Instability Point (Y/N)	
			Flashback	Blowoff
10			Y	N
12.5			Y	N
15	0.4 - 0.5 - 0.6 -0.7 - 0.8 - 0.9	0.93	Y	Y
20	0.4 - 0.5 - 0.6 -0.7 - 0.8 - 0.9 - 1.0	0.7	N	Y
25	0.4 - 0.5 - 0.6 -0.7 - 0.8 - 0.9 - 1.0	0.4	N	Y

The results of this study aimed to provide a detailed experimental basis for surface roughness analysis when dealing with jet burner configurations. This includes providing a reference dataset for future numerical work, conducted in Chapter 6, where roughness sensitivity is to be analysed.

5.2. Experimental and Diagnostic Setup

5.2.1. Premixed Jet Burner

All experimental work was conducted on a newly designed PJB in conjunction with the M1 and R2 inserts described in Section 3.2. Thermocouples were positioned at the base of the combustion chamber and along the outer edge of the burner nozzle as outlined in Section 3.2.1.3, mainly for monitoring conditions approaching flashback, lean flame blow-off (LBO) and to establish boundary conditions for future CFD simulations. The resulting thermocouple data can be found in Table D.8, Table D.9 and Table D.10 of Appendix D.4.

5.2.2. Emissions Measurements

NO_x emissions were assessed utilising the point probe setup described in Section 3.2.2.2. Normalisation to a reference value of dry, 15% O_2 was performed via equations [2.1] and [2.2] respectively. Although, as covered in Section 2.2.1, it is recognised that this emission reporting method can overstate pollutant concentrations for HHC fuels when comparing with hydrocarbons [86], the dry 15% O_2 method was considered appropriate since this study does not focus on fuel switching rather it aims to highlight relative roughness induced changes. Therefore, any differences resulting from a change in dilution or stoichiometry would be negated. Exhaust water fractions were obtained from equilibrium modelling. Measured dry O_2 fractions were then used to subsequently normalise readings to an equivalent reference 15% O_2 in accordance with ISO 11042 [83]. Typical uncertainties of approximately ±5% of measurement account for analyser specifications, linearisation, and accuracy in span gas certification.

5.2.3. OH* Chemiluminescence

Roughness induced changes in the flame topology were characterised via the high-speed OH* chemiluminescence imaging setup described in Section 3.2.2.1. A scaled target image was used to determine the image resolution, which was equal to 4 pixels/mm. The camera resolution was scaled down to reduce file sizes to 400 x 800 pixels, resulting in a field of view of 200 mm (axial, y) by 100 mm (radial, x). Due to space constraints, only Abel-deconvoluted half-flames are presented in Chapter 5, while the raw dataset is available in Appendix D.4.

5.2.4. Laser Doppler Anemometry

A 1D Dantec Dynamics Flowlite LDA System, described in detail in previous studies [42], was used for characterising the mean flow field and turbulence characteristics of isothermal airflow exiting the burner nozzle. Three isothermal air flow conditions (flowrates collected in Table D.5 of Appendix D) were investigated, with equivalent total mass flow of $\phi = 0.4$ at 25kW ($\bar{u} = 66.2$ m/s), $\phi = 0.7$ at 20kW ($\bar{u} = 33.6$ m/s) and $\phi = 0.93$ at 15kW ($\bar{u} = 20.5$ m/s). This allows roughness effects to be assessed across mean bulk nozzle exit axial velocities ($\bar{u}$) ranging from 20 m/s to 60 m/s. The airflow was seeded with Al_2O_3 particles of nominal 1 µm diameter. The burst signal was processed using a BSA F60 processor and Dantec BSA Flow Software to determine the mean and RMS velocities at the control volume. To investigate the near-wall velocity and turbulence intensity at the burner exit, and building on the insights from Runyon et al. [42], as discussed in Section 4.2.1, both mean (u) and fluctuating (u'_{RMS}) axial velocities were measured 2 mm downstream of the burner exit nozzle. The quartz confinement was removed and a plate affixed to the burner 7 mm upstream of the nozzle exit to limit air entrainment, as shown in Figure 5.1.

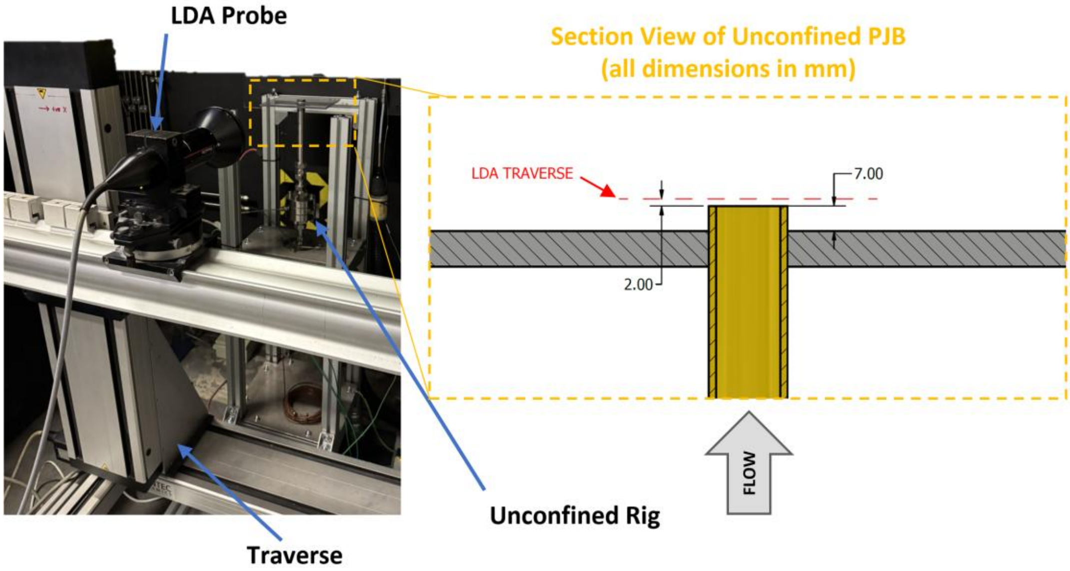

Figure 5.1 - Unconfined PJB with LDA setup [left]. Section view of the unconfined rig with traverse path shown in red [right].

The transmitter and receiver optics were mounted on a traverse system, allowing the control volume to be positioned across the flow field. Measurements were taken starting and ending 1.5 mm outside the nozzle exit at 0.5 mm increments for the outermost 2.5 mm of radial travel. Beyond this, measurements were taken at 1 mm intervals across the remaining range ($-8 \text{ mm} \le r \le 8 \text{ mm}$), resulting in a total of 27 data points. To investigate the near-wall velocity and turbulence intensity at the burner exit, the isothermal flow measurements were conducted with the quartz confinement removed. By controlling the seeding rate and density, data capture rates of up to 3500 points or 10 seconds of acquisition time were achieved.

5.3. Results and Discussion

5.3.1. Flow Characterisation

Understanding the effects of increased surface roughness on the flow-field is of crucial importance for gaining deeper insights into the phenomena discussed in Sections 5.3.2 - 5.3.3. LDA is an effective tool for this purpose, as it offers simultaneous temporal and spatial measurements of both mean and fluctuating axial velocity components. By combining u and u'_{RMS}, turbulence intensity (TI) can be quantified as shown in Equation [5.1]:

$$TI\ (\%) = \left(\frac{u'_{RMS}}{u}\right) \cdot 100 \tag{5.1}$$

Three isothermal air flow conditions were investigated, with equivalent total mass flow to ϕ = 0.4 at 25kW (20.65 g/s air), ϕ = 0.7 at 20kW (10.5 g/s air) and ϕ = 0.93 at 15kW (6.4 g/s air) combustion conditions. The latter flow rate was chosen because, under equivalent combustion conditions, flashback occurred with the M1 insert only as discussed in Section 5.3.2.2. The other two flow rates were selected to examine potential changes in the effects of roughness at progressively higher Reynolds numbers (Re). All data were collected on the same day under an ambient temperature of 286 K. Bulk flow and maximum axial velocities recorded at each isothermal condition together with percentage differences between M1 and R2 flows, and respective Re are collated in Table 5.2.

Table 5.2 *- Bulk and maximum axial velocities at the nozzle exit for all isothermal cases, along with the percentage variations between M1 and R2 values and the corresponding Re.*

		ϕ = 0.93 at 15kW	**ϕ = 0.7 at 20kW**	**ϕ = 0.4 at 25kW**
$\bar{u}$ (m/s)	**theoretical**	20.5	33.6	66.2
	M1	19.4	32.1	62.9
	R2	19.6	32.09	65.1
	% diff.	1.1	-0.06	3.51
u_{max} (m/s)	**M1**	22.5	36.6	70.7
	R2	23.3	38.2	75.3
	% diff.	3.9	4.3	6.5
Re		24169	39825	79387

Table 5.2 demonstrates a strong correlation between the theoretical bulk flow velocities, calculated from first principles, and the experimentally measured values. Differences in peak axial velocities were observed between the M1 and R2 inserts, with the R2 cases consistently exhibiting higher velocities. This increase in relative velocity with increasing roughness is proportional to the overall bulk flow velocity. Since the overall bulk flows remain largely unchanged between the respective M1 and R2 cases, this suggests a shift in the overall velocity profiles.

Axial velocity and TI profiles taken 2 mm downstream of the nozzle exit are shown in Figure 5.2 and Figure 5.3. It is important to note that, in the area outside the nozzle inner diameter (r < -10 mm or r > 10 mm), while measurements were taken, particle detection rates were often too low to produce usable data. As a result, both axial velocity and turbulence data were truncated at the boundary of this range.

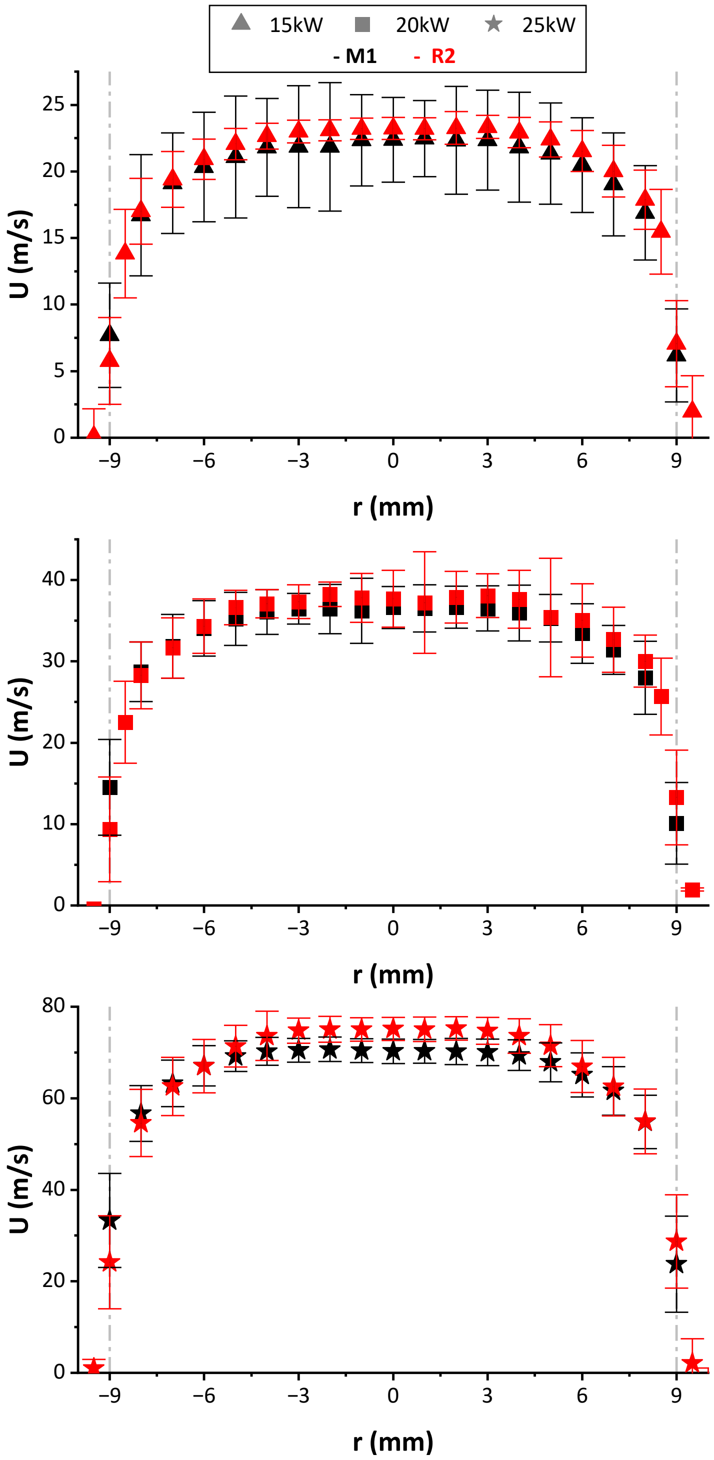

***Figure 5.2** - Axial velocity profiles at equivalent air flow to 15 kW at φ = 0.93, 20 kW at φ = 0.7 and 25 kW at φ = 0.4. Note the change in y axis scale. Vertical lines at ± 9 mm showing ID of burner nozzle. Error bars presenting a visualisation of the velocity fluctuations u' (statistical uncertainty).*

From Figure 5.2, all M1 velocity profiles exhibit a flatter and broader profile than the respective R2 counterparts. The latter presenting lower velocities in the boundary layer likely due to an increase in the turbulence intensity near the wall. The relatively higher axial velocities observed in the core flow for the R2 cases can be attributed to a virtual reduction in the core flow region, resulting from the accelerated boundary layer growth caused by the rough elements [178], the effect being amplified as the Reynolds number increases. Regarding the error bars, calculated using u'_{RMS} values collected at each point, it is evident that as velocities increase, velocity fluctuations decrease. This is partially an artifact of lower bulk flows entraining less seed and hence less seed passing through the detector over the sampling time.

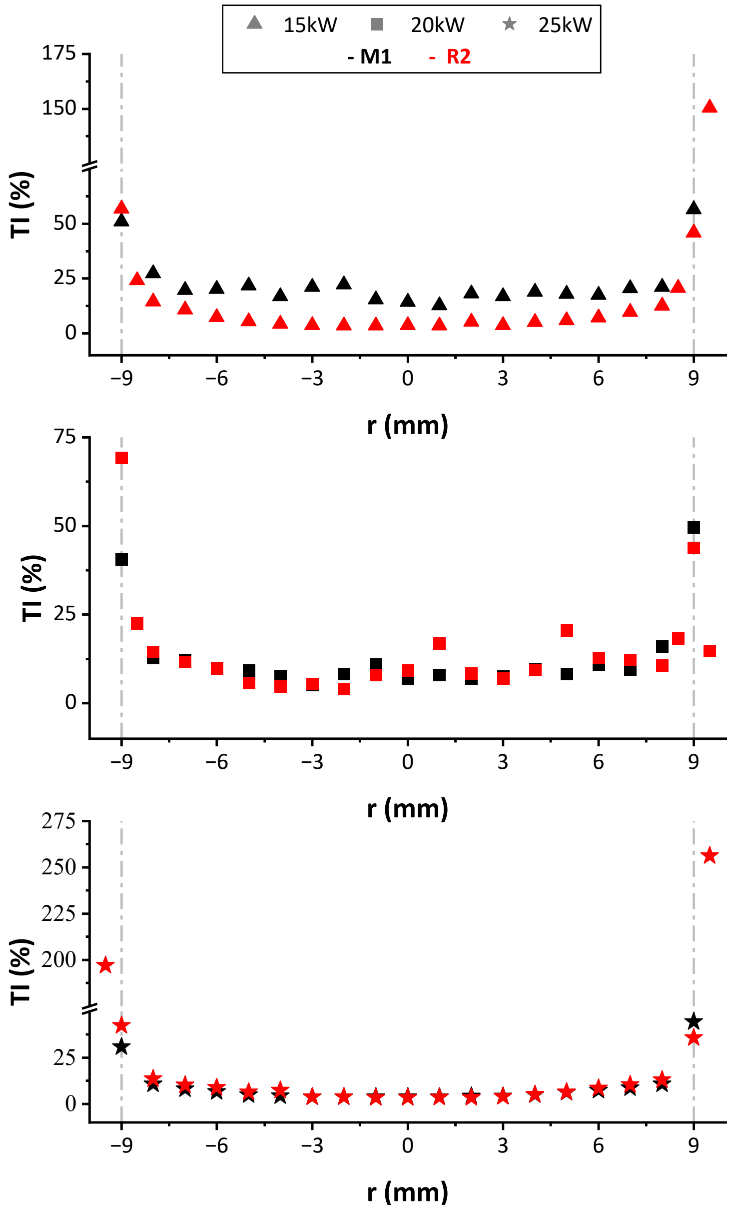

***Figure 5.3** - Turbulence intensity profiles at equivalent air flows to 15 kW at φ = 0.93, 20 kW at φ = 0.7 and 25 kW at φ = 0.4. Note breaks in the y-axis for top and bottom plots. Vertical lines at ± 9 mm showing ID of burner nozzle.*

Figure 5.3 indicates that, for the 15 kW flow conditions (without fuel flow and hence isothermal), the M1 flow field presents greater turbulence in the core flow compared to its R2 counterpart, while the latter shows higher turbulence in the boundary layer region (± 9 mm). Similarly, in the 25 kW isothermal case, the R2 insert also demonstrates increased turbulence in the boundary layer. For the 20 kW and 25 kW isothermal conditions, differences in turbulence within the core flow ($-4\ \text{mm} \leq r \leq 4\ \text{mm}$) are less pronounced, with average R2 values being approximately 2.9% and 4.5% higher than M1 values for the 20 kW and 25 kW isothermal cases, respectively. This suggests that, particularly at higher flowrates, surface roughness has a greater effect on boundary layer turbulence compared to that in the core flow. These variations, also reflected in the velocity profile changes shown in Figure 5.2, help explain the differences in operability limits between the M1 and R2 inserts discussed in Section 5.3.2.2.

5.3.2. Flame Behaviour and Stability

5.3.2.1. Flame location

Combustion experiments were performed under thermal powers ranging from 10 to 25 kW with detailed OH* chemiluminescence data collected for 15 kW, 20 kW and 25 kW conditions. A full operability sweep from LBO to flashback was performed by varying ϕ for all three thermal powers utilising both inserts. If flashback conditions were not encountered, the operability sweep was terminated upon reaching stoichiometry ($\phi = 1$). At each thermal power, OH* chemiluminescence data was collected at 0.1 increments between $0.4 \leq \phi \leq 1$. For the M1 insert, the $\phi = 1.0$ case was not recorded at 15 kW as flashback occurred prior to reaching stoichiometry. Although the flame began showing signs of lift-off at $\phi = 0.4$ across all thermal power levels, the data was presented to emphasise any roughness-induced changes as the system approached LBO. Air and fuel flowrates for all conditions investigated during this test campaign are collected in Table D.4 of APPENDIX D.

Abel-transformed OH* chemiluminescence images for all three thermal powers are shown in Figure 5.4. Each image represents a combination of both the M1 (left half) and R2 (right half) half-flame for the given thermal power and ϕ, where the left and right flames in each image correspond to M1 and R2 inserts respectively. As a result, the field of view expands axially downstream from the burner exit nozzle ($y = 0$ mm) and radially outward from the inner edge of the quartz confinement (M1 = $0\ \text{mm} \leq r \leq 32\ \text{mm}$, R2 = $32\ \text{mm} < r \leq 64\ \text{mm}$). Images for each ϕ are shown with colormaps normalised to the maximum OH* intensity in each half-flame. To avoid any issues with flame asymmetry the right-hand half-image is shown for both M1 and R2 flames, the M1 half-flame being mirrored horizontally prior to aligning it with the respective R2 half-flame.

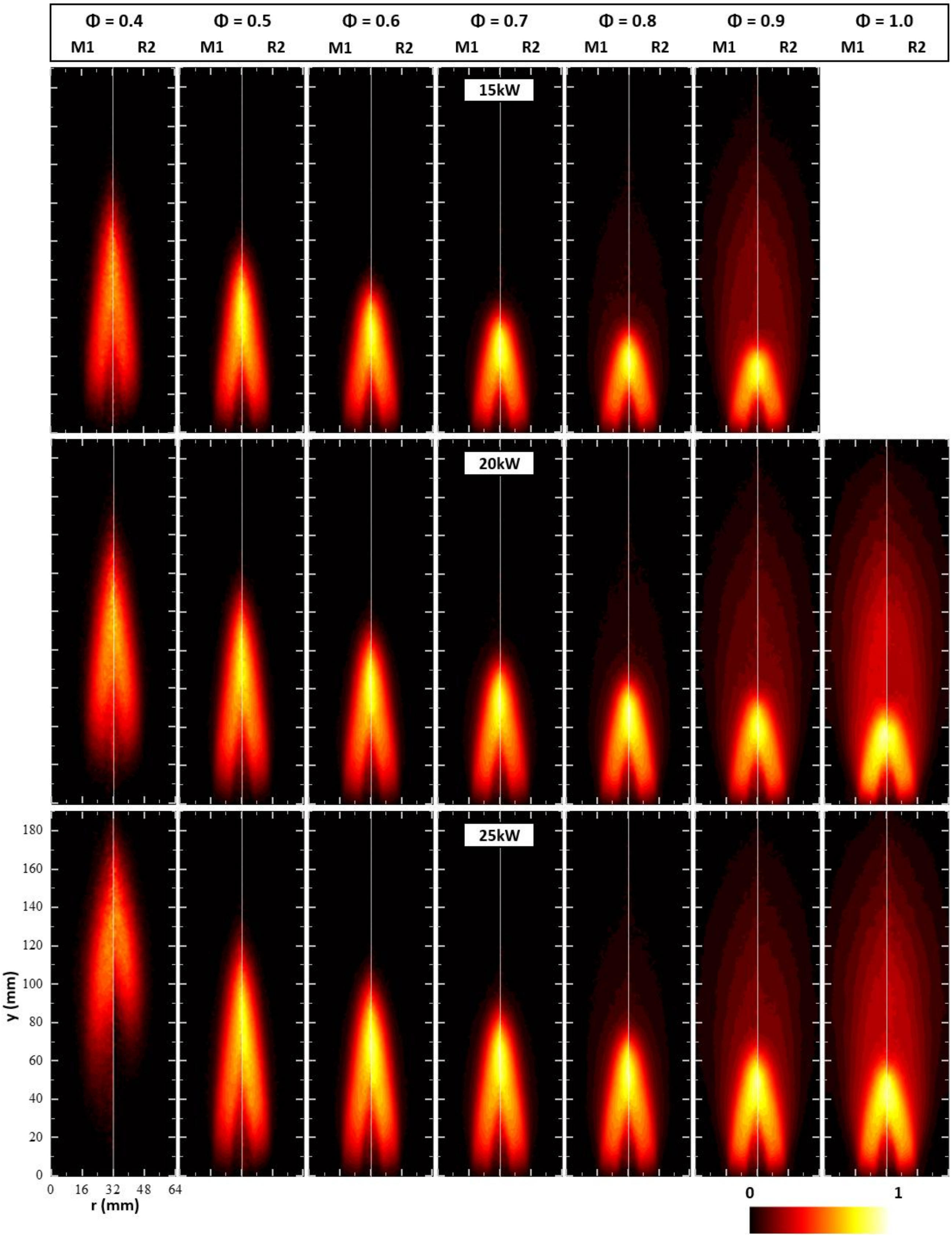

Figure 5.4 *- Abel transformed OH* chemiluminescence images for 15 kW [top], 20 kW [middle] and 25 kW [bottom] thermal powers over a range of φ. Colormap normalised to maximum OH* intensity in each half image (code available in appendix B.4). M1 results shown on the left and R2 results shown on the right for each condition.*

In Figure 5.4 it is observed that the flame moves upstream toward the burner exit with increasing ϕ, irrespective of the insert. This behaviour occurs due to a combination of decreased axial velocity and higher flame speed (see Appendix A.1 for actual flame speed values). In addition, for a given ϕ, the flame length increases with thermal power primarily due to the increase in bulk flow velocity. At ϕ = 0.4, the flame becomes progressively lifted with increasing thermal power. Focusing on the 25 kW case at ϕ = 0.4, the R2 flame appears noticeably more lifted than the M1 counterpart, suggesting that increased surface roughness, particularly the roughness-induced rise in centreline velocities at the nozzle exit observed in Section 5.3.1, leads to an earlier onset of flame lift-off and, consequently, LBO. A detailed analysis of the effects of roughness on stability limits is provided in Section 5.3.2.2.

Variations in the peak OH* intensity were found to neither be significant nor exhibit a consistent trend, indicating that surface roughness did not impact heat release intensity. However, changes in the overall flame shape were noted. For the same equivalence ratio and thermal power, the R2 flame is observed to shift axially upstream while remaining largely unchanged radially. This axial shortening becomes more pronounced as the equivalence ratio is reduced and thermal power increased. To better visualise shifts in the flame and heat release centre positions, the OH* chemiluminescence intensity centroid was calculated for both the raw averaged and Abel-deconvoluted half-flames across all cases, following the procedure described in [233]. Consistent trends were observed for both the raw average and Abel-deconvoluted centroid locations. Therefore, for brevity, only the raw average coordinates will be presented as shown in Figure 5.5.

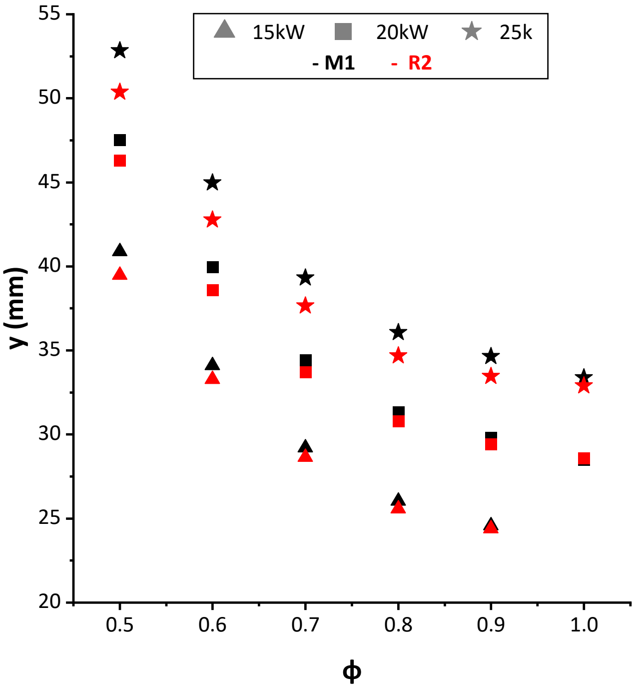

Figure 5.5 - Axial raw averaged OH centroid location movement.*

Radial shifts in centroid location were found to be small and lack a consistent trend when compared with the axial shifts. The average radial deviation of the R2 flame compared with the M1 flame was in fact only found to be ~ 1.4%. To simplify the presentation of the data, only the axial coordinates for both M1 and R2 inserts are plotted in Figure 5.5 for all thermal powers and $0.5 \leq \phi \leq 1$. The $\phi = 0.4$ centroid locations were excluded, as the flame was lifted and unstable at this equivalence ratio, particularly at higher thermal powers, preventing reliable representation of centroid location changes.

From Figure 5.5, the magnitude of axial shortening in the R2 flames increases with both higher thermal power and lower equivalence ratios, suggesting that susceptibility is proportional to the bulk flow velocity. At the $\phi = 0.5$ conditions in fact, the percentage shortening of the R2 flame compared to the M1 flame increases by ~33% and ~83% for the 20 kW and 25 kW cases respectively compared to the corresponding 15 kW shortening. This axial shortening is likely driven by roughness-induced turbulence, particularly within the boundary layer, as demonstrated in Section 5.3.1, which enhances mixing, increases local burning rates and leads to loss of energy leaving the burner. The effect becomes more pronounced at higher bulk flows and lower equivalence ratios, where the flame is more sensitive to turbulence-induced enhancements.

The positions of key operating conditions were identified on the Borghi diagram to evaluate their distribution across the various combustion regimes it defines as shown in Figure 5.6. Turbulence intensity was calculated as the spatial average of the velocity fluctuation magnitude ($\bar{u}'$) across the burner nozzle (±9 mm), based on experimental measurements obtained using isothermal LDA. Consequently, only the conditions for which isothermal LDA data were available are presented. The integral length scale (L_t) was set to 18 mm, corresponding to the inner diameter (ID) of the burner, based on the assumption that the largest eddies would have a characteristic size comparable to the burner ID. The laminar flame speed (S_l) and flame thickness (δ_l) were computed using CHEMKIN (2023 R1). While S_l values were directly provided by the software (see Appendix A.1 for actual flame speed values), δ_l was derived from the temperature profile using the following definition [269–271]:

$$\delta_l = \frac{T_{max} - T_{,in}}{\max\left(\frac{dT}{dx}\right)} \qquad [5.2]$$

Where:

T_{max} = maximal flame temperature;
T_{in} = inlet temperature;
x = axial coordinate;
dT/dx = temperature gradient.

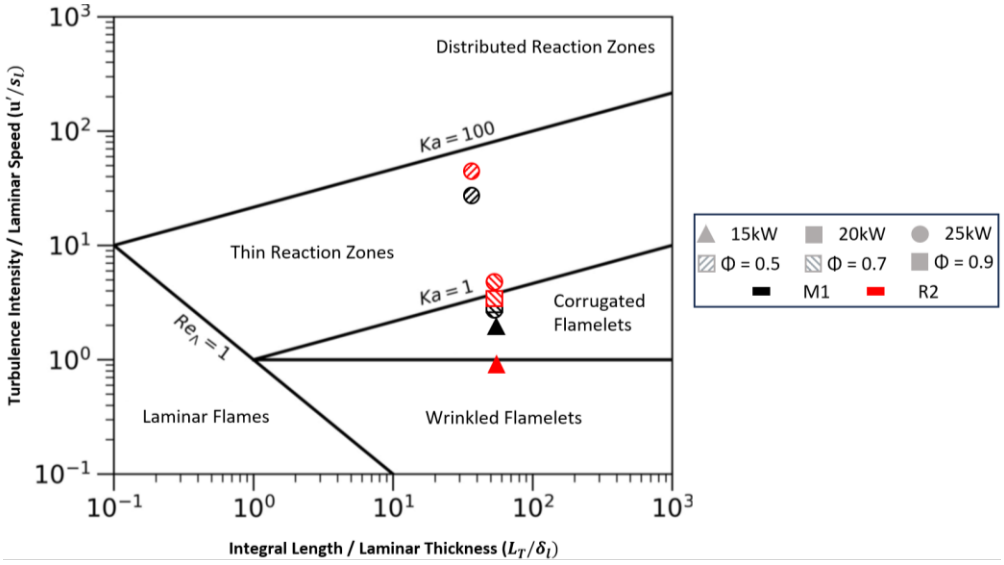

***Figure 5.6** - Borghi diagram with overlay of key smooth and rough PJB conditions.*

From Figure 5.6, it is evident that variations along the x-axis are minimal, primarily due to the relatively small differences in δ_l across the cases. In contrast, the y-axis values, which reflect *u'*, are generally higher for the rough insert configurations - except in the 15 kW cases. The latter deviates from the overall trend and may represent an outlier or be attributed to measurement uncertainty associated with lower flow rates. Most operating conditions cluster tightly within the Corrugated Flamelet regime, with leaner equivalence ratio cases extending into the Thin Reaction Zone region. The consistent influence of surface roughness across both combustion regimes suggests that the observed effects are predominantly governed by changes in bulk flow, rather than by shifts in turbulence-chemistry interaction.

5.3.2.2. Stability Limits

Operability sweeps were conducted for 15 - 20 -25 kW, as described in Section 5.3.2.1. However, flashback was observed only at 15 kW and exclusively with the M1 insert. Recognising the significant influence of surface finish on flashback behaviour, a more detailed investigation was carried out at lower thermal powers. For this study, thermal powers of 10 - 12.5 - 15 kW were tested, with flashback occurring for both inserts at all power levels except 15 kW for the range of ϕ investigated. Each flashback condition was repeated twice for every thermal power. To minimise hysteresis, after each flashback or LBO event, ignition was performed at the prescribed ϕ for the corresponding thermal power, allowing the rig to thermally stabilise before proceeding to the next flashback or extinction test. Relative changes in bulk flow velocities at the point of flashback were calculated, normalised against the smooth counterpart under each condition. Positive values therefore indicate that the rough configuration exhibited lower velocities. Results are shown in Figure 5.7.

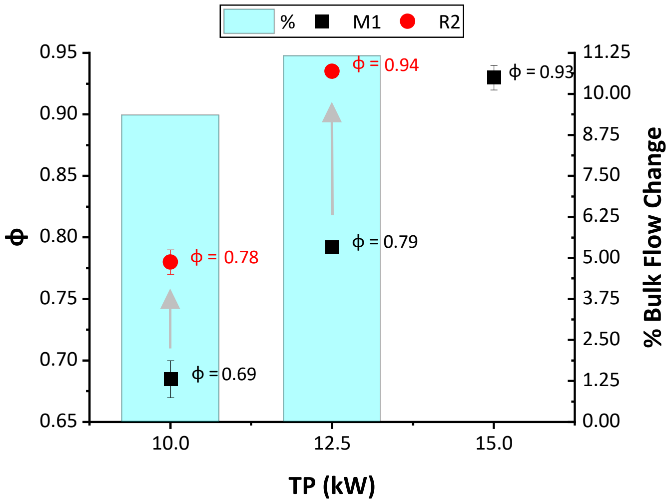

***Figure 5.7** – flashback φ vs. power setting, with bars showing roughness-induced bulk flow changes.*

The results in Figure 5.7 demonstrate that surface roughness has a measurable impact on the burner flashback limits. At all thermal powers investigated the R2 insert exhibited greater flashback resistance compared to the M1 insert. For the same thermal power, the R2 cases flashed back at a higher ϕ (lower relative ū) than with the M1 insert. This is evidenced in Figure 5.7, where the blue bar charts show reductions of approximately 9.4% and 11.2% in bulk flow velocity at flashback for 10 kW and 12.5 kW, respectively. In addition, the roughness induced flashback resistance seems to increase with increasing thermal power. At 10 kW, flashback with the R2 insert occurred at ~13% higher ϕ than with the M1 insert whilst at 12.5kW it occurred at ~19% higher ϕ. The difference in bulk flow between M1 and R2 is also observed to increase with rising thermal power.

Surface roughness was also found to influence LBO limits as mentioned in Section 5.3.2.1. Although LBO was not investigated for the lower thermal powers of 10 kW and 12.5 kW, at thermal powers between 15 kW and 25 kW, LBO was found to occur on average at ~2.5% higher equivalence ratios and at ~2.5 lower bulk flows as shown in Figure 5.8.

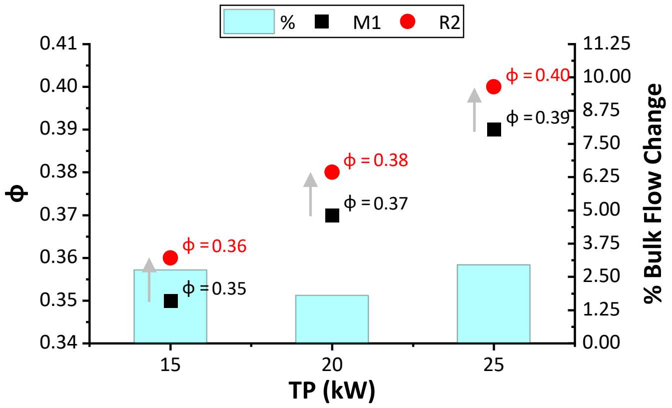

***Figure 5.8** - LBO φ vs. power setting, with bars showing roughness-induced bulk flow changes.*

The observed shifts in both flashback and LBO to higher ϕ can be partially attributed to the increased centreline velocities at the nozzle exit, as identified isothermally in Section 5.3.1. Flashback exhibiting a more pronounced shift due to its greater sensitivity to local velocity variations and turbulence near the walls, whereas LBO is primarily governed by global turbulent flame speed hence the small and consistent offsets. The significantly greater impact of roughness on flashback compared to LBO suggests that increased surface roughness positively influences operability limits.

5.3.2.3. Changes in Flashback Behaviour

As demonstrated in Section 5.3.2.2, surface roughness had a positive effect on flashback, resulting in its occurrence at higher ϕ across a range of thermal power levels. To further elucidate this phenomenon, an additional investigation was conducted to determine whether any changes in the mechanisms leading to flashback could be identified between the smooth and rough surface cases.

The burner was driven to flashback with both M1 and R2 inserts for the 12.5kW thermal power as outlined in Section 5.3.2.2. However, in this investigation, the flame was recorded using the high-speed OH* chemiluminescence (CL) camera. The peak and frame-averaged intensities were extracted from each 0.5-second raw OH* chemiluminescence recording of the flashback event. To enhance the identification of the flashback onset and ensure the use of a consistent marker across all test conditions, both the raw maximum and frame-average intensity values were normalised using the method outlined in Equation [5.3]. In this approach, *max(x)* refers to the peak or frame-average intensity of the stable flame, calculated over 500 frames, depending on the dataset being normalised. A comparison between the raw and normalised datasets is presented in Figure 5.9.

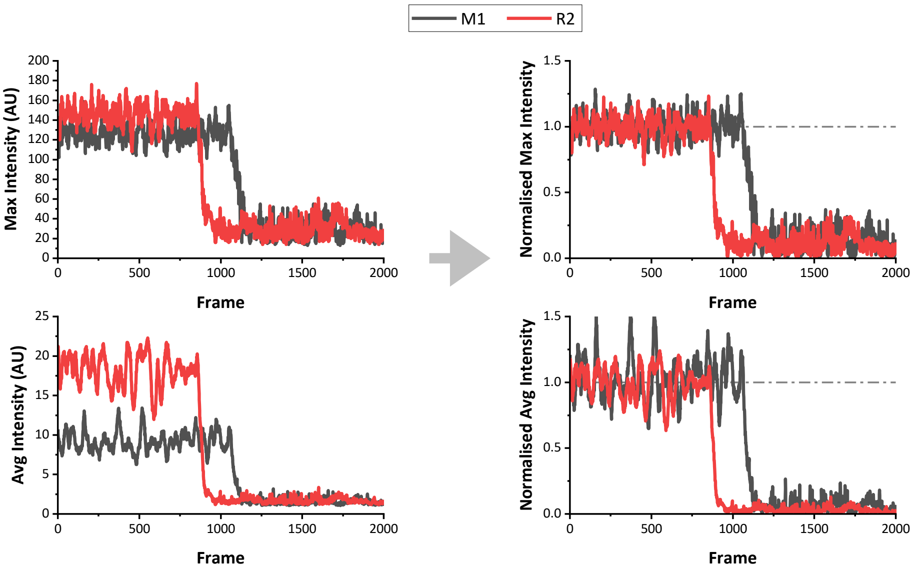

Figure 5.9 *- Comparison of raw [left] and normalised [right] maximum and average OH* CL intensities for both smooth and rough flashback events at 12.5 kW.*

$$x_{\mathrm{norm}} = \frac{x - \max(x)}{\max(x) - \min(x)}. \quad [5.3]$$

Where:

x = the frame maximum / average of the OH* CL flashback recording.

Figure 5.9 illustrates that, due to the averaging process applied to each frame, the frame-averaged intensity values exhibited reduced noise during and after the flashback event. This trend was consistently observed across all flashback events investigated. Consequently, the normalised frame-averaged intensity data were adopted from this point onward to assess the onset of flashback. Specifically, a flame was arbitrarily considered to have fully flashed back when the normalised frame-averaged intensity first reached a value of 0.2. This threshold was selected iteratively by comparing normalised flashback events across both PJB and JICF configurations (presented in Section 7.4.2.3) over a wide range of thermal powers, ensuring that a consistent value could be applied regardless of potential differences in intensity profiles during or after the flashback event. Normalised changes in frame-average OH* intensity within ±60 ms of the flashback event for all test conditions are plotted in Figure 5.10, along with the corresponding moving average curves to improve data visualisation.

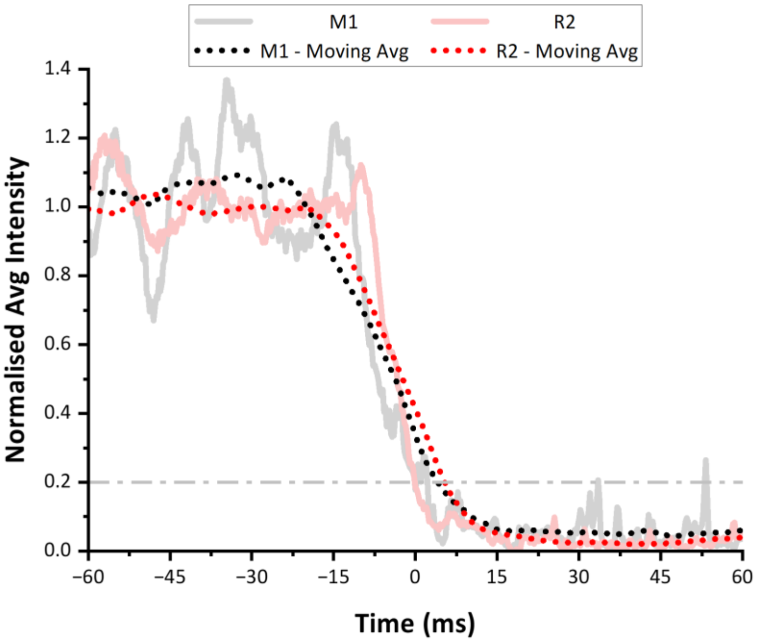

***Figure 5.10** – Normalised changes in frame-average OH* CL intensity at time = ± 60 ms of the flashback events with both M1 and R2 inserts at 12.5 kW.*

From Figure 5.10, once the normalised flame intensity decreases to ≤ 0.2 of the stable flame intensity, the values stabilise, confirming the validity of using 0.2 as a flashback indicator. A comparison of the frame-averaged intensity profiles for the M1 and R2 inserts indicates that, although the R2 configuration underwent flashback at a ~24% higher laminar flame speed (as estimated using CHEMKIN – 2023 R1, see Appendix A.1 for actual flame speed values) owing to its operation at a higher equivalence ratio, both cases exhibited broadly similar flashback behaviours.

That said, the frame-averaged values for the R2 case appear to remain stable for approximately 3.25 ms longer prior to the onset of flashback. This was determined by identifying the time at which each moving average dataset first fell below a normalised value of 0.95. This observation is further supported by analyses of the gradient of the time-averaged profiles. Specifically, when evaluating the average intensity-time gradient over a ±20 ms interval around the flashback event using linear curve fitting applied to the smoothed (moving average) datasets, the R2 case exhibited a gradient approximately 9% steeper than that of M1. This trend is also visually evident in Figure 5.11 where the 20 ms preceding flashback are shown for each condition. The frames are spaced at 1.25 ms intervals, and colour mapping is applied using the global peak intensity as the maximum value across all frames in the series.

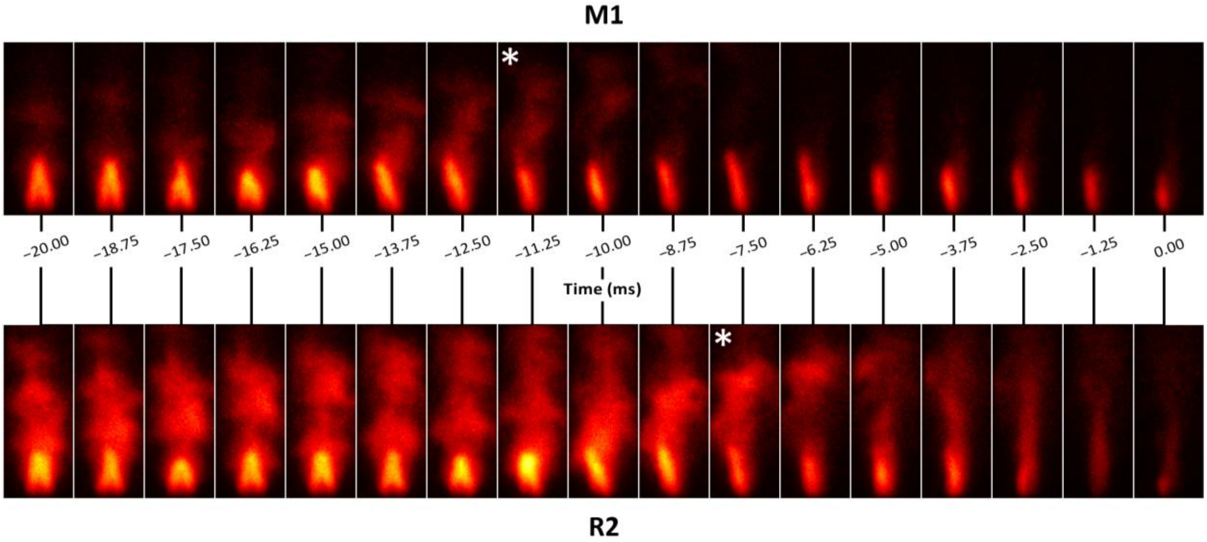

Figure 5.11 *– OH* CL visualisation of flashback at 12.5 kW with M1 [top] and R2 [bottom] inserts. Instantaneous frames spaced out every 1.25 ms. Normalisation performed based on the global maximum intensity. The * indicating the closest frame to last have a value ≥ 0.95.*

Figure 5.11 illustrates that the R2 flame exhibits a notably larger and more intense structure, as expected due to its higher equivalence ratio at the point of flashback. Furthermore, it is evident that the R2 flame remains stable for approximately three additional frames prior to the onset of the flashback event. Nevertheless, when comparing the flashback mechanisms, clear similarities are observed between the M1 and R2 flames. In both cases, flashback initiates asymmetrically on the left-hand side in a boundary-layer-driven manner [272,273] before gradually progressing upstream into the burner nozzle, indicative of a transition to a more core flow-dominated flashback behaviour [274].

It should be noted that the ignitor was located on the left-hand side of the burner and therefore may have influenced the initial location of flashback onset. However, as the ignitor position remained fixed throughout the entire test campaign, it is not expected to have affected the comparative results or the observed trends.

This further investigation into roughness-induced flashback demonstrates that, while increased surface roughness delays the onset of flashback to higher equivalence ratios at a given thermal power (as established in Section 5.3.2.2), the subsequent flashback propagation occurred more rapidly in R2 compared to M1. This can be partially attributed to the R2 case exhibiting a ~24% higher flame speed (Appendix A.1), due to the richer equivalence ratio, and a ~11% lower bulk flow rate. However, the only ~9% increase in the flame intensity–time gradient suggests the relationship between these parameters is not directly proportional, thereby complicating the comparison between the two configurations. Despite this, both inserts displayed comparable flashback mechanisms, initiating at the boundary layer and progressing into the core flow region. These observations indicate that surface roughness modifies the flame dynamics without necessarily exacerbating boundary-layer flashback.

5.3.3. Exhaust Gas Emissions

Exhaust NO_x emission measurements were taken at $\phi = 0.5$, $\phi = 0.6$ and $\phi = 0.7$ for thermal powers between 15 kW and 25 kW as shown in Figure 5.12. In these lean premixed flames, NO_x production is expected to be primarily driven by the thermal NO_x pathway [275]. However, since surface roughness has already been shown to influence flame position, stability limits, and, as was discussed in Section 5.3.1, flow-fields and turbulence, measurable changes in NO_x may be observed.

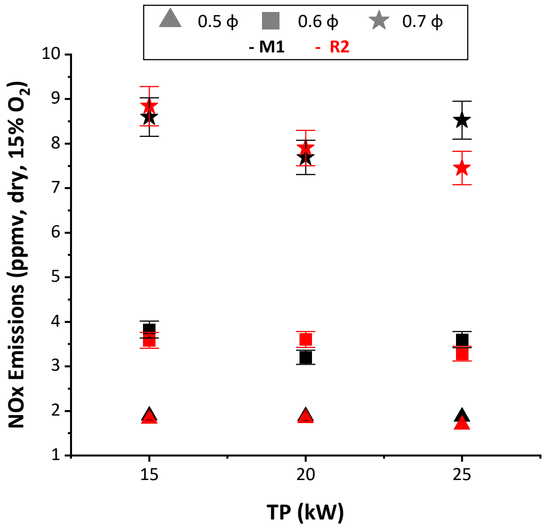

Figure 5.12 *- NO_x emissions as a function of thermal power and surface roughness. Error bars showing measurement uncertainty.*

From Figure 5.12, it can be observed that NO_x emissions below 10 ppm were achieved across all test points investigated with values at $\phi = 0.5$ and $\phi = 0.6$ being below 5ppm. For these two equivalence ratios, the minor differences observed between the M1 and R2 cases did not allow for significant conclusions. Similar findings were noted for the lower two thermal powers, where measured differences were within the error bars. A more significant effect was observed at $\phi = 0.7$ for the 25kW case, where NO_x emissions decrease by ~12.6% as surface roughness increased. It should be noted that, as covered in Section 3.2.2.2, emission measurements were performed using a single-point probe along the burner centreline, which introduces inherent limitations. From Section 5.3.2.1, it has been shown that both thermal power and ϕ affect flame length, which in turn alters the distance and residence time between the flame and the emissions measuring probe across the conditions presented in Figure 5.12. Therefore, these measurements should be interpreted with due caution.

5.4. Summary

The impact of surface roughness on the performance indicators of a recently designed, industry-relevant generic premixed jet burner fired on hydrogen was investigated under atmospheric operational conditions. Guided by recent developments, two interchangeable inserts were utilised: one conventionally machined, representing the smooth benchmark, the other having a rough surface, mimicking unprocessed “raw” AM components. Detailed experimental characterisation was performed, including measurements of emissions, flame behaviour, and stability limits. By isolating surface finish as the primary variable, building on previous research, the study offers valuable insights into the implications of roughness for burner operability and emissions.

Key findings of this work are as follows:

- **Surface roughness influenced flow-field characteristics**, with the rough insert (R2) producing both higher centreline velocities and increased turbulence intensity near the wall. These aerodynamic changes contributed to an upstream shift in the flame centroid, particularly at higher thermal powers and leaner mixtures.

- **Stability limits were significantly altered by surface roughness.** The rough insert (R2) demonstrated a wider stable operating range with measurably improved flashback resistance at the cost of marginally higher sensitivity to flame lift-off and LBO.

- **Despite factors that typically promote flashback**, including increased turbulence, richer mixtures, and reduced bulk flow, the R2 insert exhibited only a moderate increase in the rate of flashback propagation once flashback was initiated. This suggests that the elevated centreline velocities had a stabilising effect that counteracted the enhanced reactivity, thereby mitigating flashback onset.

- **NO_x emissions were consistently low** across the range of conditions considered, with slight reductions observed for the rough insert at higher thermal powers, suggesting that roughness may marginally improve emission profiles due to slight mixing improvements. Given the limitations of the measurement technique employed, these data should be interpreted with appropriate caution, and future work should focus on achieving improved characterization.

These results underscore the importance of considering surface roughness effects in the design of hydrogen combustion systems, particularly in contexts where AM is used. The study demonstrates that adopting post-processing AM components to achieve smoother surfaces may not only be unnecessary but could also diminish performance, suggesting the potential for commercial benefit. Furthermore, this comprehensive dataset provides a foundation for refining reacting computational models with roughness sensitivity on novel state-of-the-art burner geometries.

Chapter 6. Modelling of Roughness Effects on a Premixed Jet Burner via a Low-y$^+$ Approach

6.1. Research Scope

Chapter 6 aims to develop an appropriate "equivalent sand grain roughness" (k_s) correlation capable of numerically replicating the roughness-induced effects observed experimentally in Chapter 5. It builds on the findings from Chapter 4, where a novel k_s correlation, derived using methane-fired experimental data from a Generic Swirl Burner [42], successfully captured changes in flame shape, particularly under reacting conditions. Here, the objective was to determine whether roughness effects could be accurately represented in both RANS and DES simulations using either the novel correlation or the methodologies outlined in Chapter 4 when applied to a hydrogen-fired Premixed Jet Burner (PJB). If not, the goal was to develop a new correlation capable of capturing roughness effects in both isothermal and reacting conditions across the wide range of bulk flow velocities tested experimentally.

6.2. Reference Experimental Data

The impact of surface roughness on the performance and operability of a PJB was investigated experimentally under both isothermal and hydrogen-fired atmospheric pressure conditions as described in detail in Chapter 5. During the experimental test campaign, the airflow was delivered through both the main air line and a separate seed air line containing Al_2O_3 particles for flow seeding. The distribution of these splits, along with the naming conventions applied to each condition in Chapter 6, is summarised in Table 6.1. The measured bulk flow velocities (ū) correspond to the average ū values obtained with the M1 and R2 inserts, as reported in Table 5.2. Detailed surface roughness characterisation of both inserts is provided in Section 3.2.1.4.1

Table 6.1 *– Experimental isothermal flow conditions with naming conventions.*

Naming Convention	Main Air (g/s)	Seed Air (g/s)	Reacting Equivalent Condition	ū (m/s)	Ambient Temperature (C°)
Iso_20	5.8	0.6	15 kW @ ϕ = 0.93	19.5	13
Iso_32	9.9	0.6	20 kW @ ϕ = 0.7	32.1	
Iso_40	12.62	0.65	25 kW @ ϕ = 0.7	40.5	
Iso_64	20	0.65	25 kW @ ϕ = 0.4	64	

Experimental axial velocity profiles for Iso_20, Iso_32 and Iso_64 were initially presented in Chapter 5. The Iso_40 profile, obtained during the same test campaign, is presented here for the first time to extend the range of flow conditions available for validation. All experimental isothermal LDA profiles are shown in Figure 6.1.

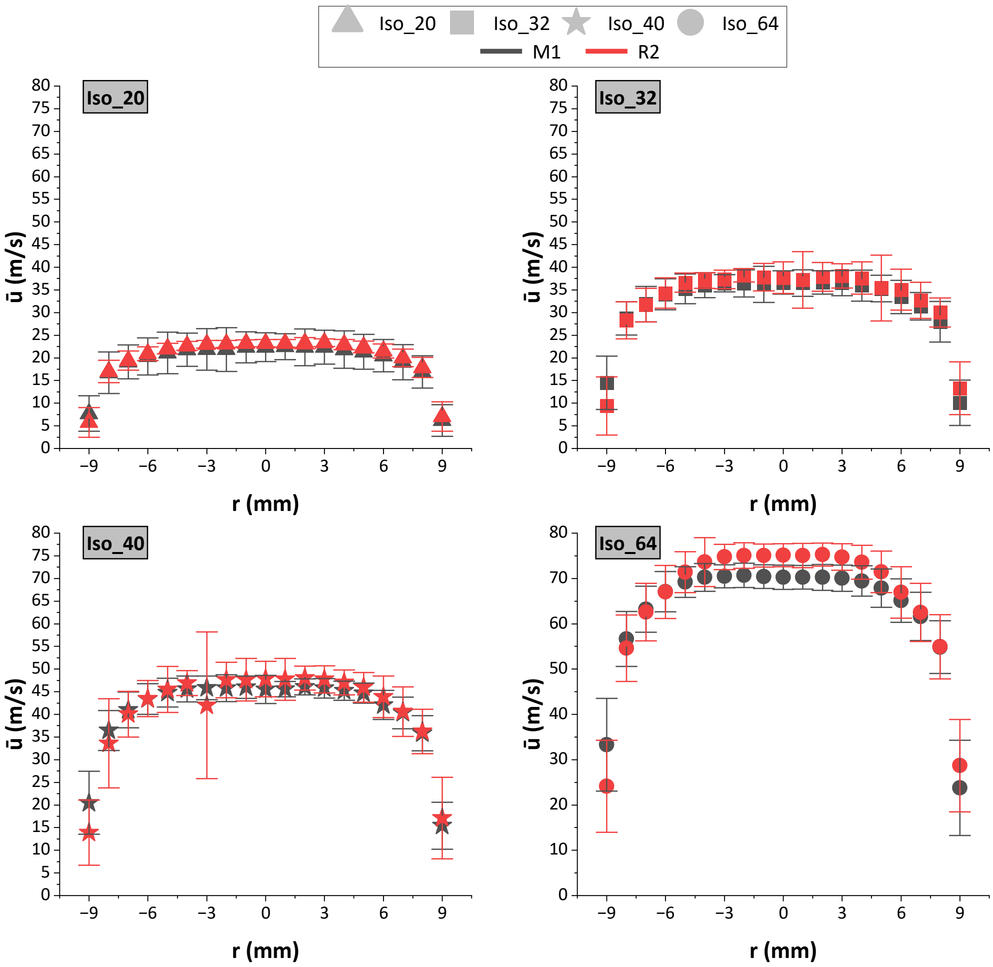

***Figure 6.1** – Experimental isothermal axial velocity profiles at various bulk flow velocities. Error bars representing statistical uncertainty via velocity fluctuation measurements (u'$_{RMS}$).*

From Figure 6.1, an outlier is observed for the Iso_40 case in the R2 velocity profile at a radial coordinate of *r* ≈ –3 mm. This data point is considered anomalous due to its unusually low velocity (~11% lower than adjacent values) and its significantly higher associated statistical uncertainty. Therefore, it is not treated as a representative data point.

For reacting flow-field validation, whilst flow-field measurements were not taken experimentally, those obtained under equivalent total mass flow isothermal air conditions are still employed. Although a direct comparison between the experimental isothermal and numerically simulated reacting velocity profiles is not strictly representative, the isothermal datasets provide a valuable qualitative reference for assessing whether the numerical flow fields behave as expected. The influence of thermal effects within the numerical simulations is anticipated to be limited, primarily because the experimental measurements were taken only 2 mm downstream of the nozzle exit. Furthermore, since the burner operates in a jetting regime with negligible swirl, the near-nozzle velocity field is predominantly governed by inertial forces rather than thermally induced effects.

Chemiluminescence data, originally presented in Section 5.3.2.1, was utilised to assess the effectiveness of modelled roughness effects on flame composition. For validation purposes, this Chapter focuses on data corresponding to $\phi = 0.5 - 0.7$ and 0.9.

6.3. Numerical Setup

Given different experimental setups were used for the isothermal and reacting datasets, confined for the reacting cases and unconfined for the isothermal equivalents, separate computational domains and physics models were required. These are detailed in the Sections 6.3.1 - 6.3.2.

6.3.1. Isothermal Simulations

6.3.1.1. Fluid Domain

To accurately replicate the unconfined flow at the burner exit, an initial computational setup was tested, incorporating a combustion chamber with a tenfold expansion relative to the nozzle inner diameter, with its top and side surfaces designated as pressure outlets. Since the fuel delivery line was not utilised during the isothermal tests, it was excluded from the CFD domain to facilitate meshing and reduce the overall mesh count. Instead, the premixing chamber was extended 200 mm upstream of the bluff body assembly to allow for sufficient flow development. The resulting initial computational domain is shown in Figure 6.2.

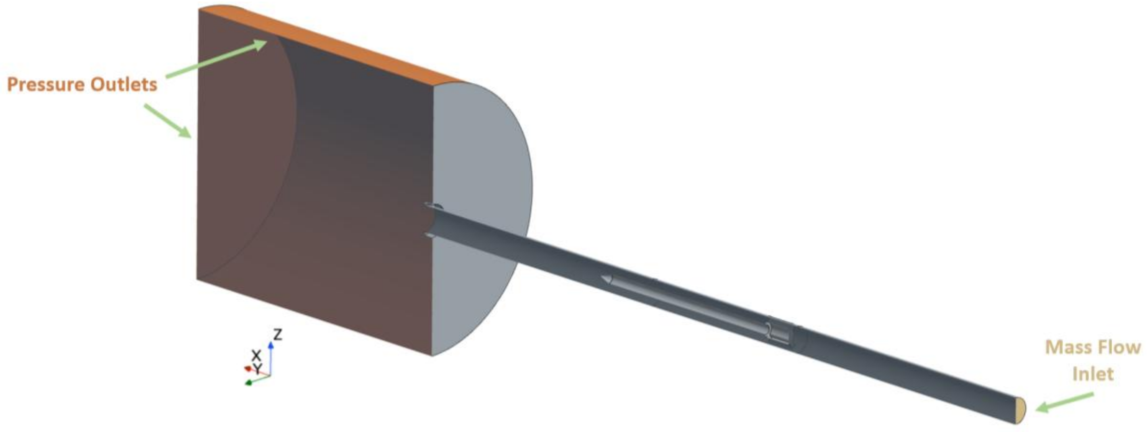

Figure 6.2 - Computational domain with 10x expansion ratio. Inlet and outlet surfaces highlighted.

An initial exploratory mesh of approximately 2 x 10^6 elements was created to evaluate whether the combustion chamber diameter could be reduced without compromising the results. This reduction aimed to save mesh elements and, consequently, computational time. To assess this, line probes were placed across the full diameter of the combustion chamber, starting 2 mm above the nozzle exit and spaced every 60 mm. The simulation employed the Realizable k- ε Two-Layer RANS turbulence model alongside the Segregated Fluid Isothermal solver. Default atmospheric pressure was maintained, and the continuum temperature was set to 286 K to align with experimental data. Results for the Iso_20, Iso_32 and Iso_64 cases are collected in Figure 6.3.

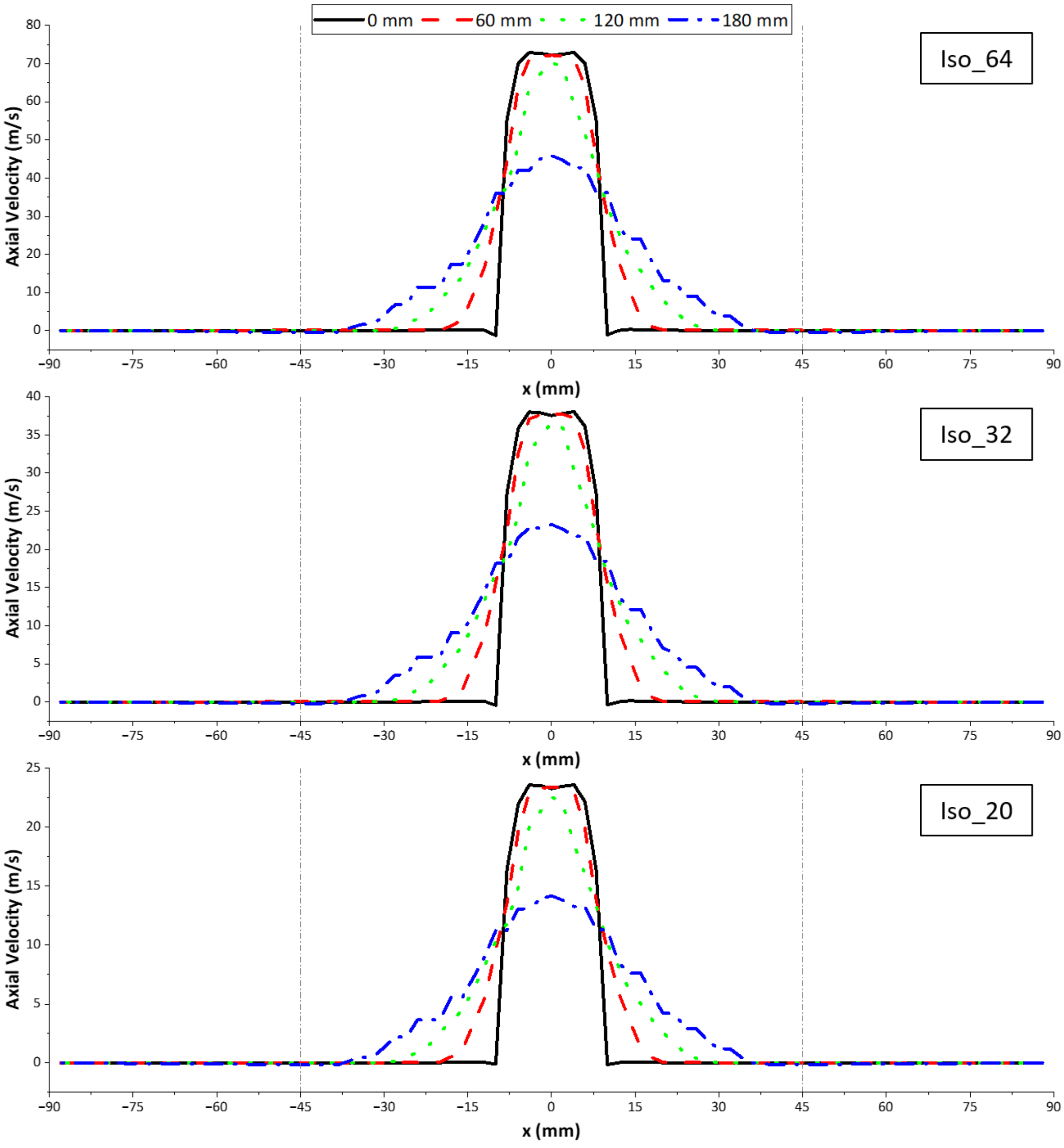

Figure 6.3 *- Axial velocity profile development across the unconfined combustion chamber with 10x expansion. Line probes placed at 60mm intervals covering the entire combustion chamber starting from 2mm above the nozzle exit.*

From these results it can be seen that, as the axial distance from the nozzle exit increases, the velocity profiles progressively widen, while the peak velocity decreases. Disregarding the variations in velocity magnitudes across the three different flow rates, the rate of profile widening appears to remain consistent, with velocities beyond a radius of 35 mm reaching zero. This suggests that reducing the combustion chamber expansion ratio from 10× (r = 90 mm) to 5× (r = 45 mm) should not adversely impact the results.

To evaluate the impact of reducing the combustion chamber diameter on the flow field, axial velocity iso-surfaces were plotted at 5 m/s increments, starting from 0 m/s, for both the 5× and 10× expansion ratio combustion chambers. Results for the Iso_20 and Iso_64 cases are shown in Figure 6.4. The results indicate that changes in the flow fields are minimal, particularly within the main jet flow, which is the primary focus of this numerical investigation. Herein the combustion chamber with 5x expansion was therefore utilised.

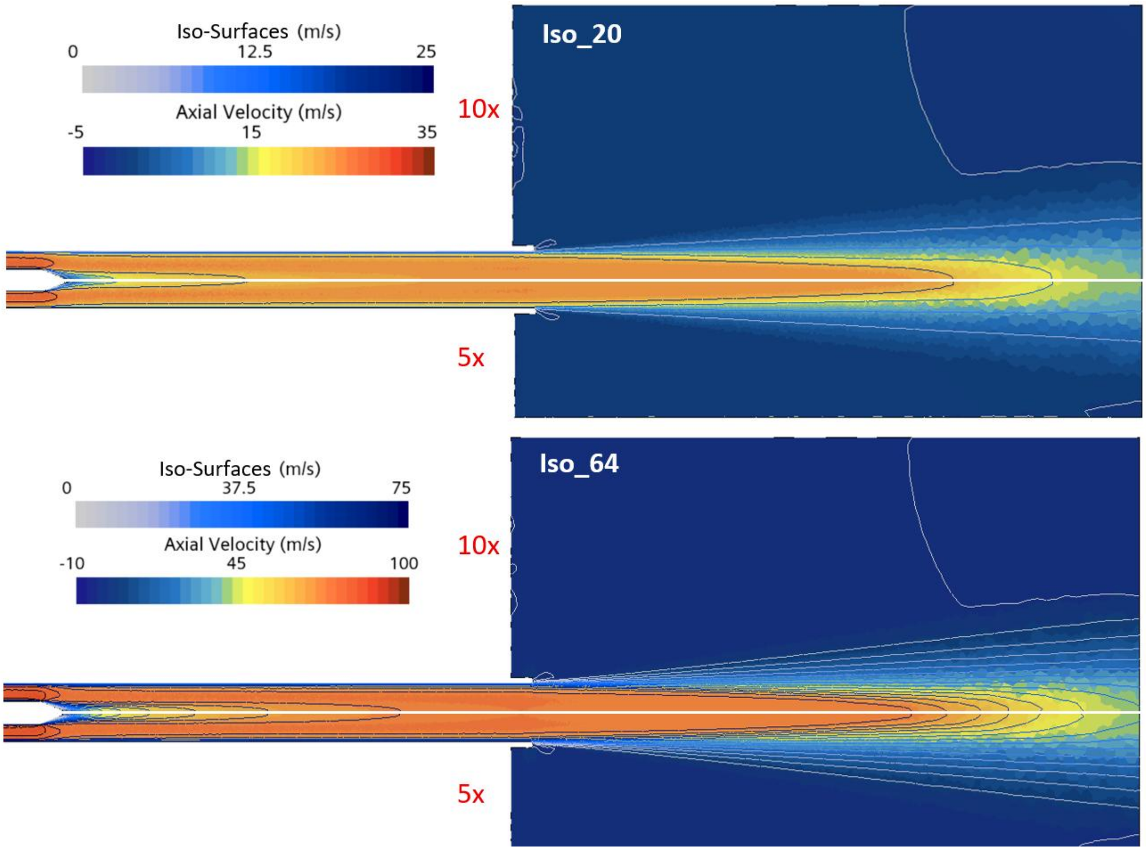

***Figure 6.4** – Comparison of axial velocity flow fields with 10x (top) and 5x (bottom) expansion ratios for Iso_20 and Iso_64 conditions. Iso-surfaces set at 5 m/s increments.*

6.3.1.2. Physics Setup

The isothermal cases were initiated as follows; the Segregated Flow Isothermal model was utilised and the temperature set to 286 K. The reference pressure was set to atmospheric (0.101 MPa) and the default STAR CCM+ material properties for air were left unchanged. As for the exploratory simulations performed in Section 6.3.1, a mass flow inlet was applied to the base of the premixing section whilst pressure outlets were applied to the top and perimeter of the combustion chamber as shown in Figure 6.5.

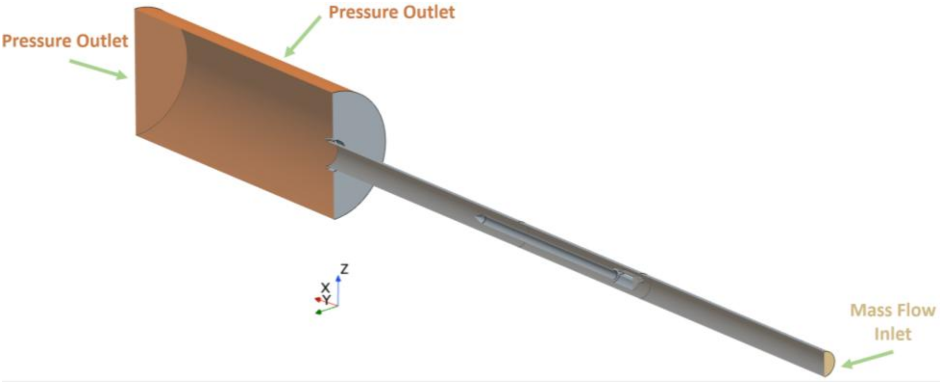

Figure 6.5 *- Computational domain with 5x expansion ratio. Inlet and outlet surfaces highlighted.*

For the RANS simulations, the k- ε Elliptic Blending (EB) turbulence model was employed due to its robustness, discussed in Section 3.1.1.2.2, which theoretically enable it to account for roughness effects even with meshes where $y^+ \approx 1$. For the DES cases, the DDES k- ε EB turbulence model was selected, as findings from Chapter 4 indicated it proved the most capable at capturing roughness effects when combined with a low-y^+ mesh.

Time-step and flow through time (FTT) choices for the DES simulations were informed utilising the respective RANS simulations. Time-steps were calculated as per Section 4.2.2.3 with FTTs approximated via the surface averaged axial velocity of section planes of the length of the burner. Simulations ran for 1 FTT before initiating time-averaging which was performed for a maximum of 5 FTTs. Due to the computational demand of DES, the effectiveness of roughness correlations was only assessed on the most extreme cases with the temporal parameters collected in Table 6.2.

Table 6.2 *- Temporal settings for isothermal DES simulations.*

	Iso_20	**Iso_64**
FTT (s)	0.076	0.023
Total Time (s)	0.46	0.14
Inner Iterations	15	20
Time-Step (μs)	6	

Initial smooth RANS simulations were performed utilising the total mass flow rates (main air + seed air) from the experimental campaign outlined in Table 6.1. However, as shown in Figure 6.6, the smooth numerical simulations consistently generated velocity profiles with higher values in the core flow region compared to the reference experimental data.

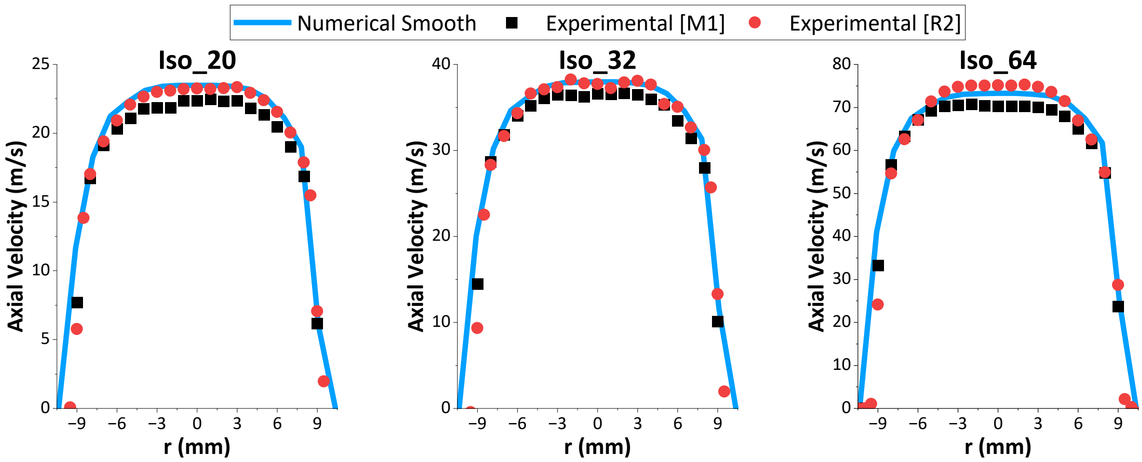

***Figure 6.6** - Initial smooth isothermal simulations with mass flow set to the total experimental mass flow. Numerical values taken 2 mm above the nozzle exit, consistent with the experimental measurements. R2 profiles included to aid visualisation of issues with numerical overprediction.*

Figure 6.6 shows that while the overall numerical profiles match those of the experimental data, in the core flow (-5 mm ≤ r ≤ 5 mm), numerical velocities were found to present a consistent positive velocity offset. This offset is ~3.8% for the Iso_32 and Iso_64 cases and ~ 5.8% for the Iso_20 case. Consequently, bulk flow velocities were also found to be higher for the numerical profiles, though the relative difference was found to decrease with increasing flowrates, from ~5% for Iso_20 to ~3.3% for Iso_64.

Although the overall discrepancies were relatively minor, the objective was to compare numerically generated rough and smooth velocity profiles, which, as indicated by the experimental data, exhibit only subtle differences. The observed offset introduces challenges in conducting such assessments. For instance, as illustrated in Figure 6.6, the smooth numerical profiles already demonstrate a closer resemblance to the reference rough data. Consequently, accurately evaluating the numerical rough profile's fidelity under these conditions becomes challenging.

To address these discrepancies, the simulations were repeated using adjusted mass flow rates, collected in Table 6.3, to replicate the measured experimental bulk flow velocities. As shown in Table 6.3, these revised flow rates exhibited a consistent offset relative to the total mass flow rates used in the experiments and closely aligned with the main air flow rates.

Table 6.3 *– Adjusted airflows compared with experimental values.*

	Adjusted Airflow (g/s)	Experimental Airflow		% Difference: CFD vs. Exp Air
		Main (g/s)	Seed (g/s)	
Iso_20	6.1	5.8	0.6	-4.69
Iso_32	10	9.9	0.6	-4.76
Iso_40	12.65	12.62	0.65	-4.67
Iso_64	19.97	20	0.65	-3.3

The velocity profiles generated with these amended flow rates are shown in Figure 6.7. As can be seen, a significantly improved agreement with the smooth experimental data is achieved, eliminating any ambiguity regarding whether they better correspond to the smooth or rough profiles. Furthermore, the numerical profiles generated for both the 5x and 10x combustion chambers can be seen to exhibit near-identical behaviour, refuting the hypothesis that the previously observed shifts were caused by the reduced combustion chamber size. The average deviation between profiles obtained with the 5x and 10x expansion ratios was approximately 0.13%. Additionally, the numerical profiles deviated from their respective experimental counterparts by an average of ~1.36% over the entire profile (-9 mm ≤ r ≤ 9 mm) and ~0.14% within the core flow region (-5 mm ≤ r ≤ 5 mm).

Given the consistent offset in flow rates required to accurately reproduce the experimental data, it can be inferred that the seed air does not influence the flow in the same manner as the main air. Additionally, the presence of a systematic error in the experimental mass flow measurements is suggested, further supported by the observed reduction in bulk flow error with increasing flow rates.

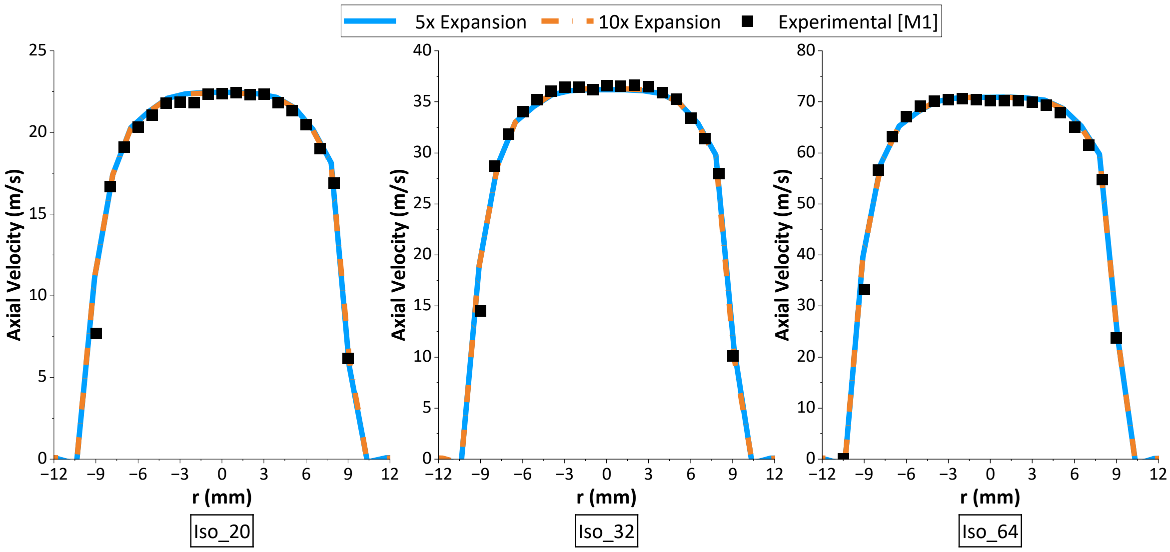

Iso_20 Iso_32 Iso_64

Figure 6.7 *– Adjusted numerical velocity profiles for Iso_20, Iso_32 and Iso_64 cases. Results shown for both the 5 and 10x expansion ratio combustion chambers and compared against the smooth experimental data. Numerical values taken 2 mm above the nozzle exit, consistent with the experimental measurements.*

6.3.1.3. RANS Mesh

While the final aim of Chapter 6 is to accurately model roughness effects using a high-fidelity DES solver, high-quality RANS initialisation data is essential. Additionally, due to the significant computational time required for DES, initial roughness modelling utilising a low-y^+ mesh was first attempted with RANS.

As explained in Section 3.1.2.3, the quality of a RANS mesh is assessed via a mesh dependency test. Iso_20, Iso_32, Iso_40 and Iso_64 flow fields were therefore simulated (using the macro shown in Appendix C.1) with progressively finer meshes. Relevant scalar fields were taken at monitoring points of interest. Mesh dependency results can be found in Figure D.11 of APPENDIX D.

Across all the conditions simulated, both pressure and axial velocity values fully converge once the mesh contains at least 4 x 10^6 elements. However, marginal variations in monitoring point values are observed for meshes with ≥ 2 x 10^6 elements. Considering the need for numerous simulations and the substantial reduction in computing time achieved by halving the mesh size, a mesh with 2.024 x 10^6 elements, shown in Figure 6.8, was chosen.

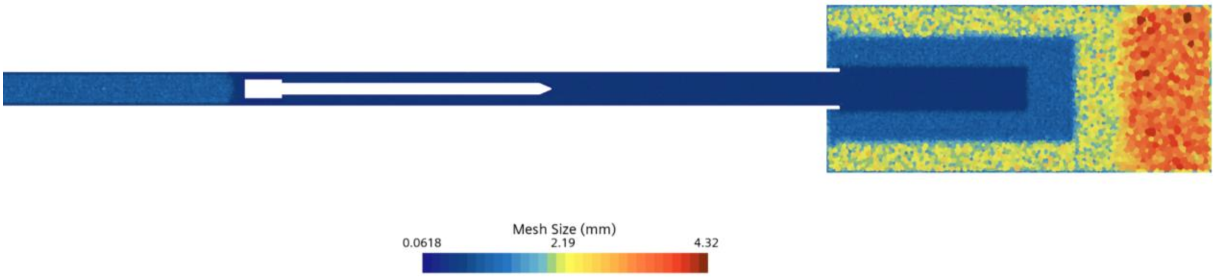

Figure 6.8 *- Final RANS mesh for unconfined isothermal simulations.*

6.3.1.4. DES Mesh

As discussed in Section 3.1.2.3, mesh dependency studies are not suitable for assessing the quality of a high-fidelity DES mesh. Instead, turbulent length scales can be utilised to determine the required mesh element sizes in different regions of the computational domain, ensuring that a sufficient proportion of turbulence is resolved to achieve accurate results. Following the methodology outlined in Section 3.1.2.3 and previously applied in Section 4.2.2.2, reference RANS simulations were used to inform cell size dimensions for the DES meshes. While the locations of various refinement zones remained consistent across the investigated conditions, variations in bulk flow velocities necessitated different cell sizes. The final meshes, presented in Figure 6.9, comprised approximately 9.5 x 10^6 and 65 x 10^6 elements for the Iso_64 and Iso_20 cases, respectively.

The substantially higher mesh resolution required for the Iso_20 case is attributed to the presence of turbulent length scales in the wake of the bluff body that are ~75% smaller than those in the Iso_64 case. This requirement is further compounded by the fact that turbulence intensity is known to increase with decreasing Re [276].

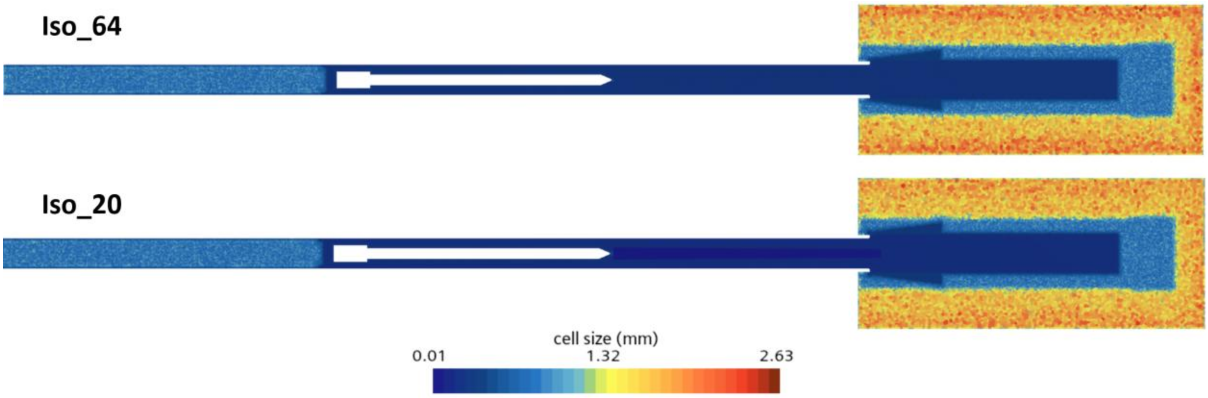

Figure 6.9 *- Iso 64 [top] and Iso_20 [bottom] DES meshes.*

6.3.2. Reacting Simulations

6.3.2.1. Fluid Domain

For the premixed jet burner domain creation, initial numerical investigations performed in Section 3.2.3 confirmed that reactants were sufficiently mixed before entering the combustion chamber. Based on these findings, and to enhance computational efficiency by simplifying the numerical model, the actual fuel injection configuration was omitted. Instead, the premixing chamber was extended 200 mm upstream of the bluff body assembly to ensure adequate flow development. The premixed fuel-air mixture was introduced into the numerical domain through a mass flow inlet positioned at the base of the model, while a pressure outlet was placed at the end of the quartz confinement to replicate the experimental setup. The finalised computational domain is illustrated in Figure 6.10.

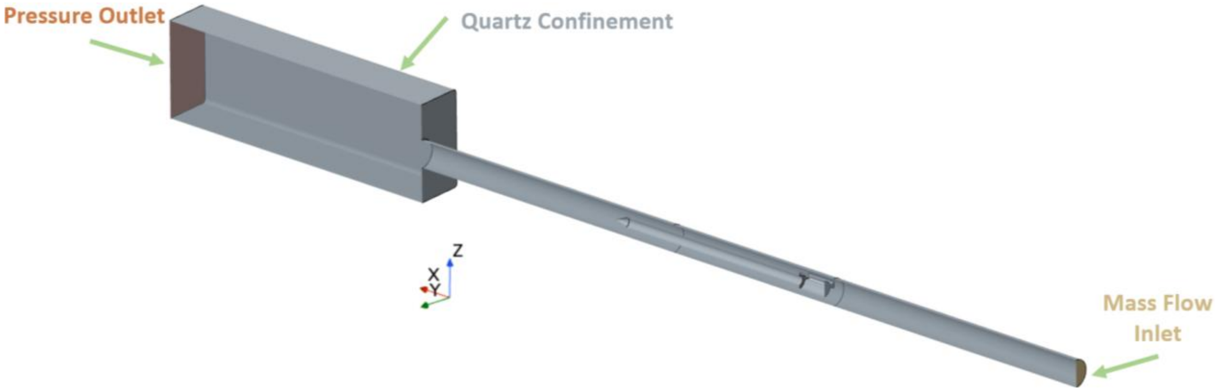

Figure 6.10 - Reacting PJB numerical domain.

6.3.2.2. Physics Setup

Reacting simulations were conducted at thermal powers of 15 kW, 20 kW, and 25 kW, each evaluated at ϕ of 0.5, 0.7, and 0.9. This resulted in a total of nine smooth and nine rough cases. Consistent with the isothermal simulations, the RANS cases employed the k–ε EB turbulence model, while the DES cases utilised the DDES k–ε EB turbulence model. The Ó Conaire [277] mechanism was utilised incorporating OH^* [254,255] via the modifications compiled in Appendix A.2, an approach equivalent to other works [256]. This reaction mechanism was selected due to its reduced number of species, which decreased computational demand, a highly desirable feature given the extensive number of simulations performed. Segregated flow enthalpy was selected in conjunction with the Complex Chemistry model. Eddy Dissipation Concept (EDC) was selected for the turbulent chemistry interactions. Inlet (T_{Inlet}), outlet (T_{EG}) and combustion chamber (T_{CC}) wall temperatures were set in accordance with measured experimental values (Appendix D.4). In both cases, the reference pressure was set to atmospheric (0.101 MPa). Inlet mass flows and wall temperatures for all conditions are summarised in Table 6.4.

Table 6.4 *- Inlet and outlet conditions for numerical reacting simulations.*

Thermal Power (kW)	**ϕ**	**$\dot{m}_{fuel/air}$ (g/s)**	**Mass Fraction**			**T_{Inlet} (K)**	**T_{CC} (K)**	**T_{EG} (K)**
			H_2	**O_2**	**N_2**			
25	0.9	8.13	0.026	0.227	0.747	284	707	1510
	0.7	10.47	0.020	0.228	0.752		683	1409
	0.5	14.46	0.014	0.230	0.756		685	1290
20	0.9	6.59	0.025	0.227	0.748		668	1472
	0.7	8.27	0.020	0.228	0.752		500	1372
	0.5	11.63	0.014	0.230	0.756		622	1262
15	0.9	4.95	0.025	0.227	0.748		668	1417
	0.7	6.25	0.020	0.228	0.752		635	1337
	0.5	8.61	0.015	0.230	0.756		634	1237

Time-step and FTT choices for the DES simulations were informed utilising the respective RANS simulations. Time-steps were calculated as per Section 4.2.2.3 with FTTs approximated via the surface averaged axial velocity of section planes of the length of the burner. Simulations ran for 2 FTT before initiating time-averaging which was performed for a maximum of 5 FTTs. Due to the high computational cost associated with DES simulations, the evaluation of roughness correlations was limited to the boundary thermal power conditions of 25 kW. As a result, the 15 and 20 kW cases were omitted, thereby reducing the total number of simulated cases by approximately 66%. Temporal parameters are collected in Table 6.5.

Table 6.5 *- Temporal settings for 25 kW reacting DES simulations.*

	ϕ = 0.5	**ϕ = 0.7**	**ϕ = 0.9**
FTT (s)	0.0176	0.0219	0.0261
Total Time (s)	0.1235	0.1536	0.1824
Inner Iterations	20		
Time-Step (μs)	5.1	6.6	8.0

6.3.2.3. RANS Mesh

Given the extensive range of reacting flow fields analysed in Chapter 6, the high computational cost associated with reacting flow simulations, and the isothermal mesh dependency results presented in Section 6.3.1.3 - where mesh-independent solutions were consistently achieved across a broad range of bulk flows - it was determined that mesh dependency tests would be conducted on the most extreme cases (25 kW at ϕ = 0.5 and 15 kW at ϕ = 0.9). Non-reacting flow fields were simulated using progressively refined meshes, with the macro outlined in Appendix C.1. Scalar fields of interest were recorded at monitoring points positioned at locations of interest.

Mesh dependency results can be found in Figure D.13 of APPENDIX D. With mesh-independent results attained for meshes containing more than 2 x 10^6 elements across both flow rates. A final mesh, depicted in Figure 6.11, comprising of approximately 2.7 x 10^6 elements was consequently employed for all reacting conditions, with only minor adjustments within the boundary layer made for each case to ensure $y^+ \approx 1$ across all flow conditions.

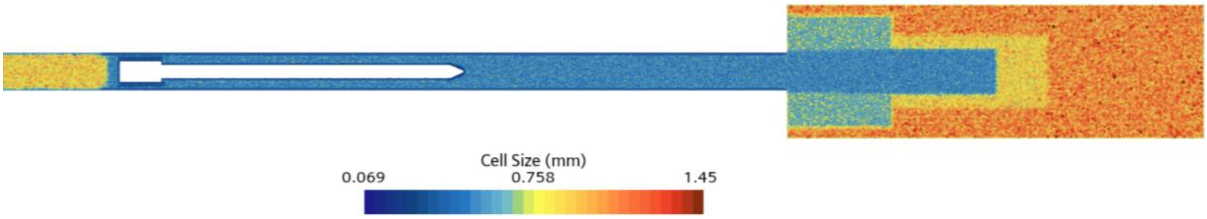

Figure 6.11 *- Final reacting RANS mesh.*

6.3.2.4. DES Mesh

Following the methodology outlined in Section 3.1.2.3 and previously applied in Sections 4.2.2.2 and 6.3.1.4, reference RANS simulations were used to inform cell size dimensions for the DES meshes. Refinement zones in the combustion chamber were varied to account for changes in flame length with changing ϕ. The final meshes are presented in Figure 6.12 together with the respective cell counts.

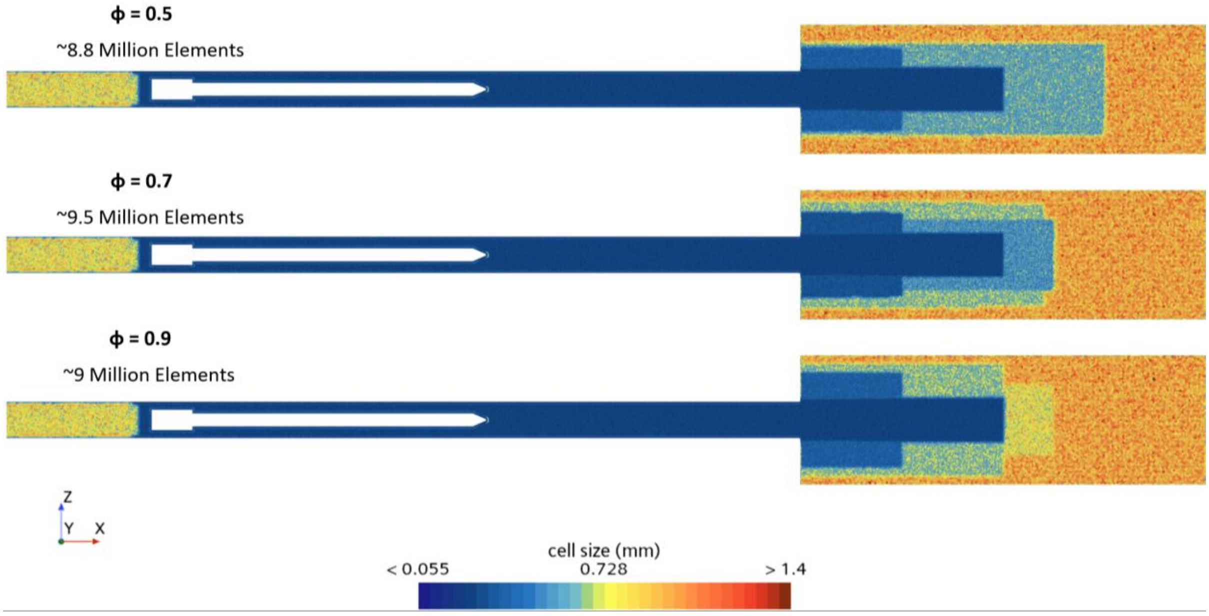

Figure 6.12 *– Reacting DES meshes for 25 kW at φ = 0.5 [top], φ = 0.7 [middle], φ = 0.9 [bottom] with associated cell counts.*

6.4. Roughness Modelling

In Section 6.4, an appropriate k_s correlation is developed to provide accurate roughness modelling over the wide range of isothermal flows measured experimentally in the PJB. The correlation derived in Chapter 4 is initially applied, followed by the application of the methodology used for its derivation. Having established a suitable correlation for the isothermal simulations, it was subsequently applied to the reacting flow fields to assess its validity under reacting conditions.

6.4.1. Isothermal Derivation and Validation

6.4.1.1. Application of k_s Correlation and Methodology from Chapter 4

In Chapter 4 a novel k_s correlation, referred to as equation [4.5], was derived for isothermal and methane-fired conditions within a premixed generic swirl burner. When utilised in conjunction with a low-y^+ DES approach, it was found to underestimate roughness effects for isothermal conditions but provide good agreement under the reacting CH_4 ones. Given the R2 insert presented an average surface roughness of Ra = 21.2 µm, this would imply a k_s value of 3.31 mm would have to be input into the CFD solver. However, such a roughness height, which would constitute over 1/6 of the burner nozzle diameter, raised concerns that it could lead to an overestimation of the roughness effects.

To address this, it was decided to derive a k_s height for a series of test conditions by applying the methodology used to derive equation [4.5]. The purpose of the equation [4.5] correlation was to ensure a k_s value high enough to reach the fully rough regime ($k_s^+ \geq 90$). Since both the flow rates and geometry simulated in Chapter 6 have changed, applying this same rationale to each test condition will allow the derivation of a new k_s correlation specific to each condition, while still ensuring $k_s^+ \geq 90$. As described in Section 4.2.2.4 (equation [4.4]), the equation for k_s^+ was rearranged to determine the required roughness height to achieve $k_s^+ \geq 90$. A surface average of the resulting field function was then calculated for the interchangeable section of each reference smooth test case simulation. The resulting k_s values calculated using both equations [4.5], referred to as FR-C (Fixed Roughness Correlation), and [4.4], referred to as GR-C (Guaranteed Roughness Correlation), for the Iso_20, 32, 40 and 64 conditions are collected in Table 6.6.

Table 6.6 - k_s correlations calculated via GR-C and FR-C for initial test cases.

	GR-C (mm)	FR-C (mm)
Iso_20	1.17	3.3072
Iso_32	0.76	
Iso_40	0.61	
Iso_64	0.41	

While the k_s value calculated using the FR-C correlation remains constant across all test conditions due to the fixed physical roughness of the insert, the values calculated using the GR-C correlation decrease with increasing bulk flow velocity. This behaviour is expected since air is used in all test cases, keeping density and viscosity constant. As a result, u^*, which is proportional to the bulk flow velocity, is the only parameter that varies in equation [4.4]. This therefore implies that the GR-C correlation is not only dependent on the measured roughness height but also on bulk flow velocity. Initial rough RANS results with both the GR-C and FR-C correlations are shown in Figure 6.13.

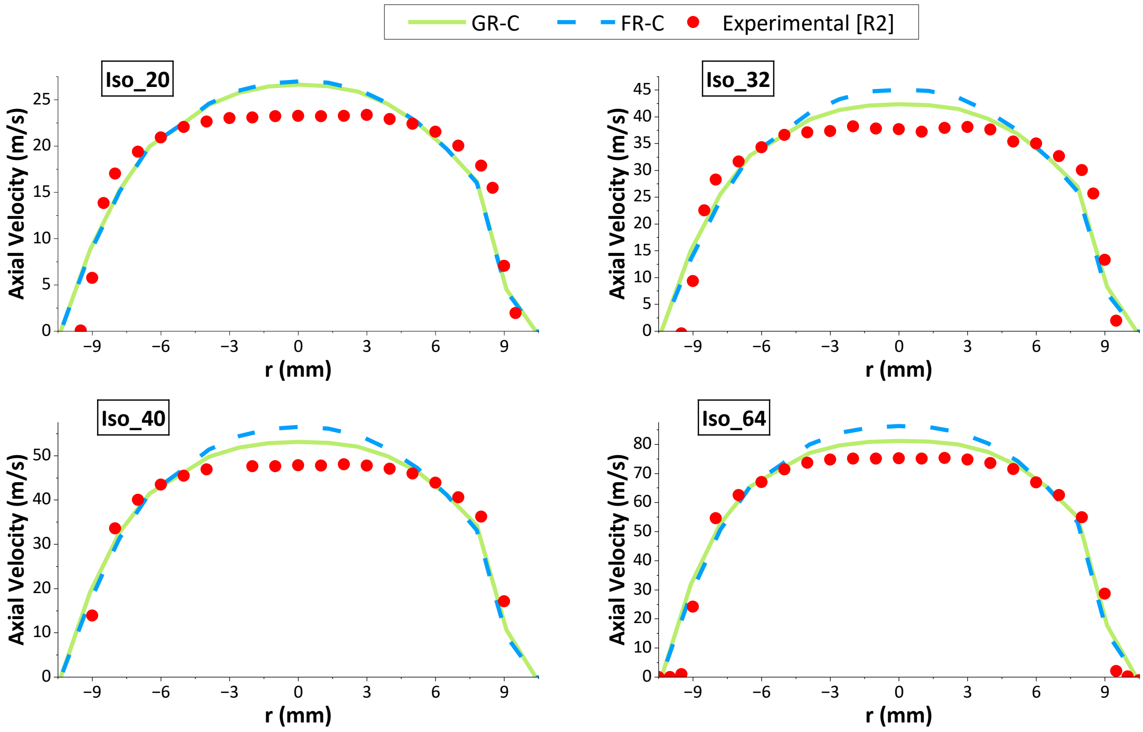

__Figure 6.13__ - Comparison of numerical RANS rough velocity profiles generated with the GR-C and FR-C correlations compared against the R2 experimental data. Numerical values taken 2 mm above the nozzle exit, consistent with the experimental measurements.

Figure 6.13 shows that roughness effects were overpredicted across all bulk flows using both the GR-C and FR-C correlations. The difference between the two numerical profiles increases with higher bulk flow rates. For the Iso_20 profiles, the peak axial velocities differ by only ~1.4%, while for all other test conditions, the GR-C correlation predicts values ~6% lower than the FR-C correlation. Additionally, as bulk flow increases, the discrepancy between the GR-C profile and the experimental data decreases, with the maximum velocity overprediction reducing from ~14% in the Iso_20 case to ~7.8% in the Iso_64 case.

From this initial trial, it is clear that neither the GR-C nor FR-C correlations provide satisfactory results across flow fields with varying bulk flow velocities. The GR-C correlation demonstrated a better fit at higher bulk flow velocities and, as shown in Table 6.7, maintained a nearly constant k_s^+ across all cases tested. However, the assumption that k_s^+ remains constant is inaccurate and contributes to greater deviations from experimental data at lower bulk flows. As bulk flow increases, the boundary layer becomes thinner, meaning that, if the roughness elements remain unchanged, they will constitute a larger portion of it (resulting in a higher k_s^+) [152,178]. In contrast, the FR-C correlation showed an increasing k_s^+ with bulk flow (Table 6.7), yet the inconsistent offset in numerical peak velocities compared to experiments suggests the need for an alternative approach.

Table 6.7 *- Peak velocities and k_s^+ values obtained with both the GR-C and FR-C correlations. Comparisons with peak experimental R2 axial velocities.*

	GR-C			FR-C		
	V_{max} (m/s)	k_s^+	V_{max} Deviation (%)	V_{max} (m/s)	k_s^+	V_{max} Deviation (%)
Iso_20	26.63	135	14.1	27.00	360	15.7
Iso_32	42.36	132	10.8	45.10	464	17.9
Iso_40	53.15	135	10.7	56.47	531	17.6
Iso_64	81.17	127	7.8	86.32	792	14.7

6.4.1.2. Novel Correlation Derivation

Section 6.4.1.1 demonstrated that for flow fields with a wide range of bulk flow velocities, neither fixing k_s^+ nor using a correlation based solely on measured roughness height provided satisfactory results. Building on the findings from the GR-C correlation, Section 6.4.1.2 derives a new correlation that also incorporates bulk flow effects. The development of this correlation began with a parametric study conducted for the Iso_20, 32, 40, and 64 cases. A range of k_s values from 0 to 3.5 mm was applied to each case, with each value being run for 1,000 iterations to ensure convergence before proceeding to the next roughness height. Both peak axial velocity and k_s^+ values were monitored throughout. Changes in k_s^+ as a function of applied k_s, along with the corresponding percentage variations in peak velocity at the nozzle exit relative to a smooth reference are presented in Figure 6.14. Percentage changes in peak velocity for different k_s values are also shown in Figure 6.15.

From Figure 6.14 it can be seen that k_s^+ values exhibit a near linear increase with increasing k_s, regardless of the simulated bulk flow. However, the rate of increase of k_s^+ is proportional to the bulk flow. As discussed in Section 6.4.1.1, higher bulk flows result in a thinner boundary layer, meaning that for a given k_s value, a larger portion of the boundary layer is occupied, leading to higher k_s^+ values.

Focusing on the relative changes in peak axial velocities at the nozzle exit, values across all conditions exhibit a linear increase with increasing k_s^+ for $k_s^+ < 90$. However, within the range $90 \leq k_s^+ < 150$, a more than twofold increase in percentage velocity change is observed across all cases. Beyond this, velocity changes appear to plateau until another distinct jump occurs at $k_s^+ \approx 372$. Following this jump, velocity changes asymptotically approach a limit, indicating a saturation effect where further increases in roughness have little to no impact on peak velocity. This occurs because, for $k_s^+ \geq 90$, the flow is classified as being in the fully rough regime. Consequently, as discussed in Section 3.1.1.2, alternative roughness function formulations are applied, as the sublayer becomes negligible due to the roughness elements exceeding its thickness [198,201].

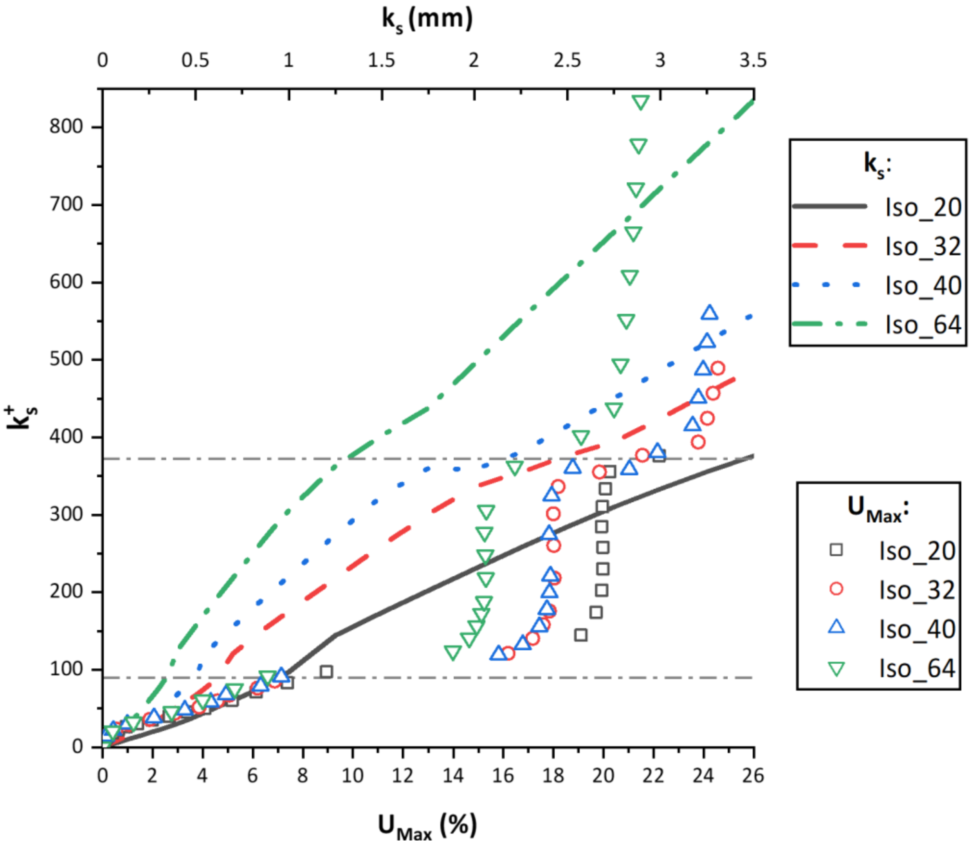

Figure 6.14 - *Changes in k_s^+ as a function of the applied ks along with percentage changes in peak velocities at the nozzle exit relative to the reference smooth data. Reference lines set at both k_s^+ = 90 and k_s^+ = 372.*

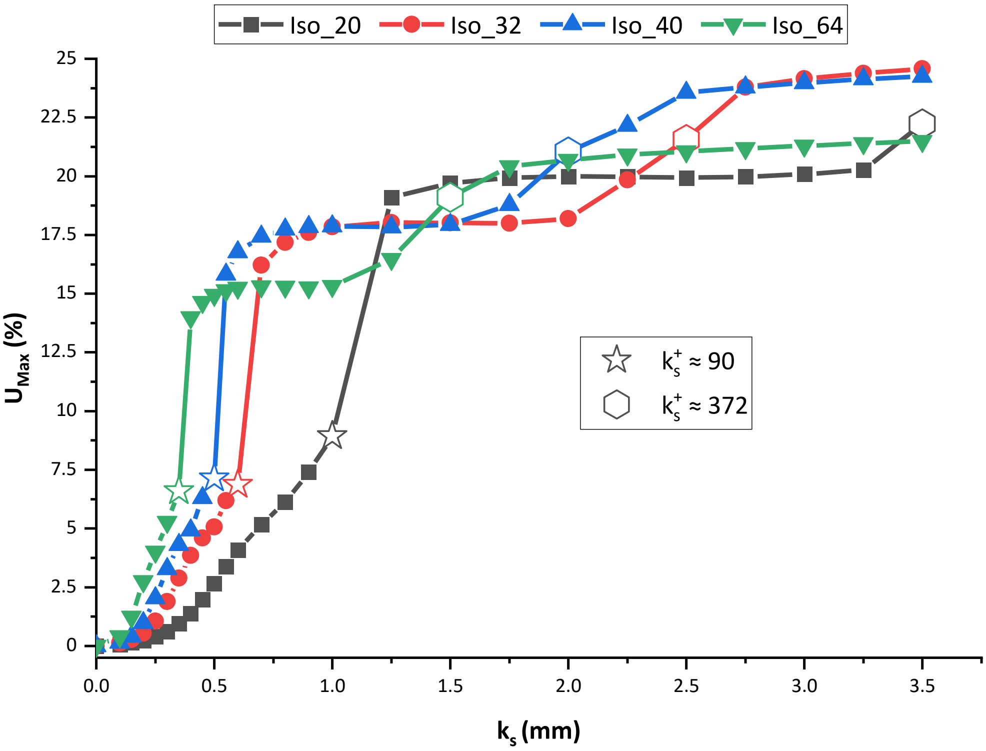

Figure 6.15 *- Percentage changes in peak velocity relative to smooth reference data as a function of k_s. The location at which a k_s^+ value of approximately 90 and 372 was reached is highlighted for each condition.*

Figure 6.15 provides a clearer visualisation of the percentage changes in peak axial velocities at the nozzle exit. Across all conditions, peak velocities increase linearly with rising k_s values until a ~7% increase over the reference smooth peak velocity is reached, corresponding to a k_s^+ value ≈ 90. Beyond this point, a sharp increase of more than twice the previous percentage change is observed across all cases, despite the subsequent k_s increase being only ~14% on average. After this spike, peak velocity changes plateau before rising again once a k_s^+ value ≥ 372 is reached. This suggests that the flow is more sensitive to roughness height in the transitionally rough regime ($2.25 \leq k_s^+ < 90$), whereas in the fully rough regime ($k_s^+ \geq 90$), larger increases in k_s are required to produce noticeable changes in peak velocity.

With an understanding of the sensitivity of peak velocity to k_s values across various bulk flows, the focus then shifted to determining the appropriate k_s required to replicate the experimental peak velocity shifts. Notably, for the bulk flows tested, the required k_s values all fell within the linear transitionally rough regime. To obtain an exact k_s, a linear trend line was applied to each dataset, generating equations where peak axial velocity served as the *x*-value and k_s as the *y*-value. By inputting the experimentally measured peak axial velocity into these equations, the corresponding k_s value was determined, as illustrated in Figure 6.16.

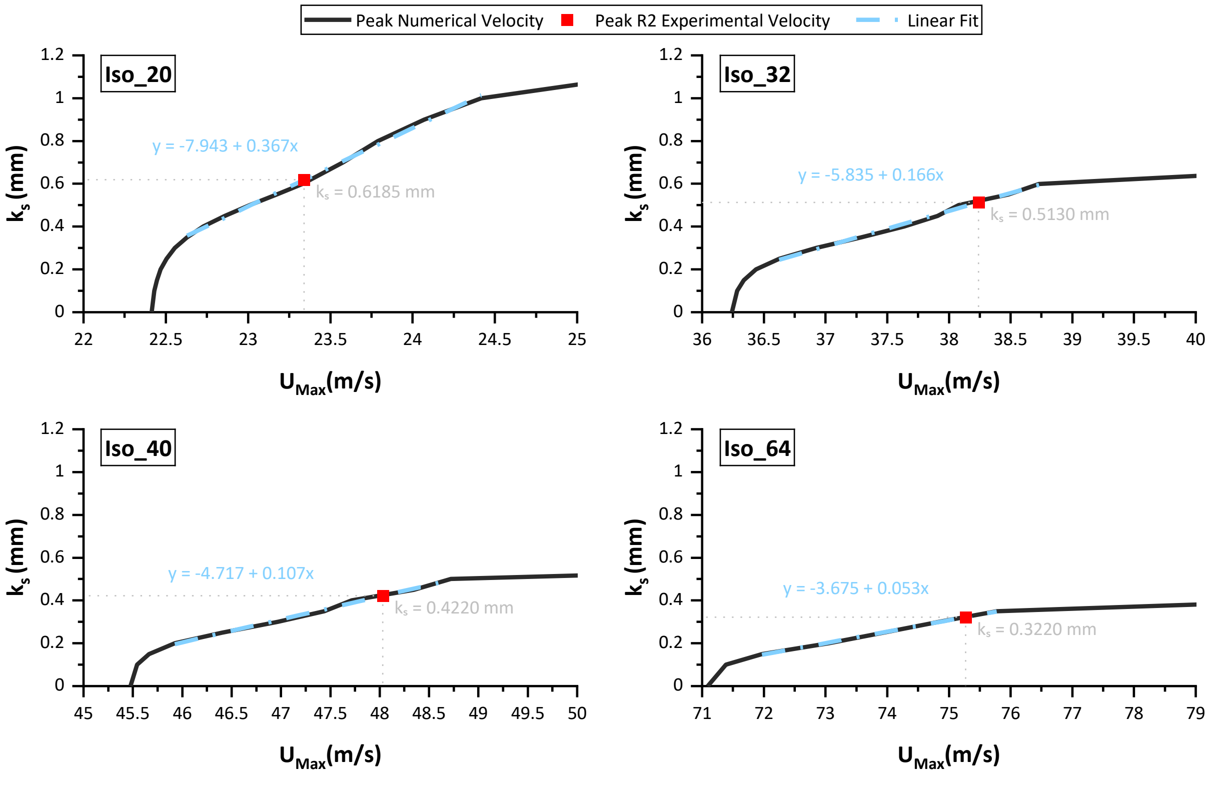

Figure 6.16 - Determination of the appropriate k_s value for each condition via application of a linear best-fit approach.

The k_s values extracted from Figure 6.16 demonstrate that as the bulk flow increases, progressively smaller values are required to replicate the roughness effects observed experimentally, similar to the behaviour seen with the GR-C correlation in Section 6.4.1.1. However, unlike the GR-C correlation, each k_s value in this section corresponds to a significantly different k_s^+ value, addressing the limitations of the GR-C approach. Specifically, as shown in Figure 6.17, while k_s values decrease with increasing bulk flow, the associated k_s^+ value increases. This representation is more appropriate since, as previously discussed in Section 6.4.1.1, for a fixed roughness height the relative contribution of roughness to the boundary layer increases with bulk flow.

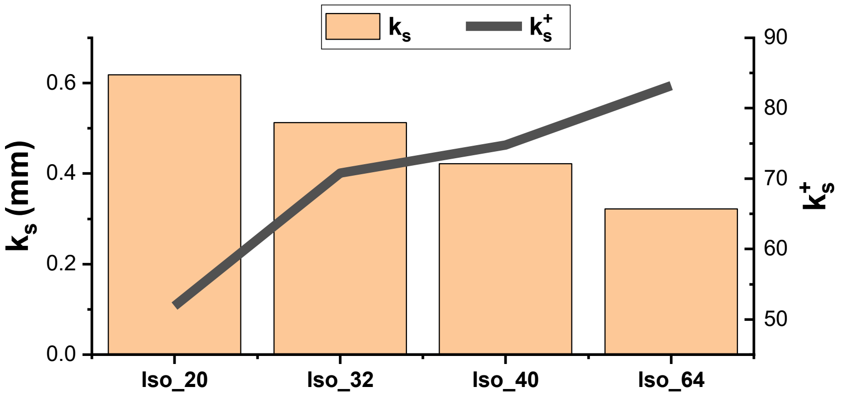

Figure 6.17 - Changes in k_s and k_s^+ with increasing bulk flow velocity.

To derive a generalised correlation from the k_s values calculated for specific bulk flows, k_s values from Figure 6.16 were plotted against bulk flow velocities. Both a linear and a second-order polynomial regression were applied, as illustrated in Figure 6.18, generating equations with k_s values as the dependent variable (y) and bulk flow velocity as the independent variable (x). This formulation enables the determination of a corresponding k_s value for any given bulk flow velocity.

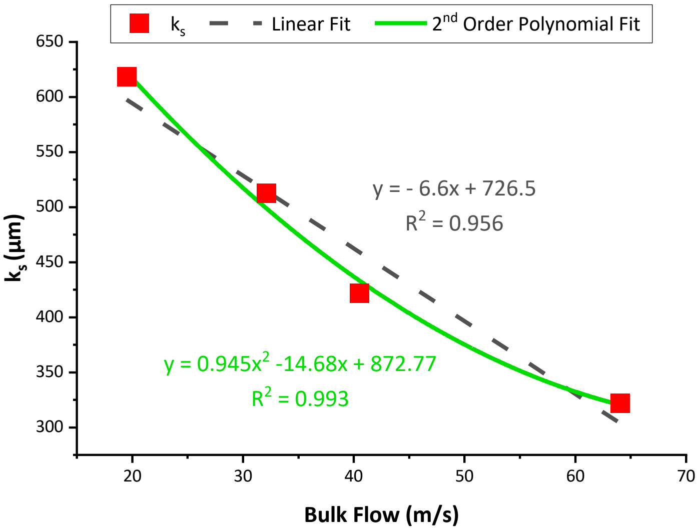

Figure 6.18 *- Linear and second-order polynomial regression applied to k_s values extracted from the parametric study.*

Figure 6.18 demonstrates that while both trend lines provide a reasonable fit, the second-order polynomial exhibits improved agreement. Moreover, the negative slope of the linear fit suggests that beyond a certain bulk flow velocity, a negative k_s value would be required, which is physically unrealistic. Conversely, the quadratic function naturally accounts for a tapering effect in k_s at higher bulk flows, aligning with the trend of diminishing sensitivity to roughness effects for $k_s^+ > 90$ observed in Figure 6.15. However, beyond the vertex of the polynomial, the function predicts increasing k_s values, which contradicts the observed roughness saturation effects. Based on these findings, it is evident that for this correlation to be broadly applicable, it must be formulated as a piecewise function, utilising the quadratic correlation for bulk flows ≤ the vertex and transitioning to a fixed linear value beyond this point. Additionally, to incorporate measured roughness effects, the roughness parameter would need to be integrated into the constant term coefficients. The final correlation is presented in Equation [6.1].

$$k_s(x) = \begin{cases} 0.0945x^2 - 14.68x + 41.17Ra, & x \leq 77 \\ 41.17Ra - 570 \quad , & x > 77 \end{cases} \qquad [6.1]$$

Where:

x = Bulk flow velocity (m/s).

Ra and k_s are in µm.

6.4.1.2.1. RANS Results

Following the development of the novel k_s correlation incorporating bulk flow sensitivity in Section 6.4.1.2, the bulk flows for the Iso 20, 32, 40 and 64 cases were input into Equation [6.1] together with the measured Ra value of the R2 insert. The corresponding k_s values were then implemented in RANS simulations for each condition. The resulting velocity profiles were systematically evaluated against reference smooth simulations as well as experimental smooth and rough velocity profiles, as presented in Figure 6.19.

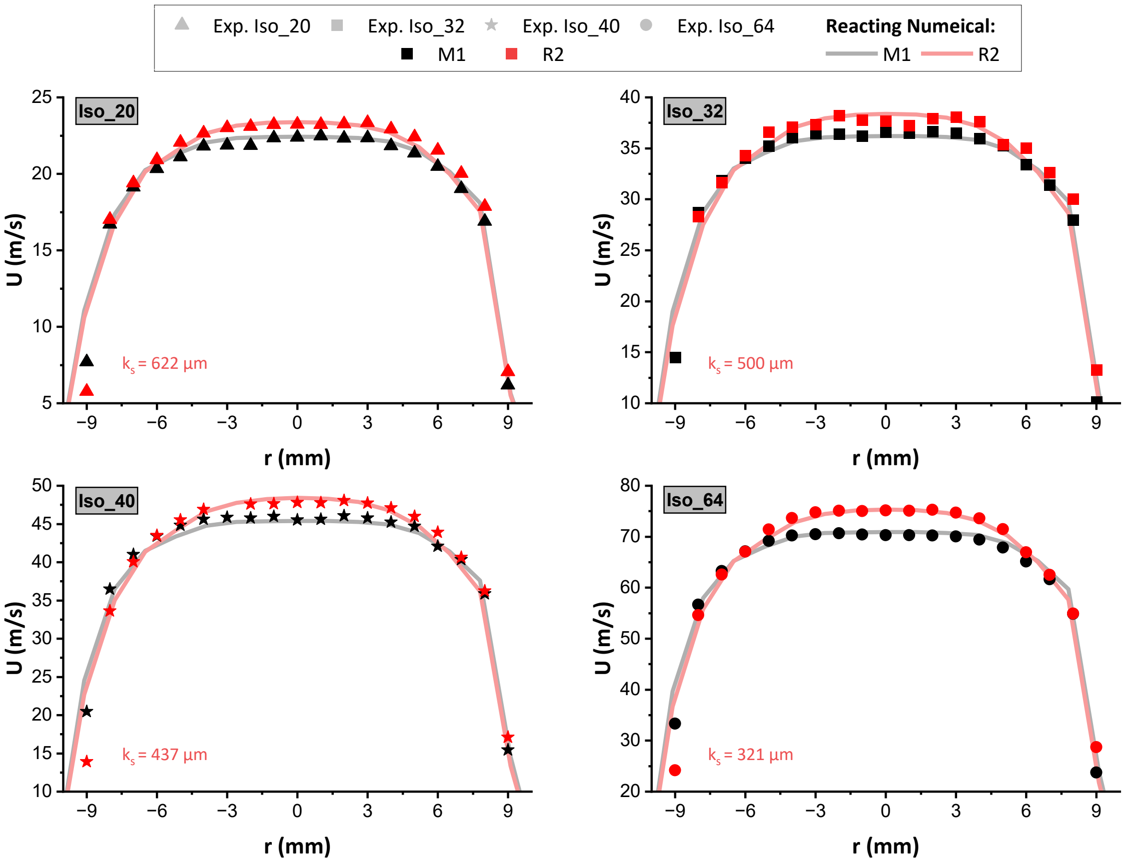

Figure 6.19 - Comparison of experimental and numerical (RANS) smooth and rough axial velocity profiles 2 mm above the nozzle exit. Numerical profiles were generated using the correlation from Section 6.4.1.2, with k_s values listed in each plot. Squares in legend indicating the colour code.

From a visual analysis, it is evident that when employing the k_s values calculated via Equation [6.1], a strong correlation with the experimental rough-wall data is achieved across all bulk flow conditions, as illustrated in Figure 6.19. While a quantitative assessment of the smooth numerical data against the reference experimental values was previously conducted in Section 6.3.1.2, demonstrating excellent agreement, a similar evaluation for the rough cases yields comparable conclusions. On average, the deviation between peak experimental and numerical rough-wall velocity data was approximately 0.5%, with velocity profiles exhibiting an average deviation of ~2.4% across the entire profile and only ~0.4% within the core flow region (−5 mm ≤ r ≤ 5 mm).

6.4.1.2.2. DES Results

As previously covered in Section 6.3.1.2, due to the computational demand of DES, the effectiveness of the novel roughness correlation was only assessed on the Iso_20 and Iso_64 cases, which represent the lower and upper bounds, respectively, of the experimentally investigated flow rates. For the rough cases, the same k_s values utilised in Section 6.4.1.2.1 (calculated via Equation [6.1]) were applied. Both numerical results and the respective experimental counterparts are presented in Figure 6.20.

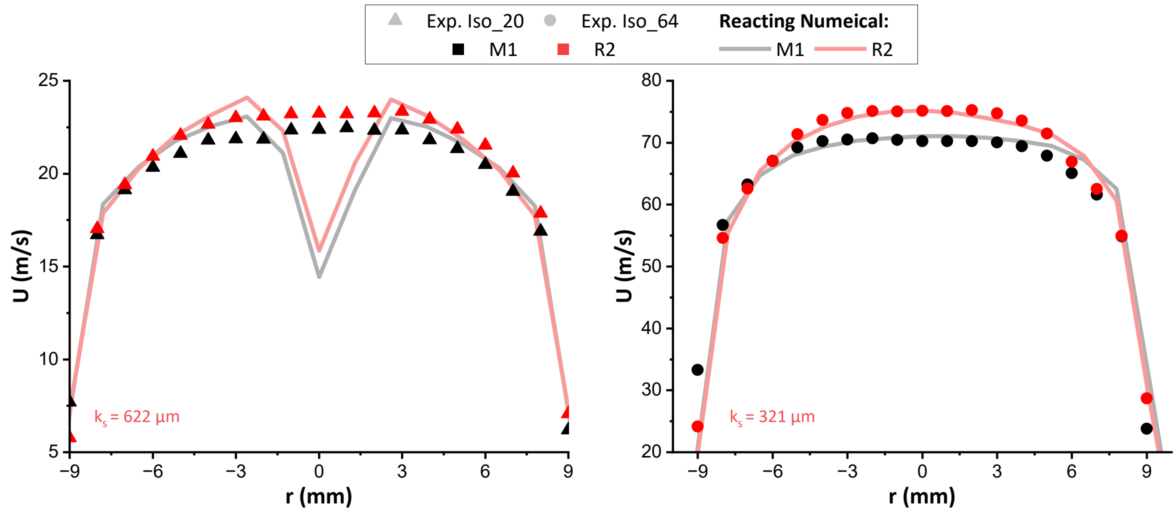

Figure 6.20 - Comparison of experimental and numerical (DES) smooth and rough axial velocity profiles 2 mm above the nozzle exit. Novel correlation developed in Section 6.4.1.2 used to generate the numerical profiles with specific k_s values utilised for each condition. Squares in legend indicating the colour code

As illustrated in Figure 6.20, the effects of surface roughness were successfully captured in both cases. In the Iso_64 scenario, a high level of agreement with the experimental data was achieved, consistent with observations made for the RANS simulations. However, in the Iso_20 case, a pronounced overrepresentation of bluff body effects on the centreline flow was evident for both smooth and rough configurations. Given no reverse flow was detected, this discrepancy is likely attributable to similar phenomena identified in Chapter 4, where DES simulations were shown to produce larger, and frequently overestimated, recirculation zones [261,262].

Despite these discrepancies, the average deviation between the peak experimental and numerical rough-wall velocity data was approximately 3% for the Iso_20 case and around 0.2% for the Iso_64 case. The greater discrepancy observed in the Iso_20 case can be attributed to the displacement of the peak velocities away from the burner centreline. Across the entire radial velocity profile, average deviations of approximately 2.7% and 0.88% were recorded for the Iso_20 and Iso_64 cases, respectively, with corresponding deviations within the core flow region (−5 mm ≤ r ≤ 5 mm) of approximately 4.2% and 0.14%.

6.4.1.2.3. Limitations

It is evident that while this novel correlation, visualised in Figure 6.21, is well-suited for bulk flows between 20 and 64 m/s, as these values were used in its derivation, its applicability at higher bulk flow velocities, particularly beyond 77 m/s, is likely to be more approximate. This is especially relevant given that, in the fully rough regime, sensitivity to k_s has been shown to diminish significantly.

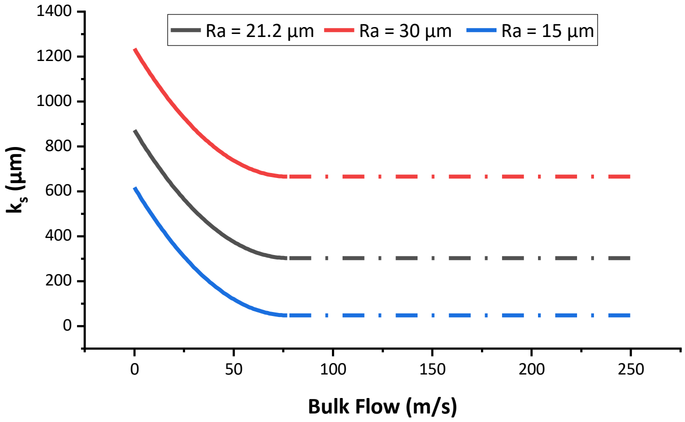

Figure 6.21 *- Novel correlation for a range of bulk flows and different Ra values. Solid and broken line indicating quadratic and linear correlations respectively.*

Furthermore, Figure 6.21 demonstrates that with the incorporation of measured roughness effects, k_s values remain proportional to the measured roughness height. However, for roughness heights below 14 µm, the correlation begins to suggest k_s values ≤ 0, which is not physically realistic. While this bulk-flow-based roughness sensitivity curve appears to be representative for the Ra value of ~20 µm utilised for the collection of the reference experimental data, its validity for other surface heights remains uncertain. This is particularly important because, for lower Ra values, a broader range of bulk flows will fall within the transitionally rough regime, where higher sensitivity to k_s has been observed, whereas for higher Ra values, bulk flows will more readily enter the fully rough regime, where sensitivity to k_s becomes less significant.

Geometric dependence remains a significant factor. When applying the novel correlation to the GSB, roughness simulations of which were already conducted in Chapter 4, k_s values an order of magnitude lower than those identified in the earlier analyses were for instance proposed. This suggests that, for swirling flows, the proposed correlation is unlikely to yield satisfactory results.

Finally, its applicability to reacting flows remains uncertain and warrants further investigation. This latter point will be addressed in Section 6.4.2, where the effectiveness of the novel k_s correlation will be evaluated in the context of reacting flow simulations.

6.4.2. Reacting Validation

Building on the efficacy demonstrated by the novel correlation when applied to isothermal PJB cases, its applicability to reacting flow simulations was further investigated using both RANS and DES approaches. For the rough-wall configurations, k_s values were calculated using Equation [6.1], as derived in Section 6.4.1.2. The specific k_s values utilised for each condition are summarised in Table 6.8.

__Table 6.8__ - k_s values utilised in the reacting simulations calculated using equation [6.1]

Thermal Power (kW)	ϕ	k_s (µm)
25	0.9	478
	0.7	423
	0.5	353
20	0.9	536
	0.7	489
	0.5	410
15	0.9	606
	0.7	565
	0.5	495

6.4.2.1. RANS Results

6.4.2.1.1. Flow Characterisation

As noted at the outset of Chapter 6, experimental flow-field measurements were conducted exclusively under isothermal conditions. Consequently, while a direct comparison between the experimental and numerically simulated (reacting) velocity profiles is not strictly representative, the impact of thermal effects within the CFD simulations is expected to be limited, particularly at higher bulk flow rates. This is primarily due to the fact that the experimental data were acquired only 2 mm downstream of the nozzle exit and, since the burner operates in a jetting regime, the near-nozzle velocity field is predominantly governed by inertial rather than thermally induced effects.

A comparison of the experimental isothermal and numerical reacting data will therefore still allow for a meaningful assessment of whether the general flow trends observed experimentally are also reproduced numerically. In this context, Figure 6.22 presents the axial velocity profiles for the various reacting smooth and rough-wall simulations, along with a comparison against the corresponding isothermal experimental data.

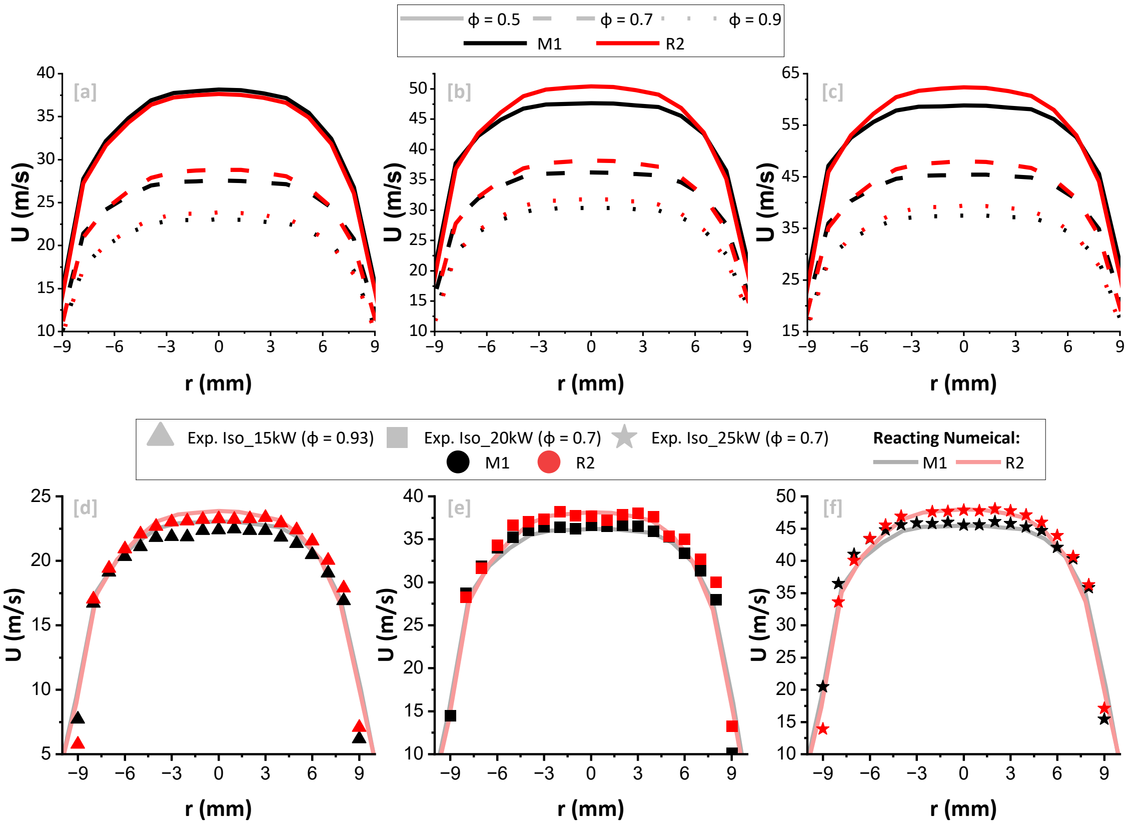

***Figure 6.22** – Comparison of reacting numerical (RANS) smooth and rough axial velocity profiles 2 mm above the nozzle exit with φ = 0.5 – 0.7 – 0.9 at thermal powers of 15kW [a], 20kW [b] and 25 kW [c]. Comparison of isothermal experimental and reacting numerical (RANS) smooth and rough axial velocity profiles 2 mm above the nozzle exit [d, e, f]. Circles in legend indicating the colour code*

From Figure 6.22 [a-c], it is evident that, as anticipated, peak axial velocities increase with rising thermal power and reducing ϕ. Moreover, with the exception of the 15 kW case at ϕ = 0.5, all rough-wall simulations exhibit higher peak centreline velocities compared to their smooth-wall counterparts, effectively replicating the trends observed experimentally. Consistent with experimental findings, the mean bulk flow velocities across all numerical cases varied by only ~1.6%, further demonstrating a redistribution of the velocity profiles caused by increased roughness.

When comparing the reacting numerical velocity profiles to the corresponding experimental isothermal data (Figure 6.22 [d-f]), a similarly strong agreement is evident. As discussed at the onset of Section 6.4.2.1.1, an exact match is not expected due to differences in thermal boundary conditions; however, particularly at the two higher thermal powers, the numerical predictions show very good agreement with the experimental data. Average deviations across the full radial velocity profiles were approximately 7.5%, 3.0%, and 1.3% for the 15 kW, 20 kW, and 25 kW cases, respectively. This trend of decreasing deviation with increasing thermal power is attributed to stronger inertial forces and lower equivalence ratios, which act to diminish the influence of thermal effects.

A more detailed assessment of roughness induced changes in peak axial velocities is presented in Figure 6.23 were both numerical (reacting) and experimental (isothermal) values are normalised against their respective smooth-walled cases.

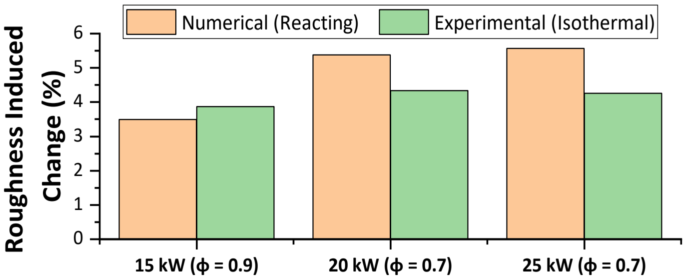

Figure 6.23 *- Roughness induced changes in experimental (isothermal) and numerical (reacting) peak axial velocity 2 mm downstream of the nozzle exit. Values have been normalised relative to the corresponding smooth-wall cases.*

Figure 6.23 further demonstrates the strong agreement between experimental and numerical results, with all reacting numerical cases reproducing the experimentally observed trend of increasing peak axial velocity with greater surface roughness. Notably, the 15 kW case exhibits a minimal deviation of ~0.4%, whereas larger discrepancies are observed at higher thermal powers. Nevertheless, given the close resemblance in the overall velocity profile shapes between the isothermal experimental and reacting numerical cases and, considering the inherent limitations in making a direct comparison due to differing thermal conditions, it can be concluded that the newly derived correlation performs well in capturing roughness-induced flow field modifications under reacting conditions.

6.4.2.1.2. Flame Behaviour

The ability of the novel correlation to accurately capture changes in flame behaviour was assessed utilising the experimentally collected Abel-transformed OH* chemiluminescence data. Figure 6.24 presents a comparison between this experimental dataset and the corresponding numerical OH* predictions for both smooth and rough-wall configurations.

From Figure 6.24, the numerical predictions do not precisely replicate the experimental observations. In particular, the simulated flames are consistently longer than those observed experimentally. This discrepancy is attributed to the specifics of the reaction mechanism employed, as well as the influence of the Lewis number of hydrogen being less than unity. Furthermore, the spatial distribution of OH* intensity within the flame also differs markedly between the numerical and experimental results. This latter discrepancy is expected and arises because, whilst the numerical data represents a direct cross-section through the flame, the Abel-transformed data represents a reconstructed cross-section based on an axisymmetric assumption applied to line-of-sight integrated measurements [278].

Nevertheless, key trends observed experimentally are well captured in the simulations. The numerically predicted flame lengths increase with both rising thermal power and decreasing ϕ. Additionally, roughness-induced effects are also reflected in the numerical data, with all rough-wall simulations exhibiting some degree of axial flame shortening relative to their smooth-wall counterparts.

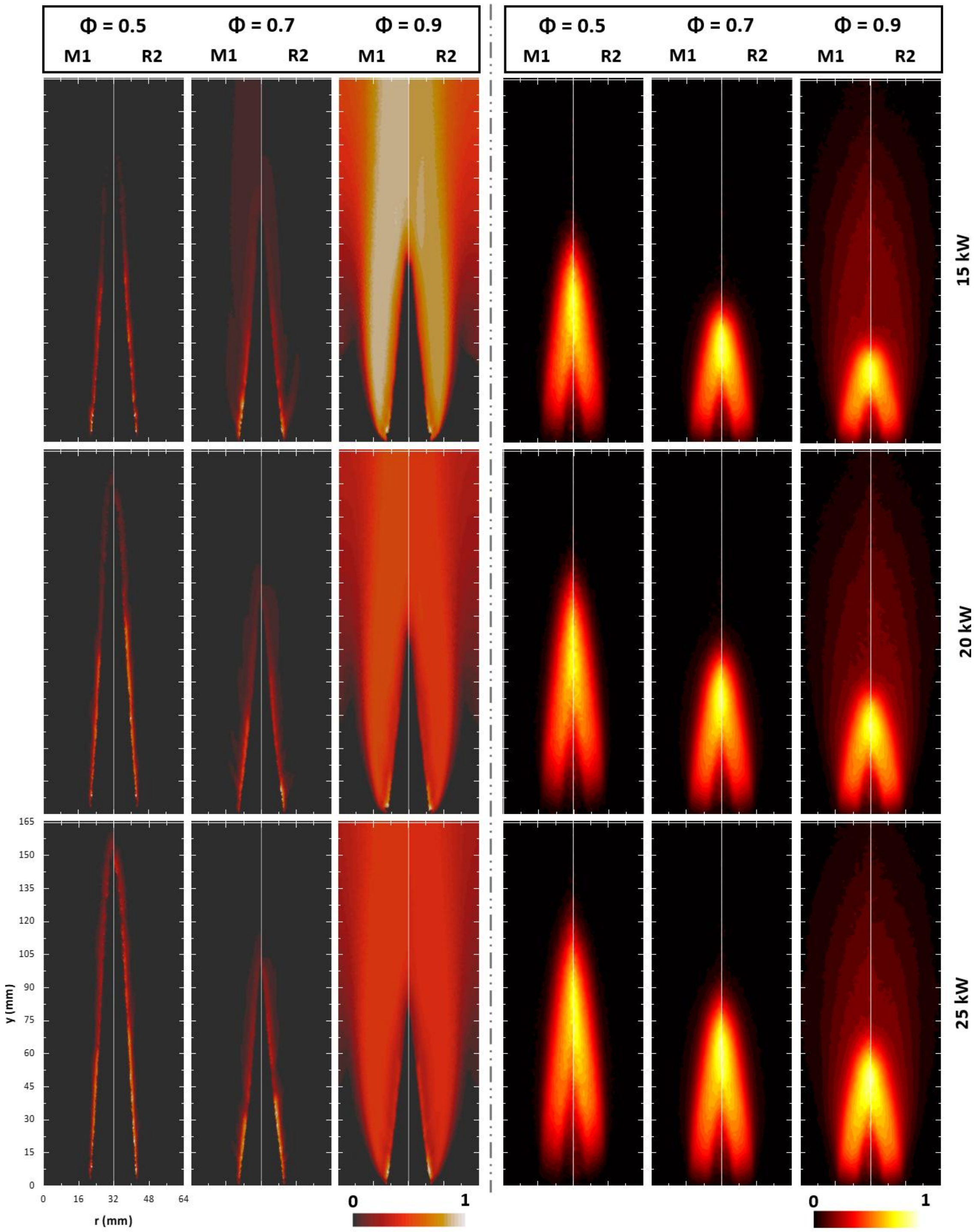

***Figure 6.24** – Numerical [left] and Abel transformed experimental [right] OH* chemiluminescence images for 15 kW [top], 20 kW [middle] and 25 kW [bottom] thermal powers over a range of φ. Colormap normalised to maximum OH* intensity in each half image. M1 results shown on the left and R2 results shown on the right for each condition.*

To enable a more statistical evaluation of the numerical simulation accuracy, flame centroid locations were determined for both the experimental and numerical cases. In the experimental data, the raw OH* chemiluminescence datasets displayed a broad, continuous triangular profile, allowing for a stable and representative centroid calculation. Conversely, the OH* fields predicted by the simulations were highly localised and filamentary, making it difficult to obtain consistent and physically meaningful centroid values due to their sensitivity to local intensity variations.

To overcome this limitation, the flame centroid in the numerical cases was instead calculated based on the spatial distribution of unreacted fuel within the combustion chamber, restricted to the flame region. As illustrated in Figure 6.25, the region containing unburned fuel closely corresponds to the core of the reacting zone, providing a reliable and physically appropriate proxy for flame location. This method offers a more consistent and robust basis for comparison with experimental results, while also reducing the influence of numerical noise and mesh resolution effects.

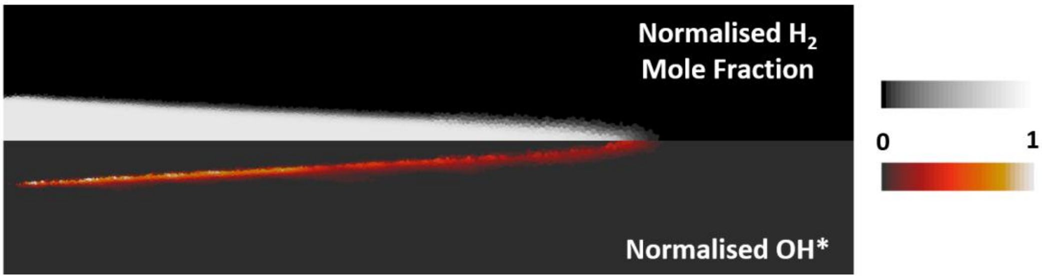

Figure 6.25 - *Comparison of normalised H2 mole and OH* mole fractions.*

In order to isolate the discrepancies in magnitude between experimental and numerical data, centroid variations were normalised both relative to the respective ϕ = 0.9 cases and based on roughness. The resulting trends achieved utilising both methods are shown in Figure 6.26 and Figure 6.27 respectively.

From Figure 6.26, it is apparent that, although the overall trend of axial flame lengthening with decreasing ϕ is well represented by the numerical simulations, consistent with the visual observations made in Figure 6.24, the numerical cases tend to overpredict the extent of this lengthening. This overprediction becoming increasingly pronounced with rising bulk flow, corresponding to higher thermal power and lower ϕ. The 15 kW cases exhibit only a minor average deviation of ~2.2% relative to the experimental results, whereas the 20 kW and 25 kW cases demonstrate considerably larger average deviations of ~21.3% and ~41.3%, respectively. More specifically, for the 20 kW cases, the ϕ = 0.7 condition yielded an average deviation of ~3.8% compared to the experimental counterparts; however, this deviation increased markedly to ~38.8% for the ϕ = 0.5 condition.

Similar trends were observed for the 25 kW cases, although with even greater deviations. These findings indicate that, as widely reported in the literature [279,280], modelling lean hydrogen flames remains highly challenging due to pronounced thermodiffusive effects. In the present study, this manifests as an overprediction of flame lengths at increasing thermal powers and decreasing ϕ.

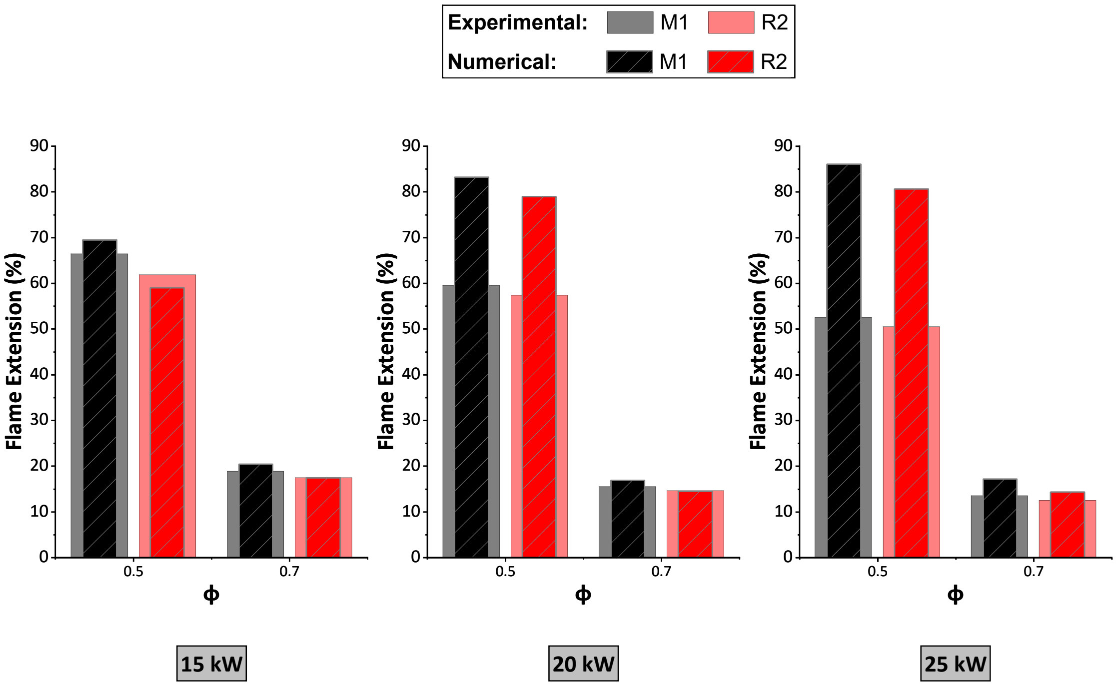

Figure 6.26 *- Changes in experimental and numerical (RANS) flame centroid location. Values have been normalised relative to the corresponding φ = 0.9 cases.*

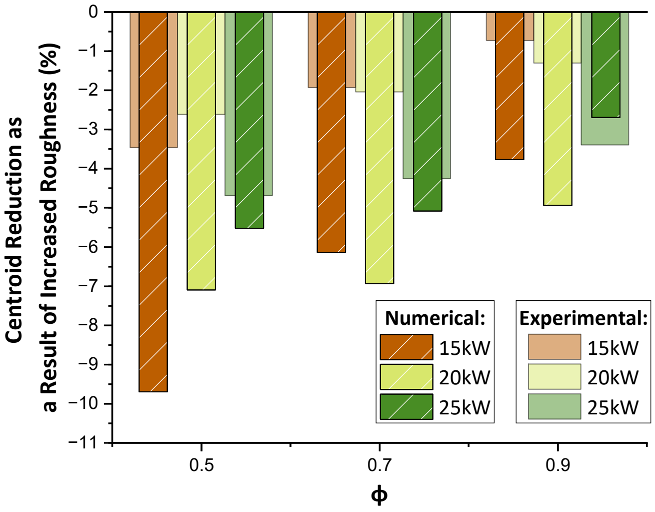

Figure 6.27 *- Reduction in the axial coordinate of numerical and experimental centroids as a function of roughness. Values have been normalised relative to the corresponding smooth-wall cases.*

When considering the roughness-induced flame shortening presented in Figure 6.27, it is evident that the experimental trend of axial shortening with increasing surface roughness is also captured by the numerical simulations. However, unlike the findings from the isothermal simulations discussed in Section 6.4.1.2.1, the numerical data do not provide an exact fit. Rather, the simulations tend to overpredict the extent of axial shortening, particularly at lower thermal powers. Specifically, thermal power average deviations of ~19.2%, ~230%, and ~271% were observed for the 25 kW, 20 kW, and 15 kW cases, respectively. It is important to note that, due to the nature of the correlation employed, the lower thermal power cases were associated with higher k_s values. Notably, the 15 kW case at $\phi = 0.5$, which utilised the highest k_s value, exhibited the greatest deviation from the corresponding experimental data. Whilst it can therefore be inferred that the higher k_s values at lower thermal powers (i.e., lower bulk flow velocities) contributed to the overestimation of roughness induced flame shortening, the absence of a direct correlation between this numerical offset and the variation in k_s values employed across the various conditions suggests that additional underlaying mechanisms are involved.

6.4.2.2. DES Results

As previously covered in Section 6.3.2.2, due to the computational demand of DES, the effectiveness of the novel roughness correlation was only assessed on the 25 kW cases. Similar analyses and methodologies employed for the reacting RANS results are applied in Sections 6.4.2.2.1 - 6.4.2.2.2.

6.4.2.2.1. Flow Characterisation

Although the experimental flow-field measurements were conducted exclusively under isothermal conditions, the reacting RANS results presented in Section 6.4.2.1.1 have demonstrated that reasonable agreement with the experimental data can nonetheless be achieved. Accordingly, Figure 6.28 presents the axial velocity profiles from the reacting DES simulations, extracted 2 mm downstream of the nozzle exit, alongside comparisons with the reference isothermal experimental data.

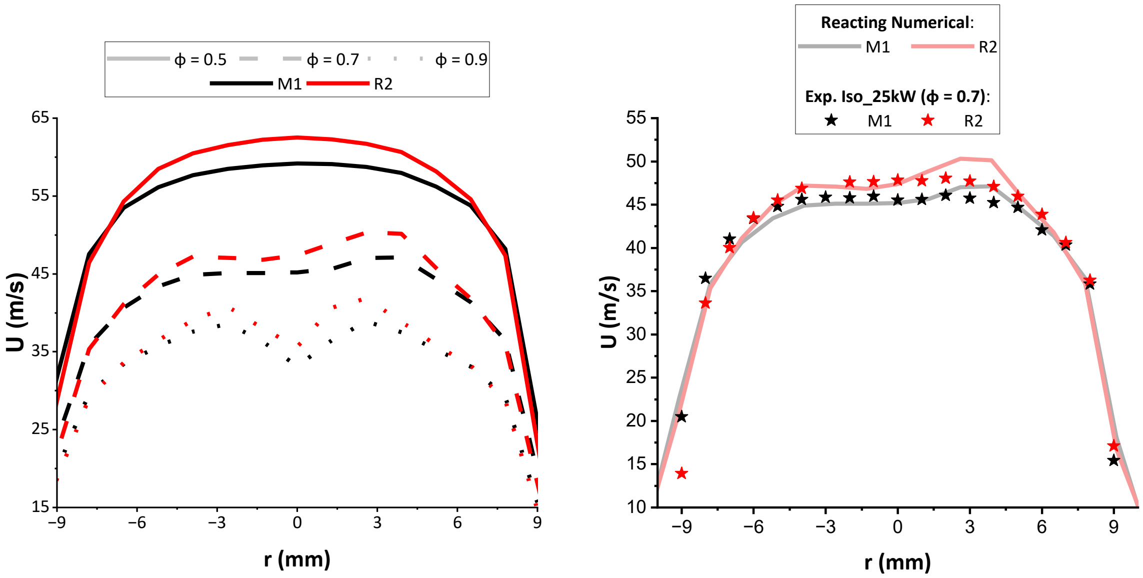

Figure 6.28 *- Comparison of reacting DES smooth and rough axial velocity profiles at 25 kW (φ = 0.5 and 0.9), 2 mm above the nozzle exit [left], and corresponding isothermal experimental vs. reacting DES profiles [right].*

From Figure 6.28, peak axial velocities increase with rising thermal power and ϕ, as expected. Moreover, all rough-wall simulations exhibit higher peak centreline velocities compared to their smooth-wall counterparts, effectively replicating the trends observed experimentally. It is also evident that, as bulk flow rates decrease, both smooth- and rough-wall velocity profiles increasingly diverge from the characteristic parabolic shape, previously observed experimentally and in the RANS simulations, and instead assume a more pronounced M-shaped profile. This deviation is attributed to the DES model overestimating the influence of the central bluff body [261,262], a behaviour previously identified in both Chapter 4 and in the isothermal simulations presented earlier in Chapter 6.

In addition, asymmetry is particularly noticeable in the ϕ = 0.7 case. This may be attributed to initial instabilities at the start of the simulation that were not fully eliminated before time averaging, as well as other factors such as limited grid resolution. Nevertheless, when comparing the DES axial velocity profiles with the corresponding RANS and isothermal experimental core-flow data (r ± 5 mm), the deviations remain within low single-digit percentages across all cases, ranging from approximately 0.4% for ϕ = 0.5 to ~3.7% for ϕ = 0.9.

A more statistical evaluation of roughness-induced axial velocity redistribution is conducted by examining percentage changes in peak velocities between smooth- and rough-wall DES cases. Comparisons are also made with the corresponding reacting RANS simulations and, where available, with isothermal experimental data (ϕ = 0.7). Collection of experimental data for all numerical condition validation not being possible as the experimental data were collected prior to the numerical work within a constrained timeframe. These results are presented in Figure 6.29.

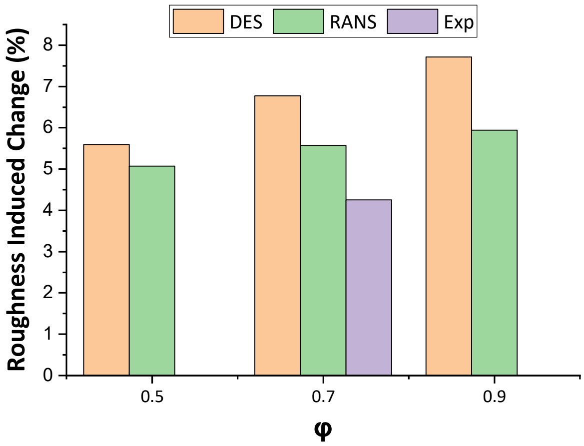

Figure 6.29 *- Roughness induced changes in experimental (isothermal) – equivalent total mass flow of air to 25 kW at φ = 0.7 - and numerical (reacting) – both RANS and DES at 25 kW - peak axial velocity 2 mm downstream of the nozzle exit. Values have been normalised relative to the corresponding smooth-wall cases.*

Figure 6.29 once again highlights how the DES approach successfully replicates the experimentally observed trends; experimental, RANS and DES changes all being within the same approximate order of magnitude. However, the data also suggest a tendency for DES to overpredict this effect at lower bulk flow rates (i.e., higher ϕ), in contrast to the trend observed in the reacting RANS results. This overprediction is primarily attributed to the increasingly pronounced M-shaped velocity profiles at reduced flow rates, as seen in Figure 6.28. In these cases, the peak axial velocities shift away from the centreline to positions approximately ±3 mm off-axis, thereby artificially amplifying the apparent impact of surface roughness.

6.4.2.2.2. Flame Behaviour

From the RANS assessment of changes in flame behaviour performed in Section 6.4.2.1.2, assessment of roughness induced axial shortening was performed by computing the flame centroid location for each case; the numerical cases being calculated based on the spatial distribution of unreacted fuel within the combustion chamber, restricted to the flame region. To isolate discrepancies in magnitude between experimental and numerical data, centroid variations were normalised both relative to the $\phi = 0.9$ case and based on roughness as already done for the reacting RANS cases. The resulting DES trends achieved utilising both methods are shown in Figure 6.30 and Figure 6.31 respectively.

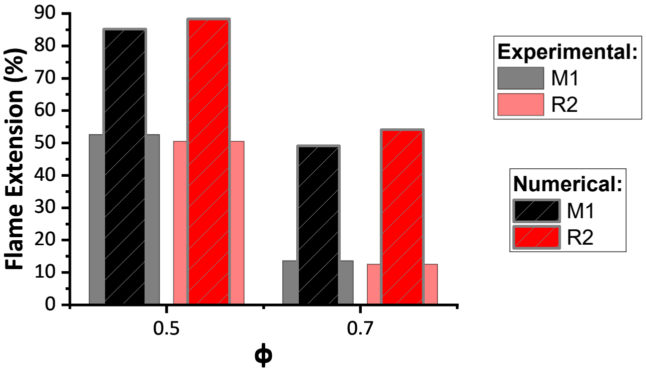

Figure 6.30 *- Changes in experimental and numerical (DES) flame centroid location. Values have been normalised relative to the corresponding $\varphi = 0.9$ cases.*

As shown in Figure 6.30, DES also captures the expected trend of flame lengthening with decreasing ϕ. However, when compared with the RANS results, a significant deviation emerges. While the DES and RANS cases at $\phi = 0.5$ yield similar flame lengths (within ~1%), the DES simulation at $\phi = 0.7$ overpredicts the axial flame extension by approximately 65%. Additionally, DES predicts greater relative flame lengths in rough-wall cases compared to the respective smooth-wall ones. This is inverse to the experimentally observed and RANS-reproduced trend of roughness-induced flame shortening at higher bulk flows. However, this does not necessarily indicate an absence of roughness effects in DES; rather, it suggests that the extent of flame shortening is less pronounced than observed experimentally, as illustrated more clearly in Figure 6.31.

Figure 6.31 shows that for the $\phi = 0.9$ case, DES captures a clear and consistent roughness-induced offset, with only a ~10% deviation from the corresponding RANS prediction. In contrast, for $\phi = 0.5$ and 0.7, the roughness-induced differences are minimal, within ±0.9% relative to the smooth-wall cases. Considering that both experimental and RANS results exhibited significantly larger offsets and noting that an inverse trend was observed for $\phi = 0.7$, it can be concluded that for these two conditions, DES fails to accurately capture the impact of surface roughness on flame structure.

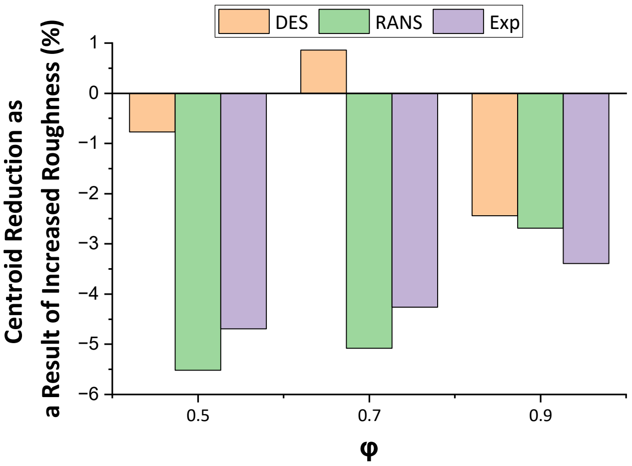

Figure 6.31 *- Reduction in the axial coordinate of 25 kW numerical and experimental centroids as a function of roughness. Values have been normalised relative to the corresponding smooth-wall cases.*

Overall, while roughness effects were successfully captured in the flow field, their replication in the flame composition proved limited. This is likely due to the more complex turbulence–chemistry interactions inherent to higher-fidelity solvers such as DES, where wall-function-based roughness models do not necessarily translate into corresponding chemical response, particularly at lower equivalence ratios, where the thermodiffusive effects associated with hydrogen become increasingly significant [73,74].

6.4.3. Changes in k_s^+

An analysis of changes in k_s^+ values between reacting and isothermal cases (the latter initially presented in Figure 6.17) revealed that, under equivalent conditions, the reacting cases exhibited an average reduction of approximately 21.6% in k_s^+ compared to the corresponding isothermal air cases with equivalent total mass flow. As demonstrated in Equation [6.2], this consistent reduction across all cases can be attributed to a decrease in fluid density resulting from the introduction of hydrogen.

$$k_s^+ = \frac{k_s\, u^*\rho}{\mu} \qquad [6.2]$$

where:

- no change between reacting and isothermal.
- minor change.
- major change.

Under equivalent conditions, k_s remains constant, and u^* experiences only minor variation (~1.7%), as bulk flow velocities are maintained between the isothermal and reacting simulations. In contrast, both density (ρ) and dynamic viscosity (μ) are affected by the presence of hydrogen. Specifically, the average reduction in density is around 22%, while dynamic viscosity decreases by approximately 1.4%. Based on the observations presented earlier in Chapter 6, as well as those discussed in Chapter 4, it can therefore be said that, although k_s^+ values are lower in reacting cases, owing to reduced density, for a given k_s value, the roughness effects under reacting conditions may in fact be more pronounced than those observed in isothermal air cases with equivalent total mass flow. While this may seem counterintuitive, the apparent increase in roughness effects can be explained by the increased sensitivity of reacting flows to wall-induced turbulence and boundary layer disturbances. In particular, flame dynamics and turbulence-chemistry interactions amplify the influence of roughness beyond what would be expected based on k_s^+ alone.

This highlights that while k_s^+ remains a useful parameter in assessing the roughness regime, its interpretation must be revisited in the context of reacting flows. This is particularly relevant for GT applications, where combustor pressures are elevated. Under such conditions, both fuel density variations and pressure-induced density increases influence the resulting k_s^+ values. Consequently, attempting to match k_s^+ across different fuels or operating pressures may yield physically inconsistent results, potentially undermining the validity of comparative analyses.

6.5. Summary

A range of approaches was investigated to numerically replicate the experimentally observed roughness effects, first introduced in Chapter 5, under both isothermal and reacting conditions, using low-y^+ meshes in RANS and DES frameworks. The correlation originally derived in Chapter 4 was first applied but consistently overpredicted roughness effects. Building on the same methodological framework, a novel roughness correlation was developed that incorporated both bulk flow and measured surface roughness as parameters.

Application of the new correlation under isothermal conditions demonstrated:

- **RANS** simulations exhibited low single-digit percentage deviations from experimental data, validating the correlation’s effectiveness while offering computational efficiency.
- **DES** simulations further improved accuracy in the Iso_64 case, although reduced performance was observed in the Iso_20 case due to overprediction of bluff body effects on the flow field.
- Given the computational cost of DES, RANS is likely to remain the preferred option for industrial applications where a trade-off between accuracy and resource usage is needed

Extending the correlation to reacting conditions, RANS results again showed good agreement with experimental observations, capturing key roughness-induced effects on the flow field and flame structure:

- Axial velocity profiles at the nozzle exit matched isothermal experimental trends of increasing peak velocity with surface roughness.
- Predicted flame shapes reproduced the observed axial lengthening with increasing equivalence ratio, though magnitudes were overpredicted at higher thermal powers.
- Roughness-induced flame shortening was captured but generally overestimated, particularly at lower thermal powers.

By contrast, DES performance was less satisfactory for reacting flames, with persistent overprediction of bluff-body effects and limited capability in reproducing roughness-driven changes in flame shape, especially under lean conditions.

Despite its strengths, the correlation’s applicability is subject to important limitations:

- **Geometry dependence**: poor performance was observed when applied to different burner designs (e.g., GSB cases from Chapter 4).
- **Range limitations**: extrapolation beyond validated roughness heights or flow regimes should be treated as a first-order estimate only.

- **Reactivity**: discrepancies in flame shape predictions raise uncertainty as to whether errors stem from the correlation itself or from the chemical mechanism employed.
- **Pressure scaling**: reacting cases frequently overpredicted roughness effects at a given k_s, despite density-driven reductions in k_s^+. This underlines the need for high-pressure validation, where increased density will substantially raise k_s^+ compared with atmospheric tests.

In summary, the novel roughness correlation has demonstrated strong capability, particularly in RANS simulations, to replicate experimental roughness-induced trends in both isothermal and reacting flows. While DES highlighted model limitations, the correlation offers a practical and effective tool for industry, provided its current constraints are recognised.

Chapter 7. Surface Roughness Effects on the Performance and Operability of a Jet-in-Crossflow Hydrogen Burner

7.1. Research Scope

Building on the preliminary numerical assessment of roughness effects on jet-in-crossflow burners which indicated a possible inversion of roughness-related trends, Chapter 7 quantifies the influence of surface roughness on an industry-relevant jet-in-crossflow burner operating under hydrogen-fired conditions at atmospheric pressure. Flame composition and stability limit investigations were undertaken for thermal powers of 15, 17.5 and 20 kW over a range of equivalence ratios ($0.6 \le \phi \le 2.0$) (~15400 - 45700 Reynolds Number). Modifications were made to the PJB maintaining the ability to investigate different surface finishes whilst changing the fuel delivery to a jet-in-crossflow configuration (JICF). The same two inserts utilised in Chapter 5 replicating both conventionally machined and “raw” unprocessed AM components were employed. The latter insert designed to replicate the surface characteristics typically produced by SLM although it was not manufactured using additive techniques. Building on the previous PJB findings, this study extends the analysis by examining how both surface finish and fuel delivery modifications influence burner operability, using high-speed OH* chemiluminescence (CL).

7.2. Initial Numerical Investigation

Following the successful capture of roughness effects on the PJB both in isothermal air and reacting physics domains in Chapter 6, exploratory non-reacting RANS simulations were conducted on a JICF configuration more representative of industrial burner setups.

As detailed in Section 3.2.1.2, critical dimensions were carried over from the PJB. The primary modification involving the replacement of the counterflow premixing arrangement with a centrally positioned fuel lance, which injects fuel radially into the airstream. As illustrated in Figure 7.1, the shift from a fully premixed to a JICF configuration leads to a significantly altered fuel distribution. Firstly, it should be noted that for the PJB, given the high diffusivity of H_2 and the more than 500 mm distance between the sampling plane location and the point of injection, the stratification observed at the nozzle exit is unexpected even though the ϕ variation remained within approximately ±2%. This behaviour is likely a consequence of the simplified non-reacting nature of the simulation, together with inaccuracies in the modelling of H_2 diffusivity, as discussed in Section 6.4.2.1.2. Nevertheless, meaningful trends can still be extracted. In the JICF case, higher fuel concentrations are observed near the chamber walls, primarily due to jet impingement. Previous experimental and numerical investigations from Chapter 5 and 6 have demonstrated that increased surface roughness enhances near-wall turbulence while simultaneously reducing local velocities. These combined effects are likely to influence hydrogen entrainment in the near-wall region, thereby playing a critical role in roughness-induced changes to flame behaviour and stability limits for the JICF configuration.

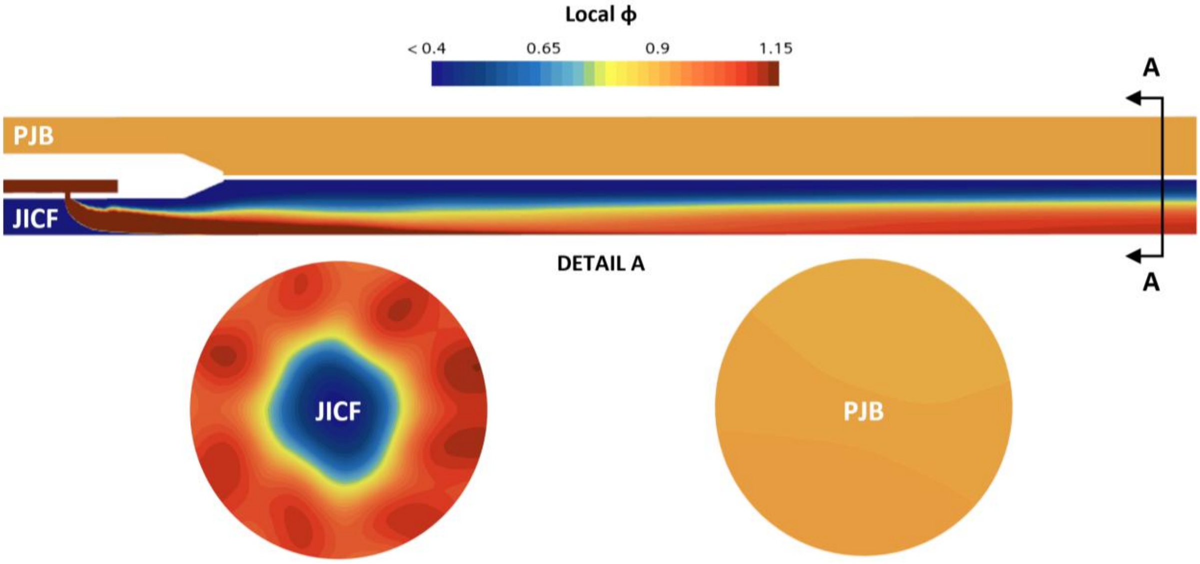

Figure 7.1 *Comparison of fuel/air mixedness for the PJB counterflow [top] and JICF [bottom] fuel injection systems. PJB data taken from the full burner simulations in Section 3.2.3. Both non-reacting cases simulated at 25 kW with global φ = 0.9.*

To assess potential roughness-induced effects, exploratory non-reacting isothermal RANS simulations with roughness sensitivity were conducted at 25 kW for ϕ = 0.5 and 0.9 (inlet conditions available in Table 6.4). Since bulk flow rates remained consistent with those used in the fully premixed simulations, the original mesh was largely retained, except for added refinement at the fuel jet exit regions to better resolve the JICF flow. The relevant k_s values, collected in Table 6.8, were carried over for the rough simulations. The physics continua, outlined in Section 6.3.2.2, were reused, with the reacting species transport and segregated flow enthalpy models replaced by non-reacting species transport and an isothermal energy formulation. To reflect the JICF configuration, the fuel and air inlets were decoupled. The updated inlet configuration and mesh refinements are illustrated in Figure 7.2.

Figure 7.2 *– Modified mesh for JICF burner with location of air and fuel mass flow inlets highlighted.*

In this preliminary analysis, flow field evaluations were conducted at the nozzle exit, just upstream of the expansion into the combustion chamber. This location was chosen to isolate and assess roughness-induced effects along the nozzle wall prior to the influence of downstream chamber flow development. While experimental measurements for the PJB configuration were taken 2 mm downstream of this point, the simulation results at the nozzle exit still provide meaningful insight into emerging trends. Distributions of axial velocity and ϕ at this location are presented in Figure 7.3.

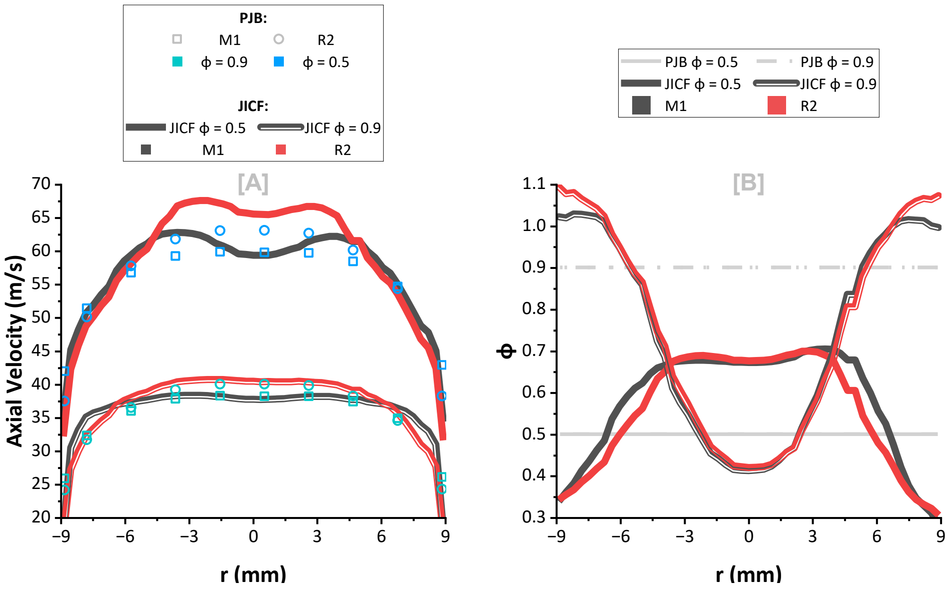

Figure 7.3 *- Roughness effects on axial velocities[A] and φ [B] in a JICF burner. Comparisons with respective PJB isothermal non-reacting data. Non-reacting 25kW simulations. Squares in legend indicating the colour code.*

As shown in Figure 7.3, the roughness-induced changes in axial velocity profiles from these exploratory JICF simulations align well with both the experimental and numerical trends observed for the PJB configuration. At ϕ = 0.9, the velocity profile shifts are consistent with those recorded in the PJB cases, while the ϕ = 0.5 cases display a more pronounced roughness effect compared to the PJB.

Regarding equivalence ratio distribution, a clear dependence on the fuel-to-air momentum fraction is observed in Figure 7.3. For the leaner ϕ = 0.5 case, fuel is more concentrated in the core region, whereas the richer ϕ = 0.9 case shows elevated fuel concentrations near the wall. This shift is expected, as richer mixtures (with greater fuel momentum) result in deeper jet penetration for a fixed thermal power [281]. Roughness effects are also evident in the ϕ profiles. Although both cases exhibit higher fuel concentrations in the boundary layer, the effect is more pronounced for ϕ = 0.9, where roughness produces significantly higher near-wall equivalence ratios. This trend aligns with the anticipated impact of increased near-wall turbulence, stronger jet impingement, and reduced axial velocities introduced by surface roughness.

To verify that the observed changes in H_2 concentration were consistent across the entire burner nozzle, a supplementary analysis was conducted. Data from a section plane located at the nozzle exit, immediately upstream of the combustion chamber expansion was extracted for each non-reacting JICF simulation as shown in Figure 7.4.

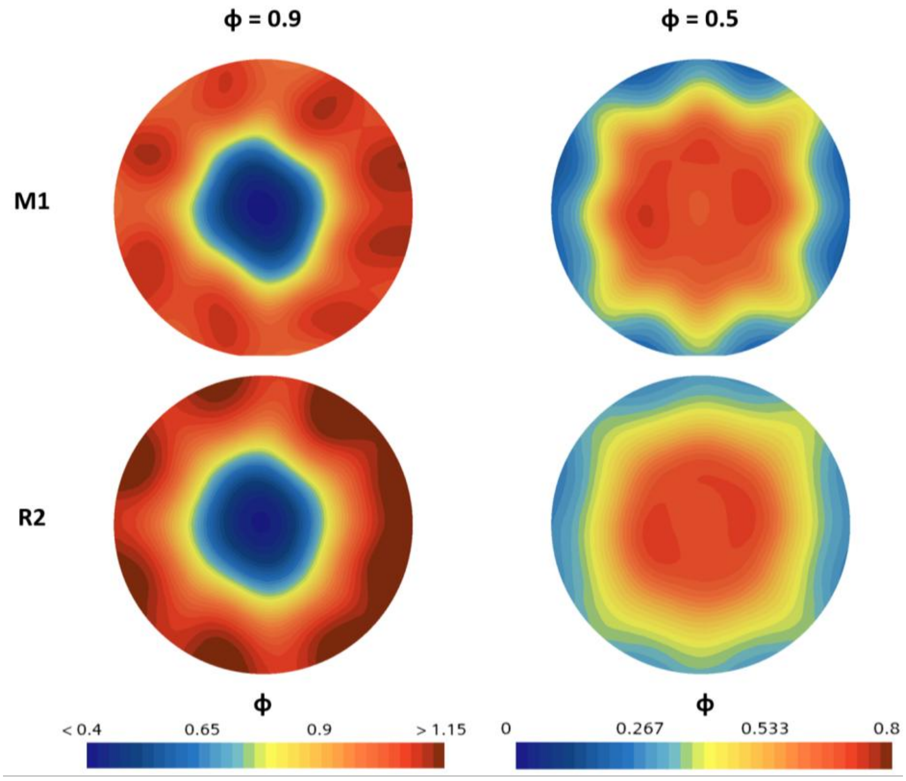

Figure 7.4 *- Comparison of smooth and rough non-reacting 25 kW simulations at φ = 0.9 [left] and φ = 0.5 [right].*

Figure 7.4 confirms that hydrogen redistribution occurs across the entire burner nozzle. For ϕ = 0.5, increased roughness primarily promotes a more uniform hydrogen distribution, whereas for ϕ = 0.9, the effect is characterised by a pronounced shift toward the burner nozzle walls. Importantly, surface-averaged equivalence ratios on these section planes varied by less than ~1.3% between smooth and rough cases, indicating that the global ϕ was effectively maintained.

To further enhance visualisation of this roughness induced H_2 redistribution, differences between the rough and smooth local ϕ values from Figure 7.4 were computed via equation [7.1]:

$$\Delta\varphi(x,y) = \varphi_{rough}(x,y) - \varphi_{smooth}(x,y) \qquad [7.1]$$

This spatial visualisation presented in Figure 7.5, further reinforces the previously observed redistribution of H_2 toward the walls, particularly under richer operating conditions.

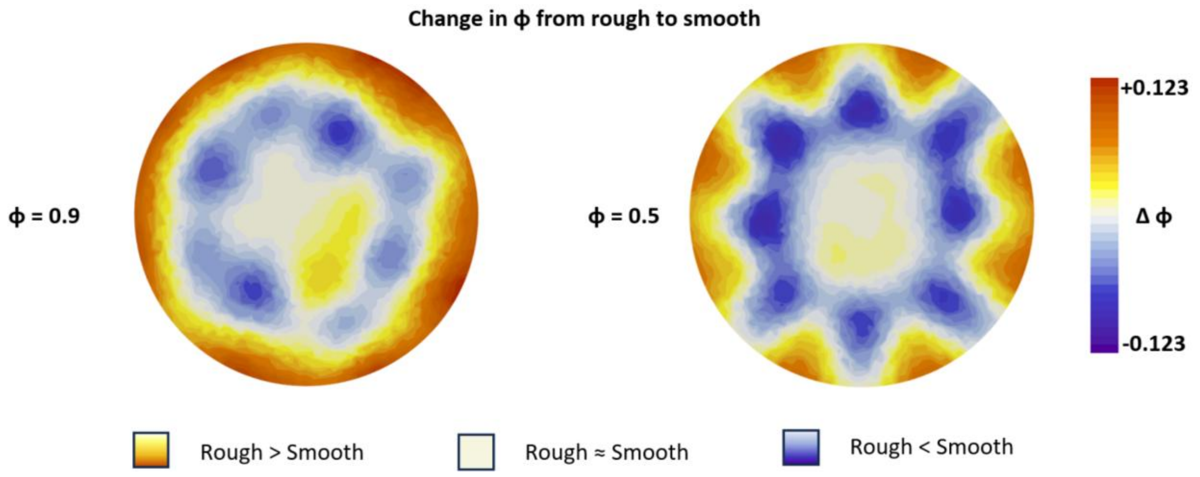

Figure 7.5 *- Roughness induced changes in φ for 25 kW JICF exploratory simulations. Same threshold used for both cases. Positive values indicating higher values for the rough simulations and vice versa.*

Although the findings from these exploratory simulations remain unvalidated, the results offer meaningful insights when considered alongside the known sensitivity of hydrogen to boundary layer flashback, as discussed in Section 2.2.3.1. The observed combination of elevated near-wall H_2 concentrations and reduced boundary layer velocities in the rough configurations suggests that the roughness-driven trends in flame location and burner stability identified for the fully premixed burner in Chapter 5 may not directly translate to the JICF configuration.

Moreover, given the greater industrial relevance of JICF systems and the fact that similar trends were observed when applying the k_s correlation developed in Chapter 6 to a Siemens Energy Industrial Turbomachinery Ltd. jet burner (results withheld due to IP constraints), there is strong justification for an experimental campaign focused on the JICF configuration. The results of this campaign are presented in Section 7.4.

7.3. Materials and Methods

7.3.1. Burner Architectures

All experimental work was conducted using the PJB and JICF burner configurations developed for this work and described in Section 3.2.1. In contrast to the experimental facility used in Chapter 5, which employed a square 64 x 64 mm quartz combustion chamber confinement, both configurations in the present study utilised a cylindrical quartz tube with a 100 mm inner diameter as covered in further detail in Section 3.2.1.1.

To evaluate the impact of surface roughness on burner operability and performance the M1 and R2 inserts, described in Section 3.2.1.4 and previously used in Chapter 5 were employed with both burner configurations. Given LDA was utilised in the Chapter 5 test campaign, both inserts were ultrasonically cleaned to remove any seeding deposits before further measurements. Surface finishes were reverified utilising the same methodology as described in Section 3.2.1.4.1, confirming that prior testing had not altered them.

7.3.2. OH* Chemiluminescence

Following repositioning of the camera from its location in the Chapter 5 test campaign, the image resolution, determined using a scaled target, was found to increase from 4 pixels/mm to 4.3 pixels/mm. Due to space constraints, only Abel-deconvoluted half-flames at 20 kW are presented in the Chapter. All other Abel-deconvoluted and raw datasets are available in Appendix D.5.

7.3.3. Stability Limit Assessment

To ensure accurate and repeatable stability limit measurements across both burner configurations and the range of thermal powers tested, a set of standardised procedures was implemented. Following each flashback or lean blowoff (LBO) event, the burner was re-lit under defined conditions and allowed to thermally stabilise before resuming data collection. Additionally, each LBO and flashback condition was repeated three times therefore providing repeatability data to enhance data reliability. It should also be noted that, although the PJB configuration was also employed in Chapter 5, all data presented here are newly acquired and were collected sequentially alongside the JICF measurements.

Lean blowoff was characterised by incrementally increasing the airflow at a fixed thermal power until flame lift-off was observed via the OH* CL live feed. In both burner configurations, lift-off consistently initiated asymmetrically on the right-hand side of the burner exit, likely due to flame anchoring effects associated with the ignitor positioned on the left-hand side. Once this condition was reached, airflow was reduced to allow the flame to reattach, after which the burner was allowed to thermally stabilise before proceeding to full extinction. A similar approach was adopted for initiating flashback. Specifically, at a fixed thermal power, the airflow was gradually reduced until either flashback occurred or $\phi = 2.0$ was reached. Further reduction in airflow beyond this point was avoided, as the laminar flame speed of hydrogen-air mixtures typically peaks near $\phi \approx 1.8$ [282,283]. Although operating under rich conditions is not directly representative of industrial practice, which typically favours lean combustion, the decision to do so was motivated by two key considerations. First, it allowed assessment of whether the roughness-induced axial shortening observed under stable operation in Chapter 5 persisted at richer conditions, where hydrogen flame speed continues to increase. Second, in the absence of preheating, achieving flashback at higher thermal powers required operation at increased equivalence ratios. When flashback did occur, the event was captured using the OH* CL diagnostic at a sampling rate of 4 kHz. The primary objective was to evaluate any variations in the flashback mechanism resulting from changes in both fuel delivery strategy and surface roughness. Due to the difficulty of timing the capture of the OH* CL with the flashback event, only one recording per condition was achieved.

To ensure consistent and objective assessment of flashback events, MATLAB scripts, originally employed in Section 5.3.2.3 were employed to extract frame-averaged OH* CL intensity values from the flashback recordings. As flashback occurred across a broad range of thermal powers and equivalence ratios, the extracted values were subsequently normalised using equation [5.3].

7.4. Results and Discussion

7.4.1. Flame Location

Combustion experiments were performed under thermal powers of 15, 17.5, and 20 kW, with full operability sweeps conducted from LBO to flashback by varying ϕ for each power setting and burner insert. If flashback did not occur, the sweep was terminated at ϕ = 2.0 with OH* CL data collected at 0.2 increments between $0.6 \leq \phi \leq 2.0$, limited by the stability boundary (i.e., the final point corresponded to the last achievable 0.2 step before LBO or flashback). Additional CL data was collected at the final stable ϕ prior to flame lift-off in the PJB. This was not repeated for the JICF configuration, as the flame became highly asymmetric, anchoring on the ignitor side (left-hand side), beyond ϕ = 0.6, and LBO occurred shortly thereafter, preventing further lean operation unlike the PJB. This difference between the JICF and PJB configurations under lean operation can be partly attributed to richer fuel mixtures near the nozzle walls resulting from radial fuel injection, as observed numerically in Section 7.2.

Abel-transformed OH* CL images for the 20 kW cases with both burners and roughness inserts between $0.6 \leq \phi \leq 1.2$ are shown in Figure 7.6. The dataset is limited to ϕ = 1.2, which represents the highest equivalence ratio at which both burner configurations remained stable with the M1 insert. Each image represents a combination of both the JICF (left half) and PJB (right half) half-flame for the given thermal power and ϕ. To maintain consistency and mitigate asymmetry effects, the left-hand half flame is shown for both burners, the PJB half-flame being mirrored horizontally before alignment with its JICF counterpart. As a result, the field of view expands axially downstream from burner exit nozzle (y = 0 mm) and radially outward from the inner edge of the quartz confinement (JICF = $0 \text{ mm} \leq r \leq 32 \text{ mm}$, PJB = $32 \text{ mm} < r \leq 64 \text{ mm}$). Images for each ϕ are shown with colormaps normalised to the maximum OH* intensity in each half-flame.

Figure 7.6 demonstrates that, under lean conditions, a consistent and pronounced difference in OH* CL intensity distribution exists between the PJB and JICF configurations for both the M1 and R2 inserts. Specifically, the JICF flames exhibit smaller regions of high intensity that are shifted further downstream. This difference diminishes as the equivalence ratio increases, suggesting that the influence of unmixedness becomes less significant at richer conditions ($\phi \geq 1$), where excess fuel beyond stoichiometry does not contribute to combustion at the flame front. Although the general OH* distribution trends between the burner configurations remained consistent across both inserts, differences in flame length were observed. With the smooth M1 insert, both burner types produced flames of similar length. Expected given that flame speed is the dominant factor and should be similar under identical ϕ. However, with the rough R2 insert, the JICF flame appeared longer than the PJB counterpart, particularly under rich conditions. This implies that surface roughness affects fuel-air mixing. Since longer flames are generally indicative of locally leaner regions, where lower flame speeds prevail, this suggests that the increased surface roughness may be driving a radial redistribution of fuel toward the burner walls as observed numerically in Section 7.2. The resulting leaner core would explain the extended flame length observed in the JICF configuration, particularly under rich overall conditions. However, other factors such as turbulence-enhanced flame stretch, thermodiffusive or anchoring effects may also contribute.

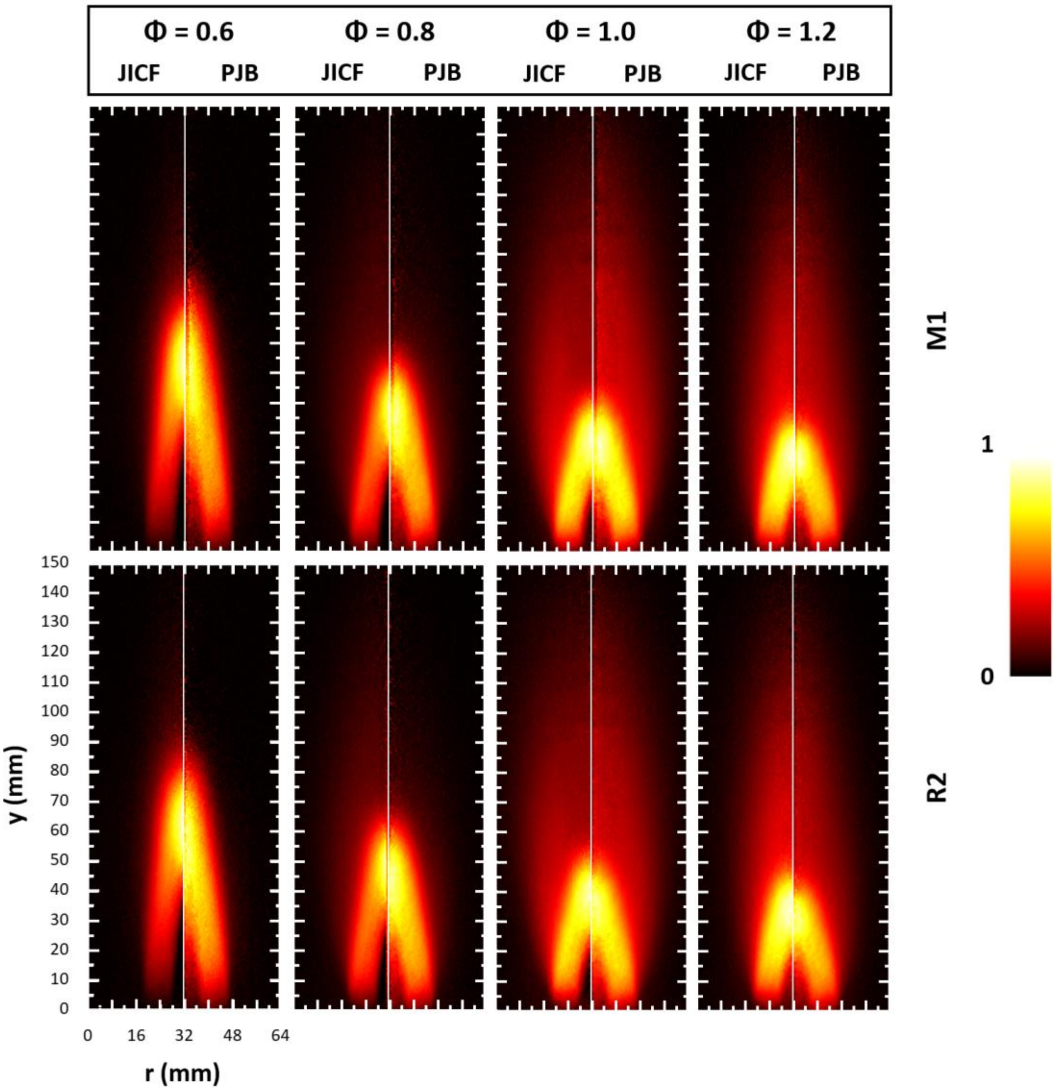

Figure 7.6 *- Abel transformed OH* CL images for 20kW over a range of φ. Colourmap normalised to maximum OH* intensity in each half image. JICF results shown on the left and PJB results shown on the right for each condition. M1 flames collected in the top row and R2 ones in the bottom row.*

To further investigate roughness-induced changes in flame location, a side-by-side comparison of M1 and R2 flames for each burner configuration is presented in Figure 7.7, using the same processing methodology as in Figure 7.6. In this case, the left and right halves correspond to the M1 and R2 inserts, respectively, for a given burner and equivalence ratio at 20 kW.

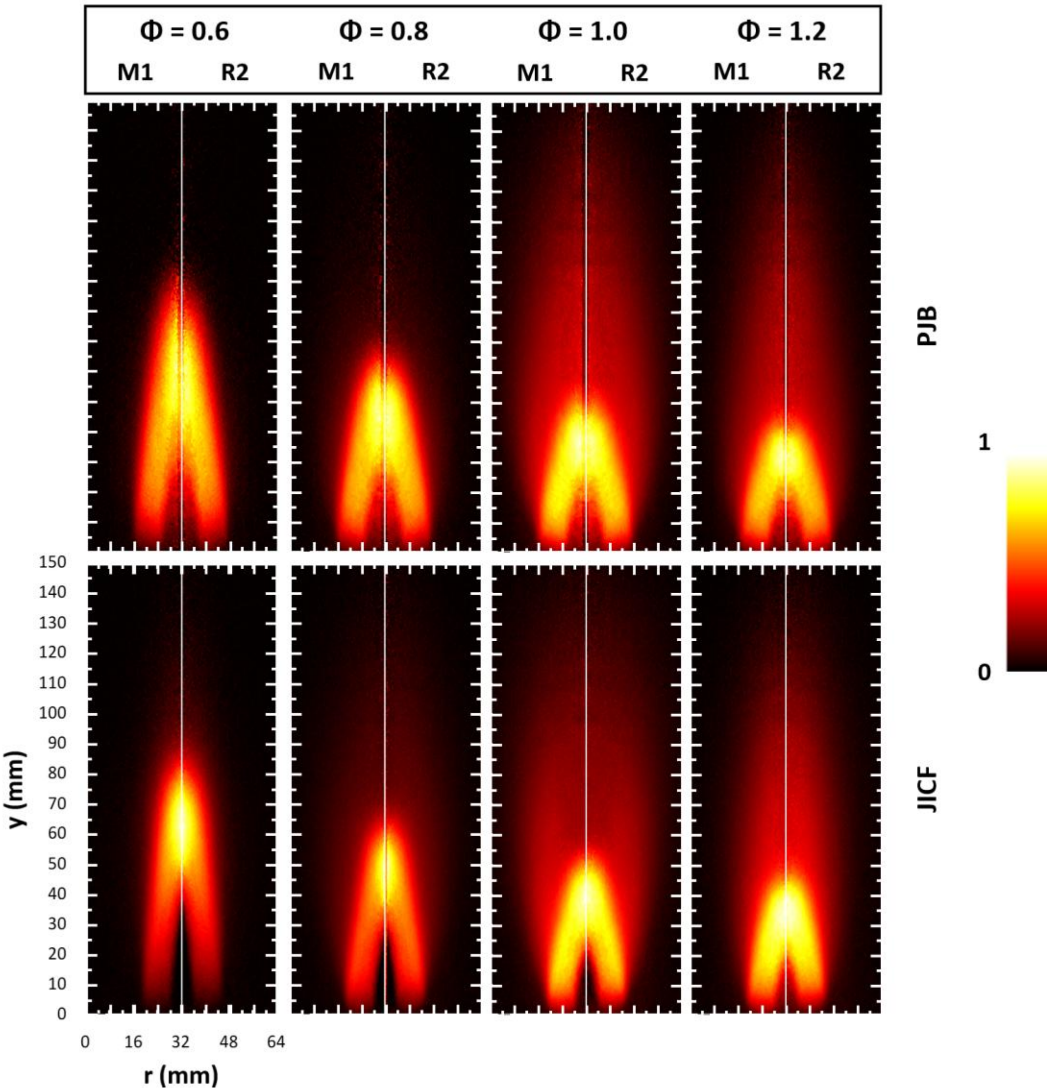

Figure 7.7 *- Abel transformed OH* CL images for 20 kW over a range of φ. Colormap normalised to maximum OH* intensity in each half image. M1 results shown on the left and R2 results shown on the right for each condition. PJB flames collected in the top row and JICF ones in the bottom row.*

Figure 7.7 highlights distinct roughness-induced trends when comparing the PJB and JICF datasets. For the PJB configuration, R2 flames are consistently shorter than the M1 counterparts. This axial shortening becomes more pronounced with increasing bulk flow velocity (higher thermal powers and lower ϕ) aligning with trends reported in other experimental studies reported in Chapter 5 and in Vivoli et al. [265]. In contrast, the JICF flames exhibit a similar, though less pronounced, shortening conditions for ϕ < 0.8, with a gradual reversal of this trend as equivalence ratio increases. Importantly, the burner- and roughness-induced variations in OH* intensity and flame length were consistently observed across all thermal power levels, with similar trends evident in each case. While results for the 15 kW and 17.5 kW cases are not shown here for brevity, they are available in Appendix D.5.

7.4.1.1. Changes in Axial Centroid Location

To better illustrate shifts in flame and heat release location, the centroid of OH* CL intensity was calculated for both the raw-averaged and Abel-deconvoluted half-flame images across all test cases. An intensity-weighted approach, applied consistently across all conditions, was used as per Chapter 5 and outlined in Runyon [233]. Repeat measurements at 15 kW (ϕ = 0.6 for the PJB and ϕ = 0.8 for the JICF) were used to estimate statistical uncertainty, calculated as ±0.29 mm and ±0.33 mm, respectively. Since both the raw-averaged and deconvoluted centroids exhibited the same trends, only the raw-averaged results are presented for brevity. Radial centroid shifts were found to be minimal and did not display any consistent trends when compared with the axial changes. On average, the radial displacement of the R2 flame relative to the M1 flame was just ~0.8% (~0.45mm) across both burner types, with the observed variation only slightly exceeding the stated uncertainty. For clarity, only axial centroid positions for both M1 and R2 inserts are shown.

A complete operability sweep from ϕ = 0.6 to 2.0 was only achieved at 20 kW using the R2 insert in both burner configurations. This is because, as demonstrated in Chapter 5 and further detailed in Section 7.4.2, the enhanced flashback resistance associated with increased surface roughness strengthens with rising thermal power. Consequently, only the highest thermal power case (20 kW) combined with the R2 insert exhibited no flashback across the tested equivalence ratio range. Figure 7.8 presents the corresponding centroid coordinates at 0.2 ϕ intervals, along with the percentage deviation in axial flame location between the JICF and PJB.

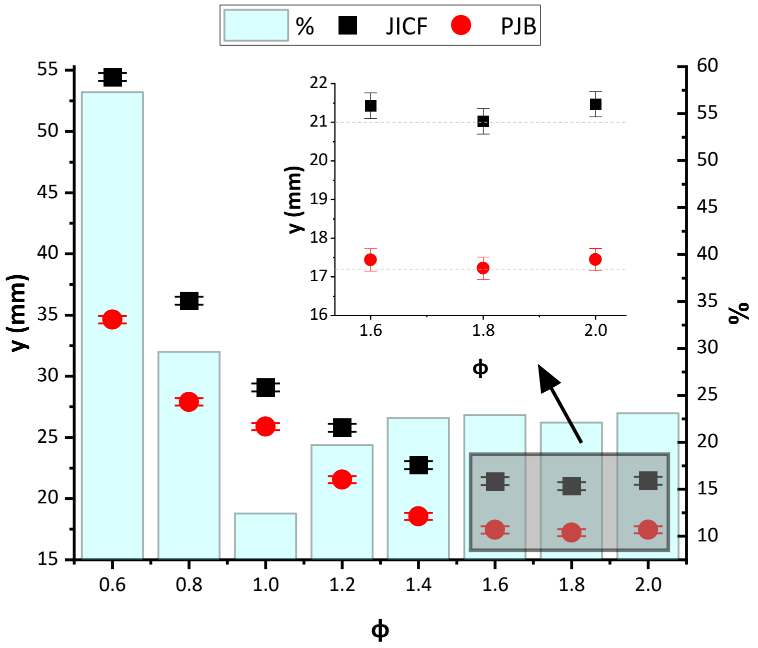

Figure 7.8 - Centroid locations for full operational sweep at 20 kW with PJB and JICF configurations. Both employing the R2 insert. Detailed view showing shortest flame location. Blue bar chart showing percentage deviation between JICF and PJB.

From Figure 7.8, both burner configurations exhibit a consistent trend of decreasing axial centroid position with increasing ϕ, aligning with the visual observations in Figure 7.6 and Figure 7.7. The shortest flame lengths were recorded at ϕ = 1.8 with both configurations, followed by a slight increase at ϕ = 2.0. This supports the conclusion, consistent with literature [282,283], that peak flame speed was reached within the tested range, and further enrichment would not yield additional insight, particularly from an industrial relevance perspective.

While notable differences in axial centroid positions were observed across all tested equivalence ratios, these deviations decreased with increasing ϕ, reaching a minimum of ~12.4% at ϕ = 1.0, before rising slightly and stabilising around ~22.7% from ϕ = 1.4 to 2.0. This trend is attributed to the reduced impact of fuel mixedness beyond stoichiometry, as excess fuel does not contribute to flame-front combustion, consistent with observations from Figure 7.6. However, Figure 7.7 highlights that roughness effects on flame shape differ between the JICF and PJB configurations, prompting a more focused analysis. To isolate roughness effects from burner-specific differences, R2 centroid positions (Y_{R2}) were normalised against corresponding M1 (Y_{M1}) values for each thermal power and ϕ via equation [7.2]. Results are presented in Figure 7.9.

$$\Delta Y = \left(\frac{Y_{R2}}{Y_{M1}} - 1\right) \times 100 \qquad [7.2]$$

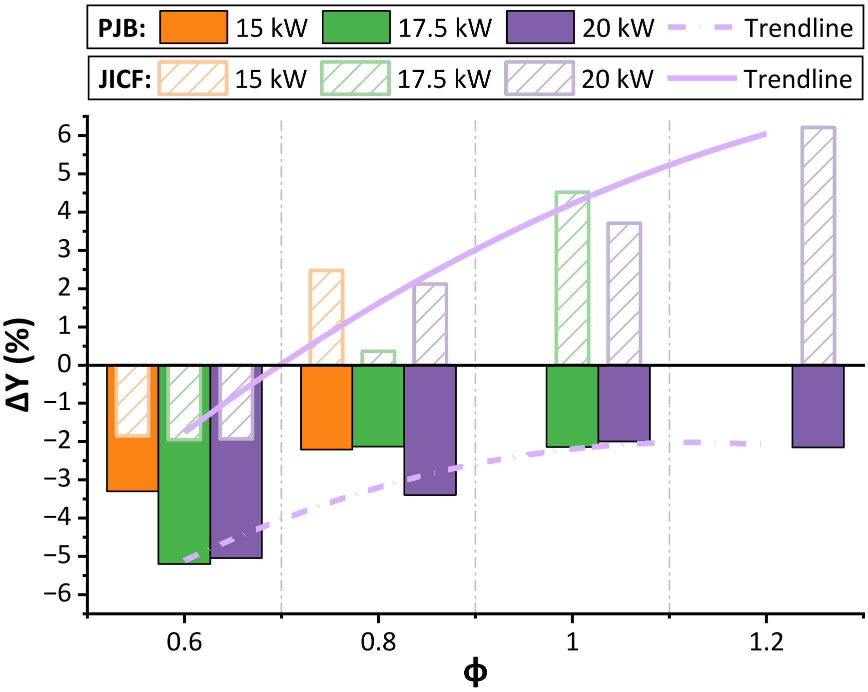

Figure 7.9 - *Changes in the axial coordinate of both burner configurations as a function of roughness. Values have been normalised relative to the corresponding smooth-wall cases. Polynomial trendlines shown for 20 kW cases.*

Figure 7.9 highlights the contrasting roughness-induced trends between the two burner configurations. In the PJB, increased surface roughness consistently results in an upstream shift of the flame centroid relative to the smooth insert, with this effect diminishing at lower thermal powers and higher equivalence ratios, aligning with previous findings from Chapter 5. The JICF burner, however, exhibits a non-monotonic response that is more strongly influenced by equivalence ratio than thermal power. At lean conditions, JICF flames show a similar but less pronounced upstream shift with increasing roughness. From ϕ ≥ 0.8 onwards, the trend reverses, rough flames becoming progressively longer and diverging from the PJB behaviour. One likely mechanism behind the observed roughness-induced axial flame shortening in both the PJB and JICF configurations is the increase in turbulence caused by surface roughness. This effect, previously observed experimentally under isothermal conditions for the PJB via LDA in Chapter 5, enhances local mixing and increases burning rates, especially at higher bulk flows and lean equivalence ratios, where flames are more sensitive to turbulence-driven enhancements.

For the JICF burner, however, the trend reversal seen under rich conditions suggests that additional mechanisms may be influencing flame behaviour. Due to the nature of JICF fuel injection, radial non-uniformities in fuel concentration arise radially across the burner nozzle. As the equivalence ratio increases, the fuel jet momentum grows, causing stronger impingement on the inner burner wall and enriching the near-wall region as highlighted numerically both by Li [281] and in Section 7.2. Roughness-induced turbulence reduced near-wall velocities, and boundary layer thickening highlighted in Section 5.3.1 may further intensify this radial fuel stratification, trapping more fuel near the walls and lowering the local equivalence ratio in the core. This redistribution likely contributes to the observed flame elongation with the R2 insert for ϕ ≥ 0.8.

7.4.1.2. Changes in Fuel/Air Momentum ratio

As previously discussed in Section 7.4.1.1, roughness-induced changes in flame centroid location in the JICF configuration exhibit a much stronger dependence on ϕ than on thermal power, unlike the PJB configuration, where variations were primarily driven by bulk flow. This is due to the nature of fuel injection in the JICF setup, where the momentum ratio between fuel and air varies with ϕ, as shown in Figure 7.10. The momentum ratio (J) here is defined as the ratio of air momentum to hydrogen momentum as shown in equation [7.3]:

$$J = \frac{momentum_{Air}}{momentum_{H_2}} = \frac{\dot{m}_{Air} \cdot U_{Air}}{\dot{m}_{H_2} \cdot U_{H_2}} \qquad [7.3]$$

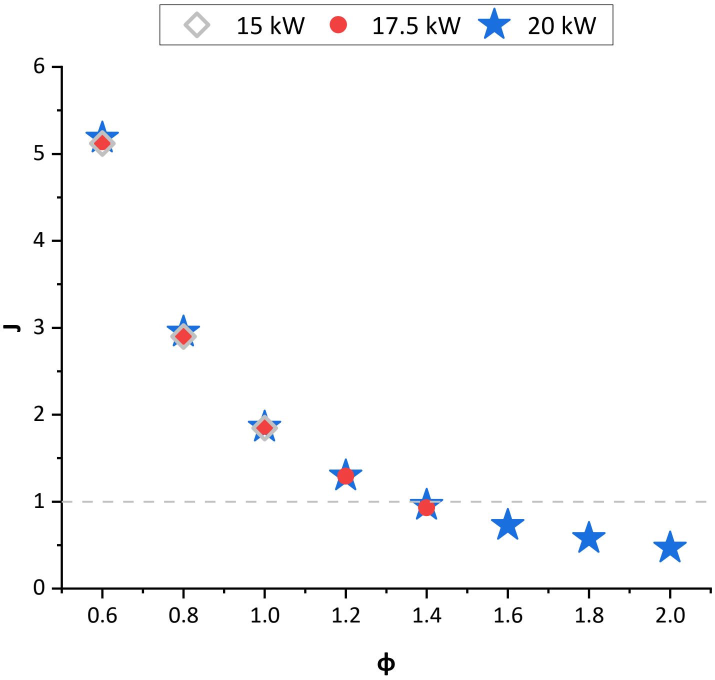

***Figure 7.10**: Changes in air/fuel momentum ratio as a function of thermal power and equivalence ratio.*

From Figure 7.10, it can firstly be seen that, as expected, for a given ϕ the momentum ratio remains constant across all thermal powers. However, a sharp decline is observed across the $0.6 \leq \phi \leq 1.4$ range, with a ~43% drop from $\phi = 0.6$ to 0.8, and a ~81% reduction by $\phi = 1.4$, where the ratio approaches unity. Consequently, jet impingement and fuel distribution evolve significantly from globally lean to rich conditions as illustrated numerically in Section 7.2. This rapid variation in momentum ratio, and consequently in jet impingement, particularly for $\phi < 1$, is likely another contributing factor to the observed differences in roughness effects on flame length between the PJB and JICF configurations.

7.4.2. Stability Limits

Sections 7.4.1 and 7.4.1.1 have highlighted how the divergent trends observed between the PJB and JICF configurations in terms of roughness effects on flame shape and heat release location may stem from the interaction between roughness-induced turbulence/velocity; changes and fuel distribution characteristics unique to the JICF setup. Specifically, it was earlier proposed that, in the JICF setup, roughness may enhance fuel trapping near the burner walls due to increased turbulence and reduced near-wall velocities leading to a lowering of the core ϕ. If this hypothesis holds, then for a given ϕ and thermal power, rough JICF burners should exhibit higher near-wall fuel concentrations compared to smooth counterparts. Such changes would be expected to influence both stability limits and potentially alter flashback mechanisms. These effects are investigated in the Section 7.4.2.1 - 7.4.2.3.

7.4.2.1. Lean vs. Rich Flashback Characteristics for the PJB

Before examining the impact of surface roughness on the stability limits of the PJB and JICF configurations, a comparison was made between the novel PJB rich-condition flashback limits (TP ≥ 15 kW) and lean-condition PJB data previously presented in Chapter 5, as shown in Figure 7.11.

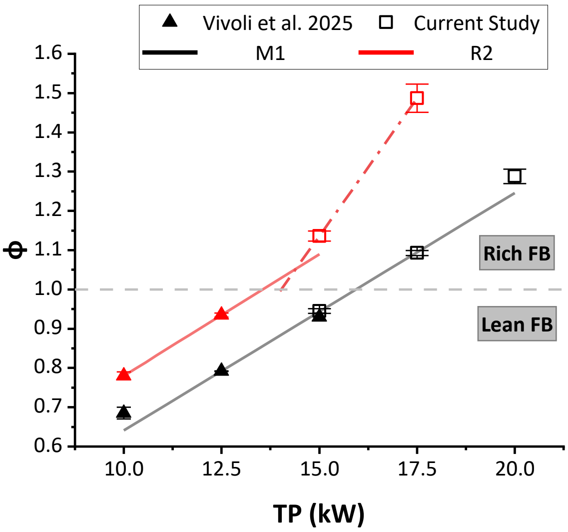

Figure 7.11 - Comparison of roughness effects on PJB flashback limits under: lean conditions (previously presented data in Chapter 5 and Vivoli et al [284]) and rich operation.

Figure 7.11 shows that, with the smooth [M1] insert, a near-linear relationship exists between previously collected lean flashback data and the current rich-condition dataset. The small deviation of approximately 0.22% in the 15 kW flashback airflow between the two datasets reinforces the reliability and consistency of the burner, indicating that the change in confinement had minimal influence. In contrast, the R2 insert deviates from this linear trend. While increased roughness improves flashback resistance in both lean and rich conditions, the effect becomes significantly more pronounced at higher thermal powers under rich conditions. For example, flashback occurring at ~30% and ~78% higher ϕ when going from 10 to 12.5 kW and 15 to 17.5 kW respectively.

Part of this enhanced resistance may stem from the decreasing sensitivity of flame speed to ϕ at richer conditions. At 10 kW, R2 flame speed was ~37% higher than M1, compared to ~22% at 17.5 kW (see Appendix A.1 for actual flame speed values). Additionally, density differences between smooth and rough configurations become more significant at higher powers. At 17.5 kW, the density difference at flashback was nearly two orders of magnitude larger than at 10 kW, potentially amplifying roughness-induced flow modifications. Both these factors may contribute to the increased impact of surface roughness on flashback resistance at higher thermal powers and should therefore be considered when looking at how changes in fuel mixedness effect stability limits.

7.4.2.2. Effects of Fuel Mixedness

Operability sweeps at 15 kW, 17.5 kW, and 20 kW were performed as outlined in Section 7.4.1. Flashback limits were recorded using both inserts across all thermal powers and burner configurations, except for the 20 kW case with the R2 insert, where flashback did not occur within the tested ϕ range. For each power setting, both the PJB and JICF configurations were driven to flashback and blow-off three times as detailed in Section 7.3.3.

For the PJB burner, the last stable equivalence ratio was noted just before flame detachment or flickering. Blow-off occurred at ϕ values approximately 3% leaner than this point, marked by rapid extinction and minimal ambiguity. In the JICF configuration, flame asymmetry became pronounced at ϕ < 0.6. Airflow was increased until complete flame extinction, which, as with the PJB, happened abruptly and unmistakably. Flashback events for both burners occurred suddenly with a distinct audible pop, clearly marking the limit. Stability limits for all tested cases with both M1 and R2 inserts are shown in Figure 7.12.

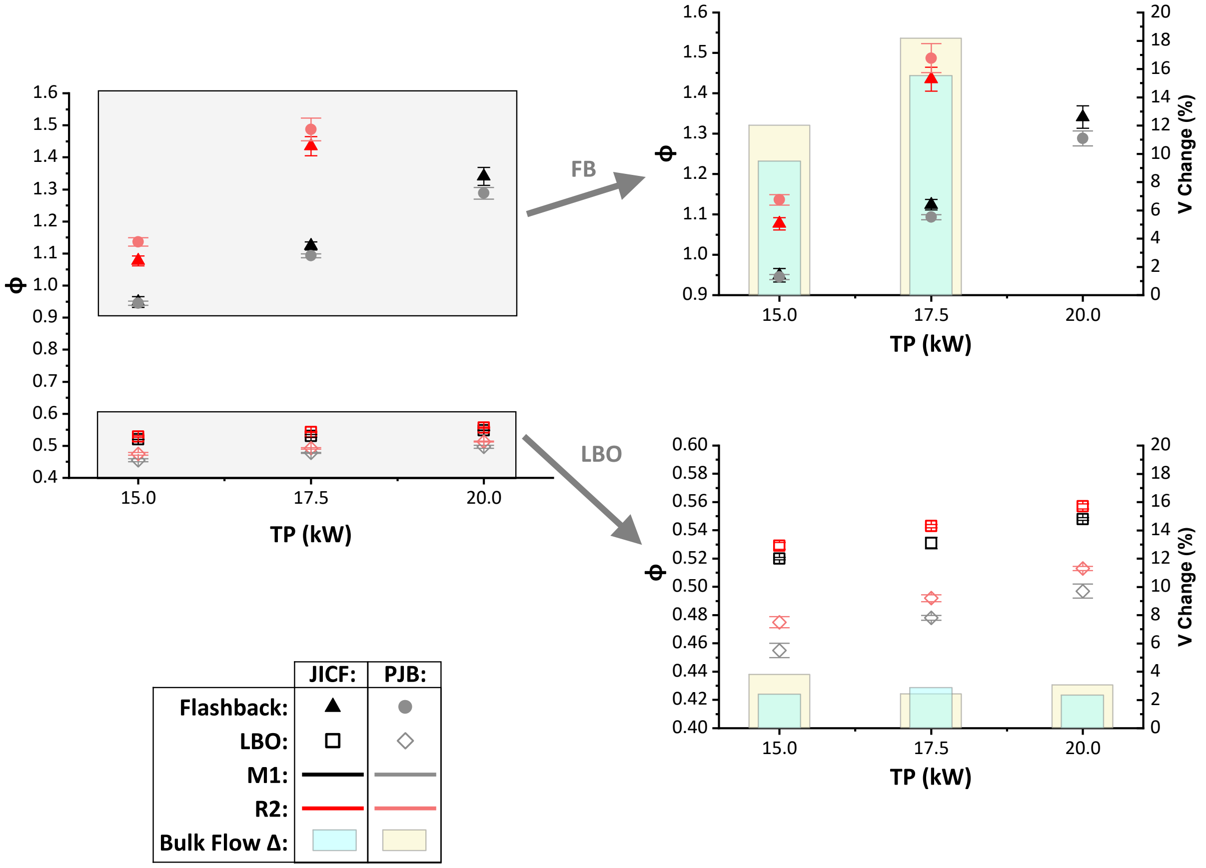

Figure 7.12 - *Roughness induced changes in stability limits with both burner configurations. Details of flashback [right top] and LBO [right bottom] boundaries, along with corresponding bulk flow changes at each thermal power.*

From Figure 7.12, it is evident that increased surface roughness improves the stable operating range across all thermal powers for both burner configurations when considered individually. At 17.5 kW, the PJB and JICF configurations show an approximate 35% and 28% increase, respectively, in the span of stable equivalence ratios when the R2 insert is used. Examining LBO and flashback separately, roughness appears to have a minor detrimental effect on LBO, more pronounced in the PJB burner, and a significant beneficial effect on flashback resistance for both configurations.

Across both M1 and R2 inserts, the PJB burner consistently demonstrates a wider stable operating range than the JICF counterpart. This is attributed to its fully premixed nature, which provides a more uniform mixture and stable combustion under varying conditions. Roughness was found to have a slightly more negative effect on LBO in the PJB configuration compared to the JICF, with an average LBO offset ~1.9% higher. One plausible explanation is that the partially premixed nature of the JICF results in locally richer zones, helping to maintain flame stability and diminishing any roughness effects. Nevertheless, the differences between the two burners in terms of LBO are small with changes in bulk flow consistently below 4% across all power levels.

With respect to flashback behaviour, both burner configurations exhibit an increasing separation between the M1 and R2 flashback limits as thermal power increases. This indicates that the influence of surface roughness on flashback resistance becomes more pronounced at higher power levels, likely due to interactions with the increased turbulence associated with higher flow rates. Both M1 configurations of the PJB and JICF burners perform comparably, with an average difference in flashback ϕ of only ~2.5%. This similarity is likely due to the fact that all flashback tests were conducted in fuel-rich conditions, under which the effects of unmixedness are less pronounced, as discussed in Section 7.4.1. For the rough configurations, however, surface roughness exhibits a greater positive impact on flashback resistance in the PJB than in the JICF. On average, the JICF burner flashes back at ϕ approximately 4.3% leaner than the PJB. To better understand why such an offset exists further analysis of the flashback mechanism across both burner configurations is performed in Section 7.4.2.3.

7.4.2.3. Changes in Flashback Behaviour

Flashback events for both burner configurations, using both the M1 and R2 inserts, were captured at 4 kHz using high-speed OH* CL imaging, as described in Section 7.3.2. The objective of this analysis was to identify potential changes in the dominant flashback mechanism, specifically, whether boundary layer or core-flow flashback was prevalent, and to determine whether the mechanism varied between the PJB and JICF configurations. Additionally, differences in flashback propagation rates were investigated.

As per the procedure described in Section 7.3.3, a MATLAB-based algorithm was used to identify the onset of flashback in each recording. This approach enabled consistent analysis across all datasets by normalising the frame-averaged OH* CL intensity within a ±60 ms window around the flashback event. The resulting intensity trends for both the M1 and R2 inserts at 15 kW and 17.5 kW are presented in Figure 7.13 for both the PJB and JICF configurations.

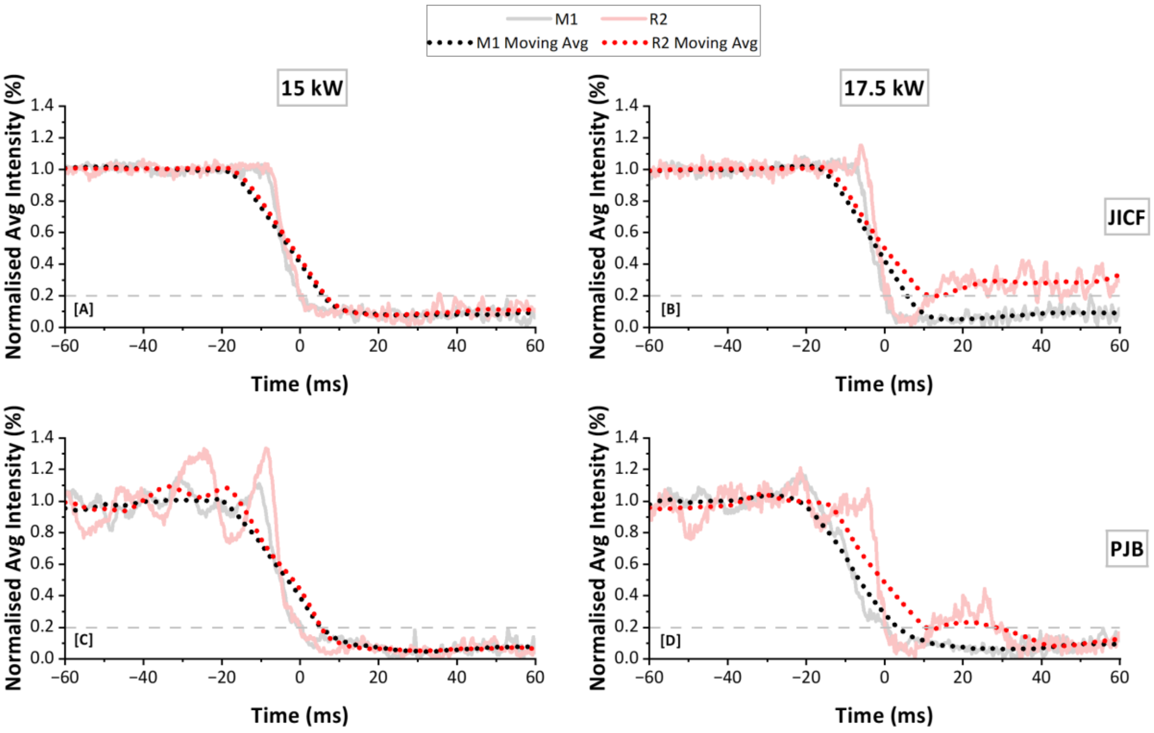

Figure 7.13 - Normalised changes in frame-average OH CL intensity at time = ± 60 ms of the flashback events with both M1 and R2 inserts at 15 kW [A, C] and 17.5 kW [B, D] for PJB [A, B] and JICF [C,D] configurations.*

From Figure 7.13, it is evident that, irrespective of thermal power, the PJB configuration exhibits significantly greater fluctuations in frame-averaged OH* intensity prior to the flashback event (t < 0) compared to the JICF configuration, particularly pronounced in the 15 kW R2 case. Moreover, when comparing M1 and R2 inserts for a given power in the PJB, the R2 flashback events appear to occur far quicker and with a steeper gradient. To assess changes in the rate of flashback, linear trendlines were fitted within ±10 ms of the flashback onset. For the PJB cases, trendline gradients were found to steepen with increasing thermal power, rising from a ~53% increase at 15 kW to ~155% at 17.5 kW. These findings align with earlier results (Chapter 5), reinforcing the observation that flashback propagates more rapidly in the R2 insert, especially under rich conditions. In contrast, the JICF

configuration shows minimal differences between M1 and R2 profiles at both power levels. Although R2 still exhibits a slightly steeper gradient within ±10 ms of flashback, the increase is modest, ~12% at 15 kW and ~10% at 17.5 kW. Notably, unlike the PJB, the gradient does not increase with power.
This could be partially explained by differing trends in flame speed. Although all rough cases exhibit an increase in flame speed at the flashback ɸ compared to their smooth counterparts, the magnitude of this effect varies by configuration and thermal power. For the JICF configuration, the 17.5 kW cases show a ~ 7% greater increase in flame speed between the M1 and R2 inserts compared to the 15 kW cases. In contrast, for the PJB configuration, the increase in flame speed at the flashback ɸ between M1 and R2 is ~5% lower at 17.5 kW than at 15 kW (see Appendix A.1 for actual flame speed values).

As outlined in Chapter 5, the time at which each moving average dataset first dropped below a normalised value of 0.95, and remained below, was used to objectively quantify the duration before complete flashback. Consistent with the trendline gradient changes, all rough cases exhibited longer stability than their smooth counterparts, with the effect being more pronounced for the PJB. For the JICF, R2 flashback occurred approximately 1.5 ms and 2.5 ms later than smooth cases at 15 kW and 17.5 kW, respectively. In contrast, for the PJB, the delay increased to about 2.5 ms at 15 kW and 12.5 ms at 17.5 kW.

To visualise any changes in flashback mechanisms, primarily if changes in mixedness could transition the burner from core-flow to boundary layer flashback, the 13.75 ms preceding flashback are shown for both burner configurations and inserts at both 15 kW and 17.5 kW in Figure 7.14 and Figure 7.15 respectively. The frames are spaced at 1.25 ms intervals, and colour mapping is applied using the global peak intensity as the maximum value across all frames in the series.

As shown in Figure 7.14, the 15 kW cases reveal distinct differences in flashback onset between burner configurations. For the JICF, both M1 and R2 inserts exhibit asymmetrical flashback initiation, predominantly originating on the right-hand side of the frame in a manner consistent with BLF [268]. In contrast, the PJB M1 case displays a more uniform upstream flame propagation characteristic of core-flow flashback. The PJB R2 case also presents some asymmetry, though less pronounced than in the JICF cases, suggesting that under these fuel-rich conditions, the addition of surface roughness may increase the susceptibility of the PJB to BLF. Although no definitive shift in flashback mechanism is observed between the JICF inserts, the persistent asymmetry in both cases implies a stronger tendency toward BLF, likely driven by the radial fuel injection promoting near-wall enrichment.

At 17.5 kW, as shown in Figure 7.15, the flashback dynamics appear more uniform across both burner configurations and insert types, making it more difficult to identify distinct trends in mechanism or roughness effects at higher thermal power. However, consistent with the trends from Figure 7.13, roughness can be seen to delay the onset of flashback in both burner types. For the JICF configuration, a consistent delay of approximately 2.5 ms is observed between the M1 and R2 inserts at both thermal powers. In the PJB configuration, however, the roughness-induced delay increases significantly with thermal power, from approximately 1.25 ms at 15 kW to 5 ms at 17.5 kW, suggesting a more pronounced sensitivity to surface roughness effects in the fully premixed case as power increases.

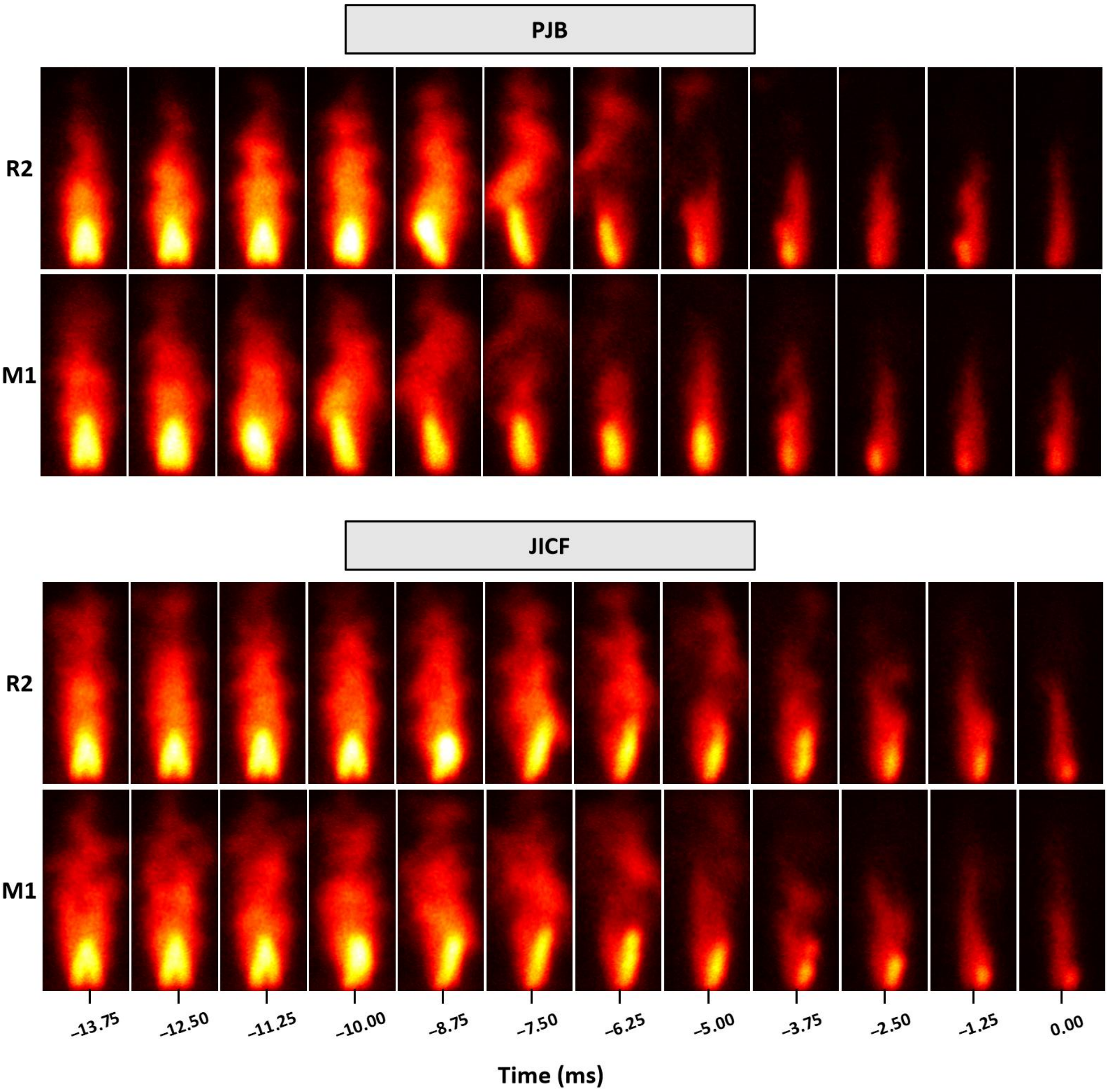

Figure 7.14 - *OH* CL visualisation of flashback at 15 kW with PJB [top] and JICF [bottom] burner configurations. Both with M1 and R2 inserts. Instantaneous frames spaced out every 1.25 ms. Normalisation performed based on the global maximum intensity.*

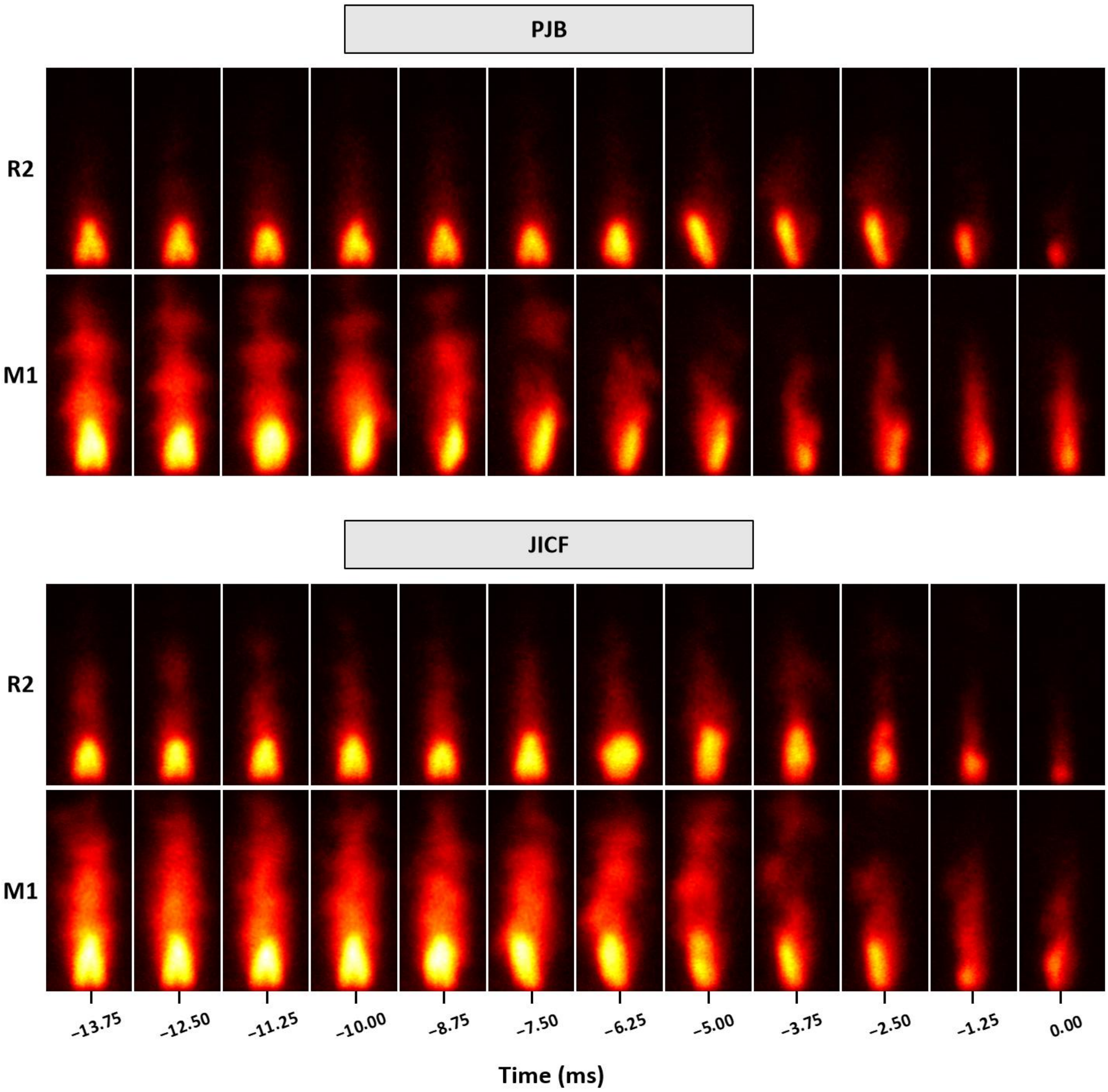

Figure 7.15 *- OH* CL visualisation of flashback at 17.5 kW with JICF [left] and PJB [right] burner configurations. Both with M1 and R2 inserts. Instantaneous frames spaced out every 1.25 ms. Normalisation performed based on the global maximum intensity.*

7.5. Summary

This study has explored the influence of surface roughness on flame behaviour, stability limits, and flashback characteristics in two distinct burner configurations: a fully premixed Jet Burner (PJB) and a Jet-in-Crossflow (JICF) system with radially injected fuel. Through a combination of operability mapping, chemiluminescence imaging, and momentum ratio analysis, the work highlights how burner geometry and fuel-air mixing strategies interact with surface roughness to affect combustion dynamics under fuel-rich conditions.

The results show that surface roughness can be beneficial in extending stable operating ranges, particularly by delaying flashback. However, the mechanisms underlying these benefits are configuration-dependent, closely tied to mixing quality, momentum distribution, and boundary layer behaviour. Flame stabilisation mechanisms differ between the PJB and JICF, especially in how roughness influences flame anchoring, flashback dynamics, and centroid positioning.

Key findings are as follows:

- Flame centroid locations shift differently with roughness in each burner. In the PJB, roughness causes a consistent upstream shift of the flame centroid with increasing ϕ. In the JICF, roughness causes a reversal in centroid trends under rich conditions, attributed to radial redistribution of fuel toward near-wall regions and reduced core equivalence ratio.
- Surface roughness extends stability by enhancing flashback resistance, with the effect strengthening at higher thermal powers and being more pronounced in the PJB configuration.
- Flashback mechanisms diverge between configurations. PJB shows a transition from core-flow to boundary-layer flashback with increasing roughness and thermal power. JICF consistently exhibits boundary-layer-driven flashback with no significant enhancement due to increased surface roughness.

These results underscore the importance of mixing strategy and local momentum dynamics, particularly in the JICF configuration, where the evolving fuel-air momentum ratio with ϕ influences jet penetration, near-wall enrichment, and flashback behaviour. Further research is needed to directly quantify roughness-induced changes in fuel-air mixing and to assess JICF flashback behaviour under lean conditions, where the mechanisms may be more sensitive and industrially relevant.

Chapter 8. Conclusions and Further Work

This thesis has contributed to the ongoing effort to prepare gas turbine technologies for a low-carbon future by advancing the understanding of surface roughness effects on burner performance, particularly under hydrogen-fired conditions. AM is playing an increasingly central role in the production of gas turbine components, offering significant design flexibility. Yet, its characteristic surface roughness has been shown to influence combustor aerodynamics and performance, particularly in the boundary layer region. Understanding and modelling these effects is essential for the safe, reliable operation of next-generation hydrogen burners. In this brief conclusion, the key findings of this study are highlighted along with a look forward to future studies.

8.1. Facilities

In the course of this study, new facilities have been designed, implemented, and optimised for the fundamental characterisation of roughness effects on the performance and operability of a hydrogen jetting flame.

These include the following:

- A new Premixed Jet Burner (PJB) has been designed and commissioned for the study of roughness effects on premixed hydrogen flames at atmospheric pressures and temperature. A fully premixed fuel-air setup was adopted to eliminate unmixedness, simplifying the rig and ensuring that any observed effects could be attributed solely to surface roughness. A bluff body with equivalent outer dimensions to a jet-in-crossflow fuel lance was used to maintain similar downstream flow-fields. Industrially relevant dimensions were chosen, and a counterflow fuel injection approach ensured effective mixing. The quartz combustion chamber provided optical access, while the final premixing section was designed to be interchangeable for testing inserts with different surface finishes.

- A Jet-in-Crossflow (JICF) burner variant of the PJB was implemented at the latter stages of this study to collect more industry relevant data on how changes in fuel mixedness affect roughness sensitivity.

- Two interchangeable inserts were developed for use with the PJB and JICF configurations: M1 with a smooth, conventionally machined finish, and R2, using EDM to replicate the rough downskin texture of angled AM surfaces.

8.2. Methodologies

Through a combination of high-fidelity numerical simulations and targeted experimental campaigns, this work provides valuable insight into the impact of AM-like surface roughness on burner operability and performance.

These include:

- STAR CCM+ 23.02 as the CFD solver. Utilising both RANS and DES, in particular the EB model was demonstrated suitable for capturing roughness effects when coupled with low-y^+ meshes.
- Non-intrusive optical diagnostics, including OH^* chemiluminescence and LDA.

Together, the data collected via these techniques offer both practical and modelling tools to support future burner design, with the ultimate aim of enabling safer and more efficient hydrogen combustion in advanced gas turbines.

8.3. Roughness Effects

Roughness effects were investigated both experimentally and numerically using conventional swirl-stabilised and jet-based burners. From a numerical perspective, the primary objective was to develop modelling frameworks capable of capturing roughness effects using low-y^+ meshes; however, the resulting simulations also provided valuable insight into the underlying roughness mechanisms. In particular, the numerical results helped elucidate roughness-induced fuel redistribution in the JICF configuration and roughness-driven changes in swirl number in the swirl-stabilised burner. Specific experimental and numerical findings are presented in Section 8.3.1 and 8.3.2 respectively.

8.3.1. Experimental Findings

Experimental results showed that increased surface roughness significantly influenced the performance and operability of the PJB across thermal powers from 10–25 kW and equivalence ratios between $0.4 \leq \phi \leq 1$. Roughness delayed the onset of flashback but caused it to occur more rapidly once triggered. While minor negative effects on lean blowoff were observed, roughness generally expanded the stable operating range. It also led to a redistribution of axial velocity profiles, with rough cases showing higher centreline velocities than smooth ones. Although emissions remained consistently low, a trend toward reduced NO_X levels at higher thermal powers was noted for the rough cases. The smooth and rough datasets have supported the development and validation of novel roughness correlations for use in resolved boundary layer simulations.

Transitioning from a fully premixed to a jet-in-crossflow fuel delivery system maintained the trend of increased flashback resistance with roughness, though to a lesser degree than with the PJB. Trend inversions were however observed for roughness effects on flame length. This attributed to a potential roughness induced redistribution of fuel within the premixing chamber

8.3.2. Numerical Findings

Numerically, the k-ε EB model proved most effective for capturing roughness effects when used with low-y^+ meshes, in both RANS and DES frameworks. Existing literature correlations performed poorly when applied to either the generic swirl burner or the PJB, highlighting the need for tailored approaches. Separate k_s correlations were developed for each configuration, underscoring the trial-and-error nature of the work. For the swirl burner, a fixed k_s^+ correlation yielded accurate results for reacting methane flows, while for the PJB, a correlation based on bulk velocity captured roughness effects well across a wide range of isothermal and reacting hydrogen cases. In both setups, reacting flows generally showed a stronger sensitivity to roughness than their isothermal counterparts for the same k_s.

8.4. Future Work

Building upon the findings of this thesis, several areas of future research are proposed to further explore and expand the understanding of surface roughness effects on hydrogen combustion systems:

- **Gas turbine condition replication:** While full gas turbine operating conditions cannot be reproduced at laboratory scale, roughness effects should be investigated at elevated pressures and inlet temperatures, within practical limits, to assess whether the trends observed at atmospheric conditions persist with similar magnitude or exhibit a dependence on operating pressure and temperature.
- **Transient Simulations and Stability Analyses:** Extend the numerical investigations to include fully transient simulations using DES to assess the impact of surface roughness on dynamic flame behaviour. This should include the study of thermoacoustic instabilities, flashback susceptibility/mechanisms, and blow-off phenomena under varying operating conditions.
- **Dynamic Data Collection:** Complement numerical work by experimentally capturing dynamic data, such as high-speed pressure measurements, during both stable operation and transient events like flashback onset. This would provide valuable insights into how roughness influences flame stability thresholds and support validation of time-resolved simulations.

- **Correlation Generalisation and Extension:** Broaden the application of the developed roughness correlation by testing it with alternative fuels or fuel blends (e.g., methane-hydrogen, ammonia-hydrogen), with particular emphasis on the effects of varying fuel reactivity and Lewis number. This could necessitate the inclusion of additional parameters, such as Lewis number or diffusivity ratios, to retain accuracy across different combustion regimes and burner geometries.
- **Expanded Roughness Characterisation:** A broader range of surface roughness profiles and geometric textures (e.g., sinusoidal vs. random patterns) should be characterised. This would clarify how both varying roughness magnitude and morphology impact key performance metrics such as flashback and blow-off limits.
- **Develop a deeper understanding of how fuel mixedness influences roughness effects:** The hypothesis that increased roughness causes fuel redistribution within the JICF burner requires experimental validation, potentially through fuel doping or similar techniques. Additionally, characterising the JICF burner with preheated air would allow flashback behaviour to be studied under lean conditions, where variations in fuel distribution are likely to have a greater impact.

These proposed directions would support the development of more robust and generalised numerical models for predicting roughness effects. Experimentally, they would provide deeper insights into how roughness influences combustion under industrially relevant conditions, ultimately helping to reduce risks associated with hydrogen deployment in next-generation combustion systems.

References

[1] European Commission. The European Green Deal. Brussels: 2019.

[2] BEIS. Net Zero Strategy: Build Back Greener. 2021.

[3] DESNZ. UK ENERGY IN BRIEF 2023. 2023.

[4] Abbass A. Hydrogen-fueled internal combustion engines in combined heat and power (CHP) systems: A decarbonization strategy. Energy Nexus 2025; 19: 100485. https://doi.org/10.1016/j.nexus.2025.100485.

[5] Arup Group Ltd. Industrial Boilers, Study to develop cost and stock assumptions for options to enable or require hydrogen-ready industrial boilers. London: 2022.

[6] Trutnevyte E, McDowall W, Tomei J, Keppo I. Energy scenario choices: Insights from a retrospective review of UK energy futures. Renewable and Sustainable Energy Reviews 2016; 55: 326–37. https://doi.org/10.1016/j.rser.2015.10.067.

[7] National Grid ESO. Future Energy Scenarios Navigation. 2023.

[8] Dixon J, Bell K, Brush S. Which way to net zero? a comparative analysis of seven UK 2050 decarbonisation pathways. Renewable and Sustainable Energy Transition 2022; 2: 100016. https://doi.org/10.1016/j.rset.2021.100016.

[9] McGarry C, Dixon J, Flower J, Bukhsh W, Brand C, Bell K, et al. Electrified heat and transport: Energy demand futures, their impacts on power networks and what it means for system flexibility. Appl Energy 2024; 360: 122836. https://doi.org/10.1016/j.apenergy.2024.122836.

[10] Li B, Basu S, Watson SJ, Russchenberg HWJ. A Brief Climatology of Dunkelflaute Events over and Surrounding the North and Baltic Sea Areas. Energies (Basel) 2021; 14: 6508. https://doi.org/10.3390/en14206508.

[11] ETN. HYDROGEN GAS TURBINES ETN Global Report Hydrogen Gas Turbines-ETN Global. 2024.

[12] McCay MH, Shafiee S. Hydrogen: An Energy Carrier. Future Energy, Elsevier; 2020, p. 475–93. https://doi.org/10.1016/B978-0-08-102886-5.00022-0.

[13] Li Z, Guo P, Han R, Sun H. Current status and development trend of wind power generation-based hydrogen production technology. Energy Exploration & Exploitation 2019; 37: 5–25. https://doi.org/10.1177/0144598718787294.

[14] International Energy Agency. Global Hydrogen Review 2023. Paris: 2023.

[15] International Energy Agency. Global Hydrogen Review 2025. 2025.

[16] IEA. Net Zero by 2050. Paris: 2021.

[17] Serbin S, Radchenko M, Pavlenko A, Burunsuz K, Radchenko A, Chen D. Improving Ecological Efficiency of Gas Turbine Power System by Combusting Hydrogen and Hydrogen-Natural Gas Mixtures. Energies (Basel) 2023; 16: 3618. https://doi.org/10.3390/en16093618.

[18] Valera-Medina A, Morris S, Runyon J, Pugh DG, Marsh R, Beasley P, et al. Ammonia, Methane and Hydrogen for Gas Turbines. Energy Procedia 2015; 75: 118–23. https://doi.org/10.1016/j.egypro.2015.07.205.

[19] Alhuyi Nazari M, Fahim Alavi M, Salem M, Assad MEH. Utilization of hydrogen in gas turbines: a comprehensive review. International Journal of Low-Carbon Technologies 2022; 17: 513–9. https://doi.org/10.1093/ijlct/ctac025.

[20] Kim D. Review on the Development Trend of Hydrogen Gas Turbine Combustion Technology. Journal of The Korean Society of Combustion 2019; 24: 1–10. https://doi.org/10.15231/jksc.2019.24.4.001.

[21] Drew R. FUEL SWITCHING. International Turbomachinery Magazine 2018.

[22] Giacomazzi E, Messina G. Hydrogen and the fuel-flexibility dilemma in gas turbines. Energia, Ambiente e Innovazione 2021: 125–9.

[23] Öberg S, Odenberger M, Johnsson F. Exploring the competitiveness of hydrogen-fueled gas turbines in future energy systems. Int J Hydrogen Energy 2022; 47: 624–44. https://doi.org/10.1016/j.ijhydene.2021.10.035.

[24] du Toit MH, Avdeenkov A V., Bessarabov D. Reviewing H2 Combustion: A Case Study for Non-Fuel-Cell Power Systems and Safety in Passive Autocatalytic Recombiners. Energy & Fuels 2018; 32: 6401–22. https://doi.org/10.1021/acs.energyfuels.8b00724.

[25] Cecere D, Giacomazzi E, Di Nardo A, Calchetti G. Gas Turbine Combustion Technologies for Hydrogen Blends. Energies (Basel) 2023; 16: 6829. https://doi.org/10.3390/en16196829.

[26] Dutta B, Babu S, Jared BH. Science, technology and applications of metals in additive manufacturing. Elsevier; 2019.

[27] Srinivasan D, Ananth K. Recent Advances in Alloy Development for Metal Additive Manufacturing in Gas Turbine/Aerospace Applications: A Review. J Indian Inst Sci 2022; 102: 311–49. https://doi.org/10.1007/s41745-022-00290-4.

[28] Gebisa AW, Lemu HG. Additive Manufacturing for the Manufacture of Gas Turbine Engine Components: Literature Review and Future Perspectives. ASME Turbo Expo 2018 Turbomachinery Technical Conference and Exposition, Oslo, Norway: American Society of Mechanical Engineers; 2018, p. 1–10. https://doi.org/10.1115/GT2018-76686.

[29] Elsevier. Scopus 2024. https://www.scopus.com/term/analyzer.uri?sort=plf-f&src=s&sid=7eada14ffb483bfe60e5e9fa4b9ff1dd&sot=a&sdt=a&sl=43&s=%22Additive+manufacturing%22+AND+%22gas+turbines%22&origin=resultslist&count=10&analyzeResults=Analyze+results (accessed April 12, 2024).

[30] Elsevier. Scopus. 2025. https://www.scopus.com/term/analyzer.uri?sort=plf-f&src=s&sid=b597f7e5782de36ba19a52c9a3eb24f6&sot=a&sdt=a&sl=9&s=ALL%28ASME%29&origin=resultslist&count=10&analyzeResults=Analyze+results (accessed December 16, 2025).

[31] Durocher A, Fan L, Francolini B, Füri M, Bourque G, Sirois J, et al. Characterization of a Novel Additive Manufacturing Micromix Nozzle Burning Methane to Hydrogen. J Eng Gas Turbine Power 2024; 146. https://doi.org/10.1115/1.4063690.

[32] Magnusson R, Andersson M. Operation of SGT-600 (24 MW) DLE Gas Turbine with Over 60 % H2 in Natural Gas. Volume 9: Oil and Gas Applications; Organic Rankine Cycle Power Systems; Steam Turbine, American Society of Mechanical Engineers; 2020. https://doi.org/10.1115/GT2020-16332.

[33] Navrotsky V, Graichen A, Brodin H. Industrialisation of 3D printing (additive manufacturing) for gas turbine components repair and manufacturing. VGB PowerTech 2015; 12: 48–52.

[34] Andersson O, Graichen A, Brodin H, Navrotsky V. Developing Additive Manufacturing Technology for Burner Repair. J Eng Gas Turbine Power 2017; 139. https://doi.org/10.1115/1.4034235.

[35] Majeed A, Ahmed A, Salam A, Sheikh MZ. Surface quality improvement by parameters analysis, optimization and heat treatment of AlSi10Mg parts manufactured by SLM additive manufacturing. International Journal of Lightweight Materials and Manufacture 2019; 2: 288–95. https://doi.org/10.1016/j.ijlmm.2019.08.001.

[36] Calignano F, Manfredi D, Ambrosio EP, Iuliano L, Fino P. Influence of process parameters on surface roughness of aluminum parts produced by DMLS. The International Journal of Advanced Manufacturing Technology 2013; 67: 2743–51. https://doi.org/10.1007/s00170-012-4688-9.

[37] Spierings AB, Herres N, Levy G. Influence of the particle size distribution on surface quality and mechanical properties in AM steel parts. Rapid Prototyp J 2011; 17: 195–202. https://doi.org/10.1108/13552541111124770.

[38] Bacchewar PB, Singhal SK, Pandey PM. Statistical modelling and optimization of surface roughness in the selective laser sintering process. Proc Inst Mech Eng B J Eng Manuf 2007; 221: 35–52. https://doi.org/10.1243/09544054JEM670.

[39] Shinonaga T, Kobayashi H, Okada A, Tsuji T. Surface smoothing of additively manufactured Ti-6Al-4V alloy by combination of grit blasting and large-area electron beam irradiation. The International Journal of Advanced Manufacturing Technology 2023; 127: 5127–37. https://doi.org/10.1007/s00170-023-11857-5.

[40] Tyagi P, Goulet T, Riso C, Garcia-Moreno F. Reducing surface roughness by chemical polishing of additively manufactured 3D printed 316 stainless steel components. The International Journal of Advanced Manufacturing Technology 2019; 100: 2895–900. https://doi.org/10.1007/s00170-018-2890-0.

[41] Giuliani F, Paulitsch N, Cozzi D, Görtler M, Andracher L. An Assessment on the Benefits of Additive Manufacturing Regarding New Swirler Geometries for Gas Turbine Burners. Volume 4A: Combustion, Fuels, and Emissions, American Society of Mechanical Engineers; 2018. https://doi.org/10.1115/GT2018-75165.

[42] Runyon J, Giles A, Marsh R, Pugh D, Goktepe B, Bowen P, et al. Characterization of Additive Layer Manufacturing Swirl Burner Surface Roughness and Its Effects on Flame Stability Using High-Speed Diagnostics. J Eng Gas Turbine Power 2020; 142. https://doi.org/10.1115/1.4044950.

[43] Ebi D, Bombach R, Jansohn P. Swirl flame boundary layer flashback at elevated pressure: Modes of propagation and effect of hydrogen addition. Proceedings of the Combustion Institute 2021; 38: 6345–53. https://doi.org/10.1016/j.proci.2020.06.305.

[44] Ding S, Huang K, Han Y, Valiev D. Numerical study of the influence of wall roughness on laminar boundary layer flashback. Phys Rev Fluids 2021; 6. https://doi.org/10.1103/PhysRevFluids.6.023201.

[45] Al-Fahham M, Hatem FA, Alsaegh AS, Valera Medina A, Bigot S, Marsh R. Experimental Study to Enhance Resistance for Boundary Layer Flashback in Swirl Burners Using Microsurfaces. Volume 4A: Combustion, Fuels and Emissions, American Society of Mechanical Engineers; 2017. https://doi.org/10.1115/GT2017-63367.

[46] Bons JP. A review of surface roughness effects in gas turbines. J Turbomach 2010;132. https://doi.org/10.1115/1.3066315.

[47] Lu M-H, Liou WW. Assessment of Two Low-Reynolds-Number k-e Models in Turbulent Boundary Layers with Surface Roughness. J Spacecr Rockets 2007; 44: 1307–16. https://doi.org/10.2514/1.30738.

[48] Krasilnikov V, Skjefstad VS, Koushan K, Rambech HJ. A Calibration Study with CFD Methodology for Self-Propulsion Simulations at Ship Scale. J Mar Sci Eng 2023; 11: 1342. https://doi.org/10.3390/jmse11071342.

[49] McClain ST, Hodge BK, Bons JP. Predicting Skin Friction and Heat Transfer for Turbulent Flow Over Real Gas Turbine Surface Roughness Using the Discrete Element Method. J Turbomach 2004; 126: 259–67. https://doi.org/10.1115/1.1740779.

[50] Aupoix B. Revisiting the Discrete Element Method for Predictions of Flows Over Rough Surfaces. J Fluids Eng 2016;138. https://doi.org/10.1115/1.4031558.

[51] Bons JP, McClain ST, Wang ZJ, Chi X, Shih TI. A Comparison of Approximate Versus Exact Geometrical Representations of Roughness for CFD Calculations of cf and St. J Turbomach 2008; 130. https://doi.org/10.1115/1.2752190.

[52] Kapsis M, He L, Li YS, Valero O, Wells R, Krishnababu S, et al. Multiscale Parallelized Computational Fluid Dynamics Modeling Toward Resolving Manufacturable Roughness. J Eng Gas Turbine Power 2020; 142. https://doi.org/10.1115/1.4045481.

[53] Stripf M, Schulz A, Bauer H-J. Modeling of Rough-Wall Boundary Layer Transition and Heat Transfer on Turbine Airfoils. J Turbomach 2008; 130. https://doi.org/10.1115/1.2750675.

[54] Taamallah S, Vogiatzaki K, Alzahrani FM, Mokheimer EMA, Habib MA, Ghoniem AF. Fuel flexibility, stability and emissions in premixed hydrogen-rich gas turbine combustion: Technology, fundamentals, and numerical simulations. Appl Energy 2015; 154: 1020–47. https://doi.org/10.1016/j.apenergy.2015.04.044.

[55] Tang C, Zhang Y, Huang Z. Progress in combustion investigations of hydrogen enriched hydrocarbons. Renewable and Sustainable Energy Reviews 2014; 30: 195–216. https://doi.org/10.1016/j.rser.2013.10.005.

[56] Lam K-K, Geipel P, Larfeldt J. Hydrogen Enriched Combustion Testing of SIEMENS Industrial SGT-400 at Atmospheric Conditions. Volume 4A: Combustion, Fuels and Emissions, American Society of Mechanical Engineers; 2014. https://doi.org/10.1115/GT2014-25527.

[57] WHA. Hydrogen Fire Risk Management Philosophy 2022. https://wha-international.com/hydrogen-fire-risk-management/ (accessed March 3, 2022).

[58] Lapenna PE, Berger L, Creta F, Pitsch H. Hydrogen Laminar Flames, 2023, p. 93–139. https://doi.org/10.1007/978-3-031-28412-0_3.

[59] Dong C, Zhou Q, Zhang X, Zhao Q, Xu T, Hui S. Experimental study on the laminar flame speed of hydrogen/natural gas/air mixtures. Frontiers of Chemical Engineering in China 2010; 4: 417–22. https://doi.org/10.1007/s11705-010-0515-8.

[60] Griebel P. Hydrogen Science and Engineering: Materials, Processes, Systems, and Technology. In: Emonts B, Stolten D, editors. vol. 2, Wiley; 2016, p. 1011–32.

[61] Faldella F, Eisenring S, Kim T, Doll U, Jansohn P. Turbulent Flame Speed and Flame Characteristics of Lean Premixed H2-CH4 Flames at Moderate Pressure Levels. J Eng Gas Turbine Power 2024; 146. https://doi.org/10.1115/1.4063524.

[62] Beita J, Talibi M, Sadasivuni S, Balachandran R. Thermoacoustic Instability Considerations for High Hydrogen Combustion in Lean Premixed Gas Turbine Combustors: A Review. Hydrogen 2021; 2: 33–57. https://doi.org/10.3390/hydrogen2010003.

[63] Ge B, Ji Y, Zhang Z, Zang S, Tian Y, Yu H, et al. Experiment study on the combustion performance of hydrogen-enriched natural gas in a DLE burner. Int J Hydrogen Energy 2019; 44: 14023–31. https://doi.org/10.1016/j.ijhydene.2019.03.257.

[64] Gupta S, Malte P, Brunton SL, Novosselov I. Prevention of Lean Flame Blowout Using a Predictive Chemical Reactor Network Control. n.d.

[65] Lieuwen T, Zinn B. Combustion Instability and Blowout Characteristics of Fuel Flexible Combustors. 2007.

[66] Boyce MP. Advanced industrial gas turbines for power generation. Combined Cycle Systems for Near-Zero Emission Power Generation, Elsevier; 2012, p. 44–102. https://doi.org/10.1533/9780857096180.44.

[67] Mitsubishi Power. The hydrogen gas turbine, successfully fired with a 30% fuel mix, is a major step towards a carbon-free society 2018. https://power.mhi.com/special/hydrogen/article_1 (accessed February 26, 2022).

[68] Lewis WK. The Evaporation of a Liquid into a Gas. Transactions of the American Society of Mechanical Engineers 1922; 44: 325–32. https://doi.org/10.1115/1.4058175.

[69] Shchepakina EA, Zubrilin IA, Kuznetsov AY, Tsapenkov KD, Antonov DV, Strizhak PA, et al. Physical and Chemical Features of Hydrogen Combustion and Their Influence on the Characteristics of Gas Turbine Combustion Chambers. Applied Sciences 2023; 13: 3754. https://doi.org/10.3390/app13063754.

[70] Bouvet N, Halter F, Chauveau C, Yoon Y. On the effective Lewis number formulations for lean hydrogen/hydrocarbon/air mixtures. Int J Hydrogen Energy 2013; 38: 5949–60. https://doi.org/10.1016/j.ijhydene.2013.02.098.

[71] Berger L, Attili A, Pitsch H. Intrinsic instabilities in premixed hydrogen flames: Parametric variation of pressure, equivalence ratio, and temperature. Part 1 - Dispersion relations in the linear regime. Combust Flame 2022; 240: 111935. https://doi.org/10.1016/j.combustflame.2021.111935.

[72] Berger L, Attili A, Gauding M, Pitsch H. LES combustion model for premixed turbulent hydrogen flames with thermodiffusive instabilities: a priori and a posteriori analysis. J Fluid Mech 2025; 1003: A33. https://doi.org/10.1017/jfm.2024.1201.

[73] Fruzza F, Chu H, Lamioni R, Grenga T, Galletti C, Pitsch H. Three-dimensional numerical investigation of flashback in premixed hydrogen flames within perforated burners. Combust Flame 2025; 274: 113987. https://doi.org/10.1016/j.combustflame.2025.113987.

[74] Fruzza F, Chu H, Lamioni R, Grenga T, Galletti C, Pitsch H. The importance of Soret effect, preferential diffusion, and conjugate heat transfer for flashback limits of hydrogen-fueled perforated burners. Proceedings of the Combustion Institute 2024; 40: 105581. https://doi.org/10.1016/j.proci.2024.105581.

[75] Raga Mexico G, Nakajima T, Ramanathan V, Ramaswamy V, Artaxo P, Berntsen T, et al. Changes in Atmospheric Constituents and in Radiative Forcing. Cambridge: 2007.

[76] EU. Directive 2010/75/EU of the European Parliament and of the Council of 24 November 2010 on industrial emissions. Official Journal of the European Union 2010; 15: 17–119.

[77] Hill SC, Douglas Smoot L. Modeling of nitrogen oxides formation and destruction in combustion systems. Prog Energy Combust Sci 2000; 26: 417–58. https://doi.org/10.1016/S0360-1285(00)00011-3.

[78] Glassman I, Yetter RA, Glumac NG. Environmental combustion considerations. Combustion, Elsevier; 2015, p. 393–475. https://doi.org/10.1016/B978-0-12-407913-7.00008-6.

[79] Boyce MP. An Overview of Gas Turbines. Gas Turbine Engineering Handbook, Elsevier; 2012, p. 3–88. https://doi.org/10.1016/B978-0-12-383842-1.00001-9.

[80] Hussain T, Talibi M, Balachandran R. Investigating the effect of local addition of hydrogen to acoustically excited ethylene and methane flames. Int J Hydrogen Energy 2019; 44: 11168–84. https://doi.org/10.1016/j.ijhydene.2019.02.182.

[81] Wei Z, Zhen H, Leung C, Cheung C, Huang Z. Effects of H2 addition on the formation and emissions of CO/NO2/NOx in the laminar premixed biogas-hydrogen flame undergoing the flame-wall interaction. Fuel 2020; 259: 116257. https://doi.org/10.1016/j.fuel.2019.116257.

[82] ETN. PROPOSED NOX EMISSIONS REPORTING FOR HYDROGEN-CONTAINING FUELS. Brussels: 2023.

[83] British Standard. ISO 11042-1:1996 Gas Turbines Exhaust Gas Emission Measurement and Evaluation. UK: 1996.

[84] Douglas C, Emerson B, Lieuwen T, Martz T, Steele R, Noble B. NOx Emissions from Hydrogen Methane Fuel Blends. 2022.

[85] Stationary source emissions - Manual and automatic determination of velocity and volume flow rate in ducts - Part 1: Manual reference method. 2013.

[86] Douglas CM, Shaw SL, Martz TD, Steele RC, Noble DR, Emerson BL, et al. Pollutant Emissions Reporting and Performance Considerations for Hydrogen–Hydrocarbon Fuels in Gas Turbines. J Eng Gas Turbine Power 2022; 144. https://doi.org/10.1115/1.4054949.

[87] Goh E, Sirignano M, Li J, Nair V, Emerson B, Lieuwen T, et al. Prediction of minimum achievable NO levels for fuel-staged combustors. Combust Flame 2019; 200: 276–85. https://doi.org/10.1016/j.combustflame.2018.11.027.

[88] Jansohn P. Overview of gas turbine types and applications. Modern Gas Turbine Systems, Elsevier; 2013, p. 21–43. https://doi.org/10.1533/9780857096067.1.21.

[89] GERSEN S, ANIKIN N, MOKHOV A, LEVINSKY H. Ignition properties of methane/hydrogen mixtures in a rapid compression machine. Int J Hydrogen Energy 2008; 33: 1957–64. https://doi.org/10.1016/j.ijhydene.2008.01.017.

[90] Noble DR, Zhang Q, Shareef A, Tootle J, Meyers A, Lieuwen T. Syngas Mixture Composition Effects Upon Flashback and Blowout. Volume 1: Combustion and Fuels, Education, ASMEDC; 2006, p. 357–68. https://doi.org/10.1115/GT2006-90470.

[91] Noble D, Wu D, Emerson B, Sheppard S, Lieuwen T, Angello L. Assessment of Current Capabilities and Near-Term Availability of Hydrogen-Fired Gas Turbines Considering a Low-Carbon Future. J Eng Gas Turbine Power 2021; 143. https://doi.org/10.1115/1.4049346.

[92] Cappelletti A, Martelli F. Investigation of a pure hydrogen fueled gas turbine burner. Int J Hydrogen Energy 2017; 42: 10513–23. https://doi.org/10.1016/j.ijhydene.2017.02.104.

[93] Jo S. Flashback in diluted hydrogen flames. Int J Hydrogen Energy 2025; 126: 159–69. https://doi.org/10.1016/j.ijhydene.2025.04.029.

[94] Bertsch J, Poinsot T, Bertier N. Boundary layer flashback of H2/Air premixed flames in a swirling flow around a central body. Combust Flame 2025; 276: 114123. https://doi.org/10.1016/j.combustflame.2025.114123.

[95] von Elbe G, Mentser M. Further Studies of the Structure and Stability of Burner Flames. J Chem Phys 1945; 13: 89–100. https://doi.org/10.1063/1.1724004.

[96] Grumer J, Margaret E. Harris, Valeria R. Rowe. Fundamental flashback, blowoff, and yellow-tip limits of fuel gas-air mixtures. Pittsburgh USA: 1955.

[97] Baumgartner G. Flame flashback in premixed hydrogen-air combustion systems. Technical University of Munich, 2014.

[98] Huang Y, Yang V. Dynamics and stability of lean-premixed swirl-stabilized combustion. Prog Energy Combust Sci 2009; 35: 293–364. https://doi.org/10.1016/j.pecs.2009.01.002.

[99] Candel S. Combustion dynamics and control: Progress and challenges. Proceedings of the Combustion Institute 2002; 29: 1–28. https://doi.org/10.1016/S1540-7489(02)80007-4.

[100] Ducruix S, Candel S, Schuller T, Durox D. Combustion Instability Mechanisms in Premixed Combustors. Combustion Instabilities in Gas Turbine Engines, Reston, VA: American Institute of Aeronautics and Astronautics; 2006, p. 179–212. https://doi.org/10.2514/5.9781600866807.0179.0212.

[101] Emmert TA. State Space Modeling of Thermoacoustic Systems with Application to Intrinsic Feedback. 2016.

[102] Morgans AS. Thermoacoustic instabilities. Combustion SIG Meeting, Imperial College London; 2017.

[103] Lam K-K, Parsania N. Hydrogen Enriched Combustion Testing of Siemens SGT-400 at High Pressure Conditions. Volume 4B: Combustion, Fuels and Emissions, American Society of Mechanical Engineers; 2016. https://doi.org/10.1115/GT2016-57470.

[104] Zhang J, Ratner A. Experimental study on the excitation of thermoacoustic instability of hydrogen-methane/air premixed flames under atmospheric and elevated pressure conditions. Int J Hydrogen Energy 2019; 44: 21324–35. https://doi.org/10.1016/j.ijhydene.2019.06.142.

[105] Emadi M, Karkow D, Salameh T, Gohil A, Ratner A. Flame structure changes resulting from hydrogen-enrichment and pressurization for low-swirl premixed methane–air flames. Int J Hydrogen Energy 2012; 37: 10397–404. https://doi.org/10.1016/j.ijhydene.2012.04.017.

[106] Moëll D, Lörstad D, Bai X-S. LES of Hydrogen Enriched Methane/Air Combustion in the SGT-800 Burner at Real Engine Conditions. Volume 4B: Combustion, Fuels, and Emissions, American Society of Mechanical Engineers; 2018. https://doi.org/10.1115/GT2018-76434.

[107] Combustion Instabilities: Basic Concepts. Combustion Instabilities in Gas Turbine Engines, Reston, VA: American Institute of Aeronautics and Astronautics; 2006, p. 3–26. https://doi.org/10.2514/5.9781600866807.0003.0026.

[108] Psomoglou I. Influence of surface roughness on burner characteristics and combustion performance of AM combustors. Doctor of Philosophy. Cardiff University, 2023.

[109] Han M, Han X, Wang X, Li L. Thermoacoustic instabilities with varying geometries of the main-stage exit in a centrally staged burner. Physics of Fluids 2022; 34. https://doi.org/10.1063/5.0113674.

[110] Stefan E, Talic B, Larring Y, Gruber A, Peters TA. Materials challenges in hydrogen-fuelled gas turbines. International Materials Reviews 2021: 1–26. https://doi.org/10.1080/09506608.2021.1981706.

[111] Wu J, Brown P, Diakunchak I, Gulati A, Lenze M, Koestlin B. Advanced Gas Turbine Combustion System Development for High Hydrogen Fuels. Volume 2: Turbo Expo 2007, ASMEDC; 2007, p. 1085–91. https://doi.org/10.1115/GT2007-28337.

[112] Asai T, Akiyama Y, Dodo S. Development of a State-of-the-Art Dry Low NOx Gas Turbine Combustor for IGCC with CCS. Recent Advances in Carbon Capture and Storage, InTech; 2017. https://doi.org/10.5772/66742.

[113] ETN. Hydrogen gas turbines - the path towards a zero-carbon gas turbine. 2020.

[114] Liu Y, Sun X, Sethi V, Nalianda D, Li Y-G, Wang L. Review of modern low emissions combustion technologies for aero gas turbine engines. Progress in Aerospace Sciences 2017; 94: 12–45. https://doi.org/10.1016/j.paerosci.2017.08.001.

[115] Magnusson R, Andersson M. Operation of SGT-600 (24 MW) DLE Gas Turbine with Over 60 % H2 in Natural Gas. Volume 9: Oil and Gas Applications; Organic Rankine Cycle Power Systems; Steam Turbine, American Society of Mechanical Engineers; 2020. https://doi.org/10.1115/GT2020-16332.

[116] Mosier S, Pierce R. Advanced combustion systems for stationary gas turbine engines. Washington, DC, USA: 1980.

[117] Guteša Božo M, Mashruk S, Zitouni S, Valera-Medina A. Humidified ammonia/hydrogen RQL combustion in a trigeneration gas turbine cycle. Energy Convers Manag 2021; 227: 113625. https://doi.org/10.1016/j.enconman.2020.113625.

[118] Samuelsen GS, Brouwer J, Vardakas MA, Holdeman JD. Experimental and modeling investigation of the effect of air preheat on the formation of NOx in an RQL combustor. Heat and Mass Transfer 2013; 49: 219–31. https://doi.org/10.1007/s00231-012-1080-0.

[119] Krebs W, Schulz A, Witzel B, Johnson C, Laster W, Pent J, et al. Advanced Combustion System for High Efficiency (ACE) of the new SGT5/6-9000HL Gas Turbine. Proceedings of ASME Turbo Expo 2022, Rotterdam: 2022, p. 1–11. https://doi.org/10.1115/GT2022-82299.

[120] Vandervort C, Leach D, Walker D, Sasser J. Commercialization and Fleet Experience of the 7/9HA Gas Turbine Combined Cycle. ASME Turbo Expo 2019: Turbomachinery Technical Conference and Exposition, Phoenix, Arizona, USA: 2019. https://doi.org/10.1115/GT2019-91594.

[121] John Marra. Advanced Hydrogen Turbine Development Final Technical Report. Orlando, Florida: 2015.

[122] Stiehl B, Genova T, Otero M, Martin S, Ahmed K. Fuel Stratification Influence on NOx Emission in a Premixed Axial Reacting Jet-in-Crossflow at High Pressure. vol. 1. 2020.

[123] Haj Ayed A, Kusterer K, Funke HH-W, Keinz J, Striegan C, Bohn D. Experimental and numerical investigations of the dry-low-NOx hydrogen micromix combustion chamber of an industrial gas turbine. Propulsion and Power Research 2015; 4: 123–31. https://doi.org/10.1016/j.jppr.2015.07.005.

[124] Lee H, Hernandez S, McDonell V, Steinthorsson E, Mansour A, Hollon B. Development of Flashback Resistant Low-Emission Micro-Mixing Fuel Injector for 100% Hydrogen and Syngas Fuels. Volume 2: Combustion, Fuels and Emissions, ASMEDC; 2009, p. 411–9. https://doi.org/10.1115/GT2009-59502.

[125] Weiland NT, Sidwell TG, Strakey PA. Testing of a Hydrogen Diffusion Flame Array Injector at Gas Turbine Conditions. Combustion Science and Technology 2013; 185: 1132–50. https://doi.org/10.1080/00102202.2013.781164.

[126] Asai T, Miura K, Matsubara Y, Akiyama Y, Karishuku M, Dodo S, et al. DEVELOPMENT OF GAS TURBINE COMBUSTORS FOR FUEL FLEXIBILITY. The Future of Gas Turbine Technology 8th International Gas Turbine Conference, Brussels: 2016.

[127] Funke HH-W, Beckmann N, Abanteriba S. An overview on dry low NOx micromix combustor development for hydrogen-rich gas turbine applications. Int J Hydrogen Energy 2019; 44: 6978–90. https://doi.org/10.1016/j.ijhydene.2019.01.161.

[128] Goldmeer J. Solving the challenge of lean hydrogen premix combustion with highly reactive fuel Solving the challenge of lean hydrogen premix combustion with highly reactive fuels. Turbomachinery Magazine 2020.

[129] Ayed AH. Numerical Characterization and development of the Dry Low NOx High Hydrogen Content Fuel Micromix Combustion for Gas Turbine Applications. Ph.D. Thesis. Aachen University, 2017.

[130] Hermeth S, Panek L, Witzel B, Grandt C, Koestlin B, Wanjura S, et al. 100% H2 DLE Gas Turbine Combustion Technology Platform Development. Volume 3B: Combustion, Fuels, and Emissions, American Society of Mechanical Engineers; 2024. https://doi.org/10.1115/GT2024-128517.

[131] Parsania N, Hermeth S, Witzel B, Yilmaz E, Fourcade S, Garmadi S, et al. HYFLEXPOWER Project: Demonstration of an Industrial Power-to-H2-to-Power Advanced Plant Concept with Up to 100% H2 in an SGT-400 Gas Turbine. Volume 2: Ceramics and Ceramic Composites; Coal, Biomass, Hydrogen, and Alternative Fuels, American Society of Mechanical Engineers; 2024. https://doi.org/10.1115/GT2024-124016.

[132] Eldrainy YA, Saqr KM, Aly HS, Jaafar MNM. CFD insight of the flow dynamics in a novel swirler for gas turbine combustors. International Communications in Heat and Mass Transfer 2009; 36: 936–41. https://doi.org/10.1016/j.icheatmasstransfer.2009.06.013.

[133] Zavaleta-Luna DA, Vigueras-Zúñiga MO, Herrera-May AL, Zamora-Castro SA, Tejeda-del-Cueto ME. Optimized Design of a Swirler for a Combustion Chamber of Non-Premixed Flame Using Genetic Algorithms. Energies (Basel) 2020; 13: 2240. https://doi.org/10.3390/en13092240.

[134] Lefebvre AH, Ballal DR. Gas Turbine Combustion Alternative fuels and emissions. 3rd ed. CRC Press; 2010.

[135] Chigier NA, Bee´r JM. Velocity and Static-Pressure Distributions in Swirling Air Jets Issuing from Annular and Divergent Nozzles. Journal of Basic Engineering 1964; 86: 788–96. https://doi.org/10.1115/1.3655954.

[136] Roux S, Lartigue G, Poinsot T, Meier U, Bérat C. Studies of mean and unsteady flow in a swirled combustor using experiments, acoustic analysis, and large eddy simulations. Combust Flame 2005; 141: 40–54. https://doi.org/10.1016/j.combustflame.2004.12.007.

[137] Wang S, Yang V, Hsiao G, Hsieh S-Y, Mongia HC. Large-eddy simulations of gas-turbine swirl injector flow dynamics. J Fluid Mech 2007; 583: 99–122. https://doi.org/10.1017/S0022112007006155.

[138] Mao R, Wang J, Zhang W, An Z, Lin W, Zhang M, et al. Effect of high hydrogen enrichment on the outer-shear-layer flame of confined lean premixed CH4/H2/air swirl flames. Int J Hydrogen Energy 2021; 46: 17969–81. https://doi.org/10.1016/j.ijhydene.2021.02.181.

[139] İlbaş M, Karyeyen S, Yilmaz İ. Effect of swirl number on combustion characteristics of hydrogen-containing fuels in a combustor. Int J Hydrogen Energy 2016; 41: 7185–91. https://doi.org/10.1016/j.ijhydene.2015.12.107.

[140] Yılmaz İ. Effect of Swirl Number on Combustion Characteristics in a Natural Gas Diffusion Flame. J Energy Resour Technol 2013;135. https://doi.org/10.1115/1.4024222.

[141] Abdelkader H, Abdelhalim B. The Effect of Swirl Intensity on the Flow Behavior and Combustion Characteristics of a Lean Propane-Air Flame. Fluid Dynamics & Materials Processing 2022; 18: 1749–62. https://doi.org/10.32604/fdmp.2022.022006.

[142] Pugh D, Bowen P, Navaratne R, Goktepe B, Giles A, Valera Medina A, et al. Influence of Variable Swirl on Emissions in a Non-Premixed Fuel-Flexible Burner at Elevated Ambient Conditions. J Eng Gas Turbine Power 2024; 146. https://doi.org/10.1115/1.4063786.

[143] Beér JM, Chigier NA. Combustion aerodynamics. Barking: Applied Science Publishers Ltd; 1972.

[144] Navrotsky V, Piegert S, Andersson O, Graichen A, Avdovic P. Industrialisation and Current Field Experience of Additively Manufactured Gas Turbine Components. The Future of Gas Turbine Technology 9th International Gas Turbine Conference, 11 October 2018, Brussels, Belgium: 2018.

[145] Siemens Energy. Additive Manufacturing. 2020.

[146] British Standard. BS 1134:2010 Assessment of surface texture - Guidance and general information. 2010.

[147] Strano G, Hao L, Everson RM, Evans KE. Surface roughness analysis, modelling and prediction in selective laser melting. J Mater Process Technol 2013; 213: 589–97. https://doi.org/10.1016/j.jmatprotec.2012.11.011.

[148] Mohamed Fahad S, Mahashar Ali J, Siddhi Jailani H. Characterization of Surface Roughness of Ground Specimens Using Image Processing. Advances in Design and Thermal Systems, Springer Singapore; 2021, p. 133–41. https://doi.org/10.1007/978-981-33-6428-8_9.

[149] Ruzova TA, Haddadi B. Surface roughness and its measurement methods - Analytical review. Results in Surfaces and Interfaces 2025; 19: 100441. https://doi.org/10.1016/j.rsurfi.2025.100441.

[150] Rossler T, Mandat D, Gallo J, Hrabovsky M, Pochmon M, Havranek V. Optical 3D methods for measurement of prosthetic wear of total hip arthroplasty: principles, verification and results. Opt Express 2009; 17: 12723. https://doi.org/10.1364/OE.17.012723.

[151] Giessibl FJ. AFM's path to atomic resolution. Materials Today 2005; 8: 32–41. https://doi.org/10.1016/S1369-7021(05)00844-8.

[152] Kadivar M, Tormey D, McGranaghan G. A review on turbulent flow over rough surfaces: Fundamentals and theories. International Journal of Thermofluids 2021; 10: 100077. https://doi.org/10.1016/j.ijft.2021.100077.

[153] Gong Y, Xu J, Buchanan RC. Surface roughness: A review of its measurement at micro-/nano-scale. Physical Sciences Reviews 2018; 3. https://doi.org/10.1515/psr-2017-0057.

[154] Schaeffler. Technical Pocket Guide. 2021.

[155] Xu W. Direct Additive Manufacturing Techniques for Metal Parts: SLM, EBM, Laser Metal Deposition. Encyclopedia of Materials: Metals and Alloys, Elsevier; 2022, p. 290–318. https://doi.org/10.1016/B978-0-12-819726-4.00095-8.

[156] Zhang C, Ouyang D, Pauly S, Liu L. 3D printing of bulk metallic glasses. Materials Science and Engineering: R: Reports 2021; 145: 100625. https://doi.org/10.1016/j.mser.2021.100625.

[157] Obilanade D, Dordlofva C, Törlind P. Surface Roughness Considerations in Design for Additive Manufacturing - A Literature Review. Proceedings of the Design Society 2021; 1: 2841–50. https://doi.org/10.1017/pds.2021.545.

[158] Sanaei N, Fatemi A. Analysis of the effect of surface roughness on fatigue performance of powder bed fusion additive manufactured metals. Theoretical and Applied Fracture Mechanics 2020; 108: 102638. https://doi.org/10.1016/j.tafmec.2020.102638.

[159] Artzt K, Mishurova T, Bauer P-P, Gussone J, Barriobero-Vila P, Evsevleev S, et al. Pandora's Box–Influence of Contour Parameters on Roughness and Subsurface Residual Stresses in Laser Powder Bed Fusion of Ti-6Al-4V. Materials 2020; 13: 3348. https://doi.org/10.3390/ma13153348.

[160] Baciu AM, Bejinariu C, Corăbieru A, Mihalache E, Lupu–Poliac M, Baciu C, et al. Influence of process parameters for Selective Laser Melting on the roughness of 3D printed surfaces in Co-Cr dental alloy powder. IOP Conf Ser Mater Sci Eng 2019; 572: 012054. https://doi.org/10.1088/1757-899X/572/1/012054.

[161] Balbaa MA, Ghasemi A, Fereiduni E, Elbestawi MA, Jadhav SD, Kruth J-P. Role of powder particle size on laser powder bed fusion processability of AlSi10mg alloy. Addit Manuf 2021; 37: 101630. https://doi.org/10.1016/j.addma.2020.101630.

[162] Louw DF, Pistorius PGH. The effect of scan speed and hatch distance on prior-beta grain size in laser powder bed fused Ti-6Al-4V. The International Journal of Advanced Manufacturing Technology 2019; 103: 2277–86. https://doi.org/10.1007/s00170-019-03719-w.

[163] Khorasani AM, Gibson I, Ghasemi A, Ghaderi A. Modelling of laser powder bed fusion process and analysing the effective parameters on surface characteristics of Ti-6Al-4V. Int J Mech Sci 2020; 168: 105299. https://doi.org/10.1016/j.ijmecsci.2019.105299.

[164] Soler D, Telleria M, García-Blanco MB, Espinosa E, Cuesta M, Arrazola PJ. Prediction of Surface Roughness of SLM Built Parts after Finishing Processes Using an Artificial Neural Network. Journal of Manufacturing and Materials Processing 2022; 6: 82. https://doi.org/10.3390/jmmp6040082.

[165] Wu D, Wei Y, Terpenny J. Surface Roughness Prediction in Additive Manufacturing Using Machine Learning. Volume 3: Manufacturing Equipment and Systems, American Society of Mechanical Engineers; 2018. https://doi.org/10.1115/MSEC2018-6501.

[166] Zhang D, Yu J, Li H, Zhou X, Song C, Zhang C, et al. Investigation of Laser Polishing of Four Selective Laser Melting Alloy Samples. Applied Sciences 2020; 10: 760. https://doi.org/10.3390/app10030760.

[167] Sagbas B. Post-Processing Effects on Surface Properties of Direct Metal Laser Sintered AlSi10Mg Parts. Metals and Materials International 2020; 26: 143–53. https://doi.org/10.1007/s12540-019-00375-3.

[168] Kaynak Y, Tascioglu E. Post-processing effects on the surface characteristics of Inconel 718 alloy fabricated by selective laser melting additive manufacturing. Progress in Additive Manufacturing 2020; 5: 221–34. https://doi.org/10.1007/s40964-019-00099-1.

[169] Lee J-Y, Nagalingam AP, Yeo SH. A review on the state-of-the-art of surface finishing processes and related ISO/ASTM standards for metal additive manufactured components. Virtual Phys Prototyp 2021; 16: 68–96. https://doi.org/10.1080/17452759.2020.1830346.

[170] Achenbach E, Heinecke E. On vortex shedding from smooth and rough cylinders in the range of Reynolds numbers 6×10 3 to 5×10 6. J Fluid Mech 1981; 109: 239–51. https://doi.org/10.1017/S002211208100102X.

[171] Antonia RA, Krogstad P-Å. Turbulence structure in boundary layers over different types of surface roughness. Fluid Dyn Res 2001; 28: 139–57. https://doi.org/10.1016/S0169-5983(00)00025-3.

[172] Yun Y il, Park IY, Song SJ. Performance Degradation due to Blade Surface Roughness in a Single-Stage Axial Turbine. J Turbomach 2005; 127: 137–43. https://doi.org/10.1115/1.1811097.

[173] Schäffler A. Experimental and Analytical Investigation of the Effects of Reynolds Number and Blade Surface Roughness on Multistage Axial Flow Compressors. Journal of Engineering for Power 1980; 102: 5–12. https://doi.org/10.1115/1.3230232.

[174] Dunn MG, Kim J, Civinskas KC, Boyle RJ. Time-Averaged Heat Transfer and Pressure Measurements and Comparison with Prediction for a Two-Stage Turbine. Volume 4: Heat Transfer; Electric Power; Industrial and Cogeneration, American Society of Mechanical Engineers; 1992. https://doi.org/10.1115/92-GT-194.

[175] Blair MF. An Experimental Study Heat Transfer in a Large-Scale Turbine Rotor Passage. J Turbomach 1994; 116: 1–13. https://doi.org/10.1115/1.2928273.

[176] Boyle RJ, Civinskas KC. Two-Dimensional Navier–Stokes Heat Transfer Analysis for Rough Turbine Blades. AIAA 1991; 2129.

[177] Boyle RJ. Prediction of Surface Roughness and Incidence Effects on Turbine Performance. J Turbomach 1994; 116: 745–51. https://doi.org/10.1115/1.2929468.

[178] Schlichting H. Boundary Layer Theory. 7th ed. New York: McGraw-Hill; 1979.

[179] Aupoix B, Spalart PR. Extensions of the Spalart–Allmaras turbulence model to account for wall roughness. Int J Heat Fluid Flow 2003; 24: 454–62. https://doi.org/10.1016/S0142-727X(03)00043-2.

[180] McClain ST, Hodge BK, Bons JP. Predicting Skin Friction and Heat Transfer for Turbulent Flow Over Real Gas Turbine Surface Roughness Using the Discrete Element Method. J Turbomach 2004; 126: 259–67. https://doi.org/10.1115/1.1740779.

[181] Bons JP, McClain ST. The Effect of Real Turbine Roughness with Pressure Gradient on Heat Transfer. J Turbomach 2004; 126: 385–94. https://doi.org/10.1115/1.1738120.

[182] Bons JP, McClain ST, Wang ZJ, Chi X, Shih TI. A Comparison of Approximate Versus Exact Geometrical Representations of Roughness for CFD Calculations of cf and St. J Turbomach 2008; 130. https://doi.org/10.1115/1.2752190.

[183] Al-Ajmi R, Al-Shaghdari M, Goktepe B, Psomoglou I, Bowen P. Critical Appraisal of Integrated Computational Fluid Dynamics/Surface Roughness Models for Additive Manufactured Swirl Burners. J Eng Gas Turbine Power 2025; 147. https://doi.org/10.1115/1.4067738.

[184] Kadivar M, Tormey D, McGranaghan G. A comparison of RANS models used for CFD prediction of turbulent flow and heat transfer in rough and smooth channels. International Journal of Thermofluids 2023; 20: 100399. https://doi.org/10.1016/j.ijft.2023.100399.

[185] Adams T, Grant C, Watson H. A Simple Algorithm to Relate Measured Surface Roughness to Equivalent Sand-grain Roughness. International Journal of Mechanical Engineering and Mechatronics 2012. https://doi.org/10.11159/ijmem.2012.008.

[186] Siemens Digital Industries Software. Simcenter STAR-CCM+ User Guide, version 2021.1 2021.

[187] Aghaei Jouybari M, Yuan J, Brereton GJ, Murillo MS. Data-driven prediction of the equivalent sand-grain height in rough-wall turbulent flows. J Fluid Mech 2021; 912: A8. https://doi.org/10.1017/jfm.2020.1085.

[188] Baker C, Johnson T, Flynn D, Hemida H, Quinn A, Soper D, et al. Computational techniques. Train Aerodynamics, Elsevier; 2019, p. 53–71. https://doi.org/10.1016/B978-0-12-813310-1.00004-6.

[189] Kundu PK, Cohen IM, Dowling DR. Boundary Layers and Related Topics. Fluid Mechanics. 6th ed., Elsevier; 2016, p. 469–532. https://doi.org/10.1016/B978-0-12-405935-1.00010-1.

[190] Panton RL. Incompressible Flow. Wiley; 2013. https://doi.org/10.1002/9781118713075.

[191] Townsend A. The structure of turbulent shear flow. 2nd ed. Cambridge university press; 1976.

[192] Launder BE, Spalding DB. The numerical computation of turbulent flows. Comput Methods Appl Mech Eng 1974; 3: 269–89. https://doi.org/10.1016/0045-7825(74)90029-2.

[193] Wilcox DC. Turbulence modeling for CFD. vol. 2. La Canada, CA: DCW industries; 1998.

[194] Reichardt H. Vollständige Darstellung der turbulenten Geschwindigkeitsverteilung in glatten Leitungen. ZAMM - Journal of Applied Mathematics and Mechanics / Zeitschrift Für Angewandte Mathematik Und Mechanik 1951; 31: 208–19. https://doi.org/10.1002/zamm.19510310704.

[195] Schlichting H. Experimental investigation of the problem of surface roughness. National Advisory Commitee for Aeronautics; 1937.

[196] Nikuradse J. Stromungsgesetze in rauhen Rohren. Vdi-Forschungsheft 1933;361.

[197] Coleman HW, Hodge BK, Taylor RP. A Re-Evaluation of Schlichting's Surface Roughness Experiment. J Fluids Eng 1984; 106: 60–5. https://doi.org/10.1115/1.3242406.

[198] Jayatilleke CVC V. The influence of Prandtl number and surface roughness on the resistance of the laminar sublayer to momentum and heat transfer. Prog Heat Mass Transfer 1 1969:193–321.

[199] ANSYS I. ANSYS Fluent User's Guide (Version 2023 R2) 2023.

[200] Khazaee R, Rahmansetayesh MA, Hajizadeh S. Calibration of a roughness function model for ship simulations in the transitionally rough regime. Physics of Fluids 2025; 37. https://doi.org/10.1063/5.0301542.

[201] Blocken B, Stathopoulos T, Carmeliet J. CFD simulation of the atmospheric boundary layer: wall function problems. Atmos Environ 2007; 41: 238–52. https://doi.org/10.1016/j.atmosenv.2006.08.019.

[202] Simcenter STAR CCM+. How Wall Roughness is modelled in Simcenter STAR-CCM+? Siemens 2025. https://support.sw.siemens.com/en-US/okba/KB000158184_EN_US (accessed August 18, 2025).

[203] Durbin PA, Medic G, Seo J-M, Eaton JK, Song S. Rough Wall Modification of Two-Layer k−ε. J Fluids Eng 2001; 123: 16–21. https://doi.org/10.1115/1.1343086.

[204] Knopp T, Eisfeld B, Calvo JB. A new extension for k– turbulence models to account for wall roughness. Int J Heat Fluid Flow 2009; 30: 54–65. https://doi.org/10.1016/j.ijheatfluidflow.2008.09.009.

[205] Rodriguez S. Applied Theory: Practical Turbulence Estimates. Applied Computational Fluid Dynamics and Turbulence Modeling, Cham: Springer International Publishing; 2019, p. 69–120. https://doi.org/10.1007/978-3-030-28691-0_3.

[206] Frisch U, Kolmogorov AN. Turbulence: The Legacy of A. N. Kolmogorov. Cambridge university press; 1995.

[207] Rodriguez S. LES and DNS Turbulence Modeling. Applied Computational Fluid Dynamics and Turbulence Modeling, Cham: Springer International Publishing; 2019, p. 197–223. https://doi.org/10.1007/978-3-030-28691-0_5.

[208] Pope SB. Ten questions concerning the large-eddy simulation of turbulent flows. New J Phys 2004; 6: 35–35. https://doi.org/10.1088/1367-2630/6/1/035.

[209] Spalart PR. Comments on the Feasibility of LES for Wings and on the Hybrid RANS/LES Approach. roceedings of the First AFOSR International Conference on DNS/LES, 1997, p. 137–47.

[210] Pan C, Zhang W. A comprehensive assessment on detached eddy simulation and delayed detached eddy simulation approaches in large-scale rotating separated flow in a centrifugal impeller under small flow rate. Physics of Fluids 2023; 35. https://doi.org/10.1063/5.0169015.

[211] Spalart PR, Deck S, Shur ML, Squires KD, Strelets MKh, Travin A. A New Version of Detached-eddy Simulation, Resistant to Ambiguous Grid Densities. Theor Comput Fluid Dyn 2006; 20: 181–95. https://doi.org/10.1007/s00162-006-0015-0.

[212] Shur ML, Spalart PR, Strelets MKh, Travin AK. A hybrid RANS-LES approach with delayed-DES and wall-modelled LES capabilities. Int J Heat Fluid Flow 2008; 29: 1638–49. https://doi.org/10.1016/j.ijheatfluidflow.2008.07.001.

[213] Xu X, Li H, Lin Y. Mesh–Order Independence in CFD Simulation. IEEE Access 2019; 7: 119069–81. https://doi.org/10.1109/ACCESS.2019.2937450.

[214] Jo H, Kang K, Park J, Ryu C, Ahn H, Go Y. Detailed assessment of mesh sensitivity for CFD simulation of coal combustion in a tangential-firing boiler. Journal of Mechanical Science and Technology 2020; 34: 917–30. https://doi.org/10.1007/s12206-020-0141-4.

[215] Russell MB, Surendran PN, Probert SD. Quantifying acceptable mesh dependencies for computational investigations of airflows within rooms. Appl Energy 2002; 72: 409–25. https://doi.org/10.1016/S0306-2619(02)00012-0.

[216] Knotek S, Schmelter S, Olbrich M. Assessment of different parameters used in mesh independence studies in two-phase slug flow simulations. Measurement: Sensors 2021; 18: 100317. https://doi.org/10.1016/j.measen.2021.100317.

[217] Seifollahi Moghadam Z, Guibault F, Garon A. On the Evaluation of Mesh Resolution for Large-Eddy Simulation of Internal Flows Using Openfoam. Fluids 2021; 6: 24. https://doi.org/10.3390/fluids6010024.

[218] Zhiyin Y. Large-eddy simulation: Past, present and the future. Chinese Journal of Aeronautics 2015; 28: 11–24. https://doi.org/10.1016/j.cja.2014.12.007.

[219] Wurps H, Steinfeld G, Heinz S. Grid-Resolution Requirements for Large-Eddy Simulations of the Atmospheric Boundary Layer. Boundary Layer Meteorol 2020; 175: 179–201. https://doi.org/10.1007/s10546-020-00504-1.

[220] Basu S, DeMarco AW, He P. On the Dissipation Rate of Temperature Fluctuations in Stably Stratified Flows 2020. https://doi.org/10.1007/s10652-020-09761-7.

[221] Psomoglou I, Goktepe B, Crayford A, Bowen P, Morris S, Jones N. Influence of AM Generated Burner Surface Roughness on NO x Emissions and Operability of Hydrogen-Rich Fuels. Combustion Science and Technology 2024: 1–20. https://doi.org/10.1080/00102202.2024.2390699.

[222] Stavropoulos P, Foteinopoulos P, Papacharalampopoulos A, Tsoukantas G. Warping in SLM additive manufacturing processes: estimation through thermo-mechanical analysis. The International Journal of Advanced Manufacturing Technology 2019; 104: 1571–80. https://doi.org/10.1007/s00170-019-04105-2.

[223] Vafadar A, Guzzomi F, Rassau A, Hayward K. Advances in Metal Additive Manufacturing: A Review of Common Processes, Industrial Applications, and Current Challenges. Applied Sciences 2021; 11: 1213. https://doi.org/10.3390/app11031213.

[224] Ablyaz TR, Shlykov ES, Muratov KR, Sirotenko LD, Matygullina E V. Creation of Textured Surfaces by Electrical Discharge Machining. Russian Engineering Research 2020; 40: 880–1. https://doi.org/10.3103/S1068798X20100044.

[225] Karmiris-Obratański P, Zagórski K, Papazoglou EL, Markopoulos AP. Surface texture and integrity of electrical discharged machined titanium alloy. The International Journal of Advanced Manufacturing Technology 2021; 115: 733–47. https://doi.org/10.1007/s00170-020-06159-z.

[226] Mehra R, Singh H, Chaubey SK. Evaluating Surface Roughness of Ductile Cast Iron Machined by EDM Using Solid and Hollow Cylindrical Copper Electrodes. Periodica Polytechnica Mechanical Engineering 2025; 69: 46–54. https://doi.org/10.3311/PPme.38763.

[227] Subramanian R, Rule D, Nazik O. Dependence of LPBF Surface Roughness on Laser Incidence Angle and Component Build Orientation. Volume 7: Industrial and Cogeneration; Manufacturing Materials and Metallurgy, American Society of Mechanical Engineers; 2021. https://doi.org/10.1115/GT2021-59755.

[228] Koutiri I, Pessard E, Peyre P, Amlou O, De Terris T. Influence of SLM process parameters on the surface finish, porosity rate and fatigue behavior of as-built Inconel 625 parts. J Mater Process Technol 2018; 255: 536–46. https://doi.org/10.1016/j.jmatprotec.2017.12.043.

[229] Lieneke T, Denzer V, Adam GAO, Zimmer D. Dimensional Tolerances for Additive Manufacturing: Experimental Investigation for Fused Deposition Modeling. Procedia CIRP 2016; 43: 286–91. https://doi.org/10.1016/j.procir.2016.02.361.

[230] Lieneke T, Lammers S, Zimmer D. Geometrical Deviations in Additive Manufacturing-Influences on the Manufacturing Accuracy. Proceedings of the 32nd Annual International Solid Freeform Fabrication Symposium, 2021.

[231] Klingaa CG, Dahmen T, Baier-Stegmaier S, Mohanty S, Hattel JH. Investigation of the roughness variation along the length of LPBF manufactured straight channels. Nondestructive Testing and Evaluation 2020; 35: 304–14. https://doi.org/10.1080/10589759.2020.1785445.

[232] Runyon J, Marsh R, Bowen P, Pugh D, Giles A, Morris S. Lean methane flame stability in a premixed generic swirl burner: Isothermal flow and atmospheric combustion characterization. Exp Therm Fluid Sci 2018; 92:125–40. https://doi.org/10.1016/j.expthermflusci.2017.11.019.

[233] Runyon J. Gas Turbine Fuel Flexibility: Pressurized Swirl Flame Stability, Thermoacoustics, And Emissions. Doctor of Philosophy. Cardiff University, 2017.

[234] Broida HP, Gaydon AG. The mechanism of formation of OH, CH and HCO in flame spectra, using deuterium as tracer. Proc R Soc Lond A Math Phys Sci, 1953, p. 60–9.

[235] Kojima J, Ikeda Y, Nakajima T. Basic aspects of OH(A), CH(A), and C2(d) chemiluminescence in the reaction zone of laminar methane–air premixed flames. Combust Flame 2005; 140: 34–45. https://doi.org/10.1016/j.combustflame.2004.10.002.

[236] Hall JM, Petersen EL. An optimized kinetics model for OH chemiluminescence at high temperatures and atmospheric pressures. Int J Chem Kinet 2006; 38: 714–24. https://doi.org/10.1002/kin.20196.

[237] Zhao M, Buttsworth D, Choudhury R. Experimental and numerical study of OH* chemiluminescence in hydrogen diffusion flames. Combust Flame 2018; 197:369–77. https://doi.org/10.1016/j.combustflame.2018.08.019.

[238] Kathrotia T, Fikri M, Bozkurt M, Hartmann M, Riedel U, Schulz C. Study of the H+O+M reaction forming OH∗: Kinetics of OH∗ chemiluminescence in hydrogen combustion systems. Combust Flame 2010; 157: 1261–73. https://doi.org/10.1016/j.combustflame.2010.04.003.

[239] Hall JM, Petersen EL. An optimized kinetics model for OH chemiluminescence at high temperatures and atmospheric pressures. Int J Chem Kinet 2006; 38:714–24. https://doi.org/10.1002/kin.20196.

[240] Carrington T. Electronic Quenching of OH(2Σ+) in Flames and Its Significance in the Interpretation of Rotational Relaxation. J Chem Phys 1959; 30: 1087–95. https://doi.org/10.1063/1.1730086.

[241] Kathrotia T, Fikri M, Bozkurt M, Hartmann M, Riedel U, Schulz C. Study of the H+O+M reaction forming OH∗: Kinetics of OH∗ chemiluminescence in hydrogen combustion systems. Combust Flame 2010; 157: 1261–73. https://doi.org/10.1016/j.combustflame.2010.04.003.

[242] Gaydon AG. The Spectroscopy of Flames. 2nd ed. Netherlands: Springer Netherlands; 1974.

[243] Dasch CJ. One-dimensional tomography: a comparison of Abel, onion-peeling, and filtered backprojection methods. Appl Opt 1992; 31: 1146. https://doi.org/10.1364/AO.31.001146 .

[244] Pugh D, Runyon J, Bowen P, Giles A, Valera-Medina A, Marsh R, et al. An investigation of ammonia primary flame combustor concepts for emissions reduction with OH*, NH2* and NH* chemiluminescence at elevated conditions. Proceedings of the Combustion Institute 2021; 38: 6451–9. https://doi.org/10.1016/j.proci.2020.06.310.

[245] Pugh D, Valera-Medina A, Bowen P, Giles A, Goktepe B, Runyon J, et al. Emissions Performance of Staged Premixed and Diffusion Combustor Concepts for an NH3/Air Flame with and Without Reactant Humidification. J Eng Gas Turbine Power 2021; 143. https://doi.org/10.1115/1.4049451.

[246] Turns SR. Introduction to combustion. vol. 287. New York, USA: McGraw-Hill Companies; 1996.

[247] Tropea C. Laser Doppler anemometry: recent developments and future challenges. Meas Sci Technol 1995; 6: 605–19. https://doi.org/10.1088/0957-0233/6/6/001.

[248] Doran PM. Fluid Flow. Bioprocess Engineering Principles, Elsevier; 2013, p. 201–54. https://doi.org/10.1016/B978-0-12-220851-5.00007-1.

[249] Rohde M, Planquart P, Spaccapaniccia C, Bertocchi F. Rod bundle and pool-type experiments in water serving liquid metal reactors. Thermal Hydraulics Aspects of Liquid Metal Cooled Nuclear Reactors, Elsevier; 2019, p. 49–82. https://doi.org/10.1016/B978-0-08-101980-1.00011-9.

[250] Vivoli R, Pugh D, Goktepe B, Bowen PJ. Modeling of Roughness Effects on Generic Gas Turbine Swirler via a Detached Eddy Simulation Low-y+ Approach. Energies (Basel) 2025; 18: 5240. https://doi.org/10.3390/en1819524 0.

[251] Runyon J, Marsh R, Bowen P, Pugh D, Giles A, Morris S. Lean methane flame stability in a premixed generic swirl burner: Isothermal flow and atmospheric combustion characterization. Exp Therm Fluid Sci 2018; 92: 125–40. https://doi.org/10.1016/j.expthermflusci.2017.11.019.

[252] Pugh D, Bowen P, Valera-Medina A, Giles A, Runyon J, Marsh R. Influence of steam addition and elevated ambient conditions on NOx reduction in a staged premixed swirling NH3/H2 flame. Proceedings of the Combustion Institute 2019; 37: 5401–9. https://doi.org/10.1016/j.proci.2018.07.091.

[253] P. Smith G, M. Golden D, Frenklach M, W. Moriarty N, Eiteneer B, Goldenberg M, et al. The ‘GRIMech 3.0’ chemical kinetic mechanism 1999. http://combustion.berkeley.edu/gri-mech/version30/text30.html (accessed March 5, 2024).

[254] Kathrotia T. Reaction Kinetics Modeling of OH*, CH*, and C2* Chemiluminescence. German Aerospace Center (DLR), 2011.

[255] Burcat A. Prof. Burcat’s Thermodynamic Data 2006. http://garfield.chem.elte.hu/Burcat/burcat.html (accessed May 28, 2024).

[256] Panoutsos C, Hardalupas Y, Taylor A. Numerical evaluation of equivalence ratio measurement using OH∗ and CH∗ chemiluminescence in premixed and non-premixed methane–air flames. Combust Flame 2009; 156: 273–91. https://doi.org/10.1016/j.combustflame.2008.11.008.

[257] Detomaso N, Hok J-J, Dounia O, Laera D, Poinsot T. A generalization of the Thickened Flame model for stretched flames. Combust Flame 2023; 258: 113080. https://doi.org/10.1016/j.combustflame.2023.113080.

[258] Castellani S, Nassini PC, Andreini A, Meloni R, Pucci E, Valera-Medina A, et al. Numerical Modeling of Swirl Stabilized Lean-Premixed H2–CH4 Flames with the Artificially Thickened Flame Model. J Eng Gas Turbine Power 2024; 146. https://doi.org/10.1115/1.4063829.

[259] Gritskevich MS, Garbaruk A V., Schütze J, Menter FR. Development of DDES and IDDES Formulations for the k-ω Shear Stress Transport Model. Flow Turbul Combust 2012; 88: 431–49. https://doi.org/10.1007/s10494-011-9378-4.

[260] Barlow DN, Kim YW. Effect of Surface Roughness on Local Heat Transfer and Film Cooling Effectiveness. Houston, Texas: 1995.

[261] Pereira FS, Vaz G, Eça L, Girimaji SS. Simulation of the flow around a circular cylinder at Re =3900 with Partially-Averaged Navier-Stokes equations. Int J Heat Fluid Flow 2018; 69: 234–46. https://doi.org/10.1016/j.ijheatfluidflow.2017.11.001.

[262] Pereira FS, Vaz G, Eça L. Evaluation of RANS and SRS methods for simulation of the flow around a circular cylinder in the sub-critical regime. Ocean Engineering 2019; 186: 106067. https://doi.org/10.1016/j.oceaneng.2019.05.049.

[263] Vignat G, Durox D, Candel S. The suitability of different swirl number definitions for describing swirl flows: Accurate, common and (over-) simplified formulations. Prog Energy Combust Sci 2022; 89: 100969. https://doi.org/10.1016/j.pecs.2021.100969.

[264] Shepherd IG, Cheng RK. The burning rate of premixed flames in moderate and intense turbulence. Combust Flame 2001; 127: 2066–75. https://doi.org/10.1016/S0010-2180(01)00309-1.

[265] Vivoli R, Pugh D, Goktepe B, Hewlett S, Giles A, Marsh R, et al. Surface Roughness Effects on the Operability and Performance of a Hydrogen Jet Burner. J Eng Gas Turbine Power 2026; 148: 1–33. https://doi.org/10.1115/1.4069474.

[266] Al-Fahham M, Hatem FA, Alsaegh AS, Valera Medina A, Bigot S, Marsh R. Experimental Study to Enhance Resistance for Boundary Layer Flashback in Swirl Burners Using Microsurfaces. Volume 4A: Combustion, Fuels and Emissions, American Society of Mechanical Engineers; 2017. https://doi.org/10.1115/GT2017-63367.

[267] Reichel TG, Terhaar S, Paschereit O. Increasing Flashback Resistance in Lean Premixed Swirl-Stabilized Hydrogen Combustion by Axial Air Injection. J Eng Gas Turbine Power 2015; 137. https://doi.org/10.1115/1.4029119.

[268] Kıymaz TB, Böncü E, Güleryüz D, Karaca M, Yılmaz B, Allouis C, et al. Numerical investigations on flashback dynamics of premixed methane-hydrogen-air laminar flames. Int J Hydrogen Energy 2022; 47: 25022–33. https://doi.org/10.1016/j.ijhydene.2022.05.230.

[269] Vancoillie J, Demuynck J, Galle J, Verhelst S, van Oijen JA. A laminar burning velocity and flame thickness correlation for ethanol–air mixtures valid at spark-ignition engine conditions. Fuel 2012; 102: 460–9. https://doi.org/10.1016/j.fuel.2012.05.022.

[270] Liu X, Wang G, Si J, Li P, Wu M, Mi J. Distinct combustion characteristics of a one-dimensional premixed laminar flame of ammonia under various combustion regimes. Carbon Resources Conversion 2024; 7: 100229. https://doi.org/10.1016/j.crcon.2024.100229.

[271] Sun CJ, Sung CJ, He L, Law CK. Dynamics of weakly stretched flames: quantitative description and extraction of global flame parameters. Combust Flame 1999; 118: 108–28. https://doi.org/10.1016/S0010-2180(98)00137-0.

[272] Porath P, Altenburg LA, Klein SA, Tummers MJ, Ghani A. Low velocity streaks combined with intrinsic flame instabilities provoke boundary layer flashback in a turbulent premixed jet-stabilized hydrogen flame. Combust Flame 2025; 278: 114236. https://doi.org/10.1016/j.combustflame.2025.114236.

[273] Eichler C, Baumgartner G, Sattelmayer T. Experimental Investigation of Turbulent Boundary Layer Flashback Limits for Premixed Hydrogen-Air Flames Confined in Ducts. J Eng Gas Turbine Power 2012; 134. https://doi.org/10.1115/1.4004149.

[274] Fruzza F, Lamioni R, Tognotti L, Galletti C. Flashback of H2-enriched premixed flames in perforated burners: Numerical prediction of critical velocity. Int J Hydrogen Energy 2023; 48: 31790–801. https://doi.org/10.1016/j.ijhydene.2023.04.252.

[275] Prade B. Gas turbine operation and combustion performance issues. Modern Gas Turbine Systems, Elsevier; 2013, p. 383–423e. https://doi.org/10.1533/9780857096067.3.383.

[276] Varadharajan R. Reynolds number effects on transition, turbulence intensity and axial-velocity decay rate of turbulent round jets. ArXiv Preprint 2017. https://doi.org/https://doi.org/10.48550/arXiv.1708.03140.

[277] Ó Conaire M, Curran HJ, Simmie JM, Pitz WJ, Westbrook CK. A comprehensive modeling study of hydrogen oxidation. Int J Chem Kinet 2004; 36: 603–22. https://doi.org/10.1002/kin.20036.

[278] Schmidt BE, Page WE, Sutton JA. On the Application of the Abel Transformation in Statistically Axisymmetric Turbulent Flows. AIAA Journal 2022; 60: 2169–77. https://doi.org/10.2514/1.J060819.

[279] Trisjono P, Kleinheinz K, Hawkes ER, Pitsch H. Modeling turbulence–chemistry interaction in lean premixed hydrogen flames with a strained flamelet model. Combust Flame 2016; 174: 194–207. https://doi.org/10.1016/j.combustflame.2016.07.008.

[280] Howarth TL, Hunt EF, Aspden AJ. Thermodiffusively-unstable lean premixed hydrogen flames: Phenomenology, empirical modelling, and thermal leading points. Combust Flame 2023; 253: 112811. https://doi.org/10.1016/j.combustflame.2023.112811.

[281] Li J. Numerical investigation of hydrogen-air mixing in jet-in-crossflow configuration for future low emission gas turbines. Master's Thesis. University College London, 2022.

[282] Rrustemi DN, Ganippa LC, Megaritis T, Axon CJ. New laminar flame speed correlation for lean mixtures of hydrogen combustion with water addition under high pressure conditions. Int J Hydrogen Energy 2024; 63: 609–17. https://doi.org/10.1016/j.ijhydene.2024.03.177.

[283] Hu E, Huang Z, He J, Jin C, Miao H, Wang X. Measurement of laminar burning velocities and analysis of flame stabilities for hydrogen-air-diluent premixed mixtures. Sci Bull (Beijing) 2009; 54: 846–57. https://doi.org/10.1007/s11434-008-0584-y.

[284] Vivoli R, Pugh D, Goktepe B, Hewlett S, Giles A, Marsh R, et al. Surface Roughness Effects on the Operability and Performance of a Hydrogen Jet Burner. Volume 3A: Combustion, Fuels & Emissions, American Society of Mechanical Engineers; 2025. https://doi.org/10.1115/GT2025-151389.

APPENDIX A. Hydrogen Chemistry

A.1. H_2 Flame speeds

Flame speeds were calculated via CHEMKIN (2023 R1) utilising the Ó Conaire [277] reaction mechanism. Air and fuel inlet temperature set to 286 K. Values are presented in Table A.1.

Table A.1 *- Flame speed of H_2 against equivalence ratio.*

ϕ	flame speed (cm/s)
0.50	37.79
0.60	70.99
0.685	107.04
0.690	109.24
0.70	114.12
0.780	147.02
0.792	151.53
0.80	154.80
0.90	189.45
0.930	198.91
0.935	200.35
0.945	203.40
0.949	204.60
1.00	219.19
1.077	238.16
1.093	241.88
1.124	248.92
1.136	251.24
1.288	277.04
1.341	283.46
1.435	292.74
1.487	296.09

A.2.OH* Modification

Transport:

```
OH*          1   80.0     2.75     0.00     0.00     0.0  ! = OH
```

Kinetics and Thermo:

```
! Burcat / Goos 2016
OH*              H 1  O 1         G  0300.00   3000.00  1000.00                    1
 2.75582920E+00 1.39848756E-03-4.19428493E-07 6.33453282E-11-3.56042218E-15    2
 5.09751756E+04 5.62581429E+00 3.46084428E+00 5.01872172E-04-2.00254474E-06    3
 3.18901984E-09-1.35451838E-12 5.07349466E+04 1.73976415E+00                   4

!----------- Chemiluminescence OH* MECHANISM ----------------------------------
 H+O+M=OH*+M                      1.500E+13    0.00   5.975E+03  ! T. Kathrotia  2010
 H2/1.0/H2O/6.40//O2/0.45/N2/0.40/AR/0.35/      ! Griffith & Barnard
 OH*=OH                           1.450E+06    0.00   0.000E+00  ! T.Kathrotia 2011
 OH*+O2=OH+O2                     2.100E+12    0.50  -4.824E+02  ! T.Kathrotia 2011
 OH*+H2=OH+H2                     2.950E+12    0.50  -4.543E+02  ! T.Kathrotia 2011
 OH*+N2=OH+N2                     1.080E+11    0.50  -1.243E+02  ! T.Kathrotia 2011
 OH*+AR=OH+AR                     1.690E+12    0.00   4.137E+03  ! T.Kathrotia 2011
 OH*+H2O=OH+H2O                   5.930E+12    0.50  -8.608E+02  ! T.Kathrotia 2011
 OH*+OH=OH+OH                     6.010E+12    0.50  -7.652E+02  ! T.Kathrotia 2011
 OH*+H=OH+H                       1.310E+12    0.50  -1.674E+02  ! T.Kathrotia 20
```

APPENDIX B. MATLAB Codes

B.1. Image Superimposition

This code calculates and saves the average of all images in located in a specified directory. The file extension of both the read and written superimposed images can be changed as needed.

```
% Define the directory where your images are located
imageDir = 'image_directory';

% List all image files in the directory
imageFiles = dir(fullfile(imageDir, '*.png')); % Update the file extension as
needed

% Initialize variables to store the sum and count of images
sumImage = zeros(size(imread(fullfile(imageDir, imageFiles(1).name))));
imageCount = 0;

% Loop through the image files and accumulate them
parfor i = 1:numel(imageFiles)
    % Read the current image
    currentImage = double(imread(fullfile(imageDir, imageFiles(i).name)));

    % Add the current image to the sum
    sumImage = sumImage + currentImage;

    % Increment the image count
    imageCount = imageCount + 1;
end

% Calculate the average image
averageImage = uint8(sumImage / imageCount);

% Display the average image
imshow(averageImage);
title('Average Image');


% Specify the file path and name for saving the average image
outputFileName = 'file_name.png'; % Change the file extension to match the desired
format (e.g., .jpg, .png)

% Use the imwrite function to save the average image
imwrite(averageImage, fullfile(imageDir, outputFileName));
```

B.2. Centroid of Flame Calculator

The code shown below was setup to calculate and display the centroid of binarized flame images. Black and with images were generated in STAR CCM+ ensuring the inside of the flame was shown as white. Once run, the code was made to show the imported image with an overlay of the centroid location and XY coordinates. It is important to note that all coordinate values were calculated from the top left corner of the image and would therefore need to be adjusted after the fact depending on the image orientation. An example output image is shown in Figure B.1.

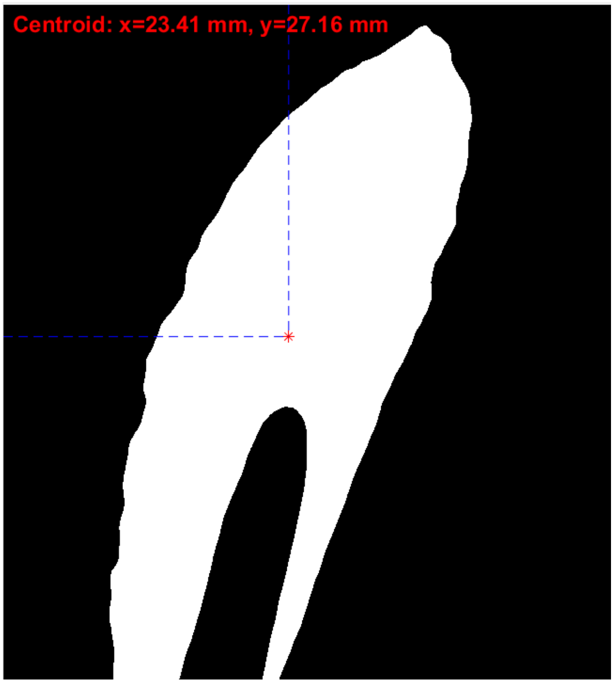

Figure B.1 *- MATLAB output for calculated centroid location.*

```
% Specify the folder containing the images
folder = 'folder_path’;

% Get a list of all image (png) files in the folder
image_files = dir(fullfile(folder, '*.png'));

% Open a CSV file to store results
output_file = fopen('image_coordinates.csv', 'w');

% Write header
fprintf(output_file, 'File,Centroid_x_mm,Centroid_y_mm\n');

% Loop through each image file
for i = 1:length(image_files)
    % Read the binarized image
    img_path = fullfile(folder, image_files(i).name);
```

```matlab
    image = imread(img_path);
    binary_image = im2bw(image);

    % Find the centroid
    props = regionprops(binary_image, 'Centroid');
    centroids = cat(1, props.Centroid);

    % Calculate the conversion factors from with of % burner
    conversion_factor_x =  50 / size(binary_image, 2); % mm/pixel

    % Convert centroid coordinates to mm
    centroid_mm = [centroids(:, 1) * conversion_factor_x, centroids(:, 2) * conversion_factor_x];

    % Output x, y coordinates to CSV file
    [~, name, ~] = fileparts(img_path);
    fprintf(output_file, '%s,%.2f,%.2f\n', name, centroid_mm(1), centroid_mm(2));

    % Display the centroid
    imshow(binary_image);
    hold on;
    plot(centroids(:,1), centroids(:,2), 'r*');

    % Add lines from centroid to axes
    line([centroids(1), centroids(1)], [0, centroids(2)], 'Color', 'blue', 'LineStyle', '--');
    line([0, centroids(1)], [centroids(2), centroids(2)], 'Color', 'blue', 'LineStyle', '--');

    % Display centroid coordinates in the top-left corner
    centroid_text = sprintf('Centroid: x=%.2f mm, y=%.2f mm', centroid_mm(1), centroid_mm(2));
    text(10, 20, centroid_text, 'Color', 'red', 'FontSize', 12, 'FontWeight', 'bold');

    hold off;

    % Pause to display the image
    pause(1);
end

% Close the output file
fclose(output_file);
```

B.3. Area Calculator

The following code was utilised to calculate the white area of a binarized image. The black and white images were created within STAR CCM+ with values ≤ than the value of interest being shown as white. Part surfaces were usually removed from the scene though, if necessary for scaling in MATLAB, critical faces were left and set to a dark grey colour so they would be ignored in the binarization process. To show any potential errors, the code was setup to display the imported image with the white regions it had detected highlighted by a red outline and light blue infill. An example output image is shown in Figure B.2.

Figure B.2 *- Binarized 0 velocity MATLAB output with overlay of detected white regions.*

```
% Specify the path to the image
image_path = "file_path";

% Read the image
image = imread(image_path);

% Convert the image to binary (assuming white is the region of interest)
binary_image = im2bw(image);

% Plot the original image and highlight the white region
figure;
imshow(image);
title('Original Image');

% Highlight the white region
hold on;
boundaries = bwboundaries(binary_image);
```

```
for k = 1:length(boundaries)
    boundary = boundaries{k};
    plot(boundary(:,2), boundary(:,1), 'r', 'LineWidth', 2);

    % Fill the area under the curve
    fill(boundary(:,2), boundary(:,1), 'c', 'FaceAlpha', 0.3);
end
hold off;

% Draw scaling Line
    scale_line = drawline;
    end_position = scale_line.Position; % Find x, y position of each end point
    x1 = end_position(1,1);
    y1 = end_position(1,2);
    x2 = end_position(2,1);
    y2 = end_position(2,2);

% Calculate length of line in pixels
    pix_dist = sqrt( (x2-x1).^2 + (y2-y1).^2);

% Create popup to ask for physical distance
    prompt = {'Enter Physical distance:','Enter units (m, cm, mm, um)'};
    phys_dist = inputdlg(prompt,'Physical Distance');
    LengthEditField.Value = str2double(phys_dist{1});
    UnitsEditField.Value = phys_dist{2};

  pixel_size_mm = LengthEditField.Value / pix_dist;

% Calculate the area under the curve in pixels
area_under_curve_pixels = sum(binary_image(:));

% Convert the area to square millimeters
area_under_curve_mm2 = area_under_curve_pixels * pixel_size_mm^2;

img_props = regionprops(binary_image,'Area');

% Display the result
fprintf('Image: %s\n', image_path);
fprintf('Area under the curve: %.2f square millimeters\n', area_under_curve_mm2);
fprintf('Pixel-to-Millimeter Ratio: %.5f pixels/mm\n', 1/pixel_size_mm);

% Close the figure
close(gcf);
```

B.4. Normalised Contour Plot

The following code was utilised to apply a contour plot to all images located in a specified file directory. The colour map was normalised based on the minimum and maximum intensity values of each image meaning each image would have intensity values ranging from 0 to 1. The code was set up to output the minimum and maximum intensity values of each reference image alongside the file name allowing for a quick visualisation of the intensity ranges within the dataset.

```
Directory containing the images
inputDir = 'file directory';
outputDir = fullfile(inputDir, 'Contoured'); % Create a subdirectory for contoured
images

% Create output directory if it doesn't exist
if ~exist(outputDir, 'dir')
    mkdir(outputDir);
end

% Get a list of all .tif files in the directory
imageFiles = dir(fullfile(inputDir, '*.tif'));

% Initialize a table to store max and min limits
summaryTable = table('Size', [length(imageFiles), 3], 'VariableTypes', {'string',
'double', 'double'}, 'VariableNames', {'FileName', 'MinValue', 'MaxValue'});

% Loop through each image file
for k = 1:length(imageFiles)
    % Read the image
    filePath = fullfile(inputDir, imageFiles(k).name);
    img = imread(filePath);

    % Convert the image to grayscale if it is RGB
    if size(img, 3) == 3
        img = rgb2gray(img);
    end

    % Calculate the min and max values of the image
    minValue = double(min(img(:)));
    maxValue = double(max(img(:)));
```

```matlab
    % Add the data to the summary table
    summaryTable.FileName{k} = imageFiles(k).name;
    summaryTable.MinValue(k) = minValue;
    summaryTable.MaxValue(k) = maxValue;

    % Normalize the image to the range [0, 1]
    normalizedImg = (double(img) - minValue) / (maxValue - minValue);

    % Smooth the normalized image using a Gaussian filter
    smoothedImg = imgaussfilt(normalizedImg, 2); % Adjust the second parameter for more or less smoothing

    % Create the filled contour plot without edges
    figure('Visible', 'off', 'Units', 'pixels', 'Position', [0, 0, 129, 770]); % Set the x1, y1, x2, y2 pixel coordinates of each image
    axes('Units', 'pixels', 'Position', [0, 0, 129, 770]);
    contourf(flipud(smoothedImg), 20, 'LineStyle', 'none'); % Remove contour lines
    caxis([0, 1]); % Set the colour limits to [0, 1]
    colormap('hot');
    axis image; % Keep aspect ratio of the image
    axis off;

    % Export the figure to match the original image dimensions
    outputFilePath = fullfile(outputDir, ['contoured_', imageFiles(k).name]);
    frame = getframe(gca); % Get the content of the axes
    imwrite(frame.cdata, outputFilePath); % Save the content as an image

    % Close the figure
    close(gcf);
end

% Write the summary table to an Excel file
writetable(summaryTable, fullfile(outputDir, 'ImageSummary.xlsx'));

fprintf('Contour plots saved to %s\n', outputDir);
fprintf('Summary table saved to %s\n', fullfile(outputDir, 'ImageSummary.xlsx'));
```

APPENDIX C. STAR CCM+ Macros

C.1. Mesh Dependency Automation

To speed up the process of performing mesh independency studies, particularly on the supercomputer, the following macro was created. Once an adequate mesh is generated, all surface and volume controls for cell size should be set back to be "Relative to Base". In the macro the user can specify the initial and final base size (i) together with the percentage reduction. The number of iterations performed per mesh generated can also be specified.

```
package macro;

import java.util.*;

import star.common.*;
import star.base.neo.*;
import star.meshing.*;

public class mesh_indi extends StarMacro {

  public void execute() {
    execute0();
  }

  private void execute0() {

// FOR SAVING THE FILE:
    Simulation sim = getActiveSimulation();
    String simPath = sim.getSessionPath();



    for (double i = 90.0; i >= 9; i *= 0.8) { // 20% decrement - mm
     AutoMeshOperation autoMeshOperation_0 =
      ((AutoMeshOperation)
sim.get(MeshOperationManager.class).getObject("Automated Mesh"));

     Units units_0 =
      ((Units) sim.getUnitsManager().getObject("mm"));
```

```
autoMeshOperation_0.getDefaultValues().get(BaseSize.class).setValueAndUnits(i,
units_0);

      sim.get(MeshOperationManager.class).executeAll();
      MeshPipelineController MPC = sim.get(MeshPipelineController.class);
      MPC.generateSurfaceMesh();
      MPC.generateVolumeMesh();
      sim.saveState(simPath);
      sim.getSimulationIterator().run(2000);  //  run  of  however  many  iterations
needed
    }
  }
}
```

APPENDIX D. Jet Burner

D.1. PJB Bill of Materials and CAD drawings

Table D.1 *- PJB Bill of Materials.*

ITEM	QTY	PART NUMBER	DESCRIPTION
1	1	SS-810-1-12	SS Swagelok Tube Fitting, Male Connector, 1/2 in. Tube OD x 3/4 in. Male NPT
2	2	SS-22M0-7-12	SS Swagelok Tube Fitting, Female Connector, 22 mm Tube OD x 3/4 in. Female NPT
3	1	SS-400-1-12-BT	SS Swagelok Tube Fitting
4	2	62mm pipe	22mm OD 2mm wall thickness SS pipe
5	1	Fuel Line	1/4" OD pipe
6	1	SS-22M0-3	SS Swagelok Tube Fitting, Union Tee, 22 mm Tube OD
7	7	SS-200-1-2RS-bored	SS Swagelok Tube Fitting, Male Connector, 1/8 in. Tube OD x 1/8 in. Male ISO Parallel Thread, Straight Shoulder
8	1	200mm Pipe (F)	22mm OD 2mm Wall Thickness SS Pipe
9	1	Large Flange (A)	350 x 350 mm Stainless Steel Plate 20 mm Thick
10	1	Rig Holding Plate (D)	10mm Thick Stainless-Steel Plate
11	12	ISO 4161 - M8	Hexagon nuts with flange-coarse thread
12	24	ISO 7089 - 8	Spring Washers
13	4	ISO 4762 - M8 x 60	Hexagon Socket Head Cap Screw
14	3	SS-22M0-1-16RS	Male connector 22mm OD x 1in. Male BSP Parallel end connection 316 stainless steel
15	2	Small Flange (B)	350 x 350 mm Stainless Steel Plate 20 mm thick
16	2	Gasket Final	Tanged Graphite
17	1	Bluff Body Holder (C)	350 x 350 mm Stainless Steel Plate 20 mm thick
18	4	ISO 4762 - M8 x 80	Hexagon Socket Head Cap Screw
19	1	Bluff Body (E)	1/4" stainless steel round bar
20	1	SS-22M0-6	SS Swagelok Tube Fitting, Union, 22 mm Tube OD
21	1	100mm pipe	22mm OD 2mm Wall Thickness SS Pipe
22	1	200mm Pipe (F)	7/8" Stainless-Steel Round Bar (interchangeable with various surface finishes)
23	1	Spark Plug	-
24	1	Top Plate (G)	10mm Thick Stainless-Steel Plate
25	1	Burner Face	Alumina (Ceramalox 99.7%)
26	1	Quartz Tube Final	64x64 ID 3mm Thick Quartz Square Tube
27	1	Insulation	-
28	1	EG Ducting	1.5 mm Thick Inconel Plate
29	4	Stud Bar M8 x 190	-

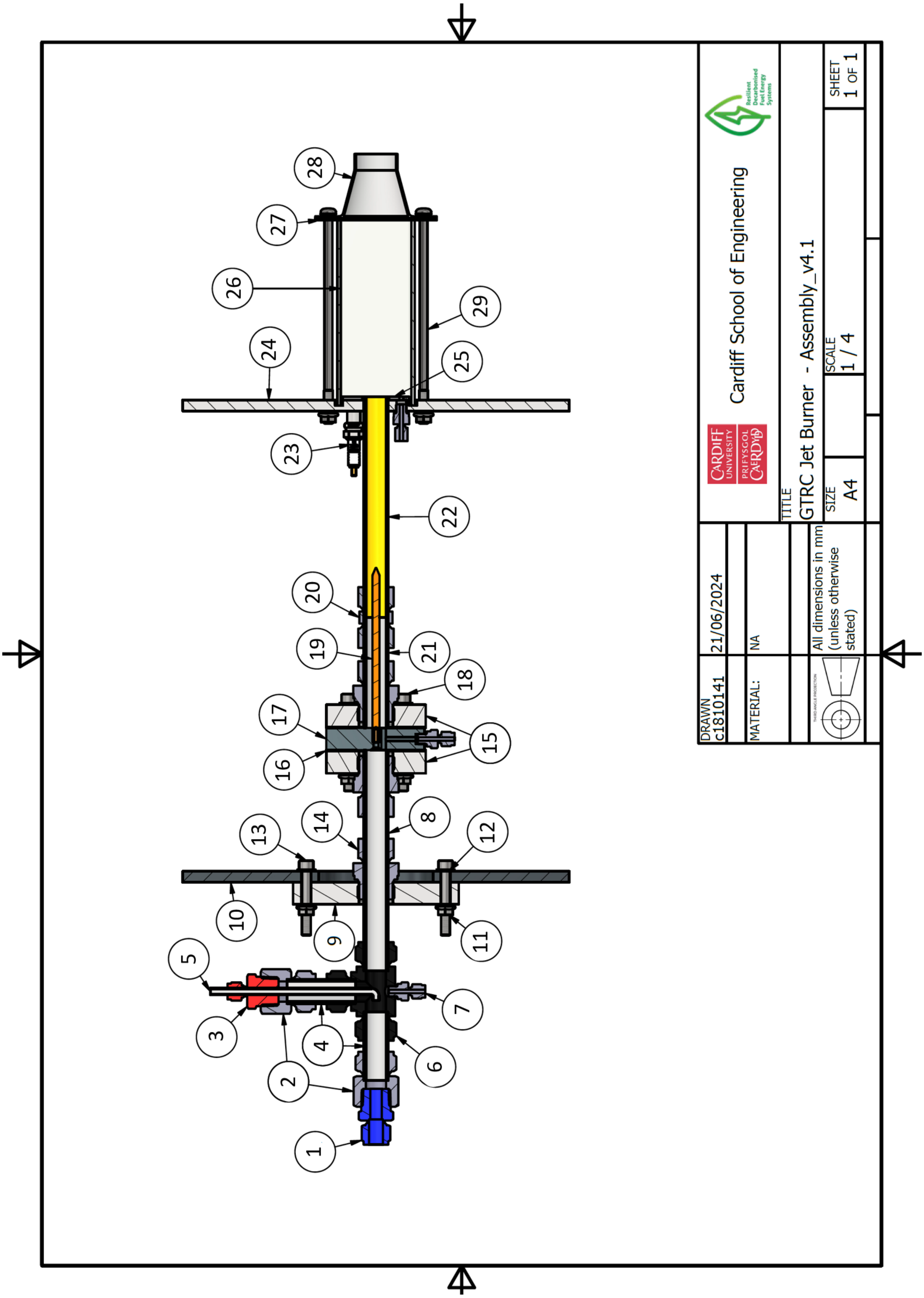

__Figure D.1__ - Assembly view with reference to different components.

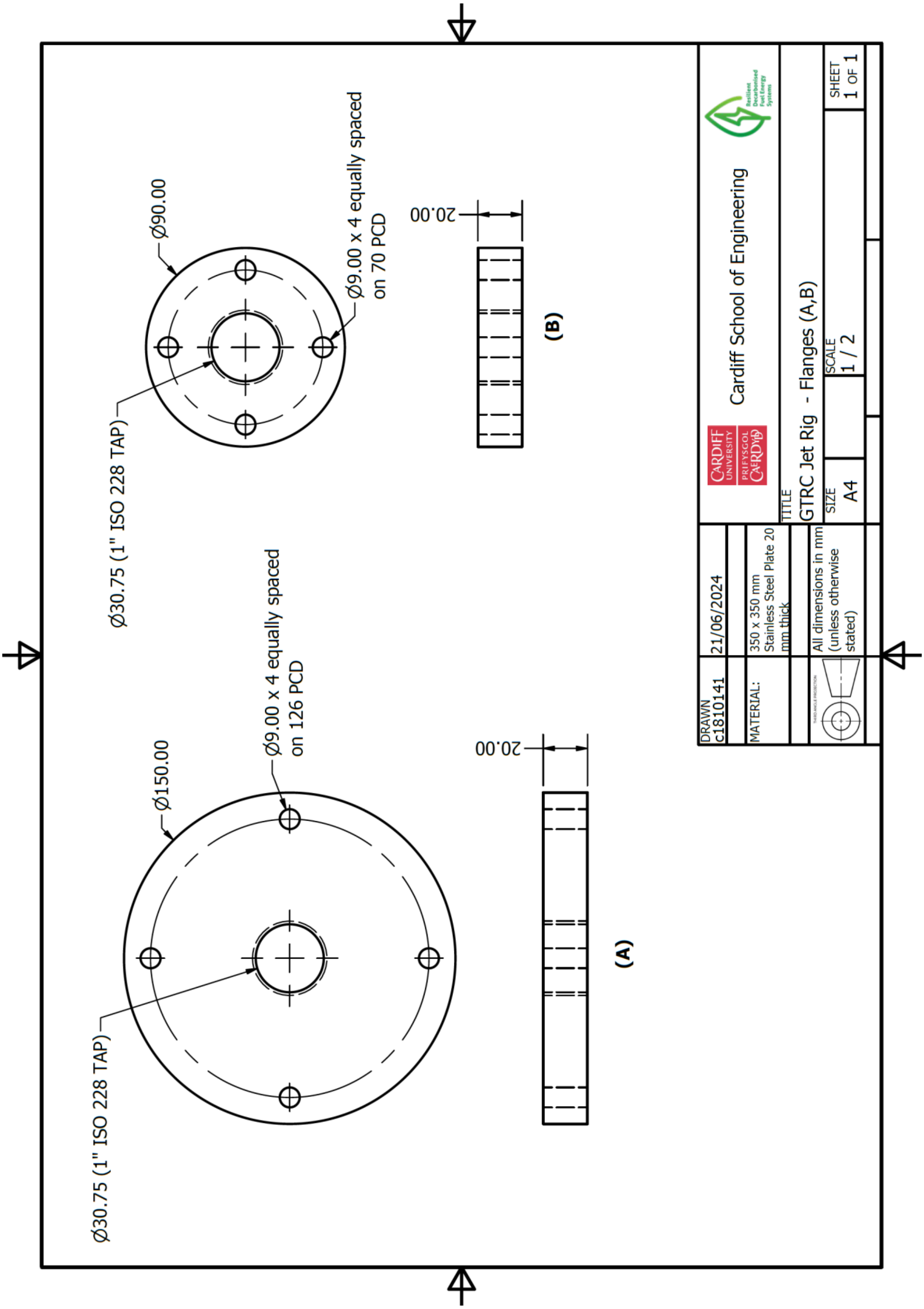

__Figure D.2__ - Flanges.

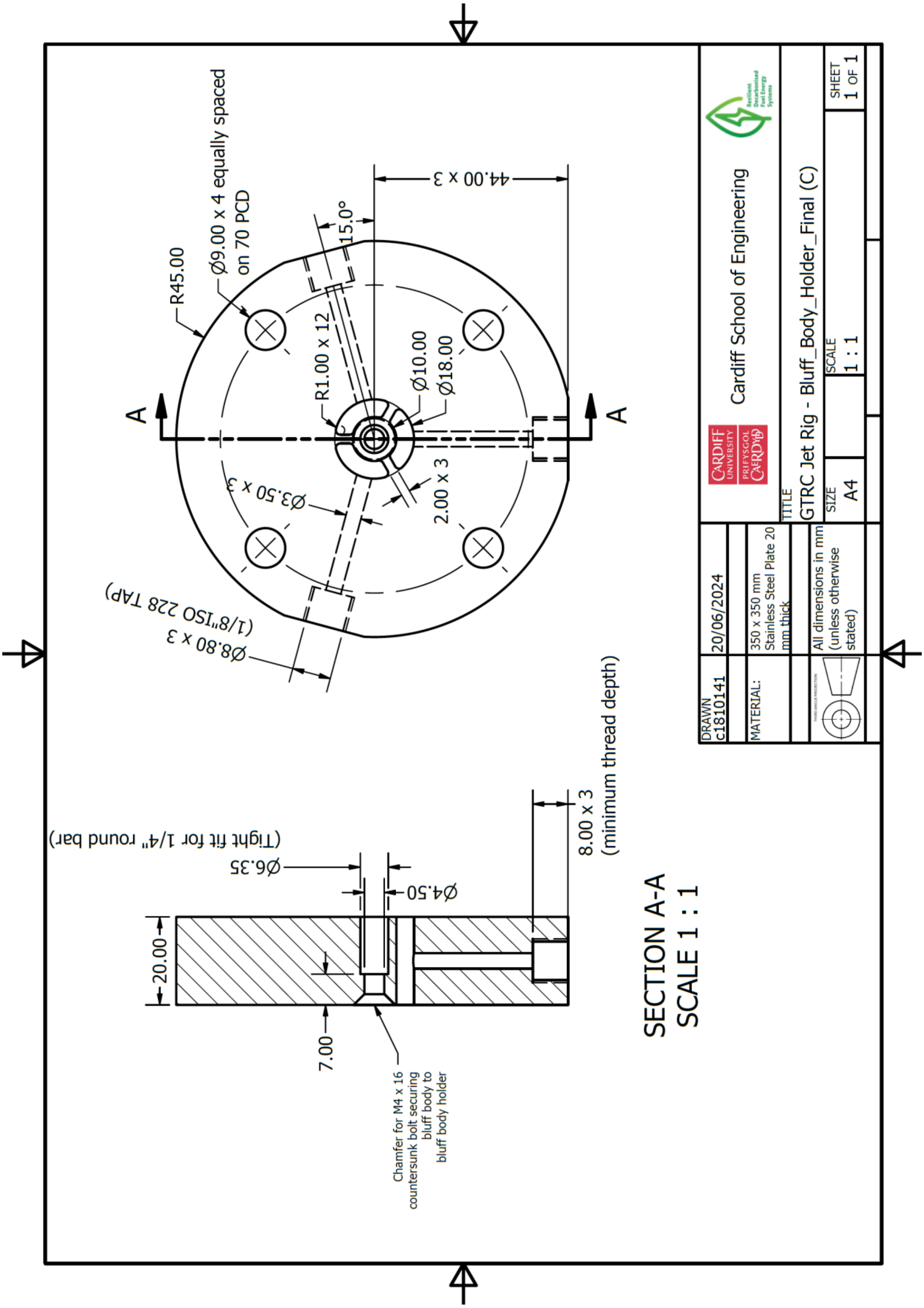

Figure D.3 - *Bluff Body Holder.*

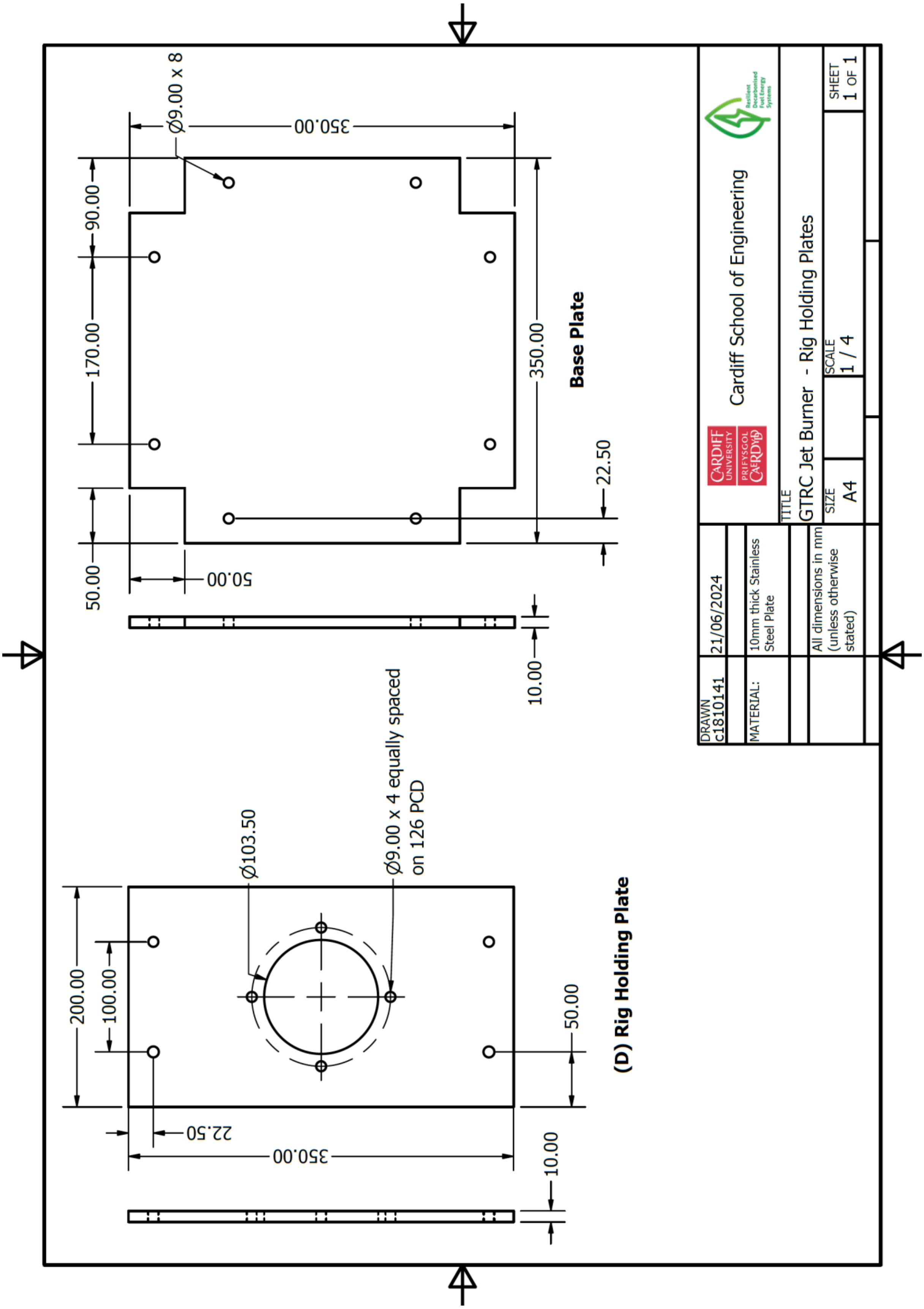

Figure D.4 *- Rig Holding Plates.*

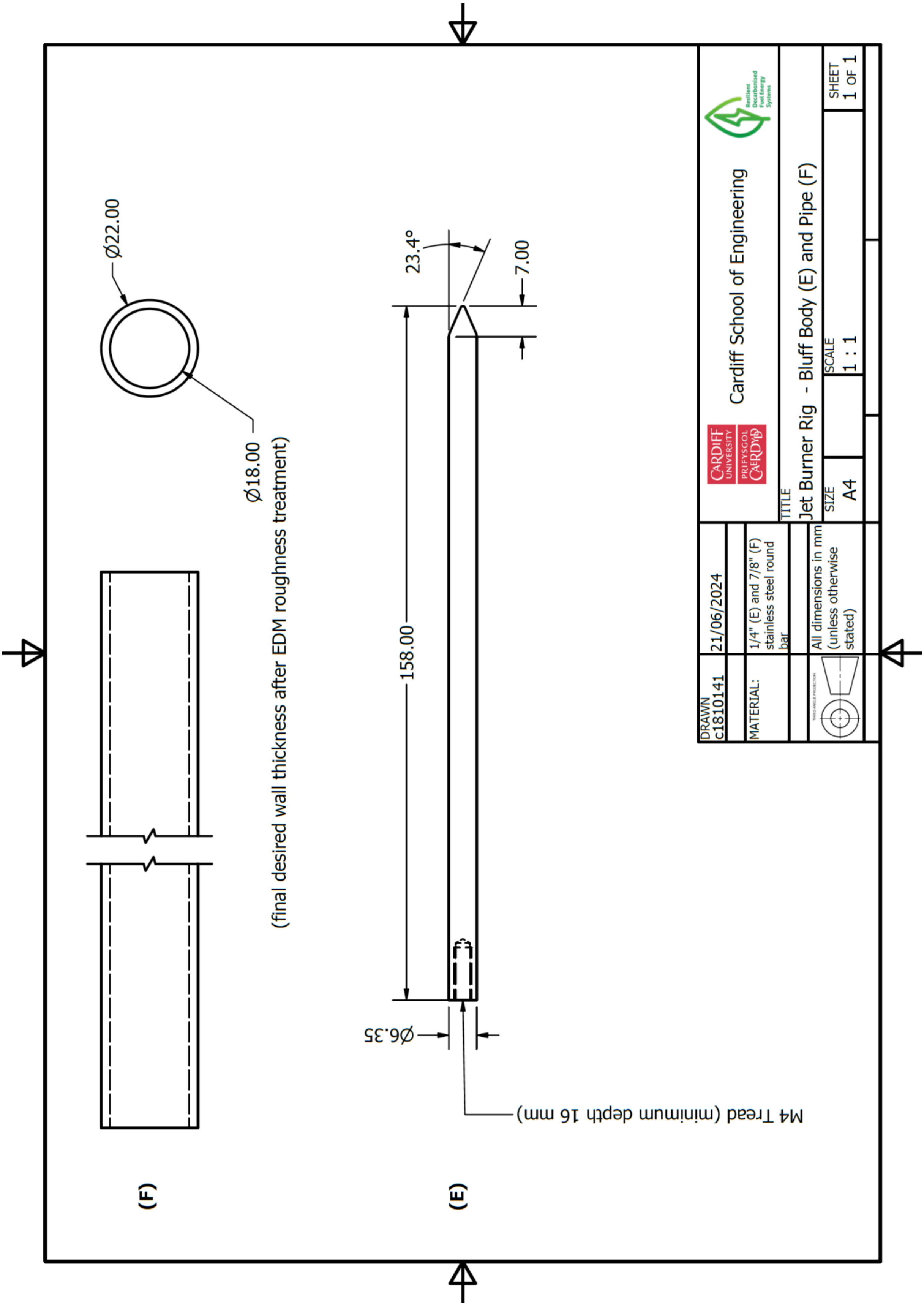

Figure D.5 *- Textured Pipe Section and Bluff Body.*

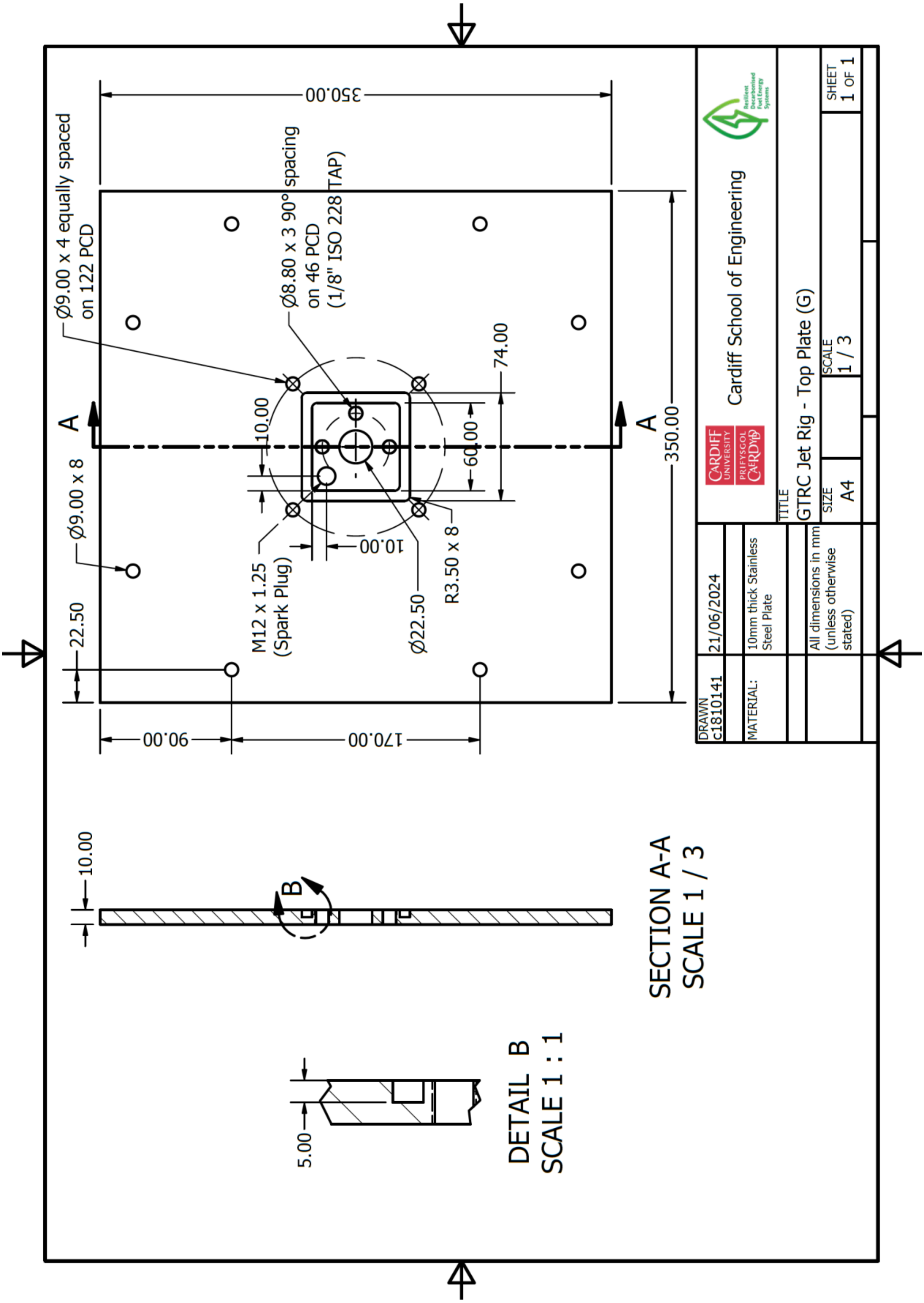

Figure D.6 - *Top Plate.*

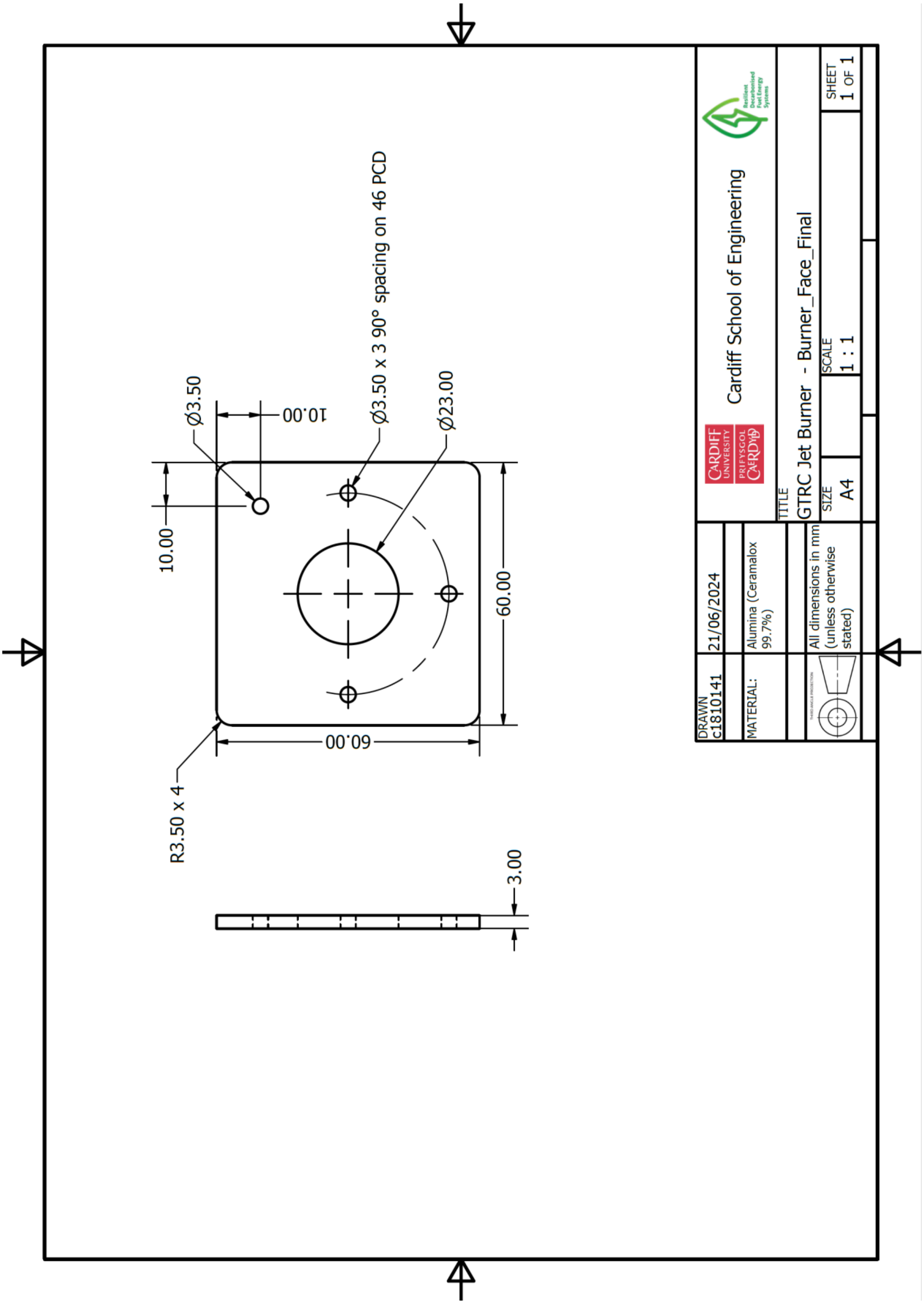

Figure D.7 *- Burner Face.*

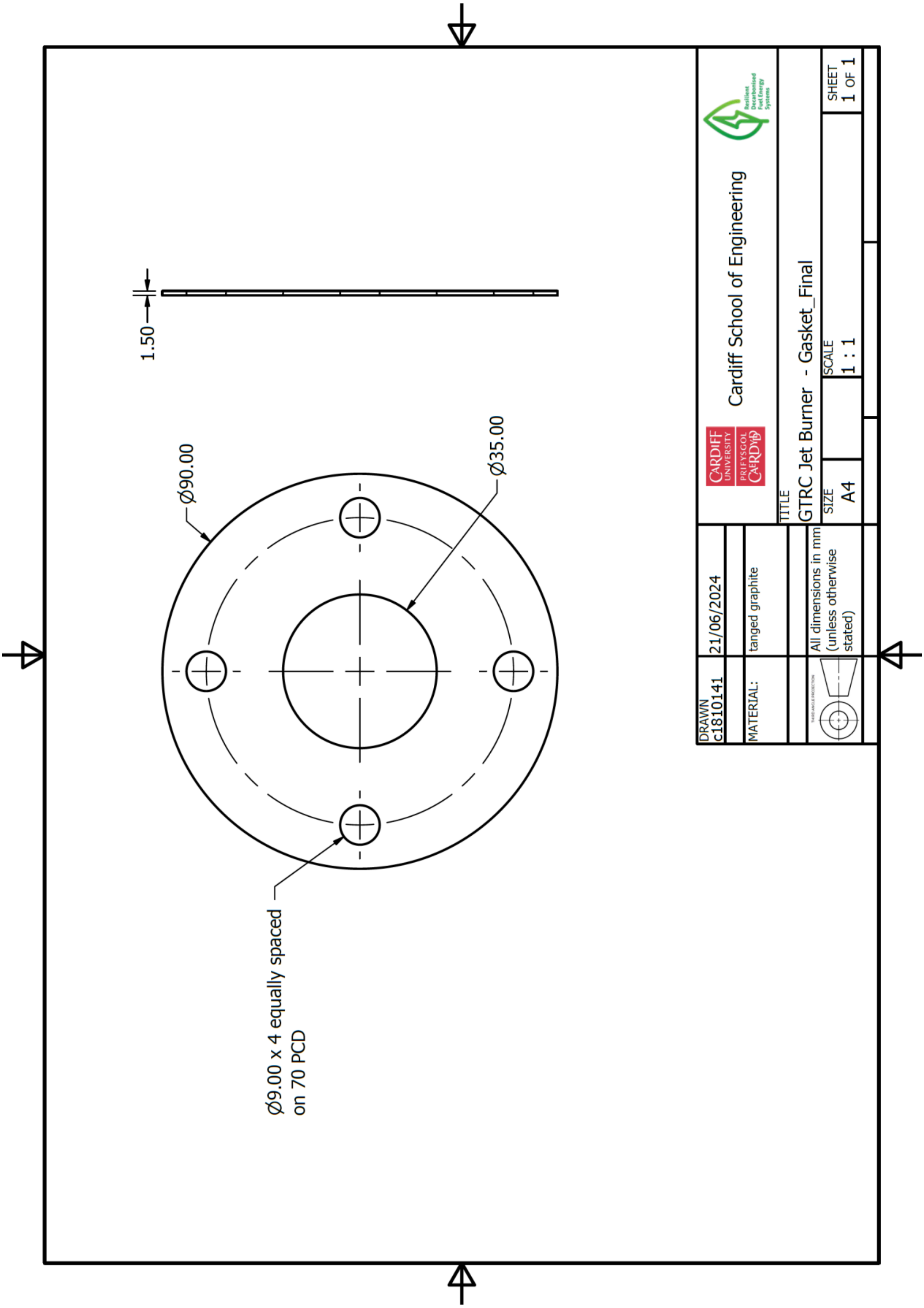

Figure D.8 *- Gaskets.*

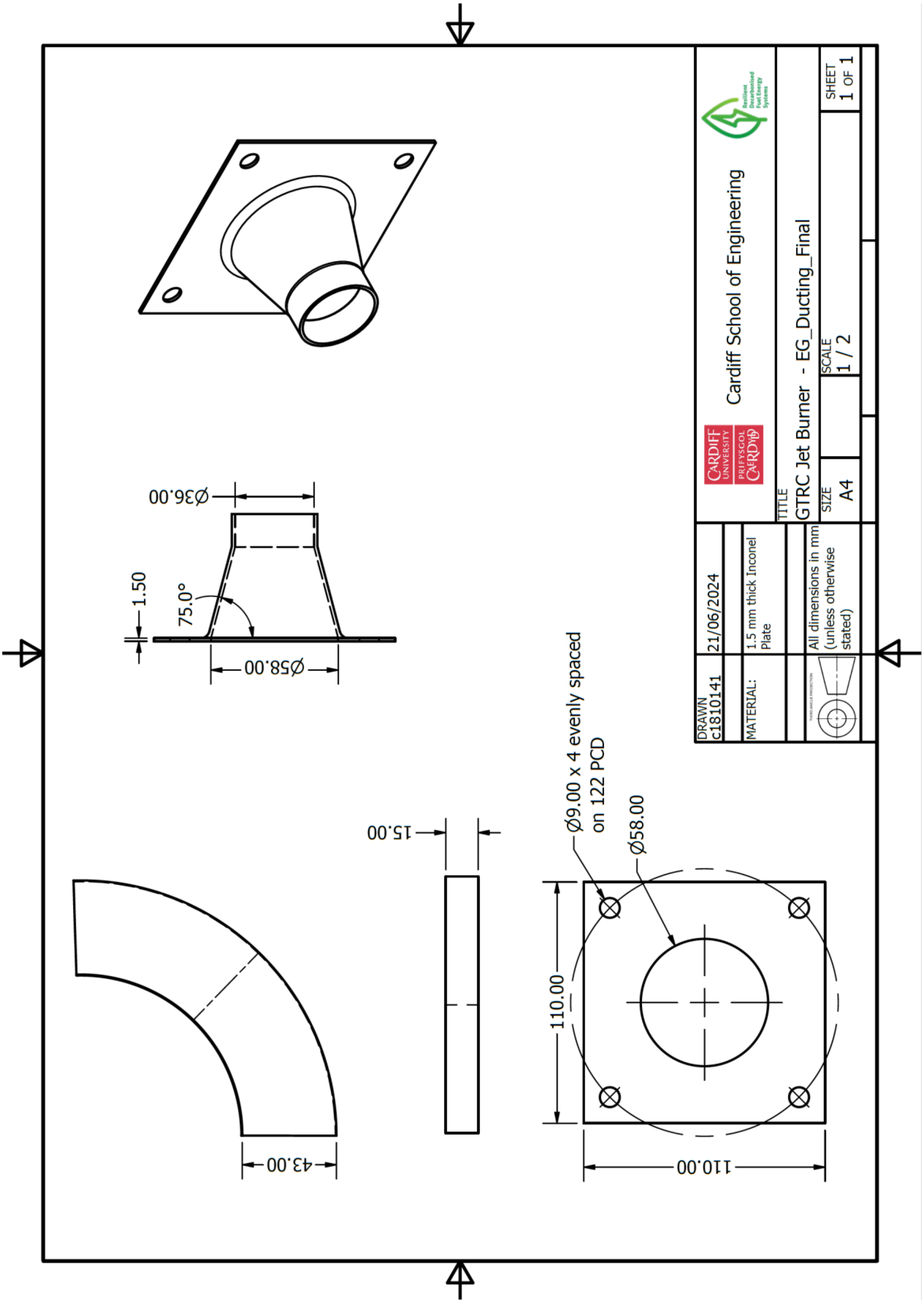

Figure D.9 *- Top Hat.*

D.2. Test Matrices

The test matrices employed during the commissioning phase of the PJB are presented in Table D.2 and Table D.3. The test matrix for all data collected with the PJB are collected in Table D.4 and Table D.5, for Chapter 5, and in Table D.6 for Chapter 7. The test matrix for all data collected with the JICF are collected in Table D.7 (also for Chapter 7).

***Table D.2** - Transition from methane to hydrogen at ER = 0.8.*

TP (kW)	H_2		CH_4		Air (g/s)	ϕ
	g/s	**vol %**	g/s	**vol %**		
12.5	0.0095	**0.25**	0.227	**0.75**	5.2876	0.80
10.0	0.0193	**0.50**	0.1536	**0.50**	4.1273	0.80
10.0	0.0259	**0.60**	0.1376	**0.40**	4.1273	0.79
10.0	0.03	**0.65**	0.1281	**0.35**	4.03	0.80
10.0	0.0344	**0.70**	0.1174	**0.30**	4.03	0.79
10.0	0.0396	**0.75**	0.105	**0.25**	3.95	0.80
11.2	0.0512	**0.80**	0.102	**0.20**	4.38	0.80
12.5	0.0657	**0.85**	0.0923	**0.15**	4.8	0.80
13.7	0.0837	**0.90**	0.074	**0.10**	5.17	0.80
15.0	0.1064	**0.95**	0.0446	**0.05**	5.51	0.80
16.25	0.1354	**1.00**	0	**0.00**	5.88	0.79
17.16	0.143	**1.00**	0	**0.00**	6.20	0.79
20.16	0.168	**1.00**	0	**0.00**	7.19	0.80

***Table D.3** - Initial operability sweep text matrix.*

TP (kW)	H_2 (g/s)	Air (g/s)	ϕ
15	0.125	4.75	0.90
		5.35	0.80
		6.11	0.70
		7.12	0.60
		8.55	0.50
18	0.15	5.70	0.90
		6.42	0.80
		7.33	0.70
		8.55	0.60
		10.26	0.50
21	0.175	6.65	0.90
		7.48	0.80
		8.55	0.70
		9.99	0.60
		11.98	0.50

TP (kW)	H_2 (g/s)	Air (g/s)	ϕ
24	0.2	7.60	0.90
		8.55	0.80
		9.78	0.70
		11.40	0.60
		13.69	0.50
27	0.225	8.55	0.90
		9.62	0.80
		11	0.70
		12.83	0.60
		15.40	0.50

__Table D.4__ - Test matrix for test campaign outlined in Chapter 5.

Date	Time	Test Point	Insert	TP (kW)	ϕ	H_2 (g/s)	Air (g/s)
26/11/2024	14:27:00	1	M1	20	0.71	0.167	8.1
	14:33:55	2			0.60	0.167	9.5
	14:36:40	3			0.50	0.167	11.4
	14:42:00	4			0.40	0.167	14.26
		5			0.37	0.167	15.4
	14:50:00	6			0.80	0.167	7.11
	14:52:00	7			0.89	0.167	6.41
	14:55:00	8			1.00	0.167	5.73
	15:01:00	9		15	0.70	0.125	6.14
	15:03:00	10			0.60	0.125	7.16
	15:05:00	11			0.50	0.125	8.5
	15:08:00	12			0.40	0.125	10.77
		13			0.35	0.125	12.2
	15:12:00	14			0.79	0.125	5.41
	15:14:00	15			0.90	0.125	4.79
		16			0.93	0.125	4.6
		17			0.92	0.125	4.65
	15:22:00	18		25	0.70	0.208	10.21
	15:23:00	19			0.60	0.208	11.87
	15:25:00	20			0.50	0.208	14.2
	15:27:00	21			0.40	0.208	17.77
		22			0.39	0.208	18.4
	15:31:00	23			0.80	0.208	8.91
	15:33:00	24			0.90	0.208	7.96
	15:35:00	25			0.99	0.208	7.19
27/11/2024			R2	20			
	17:55:00	46			0.60	0.167	9.53
	17:58:00	47			0.50	0.167	11.46
	18:00:00	48			0.40	0.167	14.32
		49			0.38	0.167	15.19
	18:04:00	50			0.80	0.167	7.17
	18:06:00	51			0.89	0.167	6.42
	18:08:00	52			0.99	0.167	5.76
	18:10:00	53		15	0.70	0.125	6.12
	18:12:00	54			0.60	0.125	7.15
	18:13:00	55			0.51	0.125	8.48
	18:15:00	56			0.40	0.125	10.82
		57			0.36	0.125	11.9
	18:19:00	58			0.79	0.125	5.42
	18:21:00	59			0.89	0.125	4.82
	18:23:00	60			1.02	0.125	4.22

	18:26:00	61		25	0.70	0.208	10.26
	18:28:00	62			0.60	0.208	11.95
	18:31:00	63			0.50	0.208	14.25
		64			0.39	0.208	18.18
	18:40:00	65			0.40	0.208	17.65
		66			0.40	0.208	17.9
	18:43:00	67			0.80	0.208	8.93
	18:45:00	68			0.90	0.208	7.92
	18:46:00	69			1.00	0.208	7.11
02/12/2024	15:51:00	80	R2	15.0	1.02	0.125	4.19
	13:52:00	81		12.5	0.69	0.104	5.14
		82		12.5	0.93	0.104	3.84
	13:58:00	83		10.0	0.69	0.083	4.1
		84		10.0	0.77	0.083	3.68
		85		12.5	0.94	0.104	3.79
		86		10.0	0.79	0.083	3.62
		87	M1	15.0	0.94	0.125	4.55
	14:42:00	88		12.5	0.69	0.104	5.14
		89		12.5	0.79	0.104	4.5
	14:47:00	90		10.0	0.59	0.083	4.8
		91		10.0	0.70	0.083	4.06
		92		12.5	0.79	0.104	4.51
		93		10.0	0.67	0.083	4.26
	14:37:00			15.0	0.70	0.125	6.14

Table D.5 *- Air flowrates utilised for isothermal cases outlined in Chapter 5.*

Main Air (g/s)	Seed Air (g/s)	Reacting Equivalent Condition
20	0.65	25 kW @ $\phi = 0.4$
12.62	0.65	25 kW @ $\phi = 0.7$
9.9	0.60	20 kW @ $\phi = 0.7$
5.8	0.60	15 kW @ $\phi = 0.93$

Table D.6 *- PJB rich flashback test matrix. N.N format representing repeats.*

Date	Time	Test Point	Insert	TP (kW)	ϕ	H_2 (g/s)	Air (g/s)
02/07/2025	10:31:30	32	**M1**	**15**	0.80	0.125	5.38
	11:07:30	33			0.60		7.12
	12:30:00	33.1			0.60		7.17
	14:02:00	33.2			0.60		7.19
	15:00:00	33.3			0.60		7.16
	11:26:50	34			0.45		9.47
	11:32:10	34.1			0.46		9.32
	11:54:00	34.2			0.45		9.48
	11:41:00	35			0.46		9.24
	12:02:30	36			0.95		4.51
	12:06:30	36.1			0.94		4.56
	12:12:50	36.2			0.94		4.55
	12:39:30	37		**17.5**	0.80	0.146	6.24
	12:47:00	38			0.60		8.35
	12:54:40	39			0.50		10.11
	12:57:40	40			0.48		10.47
	13:07:40	40.1			0.48		10.44
	13:18:30	40.2			0.48		10.51
	13:28:30	41			0.99		5.04
	13:33:47	42			1.09		4.61
	13:41:40	42.1			1.10		4.56
	13:48:20	42.2			1.09		4.58
	14:08:20	43		**20**	0.80	0.1667	7.19
	14:16:00	44			0.60		9.5
	14:19:50	45			0.50		11.33
	14:21:00	46			0.50		11.47
	14:28:40	46.1			0.49		11.64
	14:37:00	46.2			0.50		11.46
	14:44:00	47			1.00		5.74
	14:49:00	48			1.20		4.76
	14:52:00	49			1.27		4.49
	15:03:30	49.1			1.31		4.38
	15:13:46	49.2			1.28		4.46
03/07/2025	10:39:00	50	**R2**	**15**	0.60	0.125	7.2
	11:45:00	50.1			0.60		7.145
	13:34:30	50.2			0.60		7.15
	14:37:00	50.3			0.60		7.16
	10:43:00	51			0.49		8.77
	10:49:45	52			0.48		8.96
	10:58:33	52.1			0. 47		9.07

	11:05:15	52.2			0.47		9.07
	11:12:30	53			0.80		5.38
	11:20:00	54			1.00		4.29
	11:24:50	55			1.14		3.77
	11:30:50	55.1			1.15		3.74
	11:37:20	55.2			1.12		3.82
	11:50:00	56		**17.5**	0.80	0.146	6.23
	11:54:30	57			0.60		8.33
	12:00:00	58			0.52		9.7
	12:00:45	59			0.49		10.17
	12:07:44	59.1			0.49		10.23
	12:15:00	59.2			0.49		10.14
	12:28:00	60			1.00		5
	12:33:00	61			1.20		4.19
	12:38:00	62			1.40		3.57
	12:50:00	62.1			1.47		3.41
	12:58:30	62.2			1.47		3.41
	13:07:00	62.3			1.52		3.29
	13:40:10	63		**20**	7.15	0.1667	0.80
	13:46:00	64			9.51		0.60
	13:51:00	65			10.76		0.53
	13:52:00	66			11.17		0.51
	13:58:00	66.1			11.16		0.51
	14:03:00	66.2			11.12		0.51
	14:10:00	67			5.73		1.00
	14:15:00	68			4.78		1.20
	14:19:50	69			4.09		1.40
	14:24:00	70			3.58		1.60
	14:27:00	71			3.19		1.79
	14:29:30	72			2.865		2.00

Table D.7 - JICF rich flashback test matrix. N.N format representing repeats

Date	Time	Test Point	Insert	TP (kW)	ϕ	H_2 (g/s)	Air (g/s)
11/07/2025	11:13:45	88	**M1**	**15**	0.80	0.125	5.35
	12:06:40	88.1			0.80		5.35
	13:10:00	88.2			0.80		5.35
	14:08:00	88.3			0.80		5.36
	11:19:00	89			0.60		7.11
	11:21:30	90			0.52		8.25
	11:29:00	90.1			0.52		8.23
	11:36:00	90.2			0.52		8.25
	11:43:30	91			0.96		4.45
	11:48:00	91.1			0.95		4.51
	11:53:20	91.2			0.93		4.60
	11:13:45	88			0.80		5.35
	12:11:10	92		**17.5**	0.80	0.146	6.26
	12:17:20	93			0.60		8.32
	12:20:00	94			0.54		9.36
	12:28:00	94.1			0.53		9.44
	12:35:30	94.2			0.53		9.50
	12:43:00	95			1.00		5.01
	12:47:00	96			1.14		4.41
	12:51:00	96.1			1.12		4.49
	13:00:00	96.2			1.12		4.48
	13:16:40	97		**20**	0.80	0.1667	7.17
	13:21:00	98			0.60		9.47
	13:23:30	99			0.55		10.43
	13:31:00	99.1			0.55		10.46
	13:38:00	99.2			0.55		10.45
	13:43:50	100			1.00		5.72
	13:47:00	101			1.20		4.76
	13:50:00	102			1.32		4.33
	13:58:00	102.1			1.37		4.18
	14:06:00	102.2			1.33		4.30
14/07/2025	12:21:50	103	**R2**	**15**	0.800	0.125	5.36
	13:21:00	103.1			0.802		5.35
	14:57:00	103.2			0.802		5.35
	15:46:00	103.3			0.802		5.35
	12:28:00	104			0.603		7.11
	12:31:00	105			0.528		8.13
	12:39:20	105.1			0.532		8.07
	12:47:30	105.2			0.528		8.12
	12:56:30	106			1.005		4.27

	12:59:25	107			1.078		3.98
	13:07:00	107.1			1.062		4.04
	13:00:00	107.2			1.092		3.93
	13:25:00	108		**17.5**	0.802	0.146	6.25
	13:29:30	109			0.602		8.32
	13:32:40	110			0.545		9.2
	13:57:20	110.1			0.543		9.23
	14:04:41	110.2			0.543		9.23
	14:13:00	111			1.000		5.01
	14:17:30	112			1.202		4.17
	14:22:00	113			1.415		3.54
	14:35:50	113.1			1.440		3.48
	14:44:11	113.2			1.448		3.46
	14:34:00	114			1.400		3.58
	15:01:30	115		**20**	0.795	0.1667	7.20
	15:06:30	116			0.600		9.54
	15:08:00	117			0.557		10.28
	15:13:50	117.1			0.557		10.28
	15:20:00	117.2			0.559		10.23
	15:24:30	118			1.002		5.71
	15:27:30	119			1.199		4.77
	15:32:00	120			1.395		4.10
	15:35:00	121			1.603		3.57
	15:38:30	122			1.799		3.18
	15:40:40	123			2.000		2.86

D.3. Mesh Dependencies

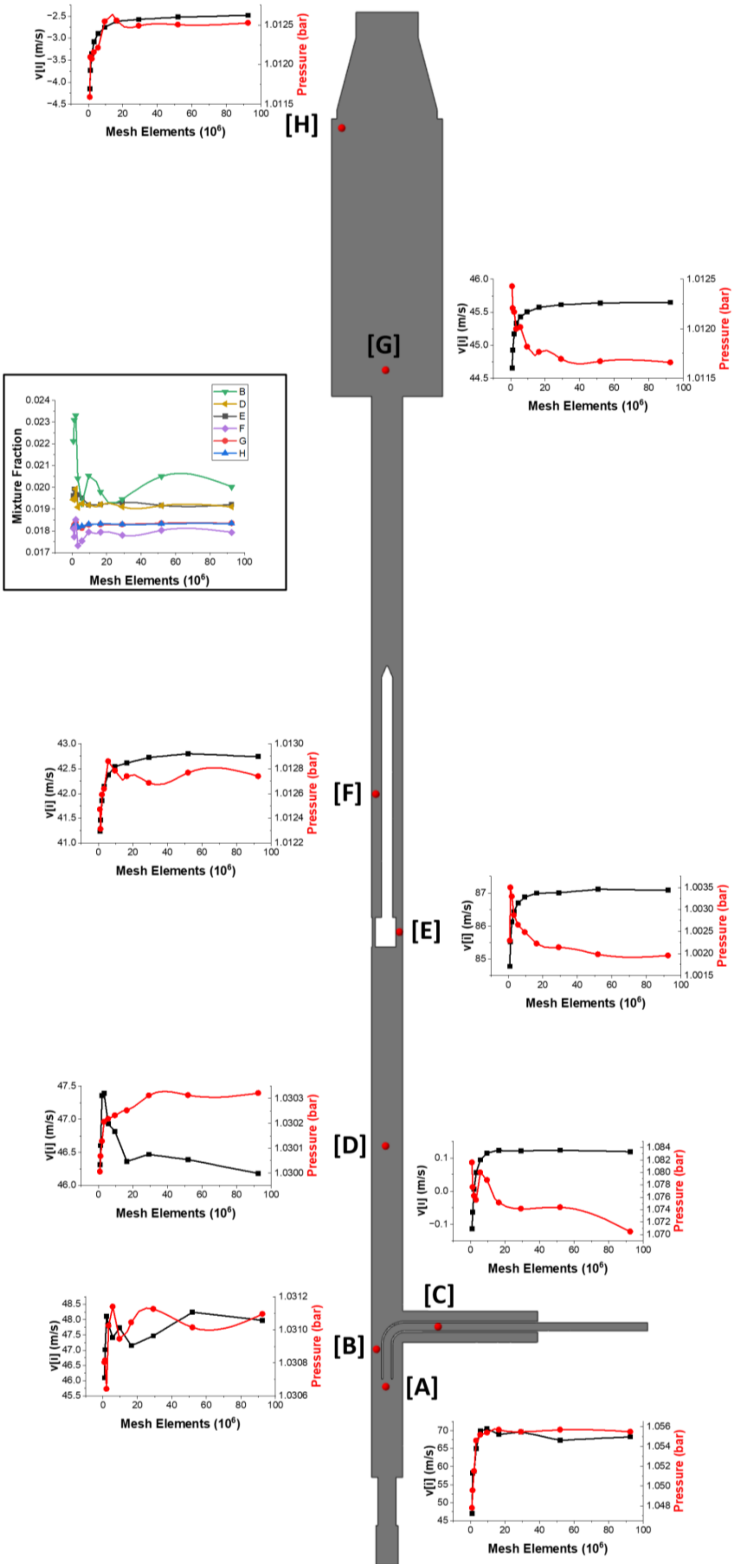

Figure D.10 - Mesh dependency results for initial CFD simulations in Section 3.2.3.

Iso_20

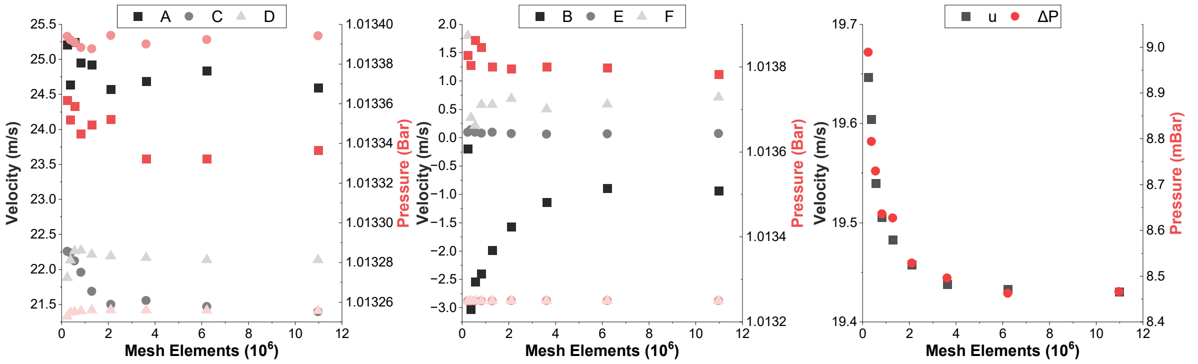

Iso_32

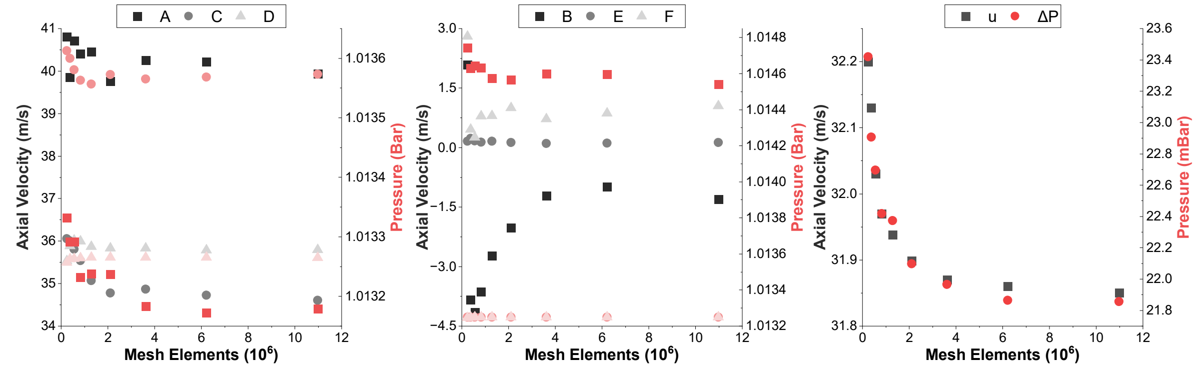

Iso_40

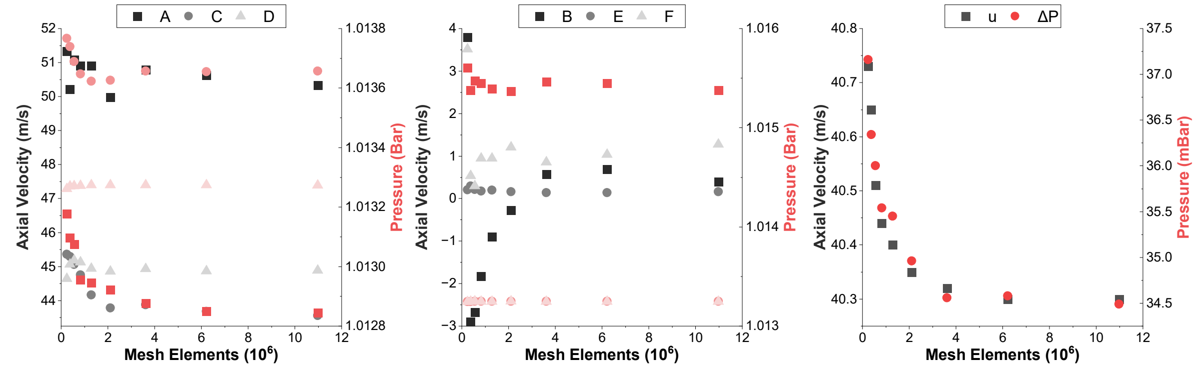

Iso_64

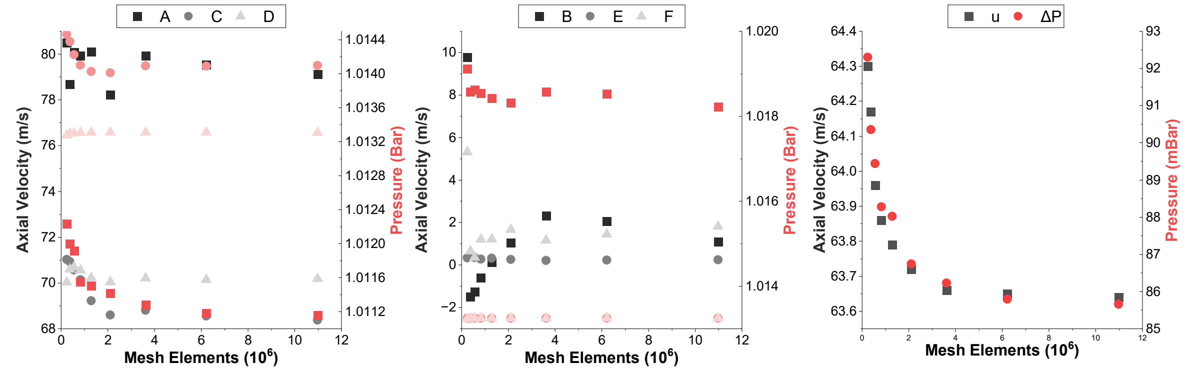

***Figure D.11** – Isothermal mesh dependency results for Iso_20, Iso_32, Iso_40 and Iso_64 simulations in Chapter 6. See Figure D.12 for point probe locations.*

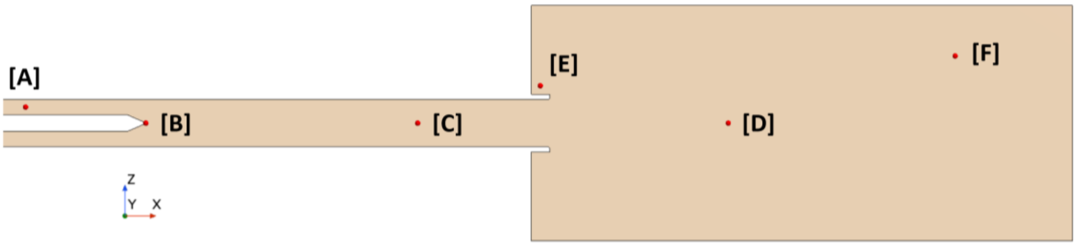

Figure D.12 - *Point Probe location for mesh dependency tests associated with Figure D.11.*

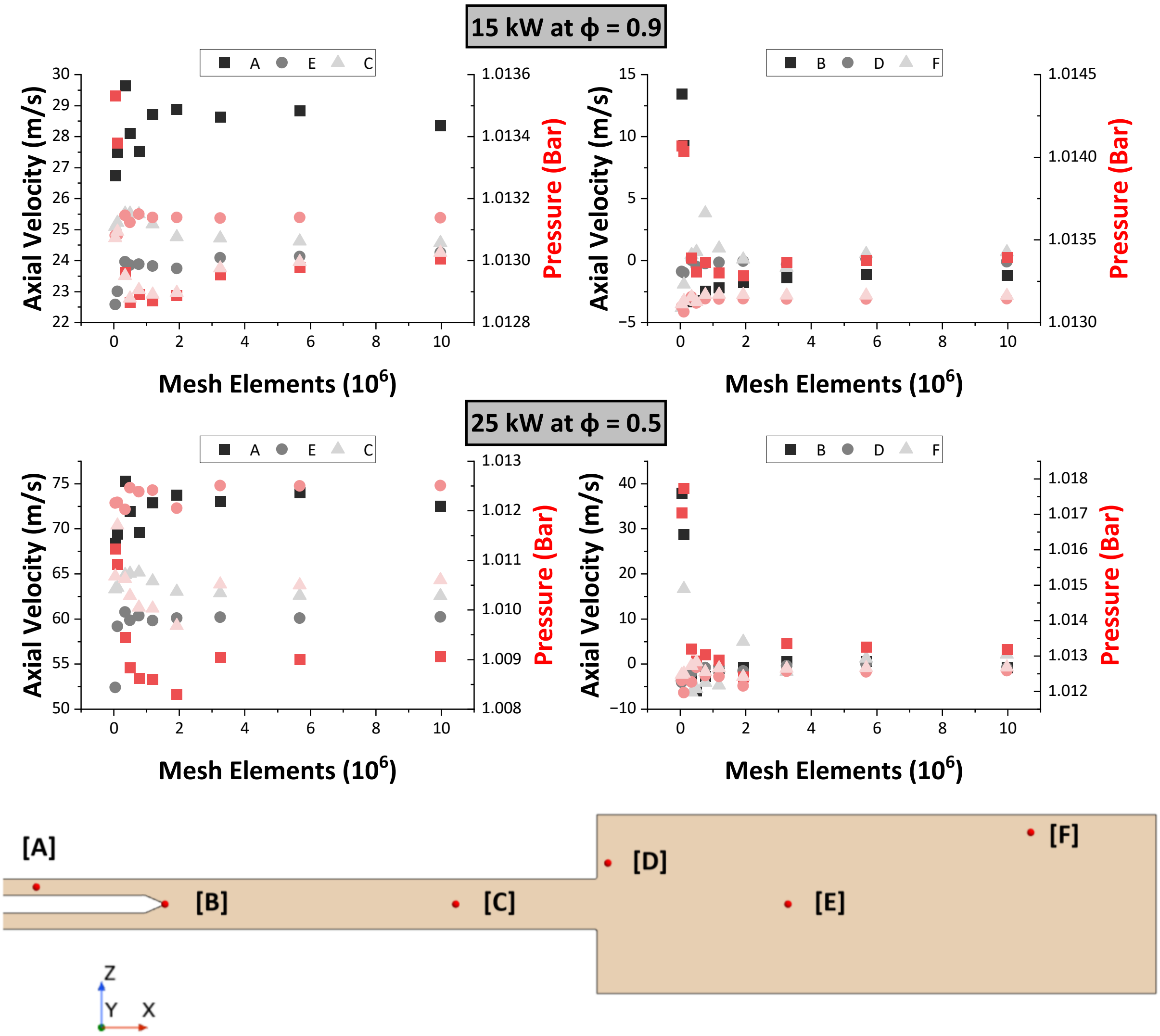

Figure D.13 - *Mesh dependency results for the most extreme reacting cases in Chapter 6 [top]. Point probe locations [bottom].*

D.4. Chapter 5 Supplementary Data

In Section D.4 supplementary data to the test campaign outlined in Chapter 5 are presented. In particular the “raw” colour mapped and time averaged OH* chemiluminescence images for all thermal powers (Figure D.14 and Figure D.15) and thermocouple data for all test points.

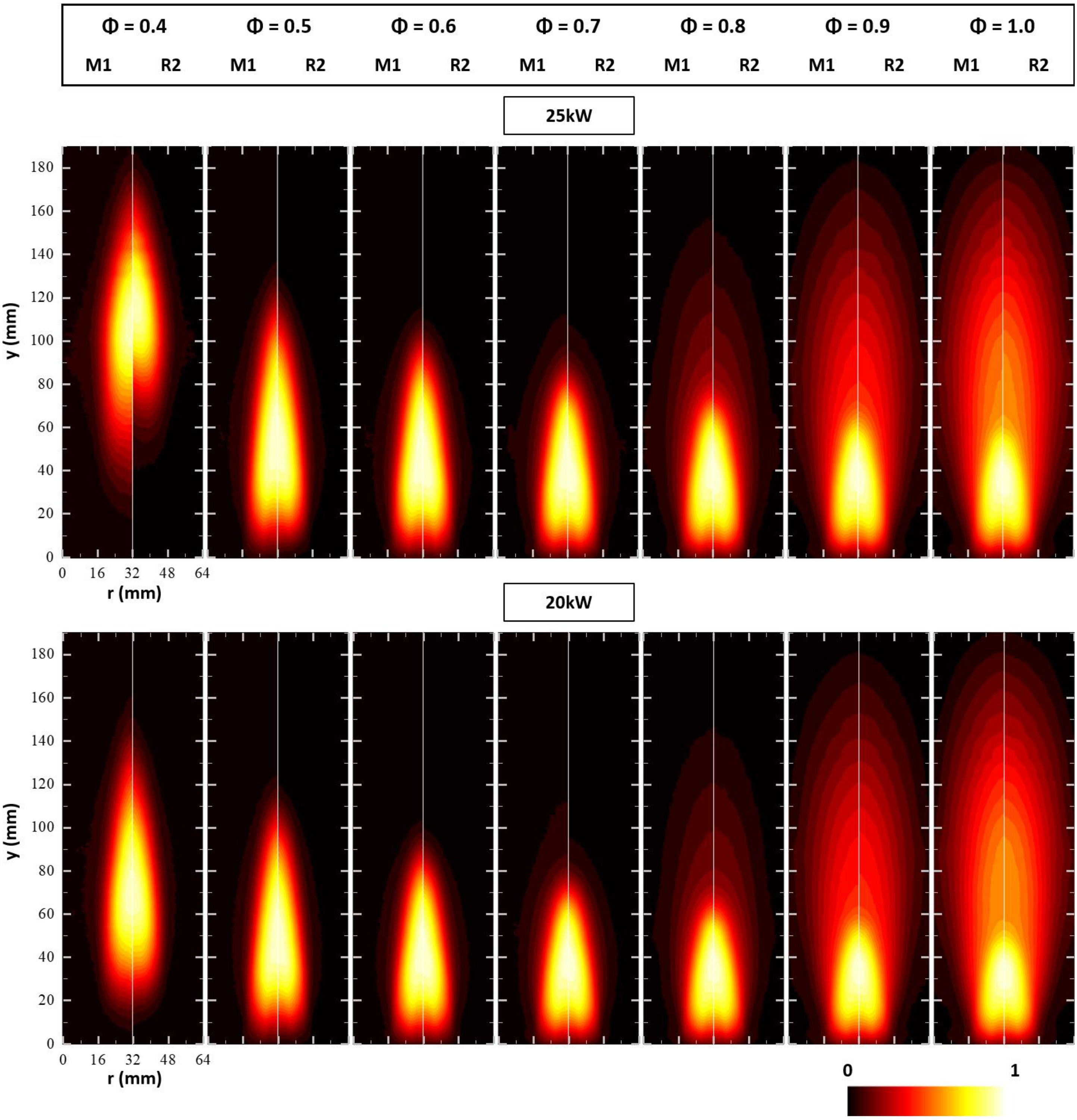

Figure D.14 *– Raw OH* chemiluminescence images for 25 kW [top] and 20 kW [bottom] thermal powers over a range of φ. Colormap normalised to maximum OH* intensity in each half image (code available in appendix A.4). M1 results shown on the left and R2 results shown on the right for each condition.*

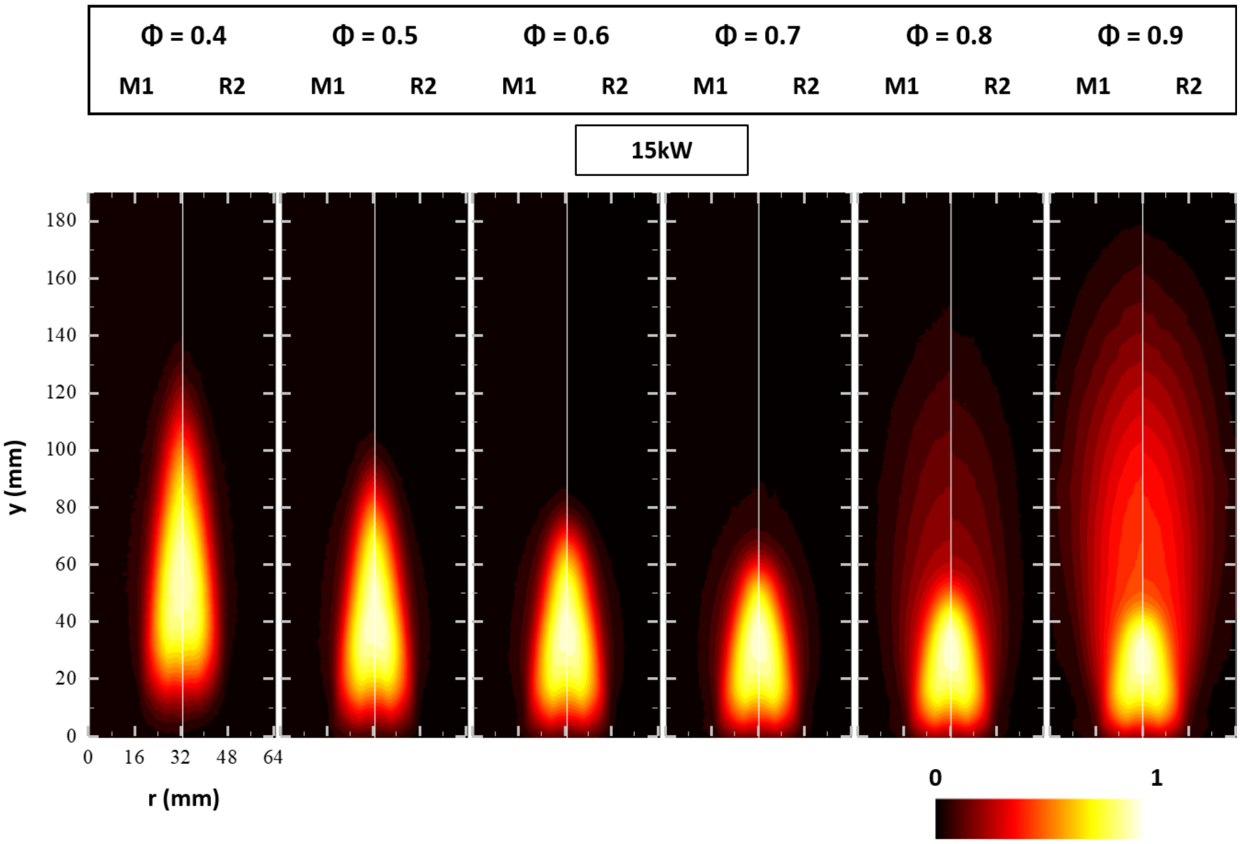

Figure D.15 *– Raw OH* chemiluminescence images for 15 kW over a range of φ. Colormap normalised to maximum OH* intensity in each half image (code available in appendix A.4). M1 results shown on the left and R2 results shown on the right for each condition.*

Thermocouple data was collected throughout the test campaign outlined in Chapter 5. Once each test condition has stabilised, both from an MFC and temperature standpoint, temperature readings were taken for 10 seconds. However, data could not be collected for test points at the outer edges of the stability map due to instability. K-type thermocouples (± 2.2 K) were used throughout. The 10 second average thermocouple data for each test point at each measured location is presented in Table D.8, Table D.9 and Table D.10. A thermocouple was positioned against the external wall of the exhaust sampling probe to measure the flue gas entry temperature into the heated sampling line (TC_{SP}). The location of the remaining thermocouples can be found in Figure D.16.

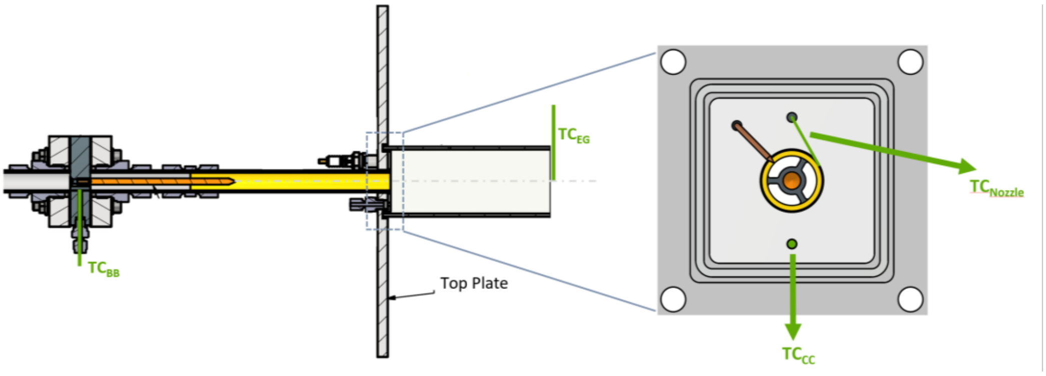

Figure D.16 *- Side [left] and top [right] view of PJB with thermocouple probe locations.*

Table D.8 - Thermocouple data for PJB stability map test campaign with M1 insert on 26/11/2024.

Test Point	TP (kW)	ϕ	TC$_{BB}$ (°C)	TC$_{CC}$ (°C)	TC$_{EG}$ (°C)	TC$_{Nozzle}$ (°C)	TC$_{SP}$ (°C)
1	20	0.71	11.5	421.4	1125	607	41.8
2		0.60	11.5	426.6	1068	584	41.3
3		0.50	11.3	408.9	1007	553	37.5
4		0.40	10.9	354.1	899.9	483	23.3
6		0.80	11.6	323.4	1143	557	20.2
7		0.89	11.7	423.4	1194	695	33.6
8		1.00	11.9	478.9	1219	726	43.0
9	15	0.70	11.8	278.4	1048	466	20.3
10		0.60	11.7	350.5	1021	519	26.3
11		0.50	11.7	361.0	966.7	507	30.3
12		0.40	11.4	350.0	877.1	474	27.9
14		0.79	11.8	323.5	1105	576	22.2
15		0.90	11.9	394.0	1149	679	28.7
18	25	0.70	11.5	405.5	1145	592	28.0
19		0.60	11.3	434.3	1094	604	34.6
20		0.50	11.0	434.2	1023	584	36.2
21		0.40	10.4	392.8	868.1	521	30.4
23		0.80	11.5	418.2	1197	630	29.2
24		0.90	11.7	483.3	1242	719	44.1
25		0.99	11.8	506.1	1268	738	49.2

Table D.9 - Thermocouple data for PJB stability map test campaign with R2 insert on 27/11/2024.

Test Point	TP (kW)	ϕ	TC$_{BB}$ (°C)	TC$_{CC}$ (°C)	TC$_{EG}$ (°C)	TC$_{Nozzle}$ (°C)	TC$_{SP}$ (°C)
45	20	0.71	10.6	226.6	1099	431	100.1
46		0.60	10.6	341.8	1057	513	104.3
47		0.50	10.4	348.8	989	488	105.6
48		0.40	10.0	325.7	900	463	105.5
50		0.80	10.5	297.9	1143	487	105.9
51		0.89	10.7	395.5	1199	620	108.6
52		0.99	10.8	451.2	1224	692	109.7
53	15	0.70	10.7	362.4	1064	529	109.5
54		0.60	10.6	370.6	1021	520	109.7
55		0.51	10.6	361.1	964	490	109.3
56		0.40	10.3	340.7	872	459	109.2
58		0.79	10.7	328.1	1099	523	109.0
59		0.89	10.8	394.9	1144	632	111.0
60		1.02	10.8	444.9	1156	687	111.1

61	25	0.70	10.3	410.1	1136	568	110.7
62		0.60	10.1	431.6	1087	576	111.3
63		0.50	9.7	411.7	1017	546	110.8
65		0.40	9.1	319.8	866	457	110.2
67		0.80	10.1	368.7	1187	568	111.3
68		0.90	10.2	434.4	1237	647	112.1
69		0.99	10.3	475.5	1268	700	113.3

Table D.10 - Thermocouple data for PJB flashback tests with both inserts (02/12/2024).

Test Point	TP (kW)	ϕ	Insert	TC_{BB} (°C)	TC_{CC} (°C)	TC_{EG} (°C)	TC_{Nozzle} (°C)
80	15	1.02	R2	12.1	438	1157	690
81	12.5	0.69	R2	12.1	343	1030	513
83	10	0.69	R2	12.3	295	989	465
85	12.5	0.94	R2	12.5	370	1053	557
86	10	0.79	R2	12.6	346	1000	519
87	15	0.94	M1	12.5	349	1095	561
88	12.5	0.69	M1	12.5	344	1036	526
89	12.5	0.79	M1	12.5	372	910	559
90	10	0.59	M1	12.4	267	939	399
92	12.5	0.79	M1	12.4	348	1043	537
93	10	0.67	M1	12.4	280	959	431

D.5. Chapter 7 Supplementary Data

In Section D.5 supplementary data to the test campaign outlined in Chapter 7 are presented. In particular the "raw" colour mapped and time averaged OH* chemiluminescence images for all thermal powers (Figure D.17, Figure D.18 and Figure D.19) and thermocouple data for all test points.

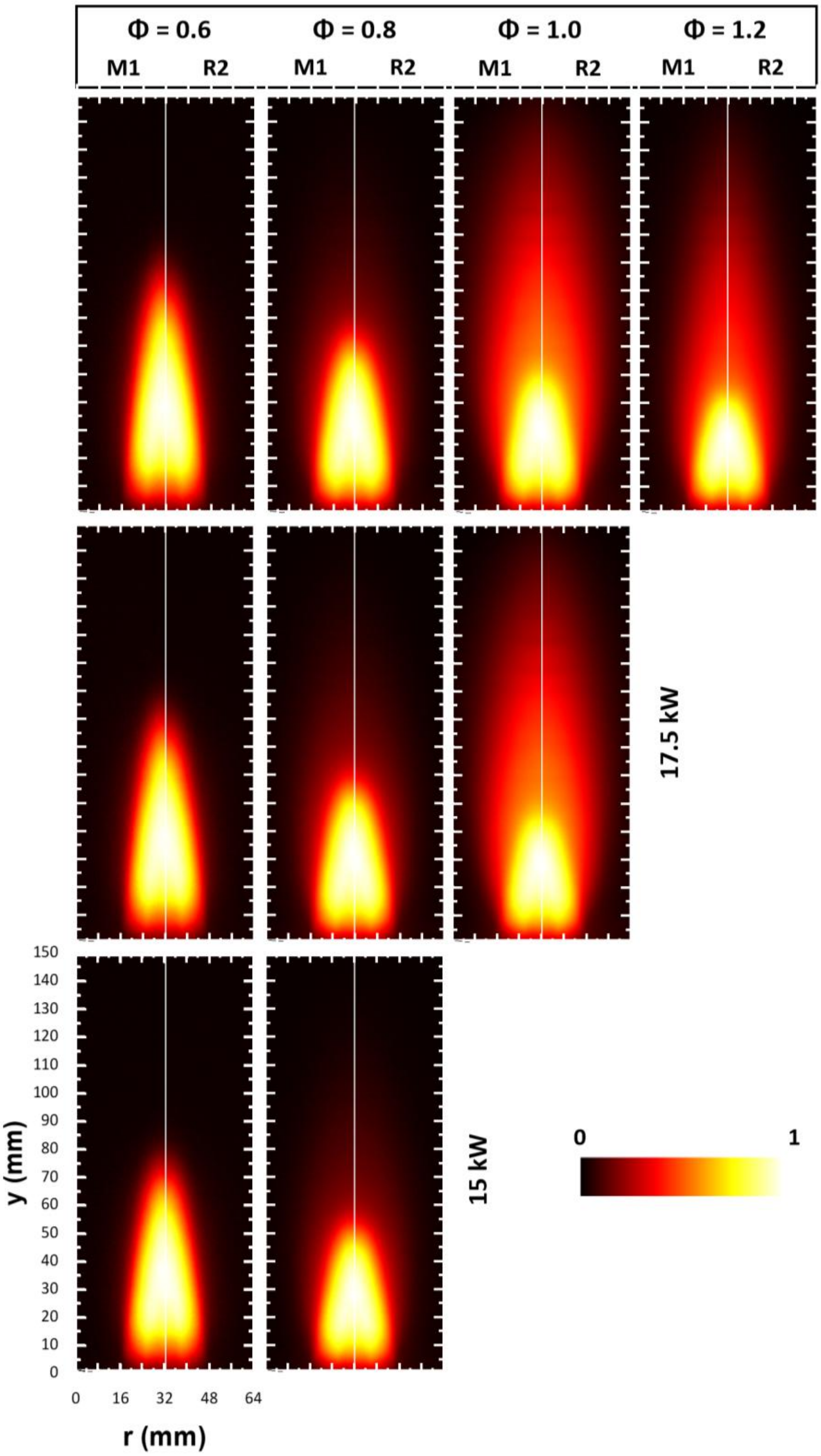

Figure D.17 – *PJB Raw OH* chemiluminescence images for 20 kW [top], 17.5 kW [middle] and 15 kW [bottom] thermal powers over a range of φ. Colormap normalised to maximum OH* intensity in each half image (code available in appendix A.4). M1 results shown on the left and R2 results shown on the right for each condition.*

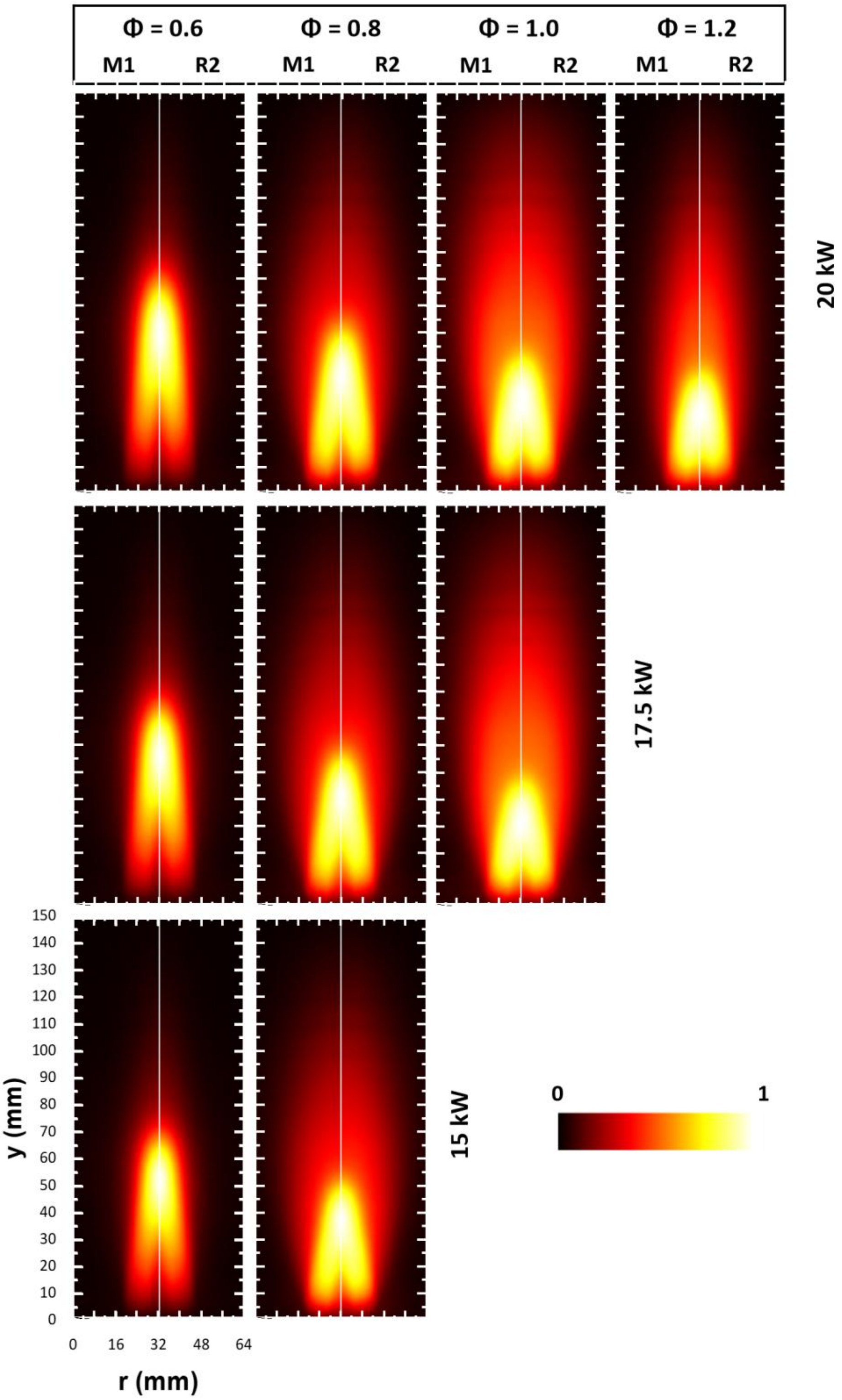

__Figure D.18__ - JICF Raw OH chemiluminescence images for 20 kW [top], 17.5 kW [middle] and 15 kW [bottom] thermal powers over a range of φ. Colormap normalised to maximum OH* intensity in each half image (code available in appendix A.4). M1 results shown on the left and R2 results shown on the right for each condition.*

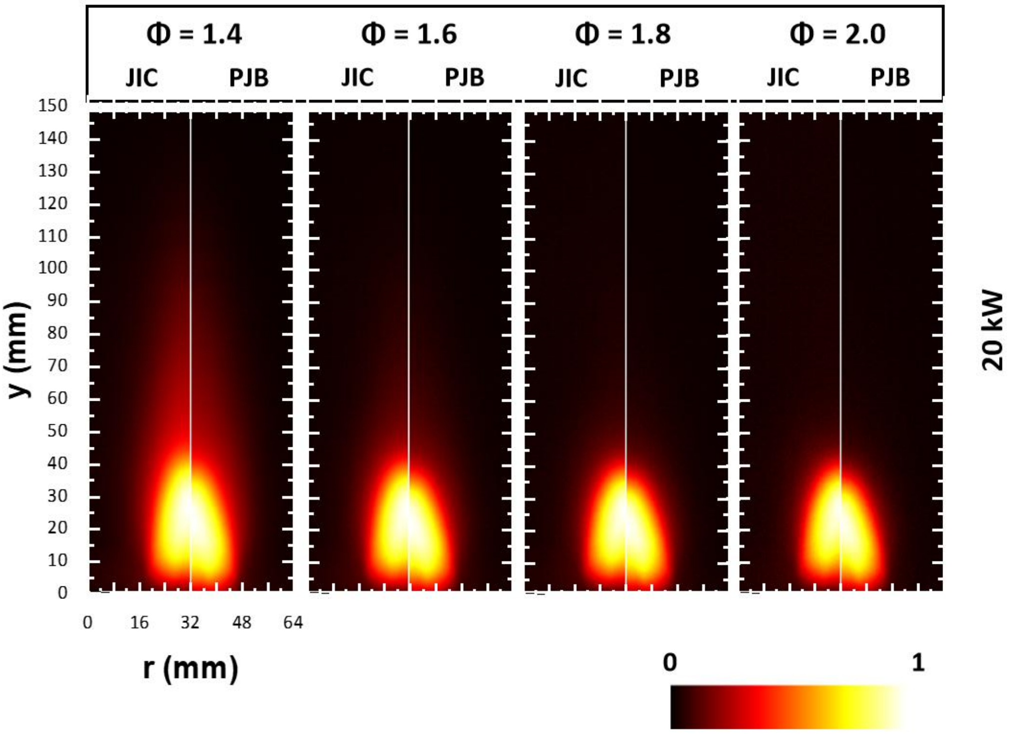

Figure D.19 – Comparison of JICF [left half flame] and PJB [right half flame] raw OH data with R2 insert. Colormap normalised to maximum OH* intensity in each half image (code available in appendix A.4).*

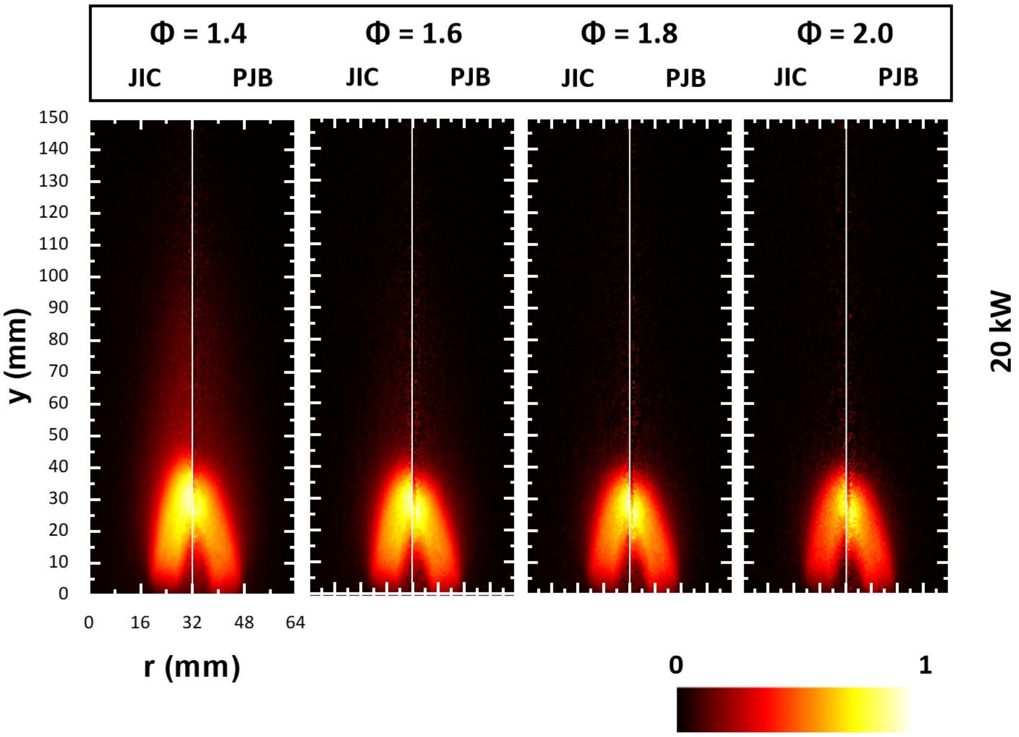

Figure D.20 - Comparison of JICF [left half flame] and PJB [right half flame] Abel Transformed OH data with R2 insert. Colormap normalised to maximum OH* intensity in each half image (code available in appendix A.4).*

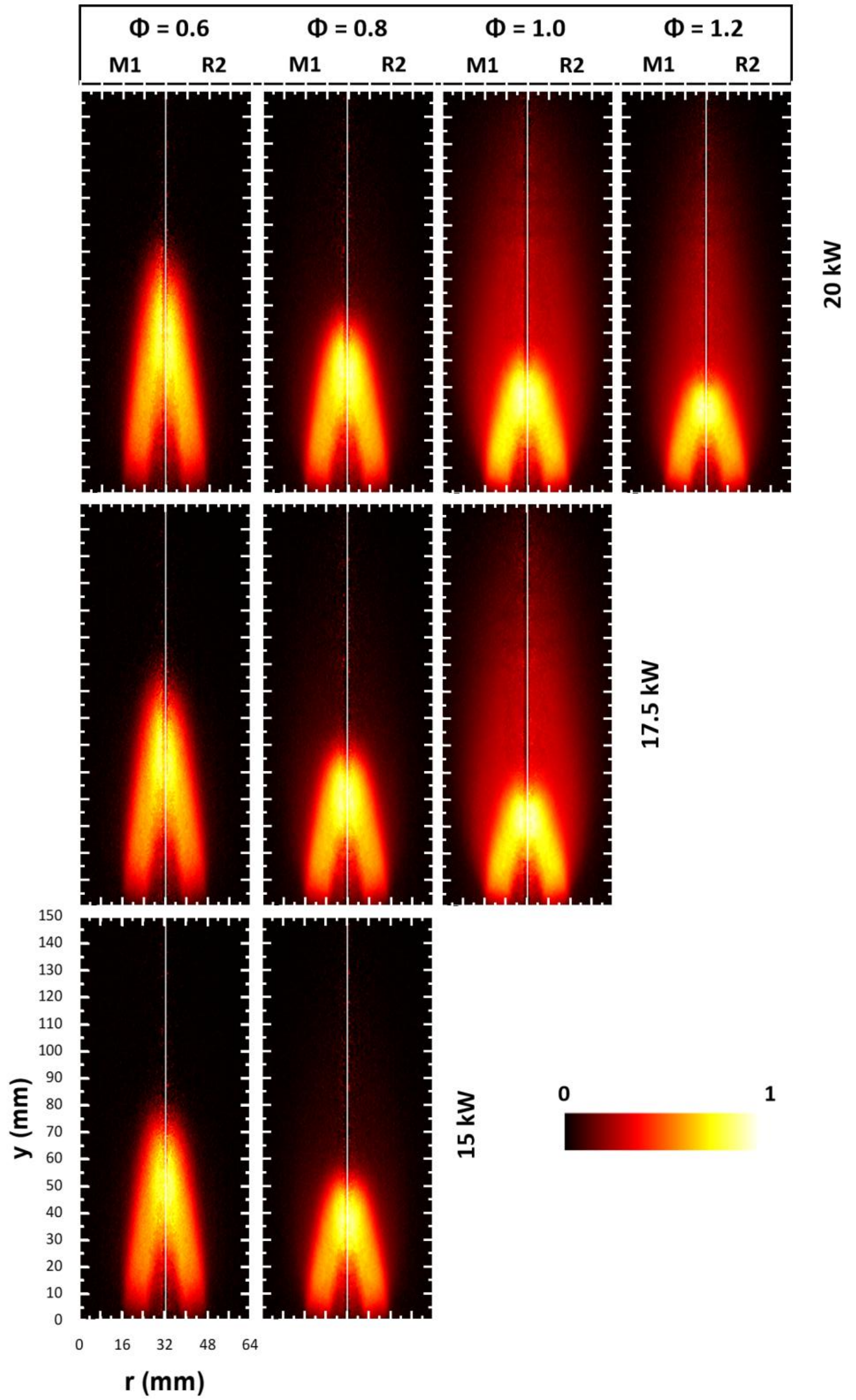

Figure D.21 *- PJB Abel Transformed OH* chemiluminescence images for 20 kW [top], 17.5 kW [middle] and 15 kW [bottom] thermal powers over a range of φ. Colormap normalised to maximum OH* intensity in each half image (code available in appendix A.4). M1 results shown on the left and R2 results shown on the right for each condition.*

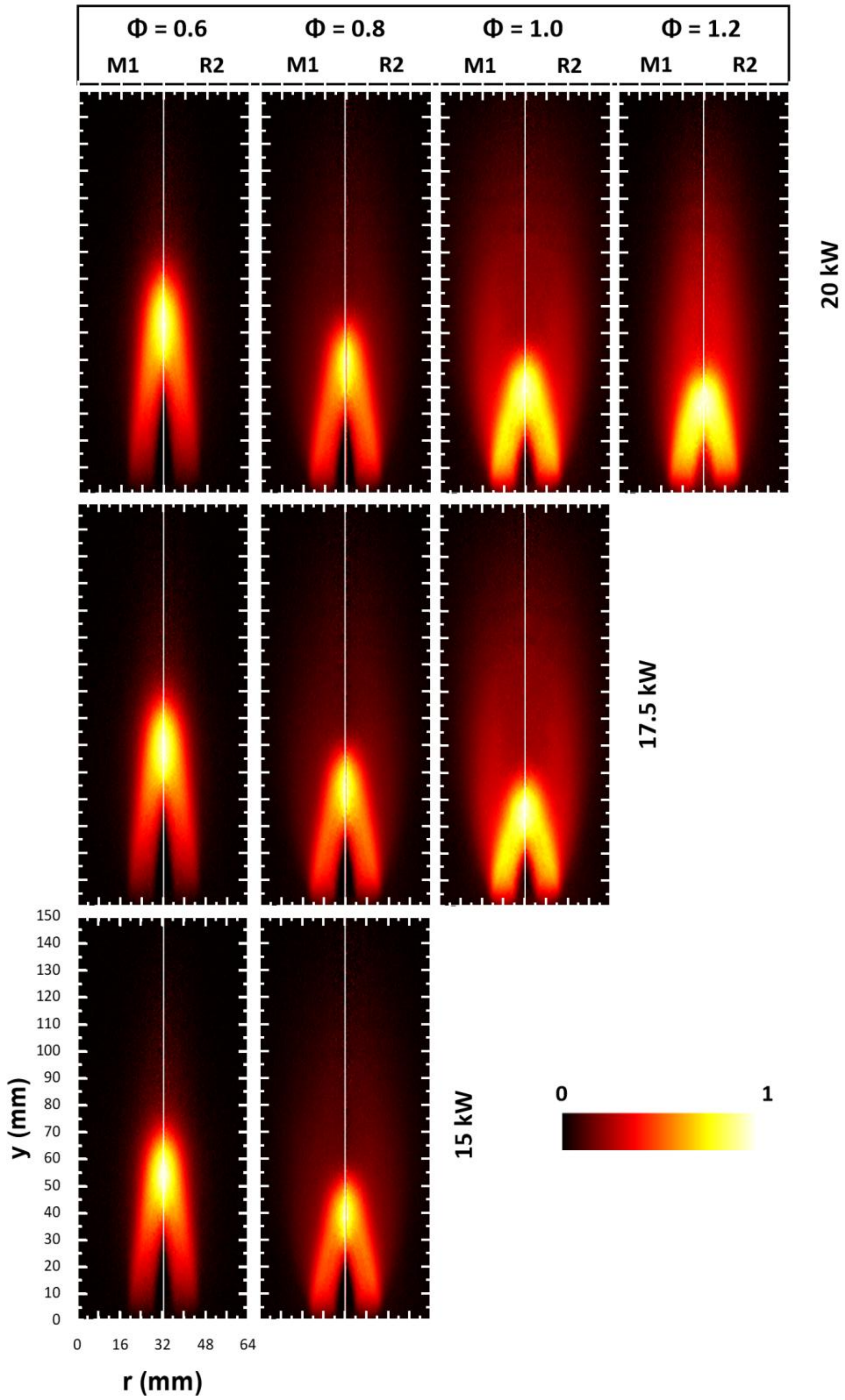

Figure D.22 *- JICF Abel Transformed OH* chemiluminescence images for 20 kW [top], 17.5 kW [middle] and 15 kW [bottom] thermal powers over a range of φ. Colormap normalised to maximum OH* intensity in each half image (code available in appendix A.4). M1 results shown on the left and R2 results shown on the right for each condition.*

The thermocouple data shown in the following four tables was obtained using the methodology and measurement locations outlined in Section D.4.

__Table D.11__ - M1 PJB rich flashback thermocouple data (collected on 02/07/2025).

Test Point	TP (kW)	ϕ	TC_{BB} (°C)	TC_{CC} (°C)	TC_{EG} (°C)	TC_{Nozzle} (°C)
32	15	0.80	18.70	325	1073	653
33		0.60	19.80	291	824	525
33.1		0.60	19.6	307	950	530
33.2		0.60	20.20	292	880	533
33.3		0.60	20.50	341	961	527
35		0.46	19.00	240	662	392
37	17.5	0.80	19.90	369	1110	662
38		0.60	19.70	326	992	544
39		0.50	19.40	270	845	434
41		0.99	20.00	404	1174	735
43	20	0.80	20.20	368	1116	669
44		0.60	20.00	334	870	556
45		0.50	19.80	280	777	433
47		1.00	20.20	410	1188	752
48		1.20	20.50	440	1166	753

__Table D.12__ – R2 PJB rich flashback thermocouple data (collected on 03/07/2025).

Test Point	TP (kW)	ϕ	TC_{BB} (°C)	TC_{CC} (°C)	TC_{EG} (°C)	TC_{Nozzle} (°C)
50	15	0.60	18.10	278	774	478
50.1		0.60	20.00	303	946	466
50.2		0.60	19.30	288	944	470
50.3		0.60	19.98	336	940	480
51		0.49	18.00	243	693	398
53		0.80	18.70	356	1058	604
54		1.00	18.80	415	1116	701
56	17.5	0.80	19.90	384	1086	603
57		0.60	19.40	345	970	495
58		0.52	19.00	291	897	413
60		1.00	19.40	428	1147	680
61		1.20	19.40	444	1130	685
62		1.40	19.60	438	1089	679
63	20	0.80	19.45	382	1100	616
64		0.60	19.10	340	980	498
65		0.53	19.10	293	919	434
67		1.00	19.60	434	1170	690
68		1.20	19.80	448	1160	690
69		1.40	20.00	443	1124	689
70		1.60	20.20	425	1095	666
71		1.79	20.40	412	1070	647
72		2.00	20.50	395	1051	618

Table D.13 *- JICF M1 rich flashback thermocouple data (collected on 11/07/2025).*

Test Point	**TP (kW)**	**ϕ**	**TC_{BB} (°C)**	**TC_{CC} (°C)**	**TC_{EG} (°C)**	**TC_{Nozzle} (°C)**
88	15	0.80	20.28	406	1080	580
88.1		0.80	21.30	408	1060	580
88.2		0.80	22.10	412	1054	560
88.3		0.80	23.00	438	1060	564
89		0.60	20.31	345	490	996
92	17.5	0.80	21.40	424	1088	595
93		0.60	21.60	349	1006	511
95		1.00	21.95	482	1140	659
97	20	0.80	22.30	444	1106	589
98		0.60	22.10	368	1016	504
100		1.00	22.60	485	1170	660
101		1.20	22.70	484	1158	666

Table D.14 *- JICF R2 rich flashback thermocouple data (collected on 14/07/2025).*

Test Point	**TP (kW)**	**ϕ**	**TC_{BB} (°C)**	**TC_{CC} (°C)**	**TC_{EG} (°C)**	**TC_{Nozzle} (°C)**
103	15	0.80	20.90	330	1051	544
103.1		0.80	21.80	374	1044	520
103.2		0.80	22.45	388	1047	527
103.3		0.80	22.70	393	1043	520
104		0.60	20.90	286	966	460
106		1.00	21.50	433	1096	605
108	17.5	0.80	21.90	387	1075	536
109		0.60	21.80	326	988	460
111		1.00	22.00	442	1132	596
112		1.20	22.30	441	1130	584
114		1.40	22.50	426	1098	574
115	20	0.80	22.40	397	1097	544
116		0.60	22.45	329	999	459
118		1.00	22.44	442	1160	590
119		1.20	22.60	448	1166	590
120		1.40	22.60	427	1131	580
121		1.60	22.70	410	1100	563
122		1.80	22.90	392	1080	532
123		2.00	23.00	380	1060	503

APPENDIX E. Measured Roughness

Surface roughness values for 8M and 8R swirlers measured by Runyon et al. [42]. There values were utilised to calculate k_s for the numerical simulations performed in Chapter 4.

***Table E.1** - Average surface roughness measurements for the 8R and 8M swirler (data from Runyon et a* [42]).

	Ra (μm)		**Rq (μm)**		**Rz (μm)**	
	8R	**8M**	**8R**	**8M**	**8R**	**8M**
Nozzle Inner	8.88	1.39	10.97	1.88	53.61	8.96
Swirler base	11.09	1.76	14.92	3.31	78.11	11.21
Swirler Curve	8.31	0.67	10.29	1.04	50.01	4.27
Swirler Flat Length	8.59	0.97	10.64	1.24	54.06	6.12